# Silicon-Based Light Emitters Towards Quantum Devices At Telecom Frequency

Mario Khoury

NNT/NL:2022AIXM0364/042ED352

# THÈSE DE DOCTORAT

Soutenue à Aix-Marseille Université

le **09/11/2022** par


# Mario KHOURY


## Silicon-Based Light Emitters Towards Quantum Devices At Telecom Frequency

**Discipline**
Physique et Sciences de la Matière

**Spécialité**
Matière Condensée et Nano-Sciences

**École Doctorale ED 352**
Physique et Sciences de la Matière

**Laboratoire/Partenaires de Recherche**
Institut Matériaux Microélectronique et Nanosciences de Provence

### Composition du Jury

| | |
|---|---|
| **Francesco BICCARI**<br>Université de Florence | Rapporteur<br>(Non-membre du Jury) |
| **Giordano SCAPPUCCI**<br>QuTech, TU Delft | Rapporteur |
| **Stefano SANGUINETTI**<br>Université de Milan | Examinateur |
| **Lydie FERRIER**<br>Université de Lyon | Examinatrice |
| **Fabienne MICHELINI**<br>Université Aix-Marseille | Présidente du Jury |
| **Marco ABBARCHI**<br>Université Aix-Marseille | Directeur de thèse |
| **Isabelle BERBEZIER**<br>Université Aix-Marseille | Co-Directrice de thèse |

# Affidavit

I, undersigned, **Mario KHOURY**, hereby declare that the work presented in this manuscript is my own work, carried out under the scientific direction of **Marco ABBARCHI** and **Isabelle BERBEZIER** in accordance with the principles of honesty, integrity and responsibility inherent to the research mission. The research work and the writing of this manuscript have been carried out in compliance with both the french national charter for Research Integrity and the Aix-Marseille University charter on the fight against plagiarism.
This work has not been submitted previously either in this country or in another country in the same or in a similar version to any other examination body.

Marseille, Tuesday, **August 21$^{th}$ 2022**

# Liste de Publications et Participation aux Conférences

### Liste des publications réalisées dans le cadre du projet de thèse:

1. **Mario Khoury**, Hugo Quard, Tobias Herzig, Jan Meijer, Sebastian Pezzagna, Sebastien Cueff, Hai Son Nguyen, Nicolas Chauvin, Marco Abbarchi, Thomas Wood, "Light emitting Si-based Mie resonators: towards a Huygens source of quantum emitters", Advanced Optical Materials, p. 2201295, August 2022, https://doi.org/10.1002/adom.202201295.

2. **M. Khoury** and M. Abbarchi, "A bright future for silicon in quantum technologies", Journal of Applied Physics, vol. 131, p. 200901, May 2022, https://doi.org/10.1063/5.0093822.

3. D. Toliopoulos, **M. Khoury**, M. Bouabdellaoui, N. Granchi, J.-B. Claude, A. Benali, I. Berbezier, D. Hannani, A. Ronda, J. Wenger, M. Bollani, M. Gurioli, S. Sanguinetti, F. Intonti, and M. Abbarchi, "Fabrication of spectrally sharp Si-based dielectric resonators: combining etaloning with Mie resonances", Optics Express, vol. 28, p. 37734, Dec 2020, https://doi.org/10.1364/OE.409001.

4. N. Granchi, M. Montanari, A. Ristori, **M. Khoury**, M. Bouabdellaoui, C. Barri, L. Fagiani, M. Gurioli, M. Bollani, M. Abbarchi, and F. Intonti, "Near-field hyper-spectral imaging of resonant Mie modes in a dielectric island", APL Photonics, vol. 6, p. 126102, Dec 2021, https://doi.org/10.1063/5.0070626.

5. Y. Baron, A. Durand, T. Herzig, **M. Khoury**, S. Pezzagna, J. Meijer, I. Robert-Philip, M. Abbarchi, J.-M. Hartmann, S. Reboh, J.-M. Gérard, V. Jacques, G. Cassabois, and A. Dréau, "Single G centers in silicon fabricated by co-implantation with carbon and proton," Applied Physics Letters, Vol. 121, No. 8, p. 084003, August 2022, https://doi.org/10.1063/5.0097407.

6. Y. Baron, A. Durand, P. Udvarhelyi, T. Herzig, **M. Khoury**, S. Pezzagna, J. Meijer, I. Robert-Philip, M. Abbarchi, J.-M Hartmann, V. Mazzocchi, J.-M Gérard, A. Gali, V. Jacques, G. Cassabois, and A. Dréau, "Detection of single w-centers in silicon", ACS Photonics, Vol. 9, No. 7 p. 2337-2345 July 2022, https://doi.org/10.1021/acsphotonics.2c00336.

## Participation aux conférences et écoles d'été au cours de la période de thèse:

1. **Oral Presentation** *"Fabrication of Si-based dielectric resonators: Combining Etaloning with Mie resonances"* presented at the 2nd Edition of World Nanotechnology Conference / $19^{th}$ - $20^{th}$ April, 2021 - University of Guyana, South America.

2. **Poster** *"Telecom-frequency, silicon-based impurities embedded in dielectric Mie resonators towards directional emission"* presented at the 31st International Conference on Defects in Semiconductor / $26^{th}$ - $30^{th}$ July, 2021 - University of Oslo.

3. **Oral Presentation** *"Telecom-frequency, silicon-based impurities embedded in dielectric Mie resonators towards directional emission"* presented at SPIE Photonics Europe / $3^{rd}$ - $7^{th}$ April, 2022 - Strasbourg, France.

4. **Poster Competition** *"Light Emitting Si-based Mie Resonators: Towards A Huygens Source Of Quantum Emitters"* presented to the IM2NP day - $15^{th}$ June 2022 - University of Marseille.

5. **Summer School** on *"Nanosciences and Nanotechnologies"* in Carry le Rouet, South of France, 19th to 24th June 2022, organized by university of Madrid, Barcelona, Rome, Tubingen, and Aix Marseille.
   **Poster Session** *"Light Emitting Si-based Mie Resonators: Towards A Huygens Source Of Quantum Emitters"*

# Abstract

The aim of this thesis it to explore the potential of complex carbon impurities in silicon (G-centers) for applications in quantum technologies. This point defect was originally highlighted in carbon-rich Si samples undergoing high-energy electron irradiation followed by high temperature annealing. A key feature of G-centers is their infrared emission, matching the important optical telecommunications wavelength O-band spreading between 1260-1360 nm. Through my PhD work we have demonstrated that we are able to create individual G-centers by ion implantation in conventional silicon on insulator, isotopically purified $^{28}$Si on insulator, and embed these emitters in photonic nanostructures such as dielectric Mie resonators. The creation of single defects was demonstrated by measuring the anti-bunching in light intensity-correlation (second order auto-correlation function). We developed a low-resolution optical lithography and plasma etching method joined with solid state dewetting (defined in chapter 4.3) of monocrystalline, ultra-thin, silicon on insulator to form monocrystalline, atomically-smooth, Mie resonators in well-controlled and large, periodic arrays. By integrating light emitting G-centers within the Si-based antennas we engineered the light emission by tuning carbon dose, beam energy and islands size in order to optimize the coupling between the emitters and the Mie resonances in space and frequency. Directional (Huygens-like) light emission at 120 K was demonstrated experimentally and confirmed by Finite Difference Time Domain simulations. We estimate that, with an optimal coupling of the G-centers emission with the resonant antennas, a collection efficiency of about 90% can be reached using a conventional objective lens. The integration of these telecom-frequency emitters in resonant antennas is relevant for their efficient exploitation in quantum optics applications and more generally to Si-based photonic metasurfaces.

***Keywords:*** *Mie Resonators, Light Emitters in Silicon, G-Centers, Telecom Frequency*

# Résumé

L'objectif de cette thèse est d'explorer le potentiel des impuretés complexes de carbone dans le silicium (G-centers) pour des applications dans les technologies quantiques. Ce défaut ponctuel a été initialement mis en évidence dans des échantillons de Si riches en carbone soumis à une irradiation électronique à haute énergie suivie d'un recuit à haute température. Une caractéristique clé des centers-G est leur émission infrarouge, correspondant à l'importante longueur d'onde de la bande O des télécommunications optiques qui s'étend entre 1260-1360 nm. Dans mon travail de doctorat, nous avons démontré que nous sommes capables de créer des centres G individuels par implantation ionique dans du silicium conventionnel sur un isolant, du $^{28}$Si isotopiquement purifié sur isolant, et des nanostructures photoniques telles que des résonateurs diélectriques de Mie vers des sources intégrées de photons uniques dans le silicium émettant dans la gamme de longueur d'onde des télécommunications. La création de défauts uniques a été démontrée en mesurant l'anti-bouclage dans la corrélation intensité-lumière (fonction d'autocorrélation de second ordre). J'ai mis au point une méthode de lithographie optique à basse résolution et de gravure au plasma, associée à un démouillage à l'état solide (Défini dans le Chapitre 4.3) de silicium cristallin ultra-mince sur isolant, afin de former des résonateurs de Mie monocristallins, atomiquement lisses, à base de silicium, sous forme de grands réseaux périodiques bien contrôlés. En intégrant des centres G émetteurs de lumière dans les antennes en Si, j'ai conçu l'émission de lumière en réglant la dose de carbone, l'énergie du faisceau et la taille des îlots afin d'optimiser le couplage entre les émetteurs et les résonances de Mie. L'émission de lumière directionnelle (vers l'avant) à 120 K a été démontrée expérimentalement et confirmée par des simulations dans le domaine temporel des différences finies. Nous estimons qu'avec un couplage optimal de l'émission des centres G avec les antennes résonantes, une efficacité de collecte d'environ 90% peut être atteinte en utilisant un objectif conventionnel. L'intégration de ces émetteurs de fréquences télécom dans des antennes résonantes est pertinente pour leur exploitation efficace dans des applications d'optique quantique et plus généralement pour les métasurfaces photoniques à base de Si.

***Mots clés:*** *Mie Résonateurs, Emetteurs De Lumière En Silicium, Centres G, Fréquence De Télécommunication*

# Acknowledgement

It is quite difficult to believe that the time has come to write this part of the thesis. And I have to say, while the thesis was actually quite easy to write, this part is giving me problems and making me somehow scared of the empty space on the paper. Not because I don't know what to write, but because there are so many people that I am grateful to, and I am afraid that I will forget some of them, even though they played an important role in my life during the previous three and something years. This was an amazing journey, during which I have met so many wonderful people, each of whom has taught me something valuable. And while I will keep them always in my mind and heart, unfortunately, it will be impossible to mention everyone, which is why, first and foremost I would like to thank to all those people, whose names are not mentioned in the next lines. Please don't feel excluded; I am eternally grateful to all of you!

Foremost, I would like to express my gratitude to my supervisor, **Marco ABBARCHI**. Thank you for your friendship, kindness, optimism, motivation, enthusiasm, trust, patience, guidance, continuous support and immense knowledge. Thank you for all the discussions that we had and all the knowledge that I have obtained because of them. Also thank you for letting me make mistakes, from which I think I learned more than from all the times I have been right about something. Thanks for teaching me, how to be professional, accurate (even for the small details) and perfect by doing things. Thanks for teaching me, how to be a leader and not a boss. I am so glad and so proud to be one of your students, as I could never have imagined having a better supervisor.

Special gratitude also goes to Isabelle Berbezier, for being a part of this thesis. Thank you for your suggestions, advices and scientific talks, it was really a very fruitful discussion.

I would like to thank all the jury members who agreed to evaluate this work. Thanks therefore to Fabienne Michelini, Giordano Scappucci, Francesco Biccari, Stefano Sanguinetti and Lydie Ferrier, it's an honor to support in front of you. Thanks, in particular to Giordano Scappucci and Francesco Biccari for reporting this thesis.

I won't forget to express the gratitude to rest of the NOVA team (Mathieu Abel, David Grosso, Luc Favre, Mathieu Koudia and Antoine Ronda), for giving the encouragement and sharing insightful suggestions. They all have played a major role during my PhD journey. Their endless guidance is hard to forget throughout my life. A special thanks goes to Drisse Hannani who was there whenever I need help inside and outside the clean room. Finally, I would like to thank the NanoTecMat platform of the IM2NP

institute in Marseille, in which my work was carried out inside.

I also need to say thank you to the young NOVA team (Jean Benoit, Mohamed, Imen, Elie, Zouhour, Zeinab, Nisrine, Merhnaz and Martin), we have been going on the same journey until now and we have shared all the burdens and faced the problems together. Having you as a support was irreplaceable experience. I wish that all of you find jobs that you desire and be happy with your careers and lives.

I would also like to thank the LENS group that I have been part of during my stay in Florence, more specifically I would like to thank Francesco Biccari from university of Florence to his guidance support and advices. Also, a special thanks go to Andrea Ristori in which we worked together for a couple of months, and this allowed a very fruitful exchange where we learned a lot from each other, thanks for your help, company and friendship; this give me a unique experience to learn about the customs, tradition and cultures of the Italian nations, and also to learn about my desires and places that I would like to visit again and maybe even live there.

To the administrative people to whom I'd like to express my gratitude: Conrad Becker, Michel Francia and Veronique Buat from the Doctoral school (ED 352). Joelle Pieret from the academic services of Aix Marseille university. Jean-Luc Autran, Delphine Sturma, Yves Klein, Lydia Carlier and Karima Khelfa from the IM2NP administrative service. I'd want to express my gratitude for your assistance and valuable administrative suggestions.

Lastly, I need to thank my family, my **Mom**, **Dad**, **Brother** and **Sister** to whom my work is dedicated. They have been my safe port, my support and the force to push me forward when I didn't want to go. Also, I am very grateful to all my friends in Lebanon and around Europe who were there for me when I needed them the most, and who will always be there for me in the future.

And finally, there is one more person I need to thank to. They say that many things happen during your PhD journey and that this is the time of your life which you will never forget, because of all the stress and hardships that you go through. But I was very lucky in that regard, because these were one of the best years in my life until now, and this is because of the person I met few months before I started my PhD. Later she proved to be my biggest support, my best friend and a woman I fell in love with. Thank you, **Maria**, for everything that you have done for me, I hope we will be very happy together in the future too.

Now it is time to close this chapter and for the life to go on. The last lines of my thesis are finally written, so it is time to open a new book and start some new challenges and be happy.

*With all my love to everyone,*
*Mario*

***Marseille, France***
***21 August 2022***

# Contents

# General Introduction

Semiconductor materials are at the heart of the technology in our knowledge society. Silicon, which has become the cornerstone of the electronics and photovoltaic industries thanks to availability of large crystalline wafers, high purity, effective conductivity engineering via doping, a high quality insulator ($SiO_2$) and a natural abundance. Still, the indirect nature of the band-gap of silicon is a severe drawback for efficient emission and absorption of light. In fact, light emitting diodes and lasers are typically made in III-V semiconducting compounds like InGaAsP for the visible and infra-red spectral ranges, and AlInGaN for the blue and ultra-violet ones, and consequently the white light domestic lightning. These materials are not easily implemented on silicon-based devices due to the large lattice mismatch between silicon and common III-V compounds.

Even though some successful exceptions in silicon are remarkable, such as the realization of Raman lasing [1] and the demonstration of ultrafast electro-optic modulation [2], the development of optical applications in silicon is one of the most important future challenges in semiconductor physics. This challenge is even more relevant in the present context of an increasing need for data transmission by optical signals from very long (Internet) to very short (rack-to-rack) distances. The spectral range for telecommunications by optical fibers is classified in terms of six so-called O-, E-, S-, C-, L-, U-bands, the original one (O-band) spreading between 1260-1360 nm, and the conventional one (C-band) between 1530-1565 nm. In these bands, silicon photonic devices have enabled state-of-the-art demonstrations of light confinement in photonic crystal nanostructures [3], nonlinear effects at extremely low power [4], modulators with low switching energy [5], and spontaneous emission control [6].

Silicon photonic devices have thus the potential for a major technological breakthrough, provided that one solves the fundamental problem of light emission, in other words making silicon an optically active material. For that purpose, many solutions have been explored by alloying silicon and germanium, doping, and strain engineering. Silicon nanostructures (e.g. nanocrystals and nanowires), through quantum confinement of carriers can provide enhanced absorption and spatially direct transitions in the visible and infrared range [7].

This PhD project aims at exploring a novel approach based on complex point defects in silicon-based devices for the fabrication of bright light sources. More specifically, in analogy to the phenomenal development of Nitrogen-Vacancy (NV) centers in diamonds, we intend to study G-centers in silicon [8, 9, 10, 11] for the implementation of quantum light sources. Our methodology relies on spatially-selective and broad-

areas implantation of impurities (such as carbon ions) in silicon-based nanostructures in order to fabricate (i) bright emitters when ultra-high G-centers densities are used (acting as classical light sources in the prospect of on-chip and out-of chip optical communications), and (ii) down to a single G-center for the demonstration of a quantum light source (in the prospect of quantum information protocols with photon-encoded quantum bits).

G-centers consist in two carbon atoms and one silicon atom (Figure 1) forming a point defect capable of trapping electron-hole pairs and emitting in the near-infrared at $\sim 1.280\ \mu$m [10, 12].

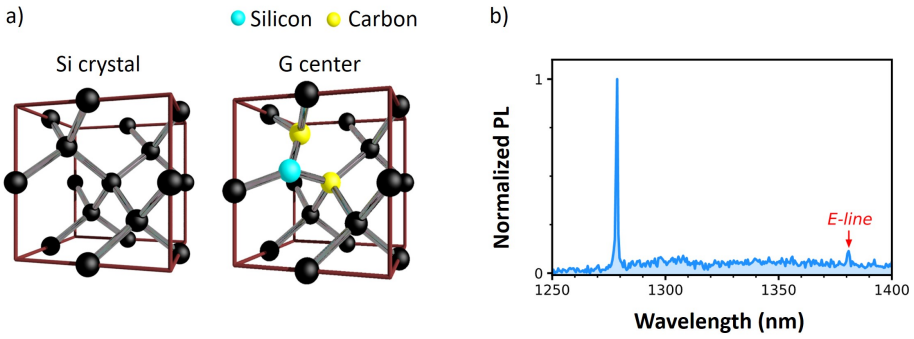


Figure 1: a) The crystalline structure of Si and G-center [13]. b) PL spectrum detected for an isolated G center by Baron et al [14].

The major advantage of the proposed emitters is their intrinsic device-friendly environment, envisioning the integration of electrical pumping through conventional silicon-doping, and also simplifying the interface between classical electronics with nanophotonic devices for quantum information. An in-depth investigation of the G-centers optical properties will enable to establish the limits of the emitters in terms of brightness, coherence and photon statistics, lifetime, thermal stability and integration with optical devices.

The G-center emission matches the O-band of telecommunications (e.g. by optical fibers) spreading between 1260-1360 nm. Besides the old studies reviewed in reference [10, 11, 15], some renewed interest for G-centers in silicon rose seventeen years ago when Cloutier et al. [8] demonstrated stimulated emission and lasing of G-centers at 1280 nm (Figure 2). This work relied on a nanopatterned silicon on insulator substrate (SOI) implanted with carbon ions, annealed for re-crystallization followed by proton irradiation.

In spite of the potential of this kind of emitters, the analysis of the state of the art in the control of G-centers creation and manipulation highlights the lack of a deep understanding and a full exploitation of its potentialities. This is sided by a complete lack of engineering with advanced photonic devices for the control of their optical properties. This last aspect is of the utmost importance and has been one of the central topic of this PhD work: the integration of a light emitter with an optical resonator, such

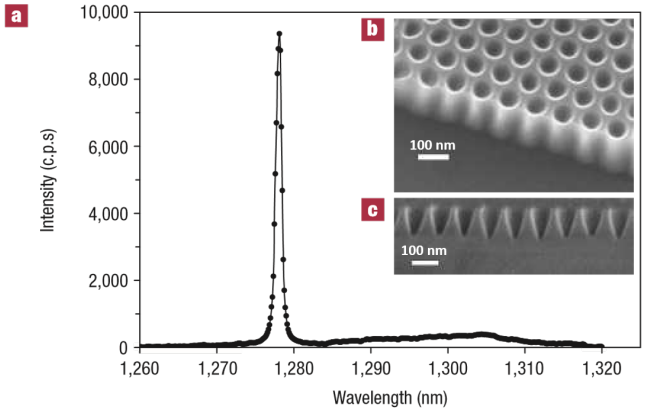


Figure 2: a) Photoluminescence emission spectrum from the nanopatterned SOI at 10 K. b) Scanning electron microscope (SEM) image of the nanopatterned SOI, tilted at 45 degrees. c) SEM cross-sectional view of a nanopatterned SOI sample observed under a scanning electron microscope [8].

as a dielectric antenna (Mie resonator).

A simple example of such a photonic device is shown in Figure 3, where a monocrystalline and faceted Si islands standing on a $SiO_2$ pedestal is showcased. Through the

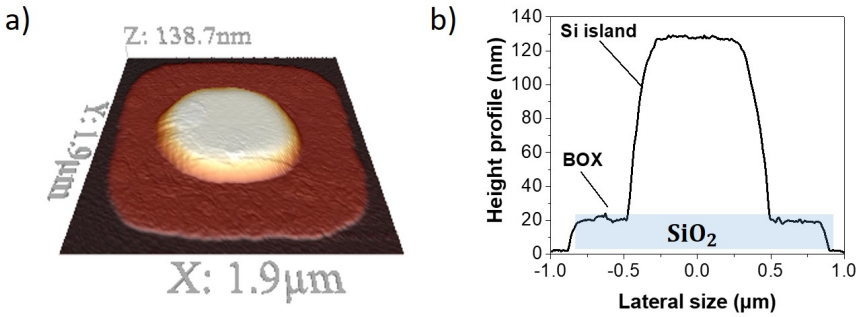


Figure 3: a) Atomic force microscope image of a monocrystalline Si island fabricated by optical lithography joined with solid state dewetting (Defined in Chapter 4.3). b) Atomic force microscope profile of an individual island.

manuscript I will progressively illustrate how the G-centers can be integrated in these devices, their fabrication and properties through experimental data and simulations. At the end it will be shown how this simple device allows coupling in the far field a large fraction of emitted light (up to 90%).

This PhD thesis is divided into six chapters where are described the main scientific results and are reported the experimental procedures to obtain them. They include sample fabrication and structural characterization, ion implant, and photoluminescence spectroscopy. Additionally, in collaboration with other people, theoretical interpretation of the experimental results is provided. Thus, the manuscript addresses the general picture of light emitters in silicon, their limits and their potential; a description of the instruments used and of the experimental procedures; an example of creation of G- and W-centers in a flat silicon on insulator wafer, and their optical signatures; a description of the optical properties of Si-based antennas featuring Mie resonances, their fabrication by solid state dewetting of thin silicon films; integration of light emitters in Mie resonators and corresponding light extraction enhancement. Finally, several Appendices describe ongoing work and other relevant information.

**Chapter 1**
**Future Challenges For Silicon-based Quantum Emitters at Telecom Frequency**
In this chapter I describe the current state-of-the art of quantum emitters in silicon and discuss the forthcoming challenges and goals towards a reliable exploitation of solid-state quantum-emitters (e.g. C, W, G and T center) in the context of quantum technologies. In particular, I examine opportunities, issues and challenges in controlling defect formation and localization, extrinsic effects, and integration in optical devices. This chapter was published as a perspective on Journal of Applied Physics in 2022.

**Chapter 2**
**Example of Creation of G and W Centers and Spectroscopy of Individual Impurities**
This chapter showcases the implant processes of carbon and silicon in conventional silicon on insulator and in isotopically purified $^{28}$Si on insulator, as well as the corresponding micro-photoluminescence spectroscopy characterization including photon-correlation experiments. Through this study we were able to detect a single defect (e.g. W and G). The single defect creation is demonstrated by the antibunching in intensity-correlation experiments, whereas the photoluminescence spectra are strictly identical in ensemble of centers and in single emitters for both W and G centers, demonstrating the establishment of a reproducible procedure for the creation of single centers. The results concerning the creation and detection of single W centers were published on ACS Photonics in July 2022, while the results concerning the detection of single G centers were published on Applied Physics Letters in August 2022.

**Chapter 3**
**Dielectric Mie Resonators: Resonant Antennas For Light Manipulation**
This chapter provides a detailed description of the electromagnetic resonant modes inside a Mie resonators in presence and absence of a substrate.

**Chapter 4**
**Dielectric Mie Resonators: Nanofabrication and Optical Properties**
This chapter is focused on solid-state dewetting. This process (which is our method to fabricate the Mie Resonator) is illustrated by describing the agglomeration mechanism,

the state of the art of the mostly used fabrication processes, including top-down and bottom-up approaches (e.g. Focused Ion Beam (FIB) and E-Beam Lithography and Reactive Ion Etching).

**Chapter 5**
**Fabrication and Characterization of Si-based Mie Resonators**
This chapter is split it into two parts; in the first part we use low-resolution optical lithography joined with solid state dewetting to form monocrystalline, atomically-smooth, silicon-based Mie resonators in well controlled large periodic arrays. Exploiting a 2 $\mu$m thick $SiO_2$ layer separating the islands and the underlying bulk, silicon wafer, we combine the resonant modes of the antennas with the etalon effect arising from the presence of the thick oxide. This part was published on Optic Express in 2020. In the second part we address the spatial and spectral mapping of multipolar Mie modes of a Si island by finite element methods simulations. The second part of the chapter was published on APL Photonics in 2022.

**Chapter 6**
**Light Emitting Si-based Mie Resonators: Towards a Huygens Source of Quantum Emitters**
In this chapter we show that, via ion beam implant, light emitting G-centers can be directly embedded within Si-based Mie resonators. Size- and position-dependent, directional light emission at 120 K is demonstrated experimentally and confirmed by finite element methods simulations. We estimate a collection efficiency of about 90% of the photoluminescence emission with a conventional objective lens. This results was published on Advanced Optical Materials in 2022.

**General Conclusions and Perspectives**
In this last chapter we draw the general conclusions and trace a possible next road-map to proceed further from the point we arrived.

**Appendices**
After discussing the "settled" results appeared in scientific publications, there are many ongoing activities that were not yet finalized. However, they gave encouraging result and relevant information for further development of this field. These are presented in the Appendices part.

Before addressing the unpublished results, we provide a description of the main tools and experimental methods used during my PhD in (Appendix A). More specifically, this chapter focuses on the fabrication techniques used to create the emitters and the photonic devices (e.g. islands and wires etc) as well as their characterization.

Beside the full wafer ion implantation techniques showed in the main part of the manuscript, we explored other approaches for creating light emitters, such as implantation with a Focus Ion Beam (Appendix B). The sample was not properly implanted and there were not arrays or emitters. However, individual W centers were revealed in some areas as well as several other unidentified individual emitters that might be related to interstitial Si-clusters.

We successfully explored the creation of G- and W-centers via laser irradiation

(Appendix C). We set laser pulse energy, duration and repetitions to create these emitters in pristine and C-implanted SOI providing an advanced stage of understanding of this method to proceed forward and address photonic structures and electronic devices with the same method but focusing in small spots.

We also successfully developed a process to produce suspended SOI membranes with embedded G-centers (Appendix D). In order to study the effect of the strain on the electronic properties of G-centers we embedded carbon ions and functionalized the membranes with SiN deposited via chemical vapor deposition. Micro Raman spectroscopy showed the onset of tensile and compressive strain in these freestanding membranes. As a result, splittings and shifts in the photoluminescence spectra, according to the amount of strain (e.g. size of the membrane) were observed.

Finally, we studied the effect of surface etching via oxidation by high-temperature annealing and chemical etching (via HF solution, Appendix E). We progressively thinned a SOI to reduce the number of emitting C-defects following the implant profile. Monitoring the photoluminescence emission we observed a "negative result": the photoluminescence intensity of the G-centers, even after only one etching cycle, quenches highlighting the detrimental role of surface defects (we ascribe this effect to creation of non-radiative recombination of electrons due to the increasing surface roughness).

**Collaborations**

During my PhD journey, I got the opportunities to work with different groups in different countries. Starting by the institute of Nanotechnology of Lyon (INL) at university of Claude Bernard Lyon 1 (Nicolas Chauvin, Sebastien Cueff, Hai-Son Nguyen, Tom Wood and Hugo Quard). The group of the Institute for Solid State Physics at Leipzig university (Tobias Herzig, Sebastien Pezzagna and Jan Meijer). The Group of Charles Coulomb (L2C) at university of Montpellier (Guillaume Cassabois, Anais Dréau, Vincent Jacques,Yoann Baron and Alrik Durand) and with CEA LETI at Grenoble Alpes university (Jean-Michel Gérard). These collaborations are carried out through the ANR projects (ULYSSES No.ANR-15-CE24-0027-01) and OCTOPUS (No.ANR-18-CE47-0013-01).

Also, other collaborations were made through the EU Project Narciso (European Union's Horizon 2020 program through the FET-OPEN project NARCISO No. 828890), firstly with the LENS group at Florence university (Nicoletta Granchi, Andrea Ristori, Francesco Biccari, Luca Fagiani, Massimo Gurioli and Francesca Intonti) and second with the L-NESS Laboratory at the university of Como (Luca Fagiani and Monica Bollani).

# Introduction Générale

Les matériaux semi-conducteurs sont au cœur de la technologie de notre société de la connaissance. Le plus important d'entre eux est le silicium, qui est devenu la pierre angulaire des industries électronique et photovoltaïque. Une combinaison unique de propriétés explique cette singularité : disponibilité de grandes tranches cristallines, grande pureté, ingénierie efficace de la conductivité par dopage, isolant de haute qualité ($SiO_2$) et abondance naturelle. Après quatre décennies où l'industrie électronique a suivi la loi de Moore, le développement de la technologie du silicium a atteint une maturité qui, associée à une bande interdite du silicium dans le proche infrarouge, a également conduit à une solution efficace et bon marché pour les applications photovoltaïques et les caméras CCD commerciales [16].

Toutefois, la nature indirecte de la bande interdite du silicium constitue un grave inconvénient pour l'émission et l'absorption efficaces de la lumière. En fait, les diodes électroluminescentes et les lasers sont généralement fabriqués dans des composés semiconducteurs III-V comme l'InGaAsP pour les gammes spectrales visibles et infrarouges, et l'AlInGaN pour les gammes bleues et ultraviolettes, et par conséquent la lumière blanche domestique. Ces matériaux ne sont pas faciles à mettre en œuvre sur des dispositifs à base de silicium en raison de l'important décalage de réseau entre le silicium et les composés III-V courants. Avec la nature indirecte de la bande interdite du silicium qui interdit l'émission de lumière, ces limitations ont relégué l'utilisation des semi-conducteurs IV-IV aux dispositifs électroniques, aux détecteurs de lumière et à la photovoltaïque. Même si certaines exceptions réussies sont remarquables, comme la réalisation de l'effet laser Raman [1] et la démonstration de la modulation électro-optique ultrarapide [2], le développement d'applications optiques dans le silicium est l'un des défis futurs les plus importants de la physique des semi-conducteurs. Ce défi est encore plus pertinent dans le contexte actuel d'un besoin croissant de transmission de données par signaux optiques sur de très longues (Internet) à très courtes (rack à rack) distances. La gamme spectrale pour les télécommunications par fibres optiques est classée en six bandes dites O-, E-, S-, C-, L-, U-, la bande originale (bande O) s'étendant entre 1260-1360 nm, et la bande conventionnelle (bande C) entre 1530-1565 nm. Dans ces bandes, les dispositifs photoniques au silicium ont permis des démonstrations de pointe de confinement de la lumière dans des nanostructures de cristaux photoniques [3], d'effets non linéaires à très faible puissance [4], de modulateurs à faible énergie de commutation [5], et le contrôle des émissions spontanées [6], même à l'échelle d'un processeur, l'introduction de la photonique dans les communications sur puce est étudiée pour contourner la limitation des vitesses d'horloge des processeurs

par les interconnexions électroniques. Une telle tâche nécessite des sources optiques à l'échelle nanométrique directement créées sur la puce de silicium, permettant ainsi une génération, un transport et une détection efficaces des bits d'information codés par la lumière.

Les dispositifs photoniques en silicium ont donc le potentiel d'une percée technologique majeure, à condition de résoudre le problème fondamental de l'émission de lumière, c'est-à-dire de faire du silicium un matériau optiquement actif. À cette fin, de nombreuses solutions ont été explorées par l'alliage du silicium et du germanium, le dopage et l'ingénierie des contraintes. De plus, dans les nanostructures de silicium, telles que les nanocristaux et les nanofils, le confinement quantique des porteurs de charge conduit à une absorption accrue et à des transitions spatialement directes dans le domaine du visible et de l'infrarouge [7].

Ce projet de thèse vise à explorer une nouvelle approche basée sur les défauts ponctuels complexes dans les dispositifs à base de silicium pour la fabrication de sources lumineuses. Plus précisément, par analogie avec le développement phénoménal des centres NV (Nitrogen-Vacancy) dans les diamants, nous avons l'intention d'étudier les centres G dans le silicium [8, 9, 10, 11] pour la mise en œuvre de sources de lumière quantique. Notre méthodologie repose sur l'implantation sélective dans l'espace et sur de larges zones d'impuretés (telles que des ions carbone) dans des nanostructures à base de silicium afin de fabriquer (i) des émetteurs brillants lorsque des densités de centres G ultra élevées sont utilisées (agissant comme des sources de lumière classiques dans la perspective de communications optiques sur puce et hors puce), et (ii) jusqu'à un seul centre G pour la démonstration d'une source de lumière quantique (dans la perspective de protocoles d'information quantique avec des bits quantiques codés par photons).

Les centres G consistent en deux atomes de carbone et un atome de silicium (Figure 1) formant un défaut ponctuel capable de piéger des paires électron-trou et d'émettre dans le proche infrarouge à $\sim$ 1,280 $\mu$m [10, 12].

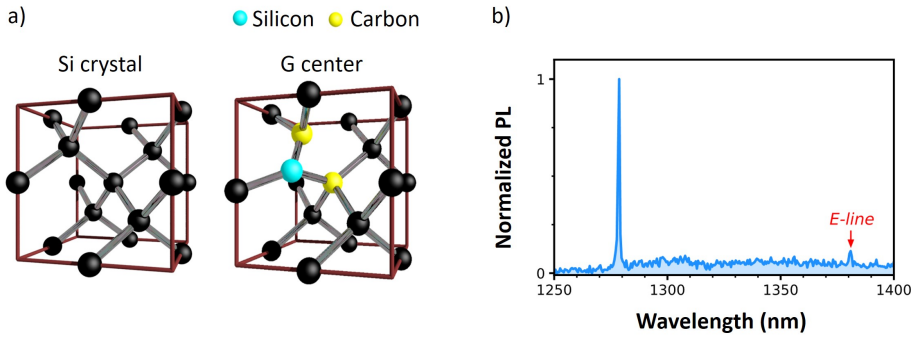


Figure 4: a) La structure cristalline d'un centre G [13]. b) Spectre PL détecté pour un centre G isolé par Baron et al [14]

Le principal avantage des émetteurs proposés est leur environnement intrinsèque-

ment convivial, qui permet d'envisager l'intégration du pompage électrique par dopage conventionnel du silicium, et qui simplifie également l'interface entre l'électronique classique et les dispositifs nanophotoniques pour l'information quantique. Une étude approfondie des propriétés optiques des centres G permettra d'établir les limites des émetteurs en termes de luminosité, de cohérence et de statistiques des photons, de durée de vie, de stabilité thermique et d'intégration aux dispositifs optiques.

L'émission du centre G correspond à la bande O des télécommunications (par exemple par les fibres optiques) qui s'étend entre 1260-1360 nm. Outre les anciennes études passées en revue dans la référence [10, 11, 15], un regain d'intérêt pour les centres G dans le silicium est apparu il y a dix-sept ans lorsque Cloutier et al. [8] ont démontré l'émission stimulée et l'effet laser des centres G à 1280 nm (Figure 2). Ce travail reposait sur un substrat de silicium sur isolant (SOI) à nano paterne implanté avec des ions carbone, recuit pour recristallisation puis irradié par des protons.

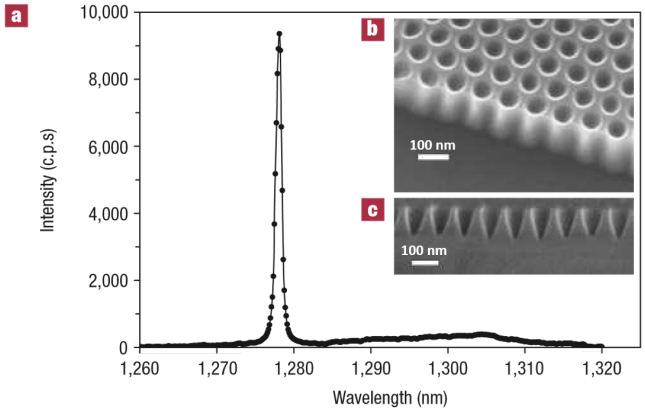


Figure 5: a) Spectre d'émission de bord du SOI à nanomotifs à 10 K. b) Vue à 45° et c) vue en coupe d'un échantillon de SOI à nanomotifs observé au microscope électronique à balayage [8].

Le cas de l'implantation d'atomes de carbone dans le silicium pour la production de centres G n'a pas encore été étudié en détail, et seule une augmentation de l'émission de lumière en fonction des doses implantées d'ions C et H a été démontrée [17] mais sans aucun indice sur la densité effective des centres émetteurs de lumière. Le positionnement précis des centres G (c'est-à-dire par rapport aux dispositifs photoniques), le contrôle de leur nombre jusqu'à un seul, et leur accord spectral possible sont encore inexplorés alors qu'ils sont des outils critiques pour une exploitation efficace des centres G comme source de lumière quantique polyvalente dans le silicium. En outre, malgré la pertinence du sujet, il manque encore une compréhension claire du mécanisme d'émission dans les centres G ou une compréhension précise de la structure fine intime provenant des interactions de spin des électrons et des trous [11], ainsi qu'un manque total d'ingénierie avec des dispositifs photoniques avancés pour le contrôle de leurs propriétés optiques. Ce dernier aspect est de la plus haute importance et a été l'un des sujets centraux de ce travail de thèse : l'intégration d'un émetteur de lumière avec

un résonateur optique, tel qu'une antenne diélectrique (résonateur de Mie).

Cette analyse de l'état de l'art des G-centers met en évidence les potentialités de cet émetteur à base de silicium mais, en même temps, également le manque de compréhension profonde et d'exploitation complète de ses potentialités. L'émission étroite de la transition de ligne à zéro phonon (3 nm de largeur à mi-hauteur, suggérant un nombre limité de configurations relatives des paires de C dans le réseau hôte) fait des G-centers des émetteurs attractants pour les dispositifs avancés où des résonances nettes sont nécessaires. Par exemple, un tel élargissement limité de la ligne peut être adapté à la mise en œuvre de dispositifs basés sur le fort couplage lumière-matière par analogie avec les excitons-polaritons dans des microcavités de haute qualité dans des composés III-V [18]. Le contrôle du nombre exact d'émetteurs implantés (et par conséquent des propriétés statistiques de l'émetteur lui-même) fait toujours défaut. Cette avancée pourrait ouvrir la voie à l'utilisation des centres G comme émetteurs quantiques (c'est-à-dire des sources de photons uniques dans la limite d'un seul ion implanté) sur une plateforme adaptée aux dispositifs.

Il est bien connu que la réflexion interne totale de la lumière dans un matériau à grande constante diélectrique tend à piéger la lumière émise (par exemple par les centres G) à l'intérieur du matériau dans lequel ils sont intégrés. Pour un semi-conducteur dont l'indice de réfraction est d'environ $\sim$3, la réflexion interne totale se produit à un angle maximal de $\sim$ 17 degrés, ce qui entraîne une très faible fraction de la lumière émise hors de la masse, environ $\sim$ 1%). Afin d'améliorer le signal de photoluminescence (PL) provenant des G-centers, des approches descendantes (par exemple, la lithographie optique) et ascendantes (par exemple, le démouillage à l'état solide de films minces de silicium sur des isolants) seront exploitées dans cette thèse pour produire des îlots de Si 3D monocristallins ainsi que des nano-architectures plus complexes [19] intégrant les G-centers. Ces îlots agissent comme des antennes diélectriques résonnantes (résonateurs de Mie) capables de rediriger de manière efficace et directionnelle l'émission PL dans le champ lointain, ce qui permet de la détecter avec une grande efficacité à l'aide d'optiques conventionnelles [20].

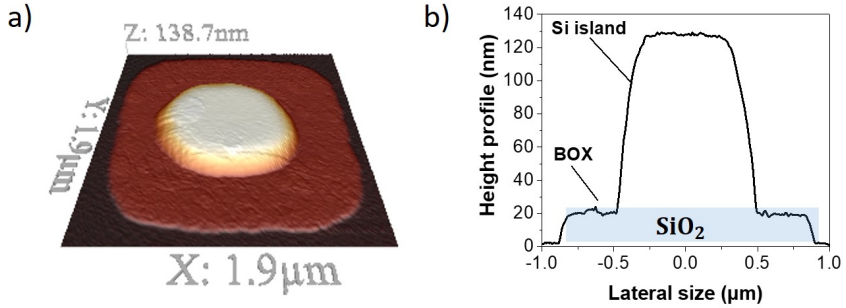


Figure 6: a) Image au microscope à force atomique d'un îlot de Si monocristallin fabriqué par lithographie optique associée à un démouillage à l'état solide (Défini dans Chapitre 4.3). b) profil d'un îlot individuelle donné avec le microscope à force atomique

Ce dispositif simple permet le couplage dans le champ lointain d'une plus grande fraction de la lumière émise (plus de 60%). Sous réserve de la taille et de la forme appropriées de l'îlot, l'activation de nanocristaux de Si avec des centres G conduit à un résonateur de Mie auto-assemblé et émetteur de lumière.

Cette thèse est divisée en six chapitres où sont décrits les principaux résultats scientifiques et sont rapportées les procédures expérimentales pour les obtenir. Celles-ci comprennent la fabrication d'échantillons et la caractérisation structurelle, l'implantation ionique et la spectroscopie de photoluminescence. En outre, en collaboration avec d'autres personnes, une interprétation théorique des résultats expérimentaux est fournie. Ainsi, le manuscrit aborde l'image générale des émetteurs de lumière dans le silicium, leurs limites et leur potentiel ; une description des instruments utilisés et des procédures expérimentales ; un exemple de création de centres G et W dans une tranche plate de silicium sur isolant, et leurs signatures optiques ; une description des propriétés optiques des antennes à base de Si présentant des résonances de Mie, leur fabrication par démouillage à l'état solide de films minces de silicium ; l'intégration d'émetteurs de lumière dans des résonateurs de Mie et l'amélioration correspondante de l'extraction de la lumière. Enfin, plusieurs annexes décrivent les travaux en cours et d'autres informations pertinentes.

**Chapitre 1**
**Défis Futurs Pour Les Emetteurs Quantiques à Base de Silicium à La Fréquence des Télécommunications**
Dans ce chapitre, nous décrivons l'état actuel de l'art des émetteurs quantiques dans le silicium et nous discutons des défis et des objectifs à venir en vue d'une exploitation fiable des émetteurs quantiques à l'état solide (par exemple, le centre C, W, G et T) dans le contexte des technologies quantiques. En particulier, nous examinons les possibilités, les problèmes et les défis liés au contrôle de la formation et de la localisation des défauts, aux effets extrinsèques et à l'intégration dans les dispositifs optiques. Ce chapitre a été publié en tant que perspective dans le Journal of Applied Physics en 2022.

**Chapitre 2**
**Exemple De Création de Centres G et W et de Spectroscopie d'Impuretés Individuelles**
Ce chapitre présente les processus d'implantation du carbone et du silicium dans le silicium conventionnel sur isolant et dans le $^{28}$Si isotopiquement purifié sur isolant, ainsi que la caractérisation correspondante par spectroscopie de micro-photoluminescence incluant des expériences de corrélation de photons. Grâce à cette étude, nous avons pu détecter un défaut unique (par exemple W et G). La création d'un défaut unique est démontrée par l'anti-bouclage dans les expériences de corrélation d'intensité, alors que les spectres de photoluminescence sont strictement identiques dans l'ensemble des centres et dans les émetteurs uniques pour les centres W et G, démontrant l'établissement d'une procédure reproductible pour la création de centres uniques. Les résultats concernant la création et la détection de centres W uniques ont été publiés dans ACS Photonics en juillet 2022, tandis que les résultats concernant la détection de centres G

uniques ont été publiés dans Applied Physics Letters en août 2022.

**Chapitre 3**
**Résonateurs Diélectriques de Mie : Antennes résonantes pour la manipulation de la lumière**
Ce chapitre fournit une description détaillée des modes résonants électromagnétiques à l'intérieur d'un résonateur de Mie en présence et en l'absence d'un substrat.

**Chapitre 4**
**Résonateurs Diélectriques de Mie : Nanofabrication et Propriétés Optiques**
Ce chapitre est consacré au démouillage à l'état solide. Ce processus (qui est notre méthode de fabrication du résonateur de Mie) est illustré par la description du mécanisme d'agglomération, l'état de l'art des processus de fabrication les plus utilisés, y compris les approches descendantes et ascendantes (par exemple, la lithographie par faisceau d'ions focalisé (FIB) et par faisceau d'électrons et la gravure ionique réactive).

**Chapitre 5**
**Fabrication et Caractérisation de Résonateurs de Mie à Base de Si**
Ce chapitre est divisé en deux parties; Dans la première partie, nous utilisons la lithographie optique à basse résolution associée au démouillage à l'état solide, pour former des résonateurs de Mie monocristallins, atomiquement lisses, à base de silicium, dans de grands réseaux périodiques bien contrôlés. En exploitant une couche de $SiO_2$ de 2 $\mu$m d'épaisseur séparant les îlots et la tranche de silicium sous-jacente, nous combinons les modes résonants des antennes avec l'effet étalon. Cette partie a été publiée dans le Journal of Optic Express en 2020. Dans la deuxième partie, nous abordons la cartographie spatiale et spectrale des modes multipolaires d'un îlot de Si par imagerie hyper-spectrale. De plus, nous explorons théoriquement et expérimentalement ces caractéristiques spatiales. Des détails aussi petits que 200 nm peuvent être détectés et sont en accord avec les simulations basées sur la méthode Finite Difference Time Domain (FDTD). Cette partie a été publiée dans le Journal of APL Photonics en 2022.

**Chapitre 6**
**Résonateurs de Mie a Base de Si Emettant de la Lumière : Vers Une Source Huygens D'émetteurs Quantiques**
Dans ce chapitre, nous montrons que, grâce à l'implantation par faisceau ionique, des centres G émetteurs de lumière peuvent être directement intégrés dans des résonateurs de Mie à base de Si. L'émission de lumière directionnelle à 120 K, en fonction de la taille et de la position, est démontrée expérimentalement et confirmée par des simulations FDTD. Nous estimons une efficacité de collecte d'environ 90% de l'émission de photoluminescence avec une lentille d'objectif conventionnelle. L'intégration de ces émetteurs télécom-fréquence dans des antennes résonantes est pertinente pour leur exploitation efficace dans des applications d'optique quantique et plus généralement pour les métasurfaces photoniques à base de Si. Ces résultats ont été publiés dans le journal of Advanced Optical Materials.

**Conclusions Générales et Perspectives**
Dans ce dernier chapitre, nous tirons les conclusions générales et traçons une éventuelle feuille de route pour aller plus loin à partir du point où nous sommes arrivés.

**Annexes**
Après avoir discuté des résultats "établis" parus dans des publications scientifiques, il existe de nombreuses activités en cours qui n'ont pas encore été finalisées. Cependant, elles ont donné des résultats encourageants et des informations pertinentes pour le développement futur de ce domaine. Elles sont présentées dans la partie Annexes. Avant d'aborder les résultats non publiés, nous fournissons une description des principaux outils et méthodes expérimentales utilisés pendant ma thèse dans (Annexe A). Plus précisément, ce chapitre se concentre sur les techniques de fabrication utilisées pour créer les émetteurs et les dispositifs photoniques (par exemple, les îlots et les fils, etc.) ainsi que sur leur caractérisation.

Outre les techniques d'implantation ionique sur tranche complète présentées dans la partie principale du manuscrit, nous avons exploré d'autres approches pour créer des émetteurs de lumière, comme l'implantation avec un faisceau d'ions focalisés (Annexe B). L'échantillon n'a pas été implanté correctement et il n'y a pas eu de réseaux ou d'émetteurs. Cependant, des centres W individuels ont été révélés dans certaines zones, ainsi que plusieurs autres émetteurs individuels non identifiés qui pourraient être liés à des amas de Si interstitiels.

Nous avons exploré avec succès la création de centres G et W par irradiation laser (Annexe C). Nous avons réglé l'énergie, la durée et les répétitions des impulsions laser pour créer ces émetteurs dans le SOI vierge et implanté de C, ce qui nous a permis d'atteindre un stade avancé de compréhension de cette méthode et d'aller de l'avant pour traiter les structures photoniques et les dispositifs électroniques avec la même méthode mais en se concentrant sur de petits points.

Nous avons également développé avec succès un processus de production de membranes SOI suspendues avec des centres G intégrés (Annexe D). Afin d'étudier l'effet de la contrainte sur les propriétés électroniques des G-centers, nous avons incorporé des ions carbone et fonctionnalisé les membranes avec du SiN déposé par dépôt chimique en phase vapeur. La spectroscopie micro Raman a montré le début de la déformation par traction et compression dans ces membranes autoportantes. En conséquence, des divisions et des décalages dans les spectres de photoluminescence, en fonction de la quantité de déformation (par exemple, la taille de la membrane) ont été observés.

Enfin, nous avons étudié l'effet de la gravure de surface via l'oxydation par recuit à haute température et la gravure chimique (via une solution HF, Annexe E). Nous avons progressivement aminci un SOI pour réduire le nombre de défauts C émetteurs suivant le profil d'implantation. En contrôlant l'émission de photoluminescence, nous avons observé un " résultat négatif " : l'intensité de la photoluminescence des centres G, même après un seul cycle de gravure, diminue, ce qui souligne le rôle néfaste des défauts de surface (nous attribuons cet effet à la création d'une recombinaison non radiative des électrons due à l'augmentation de la rugosité de la surface).

**Collaborations**
Au cours de mon parcours doctoral, j'ai eu l'occasion de travailler avec différents

groupes dans différents pays. En commençant par l'institut de nanotechnologie de Lyon (INL) de l'université Claude Bernard Lyon 1 (Nicolas Chauvin, Sébastien Cueff, Hai-Son Nguyen, Tom Wood et Hugo Quard). Le groupe de l'Institut de physique des solides de l'université de Leipzig (Tobias Herzig, Sébastien Pezzagna et Jan Meijer). Le groupe de Charles Coulomb (L2C) de l'université de Montpellier (Guillaume Cassabois, Anais Dréau, Vincent Jacques,Yoann Baron et Alrik Durand) et avec le CEA LETI de l'université Grenoble Alpes (Jean-Michel Gérard). Ces collaborations sont menées à travers les projets ANR (ULYSSES No. ANR-15-CE24-0027-01) et OCTOPUS (No. ANR-18-CE47-0013-01).

D'autres collaborations ont également eu lieu dans le cadre du projet européen Narciso (programme Horizon 2020 de l'Union européenne, par le biais du programme FET). Horizon 2020 de l'Union européenne à travers le projet FET-OPEN NARCISO No.828890), d'abord avec le groupe LENS de l'université de Florence (Nicoletta Granchi, Andrea Ristori, Francesco Biccari, Luca Fagiani, Massimo Gurioli et Francesca Intonti) et ensuite avec le laboratoire L-NESS de l'université de Como (Luca Fagiani et Monica Bollani).

# Chapter 1

# Future Challenges For Silicon-based Quantum Emitters at Telecom Frequency

## 1.1 Abstract

Silicon is the most widely used material in microelectronic devices; integration of atomic impurities in silicon via doping during growth or ion implant is now widely used as it allows to form conventional transistors. Exploiting all the knowledge accumulated over the last 60 years in the context of the second quantum revolution that is now underway would help accelerate the commercialisation of quantum technologies. Several works have already reported that silicon can be an optically active material with point-like defects emitting below the Si band gap, both in ensemble emission and absorption in natural Si as well as in isotopically purified $^{28}$Si, even under electrical pumping. Very recently, the detection of individual impurities in silicon opened the door for further exploitation of this indirect band-gap material to applications in quantum technologies, including single photon emission at near-infrared frequency, matching the telecommunication band and optical detection of individual spins. Here we describe the current state-of-the art and discuss the forthcoming challenges and goals towards a reliable exploitation of these solid-state quantum-emitters in the context of quantum technologies. In particular, we examine opportunities, issues and challenges in controlling defect formation and localization, extrinsic effects, and integration in optical devices. This chapter was published as a perspective on Journal of Applied Physics in May 2022, vol. 131, p. 200901.

## 1.2 Introduction

Quantum Technologies are poised to disrupt several industries, such as health, energy and materials discovery in the next decade, by revolutionizing communications (e.g.

quantum cryptography), sensing (weak magnetic field, solid state memories) and computation tools (quantum computing); most analysts predict that quantum computing alone will lead to productivity gains by end-users, in the form of both cost savings and revenue opportunities, around 700 billion annually [21, 22]. Quantum bits, the building blocks of quantum computing, can be based on different technologies, such as photons, trapped ions, and super-conductive circuits [23]. Depending on the target application, they each have strong and weak points, and are exhibiting different stages of maturity.

Among them, Si-based platforms remain highly entrancing as they can in principle, allow linking anchored quantum bits (e.g. spin, charge state) to flying quantum bits (photons), all while working with an established and well-known material, that constitutes the backbone of the electronics industry.

Remarkable advances in the field of silicon quantum computing include the demonstration of two-qubit gate fidelity above 99% [24, 25, 26] the CMOS-based cryogenic control of quantum circuits [27] and the fabrication of silicon qubits in a 300 mm semiconductor manufacturing facility using all-optical lithography and fully industrial processing [28].

In spite of the low temperature required, these evidences are bright examples illustrating the potential of Si-based quantum devices. This material has in fact several advantages with respect to others. To name a few: high purity and low defect density, reduced production cost, a well-developed backbone of nano-fabrication tools available "on the shelf", possibility to interface quantum devices with classical devices on the same chip, possibility to use an isotopically purified, spin-less matrix of $^{28}$Si.

In the context of light emission, several solid-state light devices have been scrutinized as potential sources of flying quantum bits: semiconductor quantum dots based on III-V semiconductor compounds are bright emitters and can be epitaxially grown with alloys emitting a telecom frequency. However, they suffer from intrinsic randomness of size, shape and nucleation sites, leading to a broad spread of emission wavelength [29, 30]. A viable alternative to quantum dots are light emitting impurities, that are point defects [31] in a semiconductor matrix combining two interesting properties: 1) uniformity of impurity species (atomic or molecule-like), 2) ability to be easily implemented by local ion implant with ultimate spatial resolution or directly generated by fs laser pulses [32, 33], or by using our new approach via Focus Ion Beam which's reported in the Appendix B.

The archetype of this latter kind of light sources are negatively charged nitrogen-vacancy pairs in diamond (NVs) [34, 35, 36, 37]. They have an optically active spin-triplet ground state, are well-isolated from the surrounding carbon lattice and have been used in many demonstrations of early quantum devices. Nevertheless, when compared to Si, this carbon-based platform is far from optimal for scaling and integration in devices working at telecom frequency; fabrication is usually limited to small wafer sizes and remains highly expensive, doping remains very difficult, and their emission is not within the near-infrared window.

Alternative quantum emitters, such as impurities in SiC, are more suitable for integration on a Si platform [38, 39, 37] as this material can be directly formed on a Si wafer. Still, in spite of its potential relevance as a material for building electronic and photonic devices, SiC is still in its infancy. A direct integration of quantum emitters in a silicon-on-insulator wafer (SOI) while covering the infrared telecom bands [40, 41]

relevant to telecommunication with optical fibers, remains a more appealing solution (also in view of a spin-photon interface [37, 42, 43, 44]).

A clear advantage of silicon over other solid-state platforms for applications in electronic, photonic and quantum devices, is its natural abundance: after oxygen, silicon is the most abundant element present on Earth's crust that is composed of this element for about one third. Albeit silicon is often found in the form of silicate minerals (e.g. bound to oxygen), the chain of its purification has been boosted by a large demand for electronic devices (monocrystalline silicon) and solar panels (poli-crystalline silicon): only in 2020 the global silicon production amounted to about eight million metric tons [45] (with two thirds produced in China, followed by Russia with a production of about a half million metric tons). In the same year, the request of Si-based wafers reached 12.41 billion square inches with an increase of about 5% with respect to 2019.

Thanks to the broad use of silicon for microelectronics, this material can be supplied in large wafers that nowadays can reach a diameter of 17.7 inch. The relevance of this semiconductor consists also in the possibility to produce a stable and high-quality insulator (stochiometric $SiO_2$) necessary for the fabrication of electronic devices and integrated photonic circuits. In this framework, SOI are available over 12 inch with a large choice of device thickness (from $\sim$10 nm up to several $\mu$m) and buried oxide thickness (BOX, from $\sim$10 nm up to several $\mu$m). The broad availability of p and n doping for bulk and SOI wafers, is another crucial element placing silicon at the apex of semiconductor materials.

Successful exploitation of this material for quantum technologies, requires high purity to ensure minimal noise from the environment and facilitate the deterministic creation and study individual light emitters. To this end, the purity of electronic grade silicon can reach 99.9999999% ("nine nines"), leaving a concentration of impurities of about $\rho_I \sim 5\times10^{13}$ cm$^{-3}$ and rendering it one of the purest materials available. For instance, in a SOI of 220 nm (that is the typical thickness used for the fabrication of integrated photonic circuits at telecom frequency), the concentration of uncontrolled impurities can be as low as $\sigma_I \sim 10$ $\mu$m$^{-2}$ to be compared with $\sigma_{Si} \sim 10^{10}$ $\mu$m$^{-2}$ Si atoms in the same area. Provided that these emitters are typically formed by two or more impurities within a cell volume (e.g. C-pairs, Figure 1.1), assuming a stochastic model [46, 47, 48] the diads density should be less than $\rho_{I-I}^2 \times V_{Si} \sim 4\times10^5$ cm$^{-3}$ (where $V_{Si}$ is the volume of the unit cell of the Si crystal $\sim 1.6\times10^{-22}$ cm$^{-3}$), that for a 220 nm thick SOI translates in $\sigma_{I-I} \sim 10^{-7}$ $\mu$m$^{-2}$.

It thus appears that electronic-grade silicon, in principle, could constitute a rather clean environment for applications in quantum optics that, in contrast with III-V or SiC, overcomes any problem related to alloy disorder. However, we also note that, this estimation may be a lower bound for the number of emitting impurities in pristine samples [49], given the existence of several unavoidable and uncontrolled issues, such as the presence of interfaces between the SOI and the underlying BOX, impurities at the wafer top surface and impurities introduced during the SOI fabrication (e.g. via oxygen implant for SIMOX or proton implant for Smart-Cut [50, 51]).

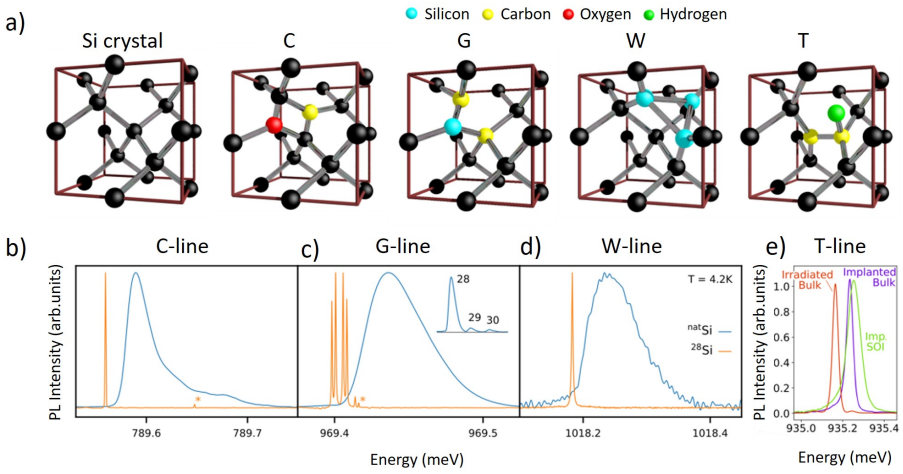


Figure 1.1: a) From the left to the right panel: crystalline structure of Si, C-center, G-center, W-center and T-center. b)-d) Photoluminescence intensity of the zero-phonon line of C, G and W centers in bulk Si (blue line) and isotopically purified bulk $^{28}$Si (orange line). e) Photoluminescence intensity of the zero-phonon line of T centers in bulk Si irradiated with electrons (red line), bulk Si implanted with protons (purple line) and silicon on insulator (SOI) implanted with protons (green line) [41, 42, 43, 13, 52].

## 1.3 State-of-the-art of Quantum Emitters in Silicon

Micro and nano-architectures based on silicon drove the electronic revolution in the 60's; as a result, the vast majority of classical electronic devices are built on a Si-based platform. Photonic devices based on Si are also a well-established technology [53]. This is possible thanks to the versatility of this material for carrier transport and to its transparency for light propagation in the near-infrared frequency range. Unfortunately, the indirect nature of its energy band-gap does not allow for efficient photoluminescence emission. However, light emission below band-gap can be recovered by exploiting extrinsic and intrinsic impurities associated to rare-earth atoms, carbon, oxygen, hydrogen impurities as well as self-interstitial to name a few [54, 37, 41, 55, 56] (Figure 1.1, 1.2 and 1.3).

These emitters are commonly known as radiation-damage centers, as they are usually created via high-energy electron irradiation or directly by ion implant. They can be created in bulk Si as well as in silicon on insulator (SOI), another attractive platform for the fabrication of electronic and photonic devices (such as integrated photonic circuits). Most of these emitters are well-known, with most studies having focused on ways of eliminating them in order to achieve high purity silicon. The list of light emitting centers in silicon is extremely long [57].

Here, we limit the description to the few ones that have been recently scrutinized for applications in quantum optics and spintronics (Figure 1.1 a), from the second to the fifth panel, respectively): the C center composed of one interstitial oxygen and an in-

terstitial carbon [58, 59], the G-center composed of two carbons atoms, one interstitial and one substitutional bound to a self-interstitial [60, 61], the W-center composed

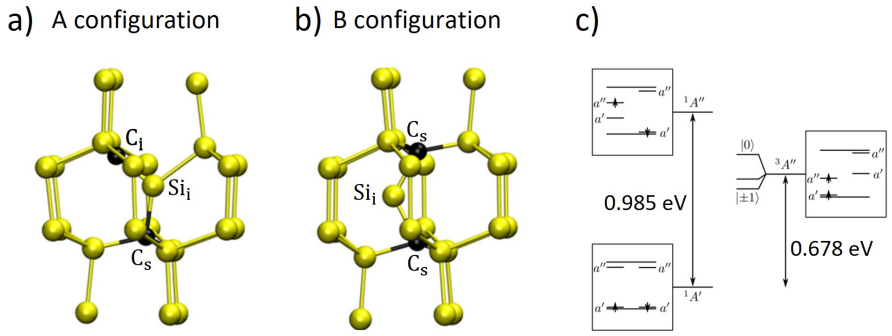


Figure 1.2: a) Structure of the A form of the G-center: $C_iSi_i$-$C_s$. b) Structure of the B form of the G-center: $C_s$-$Si_i$-$C_s$. c) Electronic levels of the G-center, B configuration [56].

of clusters of three self-interstitials [62], and the T center composed of two substitutional carbon atoms with one of the two linked to a hydrogen interstitial [63].

Despite of being discovered long ago, very little is known for many of the silicon impurities. As an example, a clear picture of the microscopic structure, electronic properties, fine and hyperfine interaction of the light emitting G-center has been addressed by first-principles calculations only very recently [56] (Figure 1.2). A similar theoretical analysis has been reported for the T-center [64]. Density functional theory calculations for the G-center provide an energy difference between the transitions ${}^1A' \leftrightarrow {}^1A''$ and ${}^1A' \leftrightarrow {}^3A''$ of respectively, 985 meV and 678 meV. The first transition is not far to what is conventionally observed in photoluminescence experiments [8, 55]. From the experimental point of view, a direct measurement of the recombination lifetime of an ensemble of G-centers was reported only in 2018 [55]. Generally speaking, this points to a deep gap in the knowledge of these emitters that leave room for improvements and potential exploitation.

Beyond applications of the ensemble emission (e.g. for lasing [8] and LED [65, 66]), one can envision quantum light sources in bulk Si and SOI [49, 67, 68, 69, 70] (Figure 1.3). The associated transitions match very well the telecommunication windows (Figure 1.1 and 1.3): *O band* (G-center, SD-2, SD-5), *E band* (SD-1, SD-2), *L band* (C-center) and exhibit promising properties as flying quantum bits: a recombination lifetime in the range of 4-40 $\sim$ns, a quantum efficiency larger than 50% [67], a Debye–Waller factor of 2-40% at $\sim$10 K [68] (Figure1.3 b)), well-defined polarization axes, accounting for single emission dipole, resilience to thermal cycles, thermal stability, non-blinking emission intensity, and a brightness exceeding $10^5$ counts per second at the detector [49] (using a superconducting nanowire single-photon detector, detection efficiency of about 90%) limited to about 2% by total internal reflection owing to the relatively large refractive index of Si ($\sim$3.5).

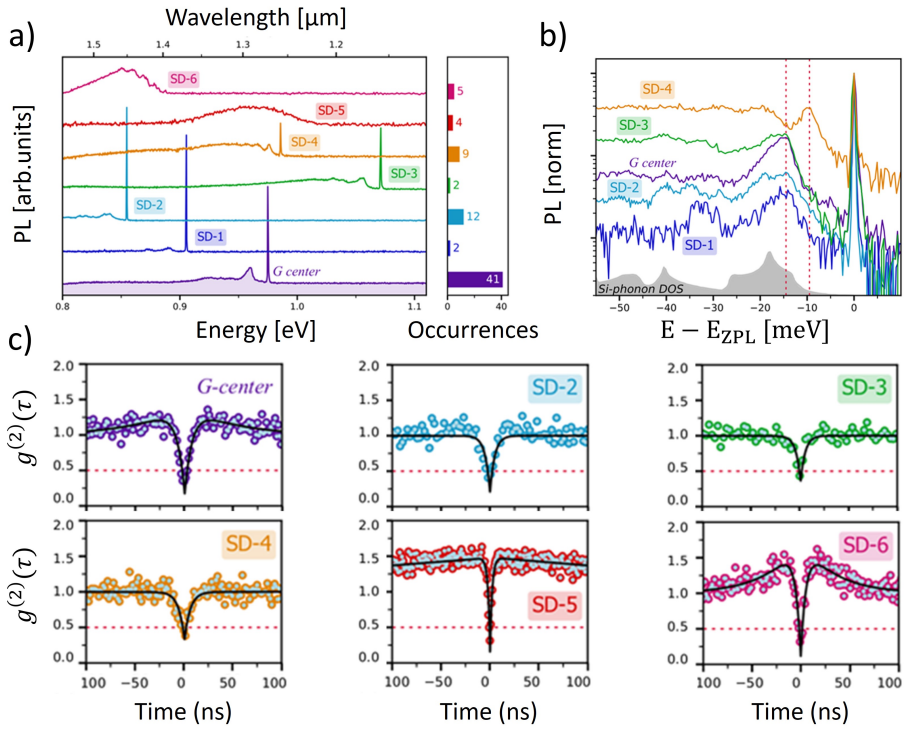


Figure 1.3: a) Photoluminescence spectrum of individual impurities in C-implanted SOI wafer (C implant at 36 keV, fluence $5 \times 10^{13}$cm$^{-2}$cm). The right inset displays the number of emitters associated to each kind of impurity detected in an area of about 600 $\mu$m$^2$. b) Photoluminescence spectra normalized to the zero phonon line peak and shifted in energy to the zero phonon line energy for impurities G, SD-1, -2, -3 and -4.The dotted, vertical lines highlight the position of the first phonon replica whereas the shaded highlight the phonon density of states of the Si matrix hosting the impurities. c) Second order autocorrelation function ($g^2(\tau)$) of six individual impurities in SOI. The horizontal, dashed lines highlight $g^2(\tau)$= 0.5, below which the emission can be ascribed to an individual two-level system [68].

Clear anti-bunching in the second order, intensity correlation function has been independently reported by three different groups for the G-center [49, 67, 68, 69], the W-center [70] and also for a new set of unknown impurities likely related to carbon [68] (Figure 1.3 c)). The smallest reported value for $g^2(0)$ is of 0.07±0.04 [49] (likely limited by the presence of spurious emission within the detection spot and by intrinsic dark counts of the detector) underlying the high quality of these emitters.

These important achievements were obtained using commercial SOI wafers and are the irrefutable proof of the atomic-like density-of-states of this class of emitters. In fact, they open the route to the implementation of quantum optical devices in a Si-based, device-friendly environment.

## 1.4 Extrinsic Effects

In spite of a rather small extension of the electronic wavefunction of light-emitting impurities at low temperature (e.g. about 1.6 Å for the light emitting G-center at 10 K [55]) that should limit the impact of nearby impurities and extrinsic effects, the associated emission is clearly sensitive to the surrounding environment [71] (Figure 1.4 and 1.5). The control of these perturbations is crucial for exploiting these impurities for quantum light emission and spin-photon interface, enhancing their coherence in view of the fabrication of arrays of identical defects emitting mutually indistinguishable single photons and scaling this approach to a large number of quantum bits.

### Spectral Diffusion

One of the relevant mechanisms affecting the coherence of individual, strongly-confined emitters are random fluctuations of the charged environment leading to a quantum-confined Stark effect (spectral diffusion). This inhomogeneous broadening, measured in the lineshape of individual quantum light sources, springs from the integration of the signal over relatively long time intervals (e.g. a few seconds) resulting in the pile-up of many photons emitted at slightly different energies due to fast changes of the surrounding charged environment [72]. Thus, lineshape and broadening measurements provide a first assessment of the quantum-confined Stark effect and of the quality of the semiconductor matrix surrounding an emitter in terms of amount and distance of the perturbing charges [73, 74, 75].

Very recently, ensemble measurements were performed on T-centers exploiting a newly-developed spin-dependent spectroscopic technique [52].

Whereas in isotopically purified $^{28}$Si and bulk Si irradiated with electrons the impact of spectral diffusion affects the linewidth (Figure 1.4 a)) with a broadening lower than $\mu$eV, the SOI counterpart that underwent ion implant, provides a value that can be between one and two order of magnitudes larger (Figure 1.4 b)). These results confirm that also for T-centers integrated in a flat SOI without any top-down etching i) the ion implant increases the overall defectivity and the associated impact on the spectral diffusion (e.g. as shown for N-V centers in diamonds [76, 77]) and ii) that the presence of interfaces close to the emitters increases electric and magnetic field noise [78, 75, 79].

Although an extensive characterization and comprehension of the impact of spectral diffusion on the electro-optical properties of individual impurities in Si is still missing, these early results strongly suggest that ion implantation adds some disorder to the crystalline matrix and that the presence of interfaces is detrimental. Ad-hoc strategies should be devised in order to address this issue. A viable solution could be improving the high-temperature annealing process that typically follows the ion implant step (e.g. for the creation of G-centers [80, 55]). However, there are limits to the thermal processing that can be used for integrating these emitters in a photonic device. 1) The BOX of SOI is high-quality, thermal $SiO_2$, but cannot be exposed to very large temperatures (after lithography and etching): Annealing above 900°C promotes intermixing between Si and $SiO_2$, potentially damaging the whole photonic device [81]. 2) Solid state dewetting (Defined in Chapter 4.3), that is a shape instability that thin films

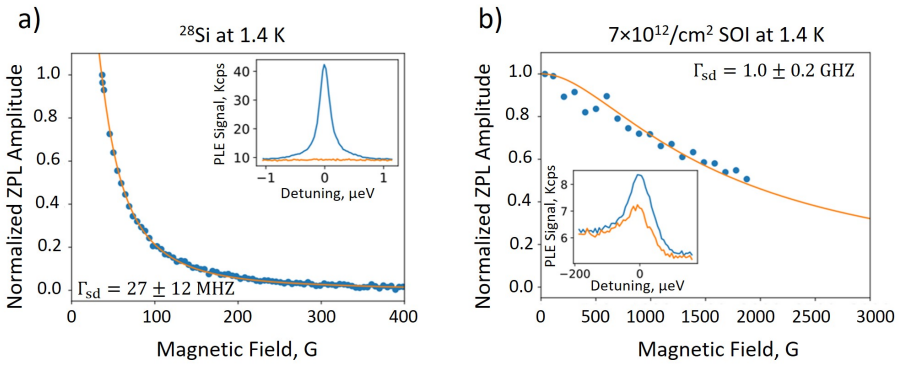


Figure 1.4: a) Zero phonon line intensity of an ensemble of T-centers as a function of the applied magnetic field at 1.4 K, for bulk $^{28}$Si. The inset show the zero phonon line at B = 36 G (blue) and 450 G (orange). b) Zero phonon line intensity of an ensemble of T-centers as a function of the applied magnetic field at 1.4 K, for SOI implanted respectively at 7 $\times 10^{12}$ cm$^{-2}$. The insets show the zero phonon line at B = 36 G (blue) and 2000 G (orange) [52].

undergo when annealed even well-below their melting temperature [82, 83], is another relevant issue that can have a detrimental impact on a tiny device implemented in a SOI substrate. 3) Owing to the rather large mobility of impurities and interstitial in silicon, high temperature annealing may destroy the light emitters and thus is not viable.

A well-established approach to circumvent the issues of spectral diffusion is a resonant-excitation scheme. This method exploit a sharp laser tuned at the same energy of the zero-phonon line exciting only the associated optical transition. This technique seems a necessary step to fully exploit the potential of these quantum emitters that brings also another relevant advantage: the resonant Rayleigh scattering from an individual two level system inherits the coherence of the laser while preserving the anti-bunching character of a quantum emitter [84]. Remarkably, the two-photon indistinguishability of a coherently driven quantum emitter can be tuned adjusting the laser coherence. In addition to a resonant pumping, more sophisticated excitation schemes include the presence of an additional, non-resonant, low-energy laser to control the presence of a charge in a quantum emitter [85] that is very important beyond the issue of spectral diffusion (e.g. in order to switch from A and B form in a G-center, Figure 1.2).

## Hyperfine Interactions

A second relevant perturbation to the electro-optical performances of these emitters can spring from hyperfine interactions between the nuclear and electron spins that may reduce photon and spin coherence. This phenomenon is ascribed to nuclear spins, that in silicon, are mostly associated to the presence of $^{29}$Si (with a nuclear spin of 1/2) that fluctuate in time. The use of $^{28}$Si (a zero isospin matrix, erasing any hyperfine interac-

tion) provides unprecedented sharp lines (less than 1 $\mu$eV) measured in the ensemble of C-, G and W-centers [41] (Figure 1.1 b)-d)). In silicon, the same phenomenology has been deeply studied [86, 72, 87, 88, 89, 90, 91] in view of the exploitation of the long spin coherence of electronic and nuclear spins for atomic-scale electronic devices based on individual dopants [92, 93].

In the framework of light emitting impurities, $^{28}$Si has been successfully exploited to show a spin-photon interface exploiting an ensemble of T-centers [43, 42]: in addition to extremely narrow spectral lines (Figure 1.4 a)), the T-center in $^{28}$Si provides a direct access to nuclear and electron spin degrees of freedom with a lifetime in the range of seconds and milliseconds, respectively. A potential drawback of this emitter is its relatively long recombination lifetime that is about 0.9 $\mu$s.

These important achievements directly point to the possibility of using $^{28}$Si as a quantum grade material [94, 95] and build quantum devices for highly coherent single photons, spin-photon entangled states and much more. However, a major step in this direction will require the fabrication of photonic devices (e.g. to create a cavity to accelerate the spontaneous emission rate, inject and extract the photoluminescence) exploiting a $^{28}$SOI platform. This calls into play the production of this material that is the most abundant stable isotope of Si (being about the 92% of the total Si composition) but requires a long process to reach a high level of purity rendering it, for the moment, highly expensive: centrifugation of $SiF_4$ to purify $^{28}SiF_4$ followed by conversion in enriched silane gas $^{28}SiH_4$ (direct centrifugation of silane is not possible owing to its low molecular mass). Other approaches to produce this material, such as mass separation, ion exchange and laser technology, are less efficient in reaching a high level of purity and are more expensive with respect to centrifugation.

Epitaxial growth of layers of $^{28}$SOI was shown using $^{28}SiH_4$ produced by Isonics Corporation in USA in collaboration with the Voltaix company between 1998 and 2005, reaching a purity better than 99.9% [96, 97]. A 5 kg boule of purified $^{28}$Si has been produced within the Avogadro project in Berlin in 2005 [98]. More recently, chemical vapor deposition of $^{28}$Si (with a purity of 99.992%) atop a thinned SOI of 300 mm diameter was shown by CEA laboratory in France, for the fabrication of CMOS-based quantum bits with a pre-industrial protocol [99, 100]. This accounts for the presence of a well-established community ready to tackle this activity with advanced fabrication protocols.

## Local Strain

The results in $^{28}$SOI discussed in the previous section demonstrate that there is sufficient interest and efforts already underway towards the engineering of quantum emitters. Recent reports showed that a local implant of Si ions in a $^{28}$SOI allows to isolate individual W-centers acting as single photon emitters with a $g^2(0) \simeq 0.12$ without any background or dark-counts correction [70]. In spite of the importance of this result, at the individual emitter level, there are relatively large spectral shifts from a W-center to the other (of about 1 meV). The same kind of effect was also reported for G-centers and other single photon sources in conventional SOI (Figure 1.5), pointing to additional, unwanted effects damaging the potential indistinguishability of photons emitted

by different sources and, in the end, the scalability of this approach.

Although a direct link to the potential source of these shift is still missing, different local strain experienced by each emitter is certainly a realistic hypothesis [71, 101]. It was in fact already reported that splittings and shifts of the zero phonon line of C- and G-centers in silicon can be ascribed to local strain [102, 103] in analogy to other systems [104, 105].

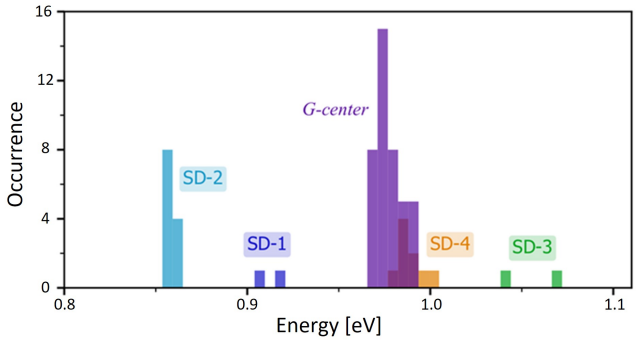


Figure 1.5: Statistics of the zero phonon line emission from individual quantum emitters measured in a carbon implanted SOI (see also Figure 1.1) [68].

There are several well-known approaches that could be used to tune several quantum bits to the same energy. Relaxing the strain by high temperature annealing may be hard to implement, given the high mobility of the interstitials composing these quantum emitters. A viable solution could be the application of a local and irreversible strain by local crystallization of metal oxides (e.g. $SiO_2$, $TiO_2$, $HfO_2$). This was efficiently exploited in III-V quantum dots showing superradiant emission from three independent sources integrated in a waveguide [106]. Alternatively, dynamic and reversible tuning of the emission could be obtained by applying a local, static electric field through an electric contact resulting in a controlled Stark-shift (e.g. in a MOS-like configuration).

## 1.5 Deterministic Fabrication of Individual Quantum Emitters

Deterministic fabrication of the impurities with $\sim$nm lateral resolution is one of the necessary steps for the controlled fabrication of this class of emitters. Examples of this kind have been widely reported for NV-centers in diamonds exploiting a pierced atomic force microscope tip [107, 108, 109] or a mass-filtered focused ion beam [110, 111]. Both methods were successful in creating an individual emitter within a photonic crystal microcavity [112, 113]. Single ion implanters are also well-established and widely used techniques that could fulfill this task, as it was already shown for phosphorous in Si [114, 115] and rare-earth in yttrium-aluminum-garnet [116].

In spite of the advanced level of these nano-fabrication techniques, these methods

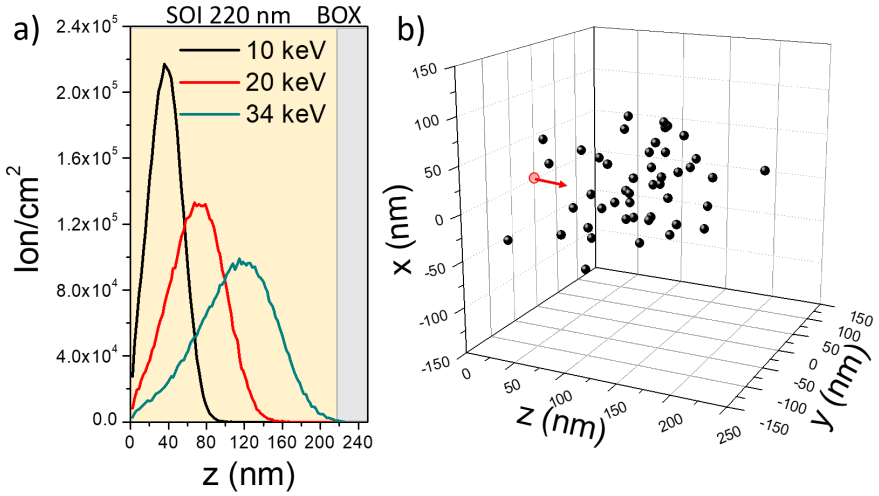


Figure 1.6: a) SRIM simulations (Defined in Chapter A.10) of carbon ion range as a function of depth z, for implant in a 220 nm thick SOI at 10, 20 and 34 keV. The profiles are obtained integrating over $10^5$ ions. The shaded areas highlight the SOI and the BOX underneath. b) 3D representation of 50 carbon ions implanted in Si at 34 keV. The red dot highlights the point of impact and the arrow the direction of the impinging ions.

are based on phenomena that are intrinsically stochastic and may have a relatively low yield in the generation of single emitters. Moreover, the above-mentioned examples, make use of relatively low energy ions limiting the ion range straggling allowing to place the ions with a precision of the order of a few tens of nm.

When complex impurities in silicon are concerned, one has to face a severe challenge: they are composed of several impurities eventually of different nature (e.g. two C and one Si for the G-center), which calls into play the need of placing them within the same unit cell potentially rendering the overall generation yield very low. As an example, we plotted the simulated ion range for C ions implanted in a 220 nm thick SOI in Figure 1.6. Ideally, in order to couple the photoluminescence emission in a photonic circuit (e.g. a waveguide or a ring resonator), the implant energy should be large enough to produce the defect at its center. This can be obtained with an ion energy of about 34 keV. However, at this energy, the profile of the implant is relatively large, featuring a full width at half maximum of about 110 nm (Figure 1.6 a). Representing the simulated ion position of 50 carbon ions implanted in Si at 34 keV, it appears that a similar spread is also present in the lateral direction. In order to limit these issues, possible strategies could include the use of thinner SOI allowing for lower implant energy at the center of the slab, or *ad-hoc* engineering of the photonic modes to work with the impurities implanted at the SOI surface.

An attractive alternative to localized ion implant, is an all-optical fabrication of individual quantum emitters. A direct control of their activation has been demonstrated in diamonds [32] and SiC [33] with fs-laser pulses: by *in situ* and *operando* monitoring the photoluminescence emission after individual laser pulses, the fabrication yield can be very close to unity. This will entail the preliminary ion implant of the impurities followed by laser activation.

## 1.6 Integration in Opto-electronic Devices

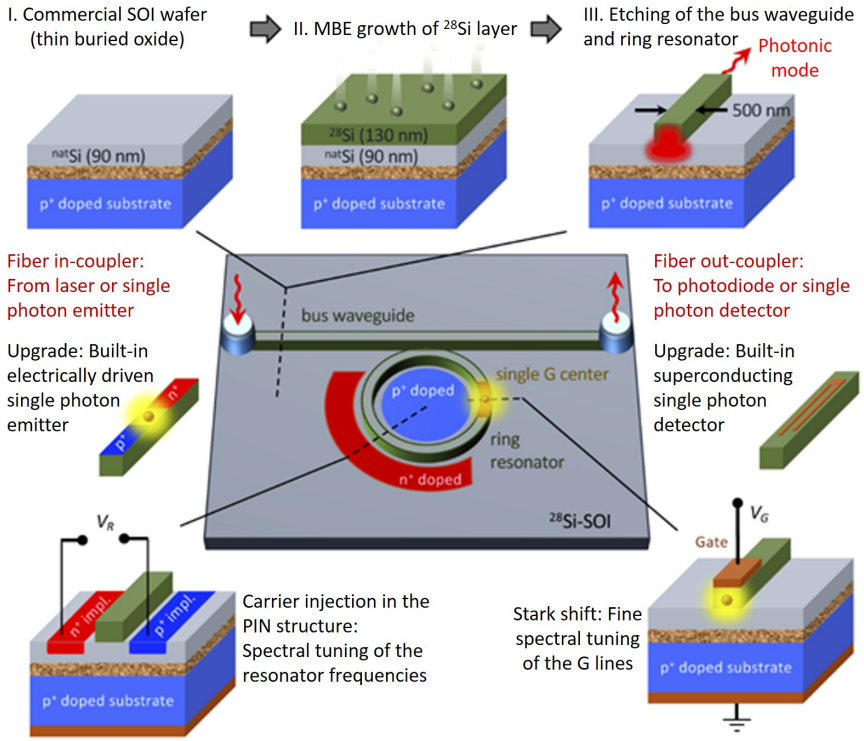


Figure 1.7: Scheme of $^{28}$SOI integrated photonic circuits and electronic devices for scalable quantum circuits based on individual emitting impurities [49].

The last aspect we consider for the scaling of this approach for quantum technologies is the integration of impurities in photonic circuits and electronic devices [117] (Figure 1.7). Electrical injection of carriers in ensembles of G-centers has been already shown exploiting a light emitting p-n junction [65, 66] and their integration in a high finesse cavity has been proposed [118, 119]. However, from power dependent photoluminescence experiments, unwanted absorption was shown, pointing to residual defects that spoils the emission. Other reports of integration of G-centers ensembles in photonic

devices demonstrated that luminescence was activated (likely at the interface between Si-air) through the top-down etching [8, 120] that in principle, may complicate the isolation of individual emitters.

The aforementioned results were obtained in SOI samples undergoing implant with large doses. For lower doses, as low as $10^{13}$ cm$^2$, coupling of individual G-centers in a waveguide was reported with clear anti-bunching ($g^2$<0.5), a lifetime compatible with that found in the ensemble ($\sim$8 ns) and with a very limited spread of the zero-phonon-line between different emitters (1279$\pm$1 nm) [69]. This promising results suggests that we stand at a turning point for quantum devices in Si: all the tools developed for silicon based integrated photonic circuits could be exploited to manipulate single photons. A pictorial representation of these tools is displayed in Figure 1.7 from reference [49] that traces a road-map for the future development of integrated photonic circuits embedding quantum emitters in $^{28}$SOI. Following the growth of $^{28}$SOI on conventional SOI and implant of emitting impurities, top-down etching will be used to define photonic devices, such as waveguides, resonators, logic gates, modulators, and light couplers. Finally, direct single photon detectors using superconductive wires (e.g. as already shown in other systems [121, 122]) will be the last step to fully operate quantum bits of light on a Si-based chip towards scaling.

## 1.7 Conclusion

In conclusion, several recent works with individual impurities in silicon have underlined their potential as quantum emitters and opened the door to intense investigations of this material for quantum devices. Although those efforts are still at an early stage, and silicon still lags behind other quantum bit technologies, important theoretical and experimental evidences are rapidly emerging, pointing to new insight, improved devices and performances in the near future. The broad availability of Si and its crystal quality, the possibility to purify a $^{28}$Si matrix, and the strength of nano-fabrication of electronic and photonic devices are key elements that can rapidly accelerate the development towards commercial quantum devices.

The possibility for defects in silicon to outperform current solutions, such as III-V-based single photon sources or spin quantum bits in NV-centers, will largely depend on the performances and scalability of this approach. To this end, there are many challenges that must be addressed in the next years. Mandatory spatial addressability of individual emitters (that should be placed with high precision within optical and electronic devices) is just one of the steps that is still missing. The control of the fluctuating electric and magnetic environment will be also a crucial step to improve the coherence of photon and spin degrees of freedom. Evidence of slight differences between nominally identical emitters point to uncontrolled extrinsic effects, likely related to residual strain, that will potentially harm the scalability of this approach. The control of these perturbations that are not yet fully understood, are a prerequisite for the fabrication of competitive quantum devices.

Quantum devices in silicon exploiting spin of individual impurities and charge state of quantum dots provide a well-established platform for quantum bit manipulation in

a device-friendly environment. The very low temperature required by these platforms (tens of mK) could be convenient also for the manipulation of the light emitters addressed in this Perspective. The detrimental effects of phonon-interactions on the Debye–Waller factor, spoiling the coherence of the emitted photons, suggest the need for much lower operating temperature channelling all the recombination in the zero-phonon line. Merging the electronic control of spin and charge states of light-emitting impurities at telecom frequency may be the next step towards a full exploitation of anchored and flying quantum bits for quantum computation and quantum information protocols in silicon.

# Chapter 2

# G- and W-centers: Spectroscopy of Individual Impurities

## 2.1 Abstract

In this chapter we provide two examples of creation of individual defects in silicon via quantum optics experiments at single-defect level, providing key experimental data on the related photophysics. Similar procedures will be followed later to create G-centers in Si-based Mie resonators (Chapter 6). Here we consider the cases of G-center and W-center, which are common radiation damage defects in silicon showing how they are created by ion implant and how they appear in photoluminescence experiments (other approaches have been explored through this PhD for activating these emitters, e.g. FIB and fs laser which are described in the Appendices B and C). The creation of single defects is demonstrated by measuring the anti-bunching in photon intensity-correlation (second order auto-correlation function), thus establishing our approach as a reproducible procedure for generating single artificial atoms in silicon. The optical characterizations for both G and W-centers are performed at Charles Coulomb laboratory at university of Montpelier. These results are published on Applied Physics Letters August 2022 (for the G-centers) and on ACS Photonics, July 2022 (for the W-center).

## 2.2 Photoluminescence Spectroscopy of Single G-centers in SOI

The investigated wafer consists of a $^{28}$Si epilayer grown on a commercial SOI wafer by chemical vapor deposition. The resulting stack is made of a 56-nm thick layer of isotopically purified $^{28}$Si and a 4-nm thick layer of natural Si, that are separated from the substrate by a 145-nm thick layer made of thermal silicon oxide. The standard process for fabricating the G-centers starts first by implanting carbon ions and then irradiating with protons. In order to heal the silicon lattice from the implantation damages, this sample is subjected to a flash annealing at 1000°C during 20 s under $N_2$ atmosphere by

rapid thermal annealing (RTA) in between the two implantation processes [55, 80].

The samples are characterized by spatially-resolved photoluminescence (PL) spectroscopy in a scanning confocal microscope built in a closed-cycle He cryostat, as described by Redjem et al. [123]. PL detection is performed with superconducting single-photon detectors (from Single Quantum) after a 1050-nm long-pass filter. Without further indications, data presented here are recorded at 30 K under CW 532-nm excitation at 10 $\mu W$.

### 2.2.1 Detection of a Set of G-centers

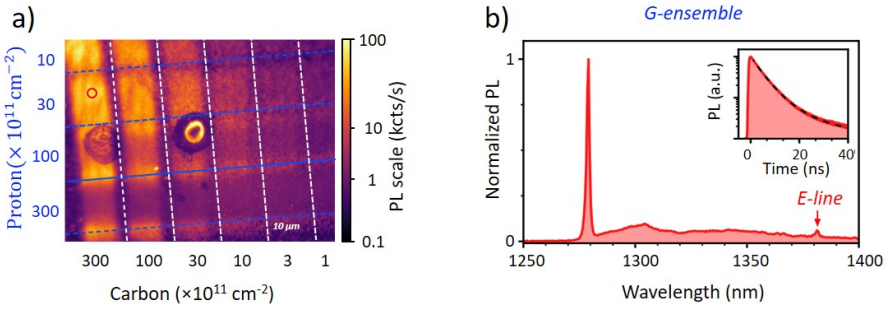


Figure 2.1: a) PL map of the SOI sample cross-implanted with carbon and proton in the region of high irradiation fluences. The vertical white (horizontal blue) dashed lines are guides for the eyes splitting the stripes with different carbon (proton) fluences, whose value is indicated in the bottom (left) axis. The two 20-$\mu$m large spots visible in the left middle of the scan are due to local sample imperfections. b) PL spectrum detected in an ensemble of G-centers at the position indicated by the red circle in a). Above data are recorded at 30 K under excitation at 532 nm with an optical power of 10 $\mu$W. Inset: time-resolved PL decay recorded with a 150-ps pulsed laser at 532 nm. The black dashed line represents data fitting with a bi-exponential function.

In this study, we have tuned the carbon and the proton implantation dose through a mica mask with a 20×200 $\mu$m aperture (Figure 2.1). A 7×7 implantation grid pattern is performed by superimposing 7 vertical carbon-implanted stripes with 7 horizontal proton-irradiated stripes separated by 10 $\mu$m. This configuration allows to probe 49 combinations of carbon and proton doses for generating G centers. The fluences vary from 0.3 to 300×$10^{11}$ $cm^{-2}$ for both carbon and proton which are implanted at energies of 8 keV and 6 keV respectively. Note that, by decreasing the irradiation doses enables to gradually switch from ensembles to isolate single defects, reaching areal densities of G centers down to $\sim 0.2$ $\mu m^{-2}$.

Figure 2.1 a) shows the PL intensity map obtained from our implanted SOI sample. We observe that the sample luminescence varies significantly from one implantation square to another. While the PL signal intensity increases monotonously with the car-

bon dose (right to left), there is a maximum at $30\times10^{11}$ cm$^{-2}$ when raising the proton concentration (top to bottom).

Figure 2.1 b) represents the PL spectrum recorded in the area with the highest PL intensity. The sharp ZPL at 1279 nm and the broad phonon-side band at longer wavelengths are characteristic of the G center in silicon, as previously reported in ensemble measurements [80]. At 1380 nm, the E line corresponds to the local vibration mode, thus is a key fingerprint of this point defect [10].

Time-resolved PL experiments were performed under 150-ps pulsed laser excitation at 532 nm (Figure 2.1 b)). The inset shows that the luminescence intensity decays with a short constant of time of $4.5 \pm 0.1$ ns, close to what was reported ($\sim 5.9$ ns) for an ensemble of G-centers in a 220-nm thick SOI wafer [55].

**Ion Distribution Profile**

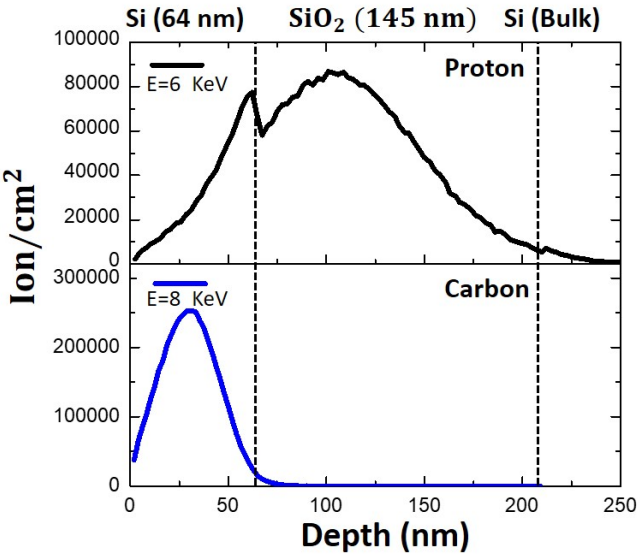


Figure 2.2: SRIM simulations (Defined in Appendix A.10) of carbon and protons ion range as a function of depth (nm) for implant in a 64 nm $^{28}$Si SOI at 8 keV and 6 keV. The profiles are obtained integrating over 300 000 ions.

Figure 2.2 represent the ion distribution profiles for 300 000 ions of carbon and proton implanted in $^{28}$SOI. The SRIM simulation show that the 8 keV implanted carbons stop in the top $^{28}$silicon layer of the SOI sample while the protons irradiated at 8 keV energy pass through this layer while producing interstitials and stop in the intermediate oxide layer.

### 2.2.2 Detection of a Single G-center

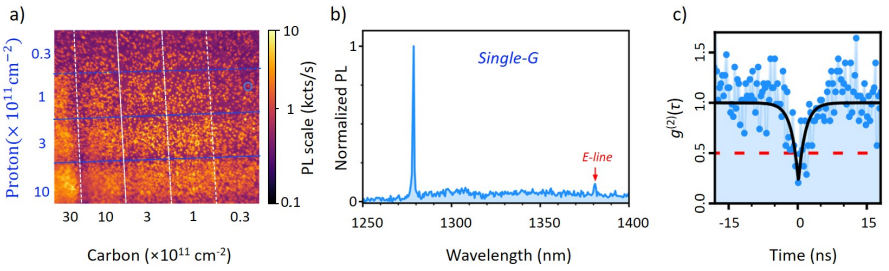


Figure 2.3: a) PL map of the SOI cross-implanted sample in the region at low ion fluency. The vertical white (horizontal blue) dashed lines are guides for the eyes splitting the stripes with different carbon (proton) fluencies. b) PL spectrum detected for an isolated G center indicated by the blue circle in a). c) Corresponding intensity-correlation function $g^{(2)}(\tau)$, evidencing the single-photon emission with $g^{(2)}(0) < 0.5$. d) Time-resolved PL trace for this single G center acquired with a 100-ps 532-nm pulsed laser.

Figure 2.3 a) shows a map of the PL signal in the low dose irradiation region of our cross-implanted SOI. The PL spectrum of an isolated bright spot in the area implanted with carbon and proton respectively at $0.3\times10^{11}$ cm$^{-2}$ and $1\times10^{11}$ cm$^{-2}$ is displayed on Figure 2.3 b).

The second-order autocorrelation function measured with a Hanbury Brown and Twiss interferometer is showcased in Figure 2.3 c): the antibunching of the intensity auto-correlation is shown with a $g^{(2)}(0) < 0.5$, accounting for the emission from a single impurity [124]. This is the demonstration of the detection of a single G center in silicon.

The estimated areal density of fluorescent defects is roughly 0.2 per $\mu$m$^2$. Since 2 carbon ions are required to form a G-center [56], the estimated creation yield in this area is on the order of 0.1%. The PL spectrum is here exactly the same for ensembles and isolated spots, as seen in Figure 2.1 b) and Figure 2.3 b). We have thus achieved the regime of single G centers in the dilute regions of our cross-implanted SOI.

## 2.3 Detection of Single W-centers in SOI

Here we studied the W-centers formed by $^{28}$Si implantation in a silicon-on-insulator (SOI) wafer at 65 keV followed by a flash annealing (T = 1000° C, 20 s, under $N_2$) for recrystallization by rapid thermal annealing (RTA). Localized implantations have been carried out to create high defect concentration areas and low defect concentration at their periphery. These low-density areas enable to isolate single W-centers and to analyze their properties by micro-photoluminescence (PL) spectroscopy.

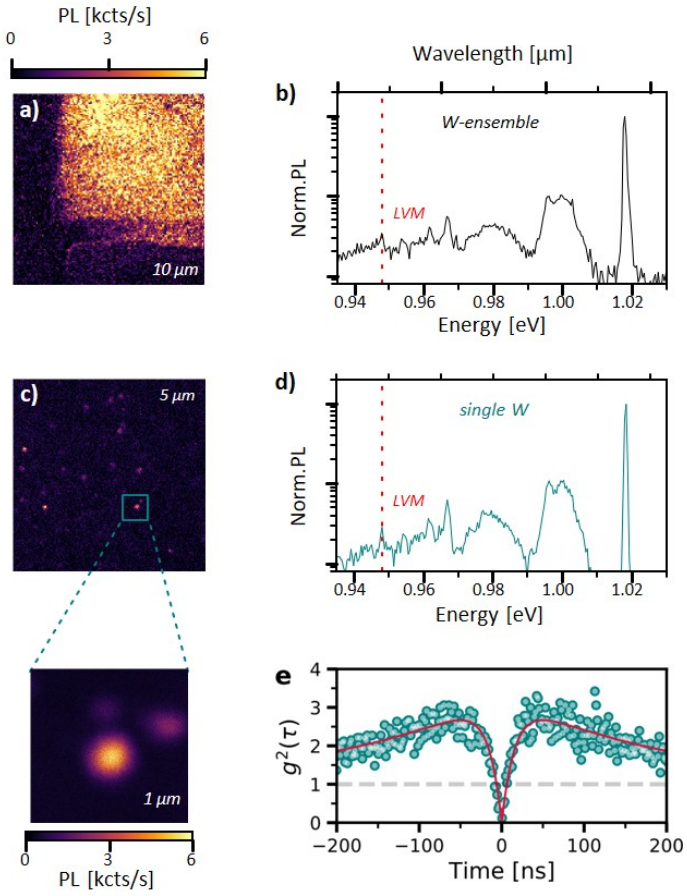


Figure 2.4: Isolation of single W-centers in silicon. a) PL raster scan of an area of the SOI sample that has been locally implanted with Si ions. b) PL spectrum recorded on a position inside the implanted area, revealing the formation of an ensemble of W-centers. The dashed red line indicates the energy of the LVM at 70 meV [125, 126]. c) PL raster scan recorded away from the highly-implanted region. d) PL spectrum from the bright spot in c), square zone with zoom. e) Second-order auto-correlation function $g^2(\tau)$ measured onto this emitter. The antibunching effect at zero delay reaches the value $g^2(0) \simeq 0.12$ , without any background or noise correction. The red curve is data fitting with the 3-level model used in [123]. All measurements are acquired at 10 K.

The optical scans of the sample performed at 10 K under 532-nm laser excitation show a high PL intensity at the location of the implanted areas Figure 2.4 a). In Figure 2.4 b), the corresponding emission is typical of the W-center in silicon, with a zero-phonon line (ZPL) at 1.018 eV (1218 nm) and a broad structured phonon-sideband that includes an emission line associated with a local vibrational mode (LVM) at 70 meV [125, 126]. In low density areas, optical scans reveal isolated PL hot spots (Figure 2.4

c)) that display exactly the same PL spectrum of the ensemble (Figure 2.4 d)) and are thus also attributed to the emission of one (or several) W-centers.

In order to check whether they stem from single defects, we measure the photon intensity-correlation: an isolated PL spot features a strong antibunching at zero delay, with $g^2(0) = 0.12 \pm 0.05$ (Figure 2.4 c)), thus evidencing the presence of a single emitter and therefore of an individual W-center. Furthermore, a bunching effect corresponding to $g^2(\tau) > 1$ is revealed in the $g^2(\tau)$ plot. It indicates that the relaxation involves a non-radiative path through a metastable level [124], an information beyond the reach of ensemble measurements.

**Ion Distribution Profile**

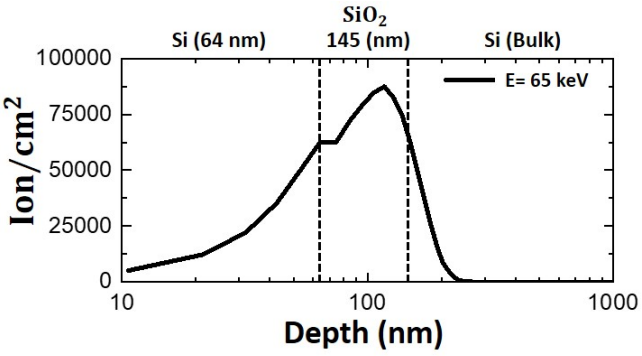


Figure 2.5: SRIM simulations (Defined in Appendix A.10) of $^{28}$Si ion range as a function of depth (nm) for implant in a 64 nm $^{28}$Si SOI at 65 keV, The profiles are obtained integrating over 300 000 ions.

Figure 2.5 represent the ion distribution profiles for 300 000 ions of $^{28}$Si implanted in $^{28}$SOI. The SRIM simulation show that the 65 keV implanted $^{28}$Si pass through the top $^{28}$silicon layer of the SOI while producing interstitials and stop in the intermediate oxide layer.

### 2.3.1 Orientation of The Emission Dipole of The W-centers

The polarization analysis of the PL emitted by individual defects provides information about the orientation of their emission dipoles [127]. Whereas the PL emission is unpolarized in W-centers ensembles, a strong linear polarization is observed at the single defect scale, as shown in Figure 2.6 a). A statistical analysis over a set of 47 individual W-centers demonstrates that this dipole projected onto the (001) sample surface can take only two possible orientations with equal probability: either along [110] or [1$\bar{1}$0]] Figure 2.6 b).

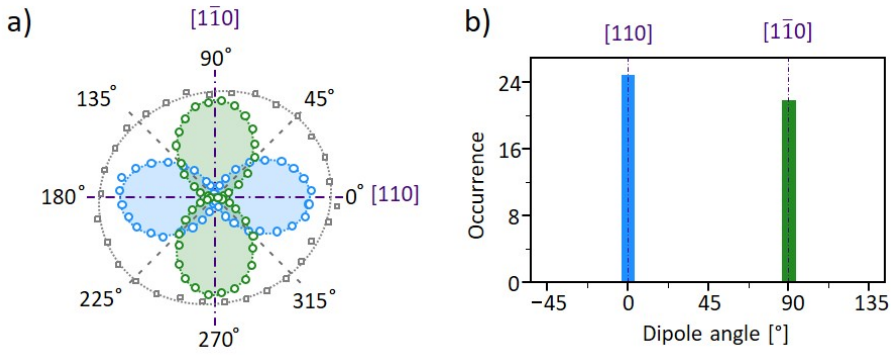


Figure 2.6: Polarization of the single photons emitted by W-centers. a) Emission polarization diagrams recorded on 2 individual W-defects (circle markers). The PL signal is measured for different angular positions of a half-waveplate rotated in front of a polarizer in the detection path [127]. The 0° and 90° directions match the crystal axes [110] and [1$\bar{1}$0]. Solid lines are fits using a $\cos\theta^2$ function. The emission polarization diagram recorded on the ensemble of W-centers is shown in comparison (square markers). Its slightly oblong shape is attributed to polarization distortion induced by the optical setup. b) Histogram of the emission dipole angle $\theta$ measured on a set of 47 individual W-centers.

## 2.4 Conclusion

By using quantum optics tools, we demonstrated the optical isolation of single W-defects and single G-defects embedded in SOI samples. For the W-defects, the polarization analysis of their single-photon emission, evidences that the W-center possesses a single emission dipole aligned onto its trigonal symmetry axis <111>. The PL spectra are strictly identical in ensemble of centers and in single emitters, for both W and G centers, demonstrating the establishment of a reproducible procedure for the creation of single centers in silicon for quantum technologies.

# Chapter 3

# Dielectric Mie Resonators: Resonant Antennas For Light Manipulation

## 3.1 Abstract

In Chapter 2 we showed two examples of creation of individual emitters in a 2D, flat silicon on insulator wafer. Here we address the case of Si-based antennas (dielectric Mie resonators) that later will serve as host for the G-centers after being activated by ion implant (as shown in Chapter 6). The chapter provides a description of the electromagnetic resonant modes formed inside a Mie resonators, the onset of directional scattering accordingly to the Kerker-like conditions and the influence of a substrate on the Mie scattering. It serves as a basis for understanding the features of the samples produced in this PhD work (see Chapter 5) and understand what are the necessary properties to enhance the light extraction form G-centers.

## 3.2 Optical Properties of High-permittivity Dielectric Particles

### 3.2.1 Scattering and Extinction Cross Section

In classical, non-relativistic physics, the scattering cross section $\sigma_s$ of a particle in any direction making angle $\theta$ with respect to the direction of propagation of the impinging electromagnetic wave (or alternatively the angle $\Psi$ with the electric field of the incident wave) is defined as the ratio of the time-averaged scattered power per unit solid angle in that direction, per unit incident power, evaluated at the location of the scattering object. Thus, it is the fraction of the total power incident that is re-radiated by the scattering object in that particular direction per unit solid angle Figure 3.1 [128].

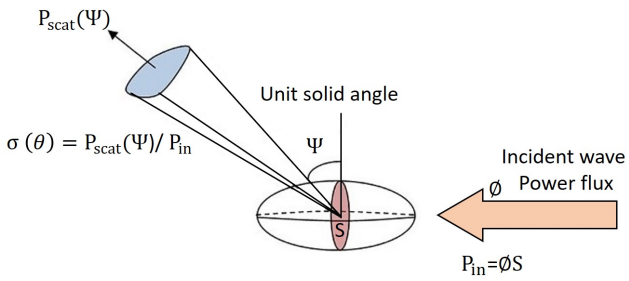


Figure 3.1: scattering cross section [128].

Extending this concept, the directional scattering cross sectional area of the scattering particle is integrated over all solid angles in all possible directions to get the total scattering cross section. It gives the ratio of the total power scattered to the total power incident on the particle.

If the object also absorbs power from the incident wave, then we can define a cross sectional area, called the total extinction cross section. This is the ratio of the total combined power lost by the wave (due to the scattering and absorption) to the total power incident on the particle. The difference between the total extinction cross section and the total scattering cross section is called the total absorption cross section.

To quantify the electromagnetic power absorbed ($W_{abs}$) and scattered ($W_{sca}$) by the particle, when $P_{in}$ is the total power incident on it, the total absorption cross section ($\sigma_{abs}$) and the total scattering cross section ($\sigma_{sca}$) can be defined as

$$\sigma_{abs} = W_{abs}/P_{in} \tag{3.1}$$

$$\sigma_{sca} = W_{sca}/P_{in} \tag{3.2}$$

Thus, the extinction cross section $\sigma_{ext}$ can be expressed as

$$\sigma_{ext} = \sigma_{abs} + \sigma_{sca} = (W_{abs} + W_{sca})/P_{in} \tag{3.3}$$

The total scattering and extinction cross section are indicated as $\sigma_s$ and $\sigma_e$ respectively. They can be obtained as a function of $a_m$ and $b_m$ coefficients derived from the boundary conditions of the solutions to Maxwell's equations. According to the Mie solution of this problem, the scattering and extinction cross section, each normalized to the particle geometric cross section $\alpha$ ($\alpha = \pi(\frac{d}{2})^2$, with and $d$ is the particle diameter), can be expressed as:

$$Q_s = \frac{\sigma_s}{\alpha} = \frac{2}{x^2}\sum(2m+1)[|a_m|^2 + |b_m|^2] \tag{3.4}$$

$$Q_e = \frac{\sigma_e}{\alpha} = \frac{2}{x^2}\sum(2m+1)[Re(a_m) + Re(b_m)] \tag{3.5}$$

where $x$=$(\frac{2\pi}{\lambda})(\frac{d}{2})$ and $\lambda$ is the wavelength of the incident wave and m is the order of the multipole expansion of the polarization due to charge oscillation inside the particle.

The coefficients $a_m$ and $b_m$ represent the contribution of the multipoles of order $m$. Note that, the absorption cross section is the difference of the extinction and scattering cross sections.

### 3.2.2 Extinction Resonances of a Dielectric Sphere

The scattering of light by spherical particles can be described by Mie theory [129], which provides an exact solution of the classical electromagnetic diffraction problem [129, 130]. For a single isolated dielectric sphere with radius $a$ and refractive index $n_p$, situated in an uniform medium of refractive index $n_m$, the scattered field can be written as an infinite series of the vector spherical harmonics, the electromagnetic normal modes of the spherical particle. Thus, the scattered electric field is characterized by the electric and magnetic Mie coefficients $a_m$ and $b_m$ of this expansion, where the $2^m$ pole term of the scattered electric field is proportional to:

$$a_m = \frac{n\Psi_m(nx)\Psi'_m(x) - \Psi_m(x)\Psi'_m(nx)}{n\Psi_m(nx)\Xi'_m(x) - \Xi_m(x)\Psi'_m(nx)} \tag{3.6}$$

and the $2^m$ - pole term of the scattered magnetic field is proportional to:

$$b_m = \frac{\Psi_m(nx)\Psi'_m(x) - n\Psi_m(x)\Psi'_m(nx)}{\Psi_m(nx)\Xi'_m(x) - n\Xi_m(x)\Psi'_m(nx)} \tag{3.7}$$

Here, $n = n_p/n_m$ is the relative refractive index, $x = k_0 a$ with the free-space wavenumber $k_0$, and the primes indicate derivation with respect to the arguments. $\Psi_m(x)$ and $\Xi_m(x)$ are the Riccati–Bessel functions, which are connected to the spherical Bessel functions $j_m(\rho)$ and the spherical Hankel functions $h_m^{(1)}(\rho)$ by:

$$\Psi_m(\rho) = \rho\, j_m(\rho), \Xi(\rho) = \rho h_m^{(1)}(\rho) \tag{3.8}$$

In this notation, $a_1$ and $b_1$ are the coefficients for the electric and magnetic dipoles, respectively, $a_2$ and $b_2$ are the coefficients for the electric and magnetic quadrupoles, and so on.

In absence of absorption, the extinction cross section $\sigma_{ext}$ of the particle and its scattering cross section $\sigma_s$ become identical and can be expressed by [131]:

$$\sigma_{ext} = \sigma_s = \frac{2\pi}{K^2} \sum_{m=1}^{\infty} (2m+1)(sin^2\alpha_m + sin^2\beta_m) \tag{3.9}$$

where $\alpha_m$ and $\beta_m$ are the scattering phase shifts and are connected to the Mie coefficients via:

$a_m = \frac{1}{2}(1 - exp(-2i_{\alpha_m}))$ and $b_m = \frac{1}{2}(1 - exp(-2i_{\beta}))$ respectively.

For particles having a large refractive index the extinction cross section is characterized by a series of sharp resonance peaks (Figure 3.2). The lowest-order mode appears at $\lambda = 2na$ (where $a$ is the radius of the particle) and corresponds to the magnetic dipole term of coefficient $b_1$. This connection between the size of the dielectric particle and its spectral resonances leads to the observation of strong color effects in the scattered light.

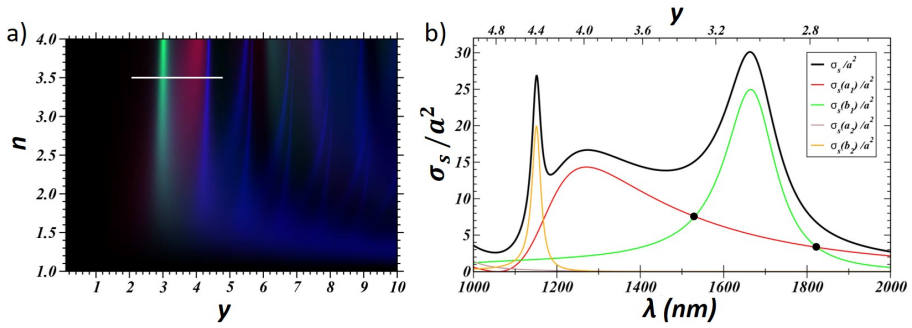


Figure 3.2: a) Scattering cross section map of a non-absorbing Mie sphere as a function of the refractive index n and the y parameter, $y = nka = n(\frac{2\pi}{\lambda}a)$ [131]. Green areas correspond to parameter ranges where the magnetic dipole contribution dominates the total scattering cross section, while red areas represent regions where the electric dipole contribution is dominating. The remaining blue-saturated areas are dominated by higher order multipoles. Brightness in the color-map is proportional to the total scattering cross section. White horizontal lines represent the y-range sowed in b). b) Scattering cross-section $\sigma_s$ normalized by the square of the particle radius $a$ versus wavelength $\lambda$ for a Si sphere having $a$ = 230 nm (the refraction index $n = 3.5$ is constant and real in this wavelength range). The contribution of each term in the Mie expansion is also shown. The green line corresponds to the magnetic dipole contribution, the red to the electric dipole and the orange one to the magnetic quadruple.

Figure 3.2 a) [131] shows the scattering cross section map for a non-absorbing Mie sphere as a function of the refractive index m and the y parameter ($y = n(\frac{2\pi}{\lambda}$a)). Brightness in the color-map is proportional to $\sigma_{ext}$ while color code represents the contribution of electric and magnetic dipoles to the total cross section. The RGB (Red, Green, Blue) code is formed by taking RGB = $\sigma_{E,1}$R + $\sigma_{M,1}$G + $\sigma_{res}B$ with $\sigma_{res}$=$\sqrt{\sigma_{ext}^2 - \sigma_{E,1}^2 - \sigma_{M,1}^2}$. The whole map is normalized to avoid over-saturation. Hence, green areas correspond to parameter ranges where the magnetic dipole contribution dominates the total scattering cross section, while red areas represent regions where the electric dipole contribution is dominating. The remaining blue-saturated areas are dominated by higher order multipoles.

As $n$ decreases, there is an increasing overlap between the wavelength dependent cross-section peaks, and the sphere resonant response smears out. Since usually non-absorbing materials present low refractive index in the infrared and visible frequency ranges, Mie resonances of small particles in these regimes have not been considered in detail. However, for Si these resonances are well visible. Figure 3.2 b) represents the scattering cross section of a Si sphere of radius $a$ = 230 nm in vacuum ($n_h$ = 1). As a result, the magnetic dipolar mode is the first resonant peak at $\lambda \approx 2na$. The second resonance is the electric dipolar mode and the third one the magnetic quadrupole. These resonances take their name from the typical shape of the electromagnetic field formed

within the sphere. This is linked to the displacement electric currents formed by the impinging electromagnetic wave that assume a shape of a doughnut for the magnetic dipolar mode (a minimum of $|\mathbf{E}|^2$ at the center of the sphere) in a analogy with a coil, or of an electric dipole (a maximum of $|\mathbf{E}|^2$ at the center of the sphere). Examples of these feature of the near field will be systematically provided through the text.

For such a Si-based spherical particle, the first two modes (dipolar-electric and dipolar-magnetic), partially overlap, as highlighted by the multi-polar expansion of the scattering cross section (black dots on Figure 3.2 b)). More specifically, there are wavelengths where the two dipolar contributions share the same amplitude (visible in the crossing of the red and green curves at about 1520 and 1820 nm). In those conditions, the simplified picture of a dielectric resonant sphere, corresponds to a magnetic and an electric dipole radiating at the same frequency in or out of phase. This feature is important in view of the interpretation and engineering of the directional far-field scattering of Si particles as discussed later in this chapter.

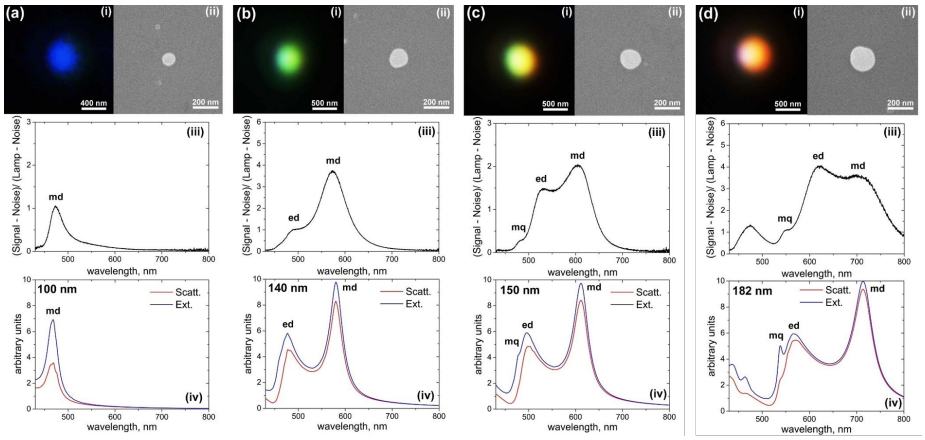


Figure 3.3: Close-view dark-field microscope (i) and SEM (ii) images of the single nanoparticles selected on the sample. (iii) Experimental dark-field scattering spectra of the nanoparticles. (iv) Theoretical scattering and extinction spectra calculated by Mie theory for spherical silicon nanoparticles of different sizes in free space. Corresponding nanoparticle sizes are defined from the SEM images (ii) and noted in each figure [132].

From an experimental point of view, this kind of resonances were reported for materials featuring a relatively large refractive index, such as Si. A. Kuznetsov showed in his work [132] that silicon spheres obtained by laser ablation and deposited on a glass slide and whose diameters span over hundreds of nanometers, can support Mie resonances (related to the terms of the scattered electric and magnetic fields) predicted by Mie theory for a dielectric particle.

Figure 3.3 shows a complete analysis done for different particles' sizes, with experimental and theoretical scattering spectra. According to this analysis, the first strongest resonance of these nanoparticles appearing in the longer wavelength part of the spec-

trum, corresponds to magnetic dipole response (MD). Magnetic dipole resonance is the only peak observed in the visible spectral range for the smallest nanoparticles (Figure 3.3 a)). At increased nanoparticle size (Figure 3.3 b) and c)) electric dipole (ed) resonance also appears in the blue part of the spectrum, while the magnetic dipole shifts to the red. For relatively small nanoparticles, the observed color is mostly defined by the strongest resonance peak and changes from blue to green, yellow, and red when magnetic resonance wavelength shifts from 480 nm to 700 nm (Figure 3.3 a-d)).

### 3.2.3 Directional Scattering and Kerker Conditions

In 1983, Milton Kerker [133] discovered an interesting effect in the scattering of electromagnetic waves by a spherical particle made of a magnetic material characterized by magnetic permeability $\mu$ and dielectric permittivity $\varepsilon$. Nowadays this study is known as Kerker effect. More specifically, Kerker and his collaborators revealed the possibility to redirect the scattered radiation to either forward or backward direction, depending on the frequency. Two main conditions were highlighted, known as first and second Kerker conditions.

Under plane wave illumination of a sphere, the first Kerker condition corresponds to a cancellation of the backward scattering (with a maximum in the forward scattering), while the second Kerker condition corresponds to a deep minimum in the forward scattering direction [134] (where backward and forward scattering are defined by the scattering along the axis of the incoming waves). Kerker and his collaborators also established that the first Kerker condition is obtained when ($\varepsilon$=$\mu$) whereas the second one is obtained when ($\varepsilon$=-$\frac{\mu-4}{\mu+1}$).

In spherical dielectric particles a directional (Kerker-like) scattering can be engineered exploiting the presence of strong Mie-type resonances of dipolar-electric and dipolar-magnetic character (first and second resonance). This can be intuitively understood from examining the scattering characteristics of an electric and a magnetic oscillating dipoles as displayed in Figure 3.4.

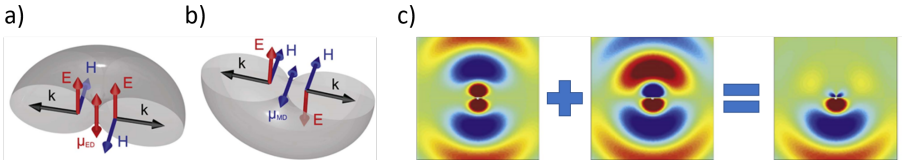


Figure 3.4: Visualization of the field polarization characteristics of (a) an electric and (b) a magnetic oscillating dipole. (c) Illustration of how the in-phase superposition of an electric and a magnetic dipole source with the same frequency leads to constructive interference in one direction and to destructive interference in the opposite direction.

While the two dipoles share the same far-field emission pattern, there is a difference in the orientation of their electric and magnetic field components Figure 3.4 a) and b). For the electric dipole, the electric fields of light propagating in opposite directions are oriented parallel one to the other, whereas the magnetic fields are oriented antiparallel.

For the magnetic dipole instead, the situation is reversed, where the magnetic and the electric fields are oriented parallel and antiparallel to each other, respectively.

Thus, by superimposing a crossed electric and magnetic dipole oscillating at the same frequency and in phase, the emitted fields interfere constructively in one direction and destructively in the opposite direction. This is illustrated in Figure 3.4 c), showing two-dimensional finite-difference time-domain simulations of the x-polarized electric field component of an individual x-polarized electric dipole (left), of an individual z-polarized magnetic dipole (middle), and of the superposition of both dipoles (right). Such a crossed electric and magnetic dipole source can be considered as a Huygens-like source where light propagates only in one semi-space [135]. Referring to Figure 3.2 b), such a condition can be found in dielectric particles that can promote a highly directional scattering of the impinging light.

This kind of directional scattering was experimentally reported in 2013 for Si-based spherical particles [136] and GaAs disks [137] However, all these examples, as well as other demonstrations reported afterwards, rely on white light illumination from the far-field of the dielectric structures that were "passive", that is non-light emitting. The Kerker-like effect was thus observed in light reflection or transmission.

Central to this PhD work and differently from the past reports, is the engineering of a Huygens-like source based on Kerker-like effect with a light-emitting Mie resonator embedding G-centers.

### 3.2.4 Dielectric Mie Resonators in Presence of a Substrate

Since most of the practical applications require particles placed on a surface (e.g. absorption in photodiodes [138], solar cells [139, 140]), a strong interaction with the substrate is even desired. This interaction will affect the resonant behavior as well as the interaction between the magnetic and electric resonances.

Van de Groep et al. [138], showed that the presence of a substrate can affect the resonant properties of the dielectric Mie resonators and the interplay between the different resonances. As an example, a cylinder of Si (diameter = 100 nm, height = 100 nm) was taken into account, on a semi-infinite substrate with a refractive index ($n_{sub}$) varying from 1 (which corresponds to a dielectric resonator in air) to 3.5 in steps of 0.25, while the refractive index of the particles ($n_{part}$) is fixed at 3.5 which correspond to the refractive index of silicon at visible and infrared frequencies Figure 3.1 a). Three characteristic features can be observed.

A change in the refractive index of the substrate from 1 to 3.5, leads to a broadening in the resonant peaks owing to an increasing of the possible radiative states and causes ED and MD peaks to spectrally overlap. For $n_{sub} > 2.25$, the ED merges with the MD peak.

To investigate the influence of particle shape, Figure 3.5 b) shows $Q_{scat}$ as a function of wavelength for the same cylinder as in a) (red), a diameter d = 114 nm of the sphere (green), and a cube with sides of length l = 92 nm (blue). The particles have the same volume, are all made of Si and the geometries are shown below a) and b).

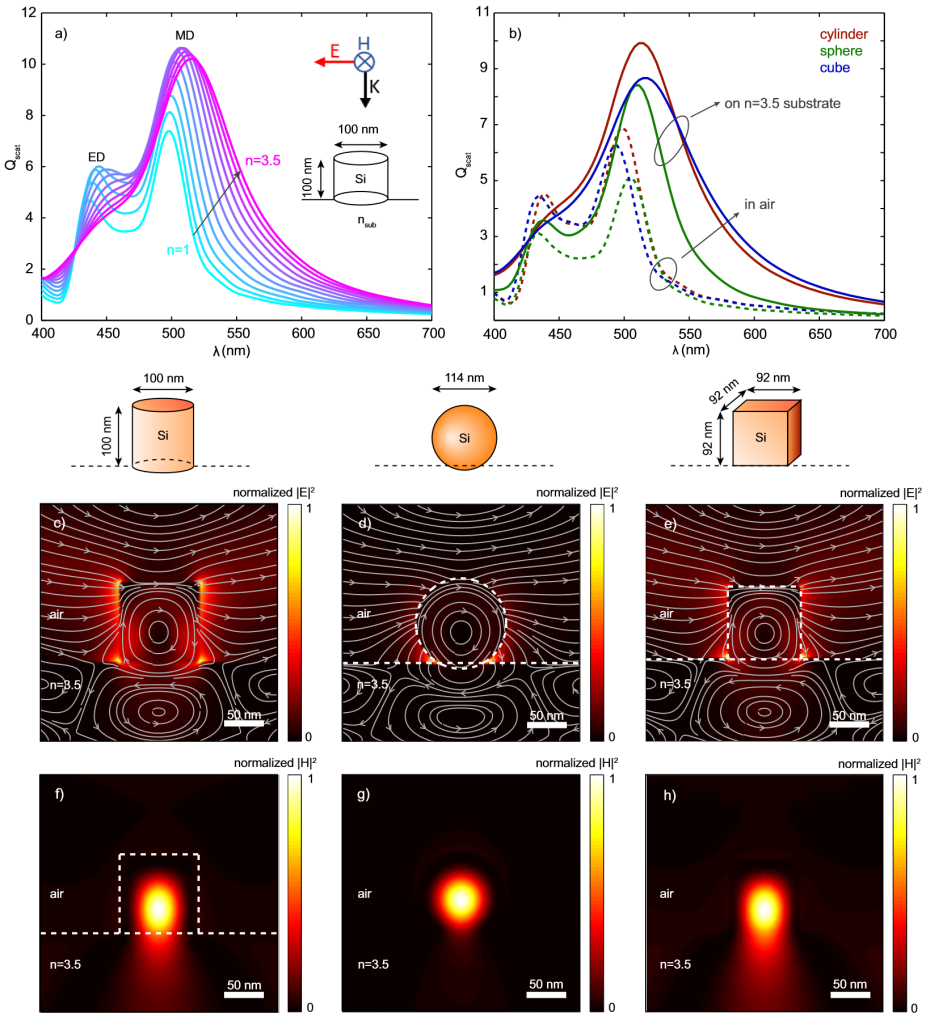


Figure 3.5: Scattering cross section, $Q_{scat}$ (Defined in Section 3.2.1), as a function of wavelength for a Si cylinder with h = 100 nm, d = 100 nm, on a semi-infinite substrate with $1 \preceq n_{sub} \preceq 3.5$, swiped in steps of 0.25. The geometry is shown as an inset. (b) $Q_{scat}$ for the same cylinder (red), a d = 114 nm sphere (green), and a l = 92 nm cube (blue) in air (dashed). All particles consist of Si and have the same volume. The three geometries are sketched below (a) and (b). Note that the sphere sticks 7 nm into the substrate to prevent an infinitely sharp contact area. (c-e) Vertical crosscuts through the center of all three particles in the plane parallel to the E-field of the source, showing the normalized $|E|^2$ (color) and electric field lines (gray). The particle surroundings and air-substrate interface are indicated with white dashed lines. The respective geometries are shown above the figures. The displacement current loops are clearly visible. (f-h) The same crosscuts as in (c-e), now showing the normalized $|H|^2$ (color) of the MD modes. The magnetic field lines are not plotted since H $\sim$ 0 in this plane (perpendicular to source $\vec{H}$)[138].

The dashed lines in Figure 3.5 b) correspond to particles in air, the solid line to particles on a semi-infinite substrate with $n_{sub} = 3.5$. Note that the sphere is sticking 7 nm into the substrate (center is at 50 nm height above the substrate) to prevent unphysical hot spots at the infinitely sharp contact area (see sketched geometry). Figure 3.5 b) shows that, when a dielectric particle is in air or on a substrate, the shape of the particle has only a small influence on the resonance wavelengths of the ED and MD modes. For all the corresponding shapes both resonances are supported, and the cylinder proves to be the most efficient scatterer. Furthermore, for all shapes $Q_{scat}$ increases significantly due to the enhanced local density of optical states (*LDOS*), when put onto a substrate. However, comparing the solid lines with the dashed lines it appears that both the cylinder (red) and the cube (blue) show a dramatic broadening of the ED and MD resonances when compared to the case in air, causing the ED to appear as a shoulder on top of the MD mode. For the sphere (green), the broadening is significantly smaller and the ED remains a separate peak.

To understand this difference, vertical crosscuts are plotted (parallel to the E-field of the driving field) through the center of all particles on the semi-infinite substrate with $n_{sub} = 3.5$ at the MD resonance wavelength. Figures 3.5 c)–e) show the normalized $|E|^2$ (color) and the electric field lines (gray), while Figures f)–h) show the normalized $|H|^2$ (color). The magnetic field lines are not plotted because H $\sim$ 0 in this plane, which is perpendicular to the H-field orientation of the driving field. Figures 3.1 c)–e) clearly show the displacement current loops that induce the magnetic dipole $\vec{m}$ of the MD mode. Both c) and e) show that for the cylinder and the cube a significant fraction of the displacement current loop extends into the substrate. For the sphere, despite the fact that it sticks into the substrate, this effect is much smaller.

As a result, the coupling to the substrate is much weaker for the sphere than for the cylinder and cube. This is also clearly observable in Figures 3.5 f)–h), which show that the magnetic field profile of the MD mode inside the substrate is much brighter for the cylinder and the cube, when compared to the sphere. The contact area of the resonator with the substrate is thus very important to get strong coupling to the substrate and provides tunability of the radiation rate $\gamma_{rad}$ into the substrate. Note that in Figures 3.5 c)–e) a second (reversed) current loop can be observed in the substrate below the particles. We attribute this to image dipoles induced by the dipole moments in the particles.

## 3.3 Conclusion

In this chapter we showed that strong scattering resonances appear for dielectric particles featuring a relatively large dielectric constant and reduced absorption losses when $\lambda$= 2na. In these conditions, strong color effects in the light scattered by the particles can be observed. Highly directional scattering (Huygens-like source) can be obtained when engineering the electric and magnetic resonance. We have also shown the influence of the refractive index of the substrate and the particle geometry on the resonant behavior of single dielectric particles coupled to a substrate.

# Chapter 4

# Dielectric Mie Resonators: Nanofabrication and Optical Properties

## 4.1 Abstract

This chapter focuses on on self-assembly of Si-based islands by solid-state dewetting that was used in this PhD work to fabricate the Mie resonator. A description of the underlying phenomenology and engineering of Si-dewetting is provided, including top-down and bottom-up approaches (e.g. Focused Ion Beam (FIB), E-Beam Lithography with Reactive Ion Etching). We finish with examples of applications of Si and SiGe-based Mie resonators to colored filters, or to form complex nano-architectures.

## 4.2 Mie Resonator Fabrication

In the last decades, several methods have been developed for the realization of Mie-resonant high-index nanoparticles. Each of these techniques has advantages and drawbacks that are not discussed here. We only mention that in the literature, the main methods to produce Mie resonators made of high permittivity materials are: Colloidal self-assembly [141], chemical alkaline etching [142], nano-imprint Lithography [139], E-beam and reactive ion etching [143, 144], and laser ablation [145].

Here, we used solid state dewetting, that is a spontaneous phenomenon and gives some advantages with respect to the other techniques.

## 4.3 Solid State Dewetting

Solid state dewetting is a very common phenomenon observed in thin films that are typically not stable under annealing even well below the material melting point. Thin

films have the tendency to break in small islands as commonly observed in films of liquids and polymers. In thin solid films, dewetting is mostly due to surface energy minimization via surface diffusion [146].

Spreading film on a substrate will result in wetting or dewetting the surface depending on: 1) the surface energy density ($\gamma$) between the substrate and the surrounding vapor phase, 2) the vapor and the film, and 3) the film and the substrate. Surface energy density, translates into force per unit length (Figure 4.1). This force applies along

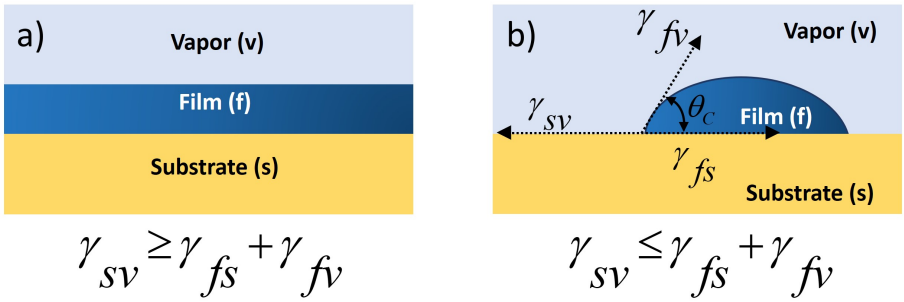


Figure 4.1: Schematic illustration of equilibrium film morphology

the interfaces and minimizes the corresponding positive surface energy. The Young equation of the equilibrium contact angle for thin films [147, 148] is given as follow:

$$\theta_C = \cos^{-1}\left[\frac{\gamma_{sv} - \gamma_{fs}}{\gamma_{fv}}\right] \tag{4.1}$$

For case a), when $\gamma_{sv} \succeq \gamma_{fs} + \gamma_{fv}$ and the equilibrium contact angle is zero, then the film wets the substrate and the equilibrium morphology is a 2D layer. If instead the opposite inequality holds, dewetting occurs and the film tends to agglomerate in islands. In this case there is an equilibrium contact angle that appears between the film and the substrate (case b).

The spatial distribution of the islands during the film retraction is controlled by a Rayleigh-like instability which is characterized first, by the formation of holes and the consequent retraction of the 2D thin film and formation of a rim that later will develop other instabilities (e.g. for monocrystalline materials: finger and bulging) that will lead to the islands formation.

### 4.3.1 Solid State Dewetting Via Capillary-driven Surface Diffusion

Unlike liquids where volume diffusion is an important parameter to be considered for dewetting, in solid films [149], the main mechanism of mass transport is surface diffusion of adatoms. These atoms are partially free to move on the surface, eventually in preferential directions determined by the symmetry of the underlying solid (e.g. as in the case of monocrystalline silicon on insulator used here). In an ideal case, at a given temperature, a uniform thin film is in an equilibrium state, where the overall speed of

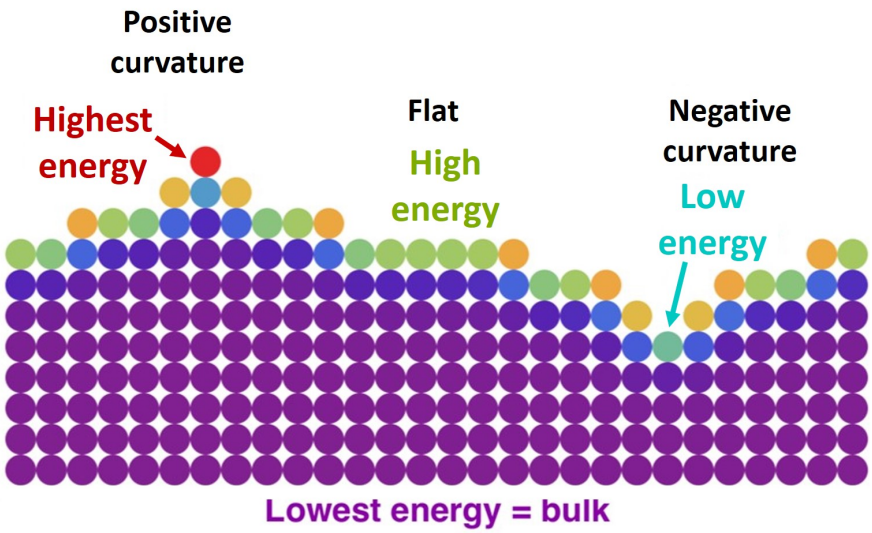


Figure 4.2: Excess surface free energy, from Dr. R. Zucker PhD [149]: the color code illustrates the energy of the atoms considering a Lennard-Jones pair potential: a bulk atom has 8 bounds; in different positions this number can larger (vallys) or smaller (hills). This number is determined by the geometrical surface curvature.

the adatoms is zero and the thickness of the film is constant in average. However, this is not a stable equilibrium state of the system, if perturbed, can evolve to a lower energy state, that is from a thin layer into islands (that eventually feature the faceted, equilibrium shape of the material composing the initial film). Although it is not clear how the dewetting is initiated, by rising the film temperature even well below the melting point of the film, holes will form, determining a radical change in the picture of the film. For sufficiently large holes (with a radius of the order of the thickness of the film), there will be a portion of the solid featuring a relevant geometric curvature, unlike the rest of the solid that is flat has a curvature identically zero.

The dewetting dynamics of a thin film is driven by capillary forces that determine the surface tension [149] (Figure 4.2). These forces can be represented as a force per unit surface. This springs from the attractive bonds between atoms or molecules in a condensed phase, as for instance a droplet of water where the inner molecules are bound (by hydrogen bounds) to the surrounding ones, whereas those at the droplet surface have only one side surrounded. This result in an excess energy and thus a compressing force agglomerating the droplet. In a solid, an alternative picture is a force springing from an excess free energy [149]. For instance an atom in a FCC crystal has 12 nearest-neighbors. However, on the surface of the solid only six nearest-neighbor bonds are present increasing free energy of the surface atoms. A rough estimation of the surface energy density of this film [150] is to be six times larger than the bond energy normalised by the surface area per atom (the square of the bond length).

Thus the surface energy density changes depending on the unsatisfied bonds and can change depending on the morphology of the film surface. For a rough surface the number can change, whereas for a flat surface it is constant (Figure 4.2). For an atom atop of a hill the number of bonds can be smaller than the flat counterpart and for an atom on a hill larger than that. This difference entails a variation of the surface energy density (increase for an atom on a hill and decrease for an atom on a valley).

More precisely, the chemical potential on the surface depends on the surface mean curvature (between the curvature on the plan of the film and orthogonal to it). The derivation of Mullins for the chemical potential is [151]:

$$\mu(s,t) = \gamma\Omega K(s,t) \tag{4.2}$$

where $\Omega$ is the atomic volume and K is the mean curvature. K is given by the averaged principal curvatures of the surface $K = 1/2(K_1 + K_2)$, where $K_1$ and $K_2$ are determined by the principal radii of curvature of the surface $K = 1/2(1/r_1 + 1/r - 2)$[149]. Thus K is determines how fast a surface will change if the interface evolves through a volume V: $K = dA/dV$ and the total interface energy will be $\int \gamma dA$. The total energy of an interface is $A\gamma dA$, where A is the total interfacial area, where dA is a surface element of the surface A and $\gamma$, is the surface energy density. For isotropic materials $\gamma$ does not depend on surface orientation (does not depend on the coordinates and can be moved of the integral) whereas for faceted solids it is anisotropic. In these latter cases the expression for the chemical potential is provided in terms of weighted mean curvature (WMC) [149]:

$$\mu = \kappa^{\gamma}\Omega \tag{4.3}$$

The dewetting phenomenology is described by the dewetting speed of atoms at the film interface (experiencing different surface energy density according to the curvature at their position on the surface of the solid). Overall, this speed translates in a outward motion of the interface parallel to the surface normal $V_n$ (normal vector $n(s,t)$, normal to the surface determines its orientation as a function of position and time; by convention, the normal vector points outwards, away from the material). This speed as a function of time and position $V_n(s,t)$ gives the complete evolution.

The expression derived by Mullins for the starts with the chemical potential and its dependence on surface curvature. The flux of surface atoms in response to curvature gradients is given by Fick's first law:

$$J(s,t) = -\frac{D_S \upsilon}{kT}\nabla_s \mu(s,t) = -\frac{D_s \gamma \Omega \upsilon}{kT}\nabla_s K(s,t) \tag{4.4}$$

where $D_s$ is the surface self-diffusivity, $\upsilon$ is the surface concentration of mobile atoms, $k$ is Boltzmann's constant, $T$ the temperature, and $\nabla_s$ is the Laplace-Beltrami operator. Physically, Fick's first law states that when a gradient in a potential is present, material tends to flow down that gradient to lower the total energy. If the flux is locally divergent, then mass leaves that location and the surface height decreases. Likewise, if the flux is convergent, the surface height is increasing, and it has a positive velocity along its normal. Thus, the surface velocity along its normal, $V_n$(s,t), is minus the divergence of the flux:

$$V_n = \frac{D_s \gamma \Omega^2 \upsilon}{kT} {\nabla_s}^2 K(s,t) \tag{4.5}$$

where the extra factor of $\Omega$ is included to convert the units to a velocity [151]. This governing equation can be generalized to include anisotropy [152, 153].

The material constants in Equation 4.5 can be collected into a single material property, (B= $D_s \gamma \Omega^2 \upsilon / kT$). The governing equation can be non-dimensionalized using B (units of length$^4$/time) and a characteristic length scale L:

$$\upsilon_n = {\nabla_s}^2 K(s,t) \tag{4.6}$$

where $\upsilon_n$ is the dimensionless normal velocity, $\upsilon_n = V_n L^4 /$ B, and $\kappa$ is the dimensionless mean curvature, $\kappa$ = KL.

This expression derived for isotropic materials justify the fact that, when a sufficiently large hole is present in a thin film (spontaneously or artificially created), the local geometrical curvature changes, resulting in a finite speed of material from that point "inward". The mass accumulates in a thick rim that will eventually evolve further with other instabilities that are not described here.

**Thin silicon film**

Let's now consider the case of a thin layer of a crystalline silicon on insulator (SOI), that is relevant to this PhD work. In this case the model of spontaneous dewetting via surface diffusion has been intensively studied [154, 155], and it is schematically illustrated in Figure 4.3. Starting with a SOI and introducing it in a molecular beam epitaxy chamber (in ultra-high vacuum), and rising the temperature (e.g. up to about 800 $^o$C) we observe the evolution of the Si film forming holes which then expand. During the lateral expansion of the holes, the thin-film breaks in fingers and islands sitting on the buried oxide (BOX).

Step 1) is the critical void formation, this can be formed due to surface defects where voids appear spontaneously (for sub-critical void the holes are filled and disappear).

Step 2) is called "void edge thickening", where a supercritical void edge causes mass to flow from this edge to the neighboring flat film region and results in a continuous uniform edge.

Step 3) above a critical size, voids grow spontaneously by expelling film matter that may partially accumulate in a thickening rim around the opening voids.

Step 4) is called "fingers formation" and growth, where the locally thinner edge regions break down forming parallel and elongated structures.

Step 5); it's the island agglomeration, the uniformly spaced Si fingers formed in step 4) break up into discrete islands. Thus, dewetting constitutes a simple and highly productive method (independent from the SOI wafer size) for the fabrication of high-index nanoparticles. On the other hand, controllable arrangement of size and shape of the particles on the sample is still a problem for this method, as it relies on a spontaneous phenomenon that brings some randomness in islands size, shape and position.

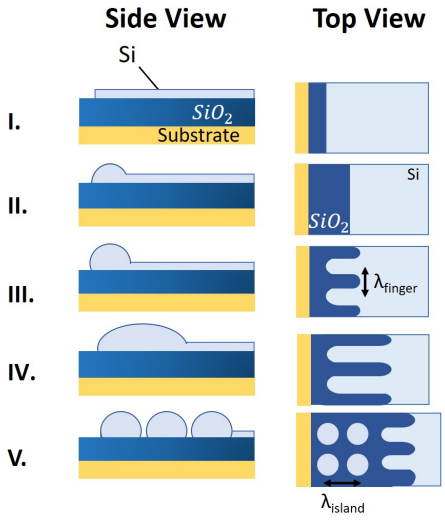


Figure 4.3: five-step capillarity-driven SOI agglomeration mechanism.

## 4.4 Spontaneous Solid State Dewetting of Thin SOI: Self-assembly of Mie Resonators

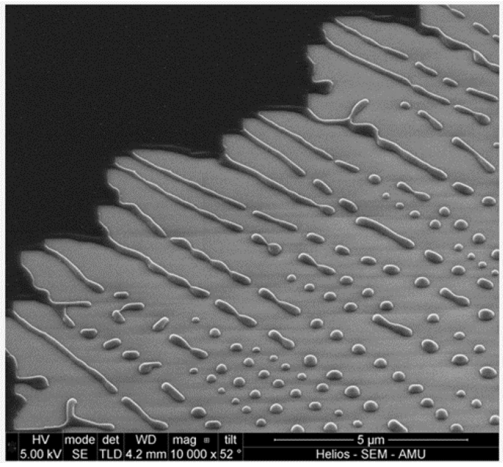


Figure 4.4: SEM image showing the uniform edge breakdown and void finger front propagation that is observed in a silicon film $\approx$ 10 nm after UHV annealed at 800° C for 1 hour and half.

Figure 4.4 represent a SEM image of a spontaneous dewetted thin silicon film (10 nm) after annealing in ultra high vacuum at 800° C for one hour and half. This is an example to show that the 3D islands produced by spontaneous dewetting lack of size and position order. In order to overcome this problem the development of lithography-based methods (e.g. FIB and optical lithography joined with solid state dewetting) towards the fabrication of highly ordered patterns of 3D islands are shown in the following paragraphs, and also in chapter 5.

After dewetting, thin-film breaks up to form isolated Si nanocrystals which finally evolve toward truncated pyramidal nanocrystals exhibiting a faceted shape with the onset of the low-energy facets: (111), (113) and (001) [156] as shown Figure 4.5 a) which is a typical transmission electron microscopy (TEM) image of a dewetted Mie resonator, attests the equilibrium shape and monocrystalline nature of the nanostructure.

In order to measure the typical scattering spectrum from a silicon nanocrystal and evaluate if the dewetting process is adapted to fabricate Mie resoanators a partially dewetted sample is investigated. Locally, it exhibits isolated nanocrystal with separation distances exceeding several microns for which electromagnetic coupling between neighboring Mie resonators can be neglected. Figure 4.5 b) (left panel) shows a reflection dark-field (DF) image of Mie resonators obtained by annealing at 850°C for 25 min, a SOI substrate featuring a 11 nm thick silicon layer on a 145 nm $SiO_2$ layer. Comparison of the same isolated Si crystals in dark-field and atomic force microscopies (AFM) on Figure 4.5 b) indicates that resonators with different shapes and sizes exhibit different resonance frequencies.

The morphological characterization of 20 scatterers using AFM (Figure 4.5 c)) shows the formation of islands with an average base size L (L is the average in-plane size ($L_m$ + $L_M$)/2 with $L_m$ and $L_m$ the small and large lengths) ranging between $\sim$ 250 and $\sim$ 400 nm and with heights h ranging between $\sim$ 50 and $\sim$ 85 nm. The vertical aspect ratio $\eta$ = h/L is close to 0.2 and stays constant in the investigated range of particle sizes.

The scattering spectra of isolated resonators are measured using a dark-field microscope fiber-coupled to an imaging spectrometer. Figure 4.5 d) (left panel) provides typical measured spectra for Si resonators with varying in-plane sizes L and heights h estimated in AFM. The result show that all the spectra are characterized by two main broad peaks (A and B) that are the signature of the resonant excitation of two different modes in the Si crystals. Both peaks are red-shifted when h and L are increased from 53 to 72 nm and 250 to 400 nm, respectively.

A numerical simulation is performed using a finite element method which is compatible with the faceted shape of the dewetted islands. By taking into account that the excitation geometry offered by reflection dark field microscopy the scattered electromagnetic field is computed in air (Figure 4.5 d) right panel) when the Mie resonator is illuminated by a plane wave with an angle of incidence of 70 degrees for the 6 resonators considered in Figure 4.5 d) (left panel). The numerical simulations confirm the excitation of two modes in the resonators with frequencies that are red-shifted for increased particle sizes.

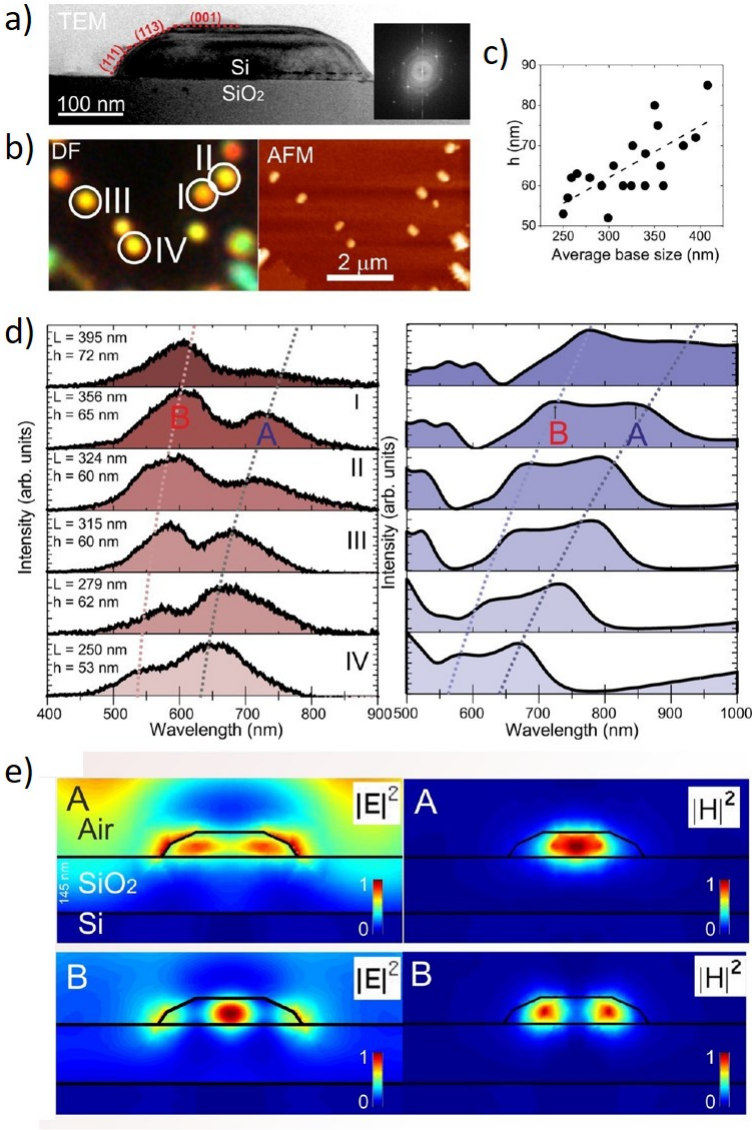


Figure 4.5: Morphological and optical characterization of single Mie resonators. a) TEM image of a single silicon Mie resonator. The crystallographic facets (111), (113) and (001) are highlighted. The inset provides the fast Fourier transform of the image, demonstrating the crystalline nature of the particle. b) Darkfield (DF) optical microscope image (100 magnification objective lens) of a partially dewetted sample (left panel) and corresponding atomic force microscope (AFM) topography (right panel). White circles surround 4 resonators whose DF spectra are shown in d). c) Mie resonator height as a function of the corresponding base size as measured by atomic force microscopy (AFM). The dashed line is a linear fit to the data. d) Left panel: DF backscattering spectra of six Mie resonators with increasing sizes from bottom to top panel (height h and base size L are given for each spectrum). Right panel: numerical simulations of the scattering spectra obtained with the finite element method considering the 6 Mie resonators shown in the left panel. The dashed lines in the two panels are guides to the eyes. e) Reconstruction of the electric $|E|^2$ and magnetic $|H|^2$ field intensity in the vicinity of the resonator I in (c) (L = 356 nm and h = 65 nm) [157].

We now address the physical origin of the A and B resonances. Their different nature is highlighted by computing the electric and magnetic field intensities at the two resonant frequencies in the vicinity of the resonator on Figure 4.5 e). The calculations are performed for the resonator denoted with L = 356 nm and h = 65 nm. The norm of the electric field $|E|^2$ is displayed when the resonator is illuminated by a plane wave with an angle of incidence of 70 degrees. As a result, an observation of different field distributions since the B resonance corresponds to the formation of a single spot in the middle of the cavity while the A mode provides two spots near the edge of the Si island and a strong field intensity outside the resonator. As shown on Figure 4.5 e), the two $|E|^2$ spots of mode A lead to an enhancement of the magnetic field in the center of the resonator. These maps indicate that mode A is dominated by an in-plane dipolar magnetic mode [138]. Symmetrically, the electric field enhancement in the center of the cavity in mode B is related to two spots of the magnetic field, indicating an electric dipolar resonance. These maps evidence the fact that the two peaks are mostly linked to the excitation of the first two Mie dipolar modes inside the Si resonators.

## 4.5 Color Filters Using SiGe-Based Mie Resonator Arrays

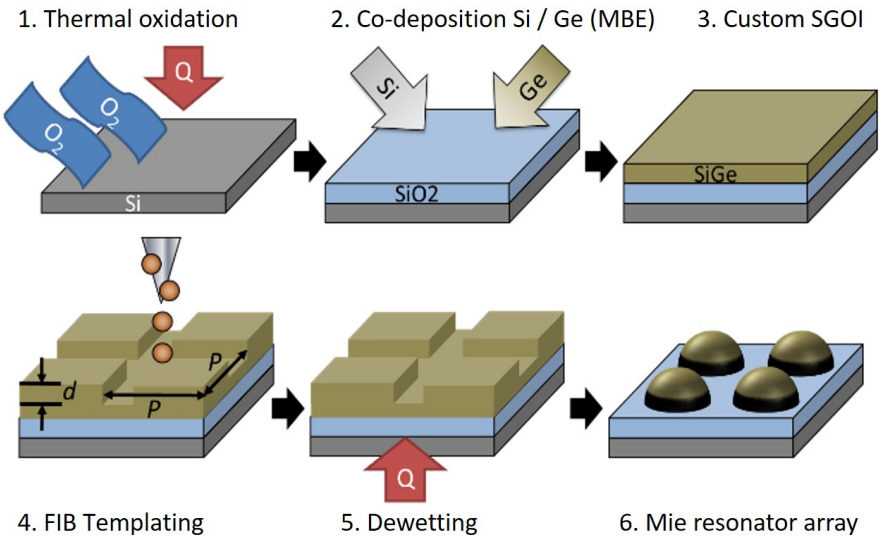


Figure 4.6: Diagram showing the steps involved in the fabrication of Mie resonator arrays. Panel 4 shows the periodicity P and milling depth d [158].

As an example of ordering of dielectric islands via solid state dewetting , we consider here the case of patterning a SiGe layer deposited via molecular beam epitaxy atop

$SiO_2$ and describe the onset of Mie resonances supporting bright colored scattering [158]. This characterization is limited to the visible part of the spectrum. Larger particles of similar shape produce the same effects at larger wavelength. We showcase the use of arrays of resonant particles formed by templated dewetting of SiGe films to produce wavelength-tunable color filters working in light reflection, transmission as well as in diffusion.

The custom substrate was prepared via a two-step process (Figure 4.6). Firstly, thermal oxidation of crystalline Si wafers was carried out in a rapid thermal processing oven (thickness BOX is fixed to 150 nm), followed by deposition of 30 nm of SiGe (percentage of Ge is about 20%) under ultra-high vacuum (UHV) in a molecular beam epitaxy (MBE) reactor.

The sample was then transferred to a mass-filtered liquid-metal ion source FIB (LMIS-FIB) milling system for templating prior to dewetting. Eight groups of square, SiGe patches having overall size of about 15 $\times$ 15 $\mu$m size were milled. The pitch between the milled trenches were P = 250, 290, 330, 360, 400, 450, 500, 550, and 600 nm, with 4 different nominal target milling depth d: 2, 4, 6, 7 nm.

After ion milling the sample was then returned to the UHV chamber of the MBE reactor for dewetting (annealing) at 700°C for 30 minutes. After annealing the dewetted islands are no longer constituted of amorphous material, but are made up of polycrystalline SiGe [159]. The prepared sample was initially characterized by bright and dark-field optical microscopy in order to observe the reflected and diffused colors, as well as to obtain an indication of the homogeneity of the resonator arrays formed.

## Optical Characterization Results

Figure 4.7 a) shows the reflected and diffused colors observed by an imaging optical microscope as a function of the array periodicity P and the milling depth d. Patterns sharing the same milling depth are arranged on a same row, with the period increasing from left to right.

The effect of these two parameters on the size of the Mie resonators formed after dewetting is best understood through the diffused colors: for a given milling depth d, increasing the pitch P yields larger resonators as shown by the diffused color transitioning from short to long wavelengths (e.g. blue to red shown on row d = 6 nm, from r1 to r5).

For the largest periodicities, the diffused colors begin to taint blue due to the Mie resonators supporting multiple resonant modes. For a fixed periodicity, increasing the milling depth yields smaller resonators due to the fact that deeper milling sputters more material and the diffused colors blue-shift. In the right of the panel (columns labelled "Spont") is an image of the spontaneously dewetted region, viewed in both bright and dark-field.

The characterizations of pixels numbered from r1 to r9 at milling depth d = 6 nm yields diffused colors covering the entire visible spectral region: Figure 4.7 b), c) show the collected diffusion (D) and reflection (R) spectra for the pixels highlighted in a white box Figure 4.7 a).

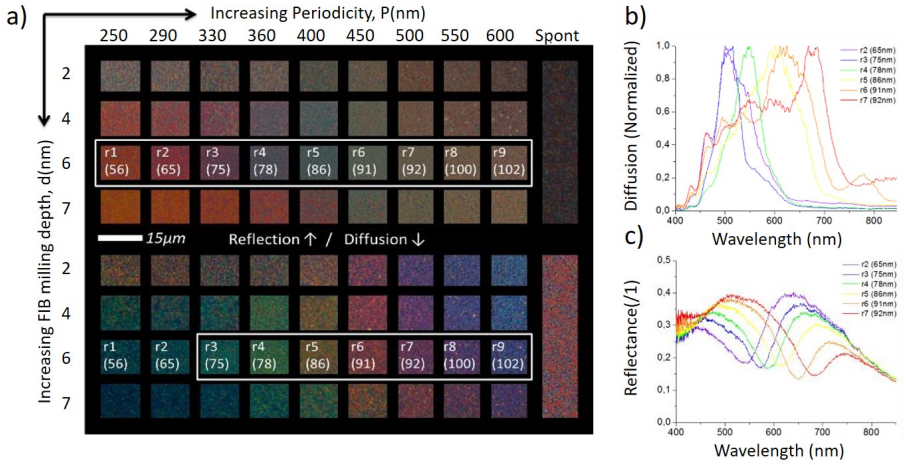


Figure 4.7: a) Palette formed from bright-field (reflectance) and dark-field (diffusion) optical images of resonator arrays of varying periodicities P with different templating milling depths d. To the right of each panel (columns labelled "Spont") is an image of the spontaneously dewetted region of each sample viewed in both bright- and dark-field. The numbering of arrays is used in the optical characterization. The numbers in brackets correspond to the estimated resonator radii in nm. Each $15\mu$m $\times$ $15\mu$m dewetted pattern is here surrounded by a black cornice in order to better highlight and compare the reflected and scattered colors. b), c) Scattering and Reflectance spectra for selected pixels, each curve is self-normalized [158].

The general trends can be summarized as follows: as the resonator size increases, the peaks in the diffusion spectra are seen to shift from blue to red (r2 through to r7/8), as well as multiplying in number for the largest periodicities (r6, r7 and r8), corresponding to the presence of multiple resonance orders in the islands.

In the reflection spectra, minima can be observed at spectral positions near the diffusion peaks due to the substrate coupling phenomenon. At the sides of these minima, the reflection spectra are seen to exhibit maxima whose positions determine the apparent reflected color of the arrays.

In conclusion, reflection and diffusion filters can be formed via dewetting of amorphous layers previously milled with square lattices of varying pitch using the LMIS-FIB. The ability to tune the operating wavelength by varying the size of the islands allows for a flexible design that can be adapted to many different applications. Later, in Chapter 5 and 6 we will show how to engineer large Si islands with an alternative method and how to integrate light emitting G-centers within.

## 4.6 Complex Nano-Architectures and Si-based Nanowires

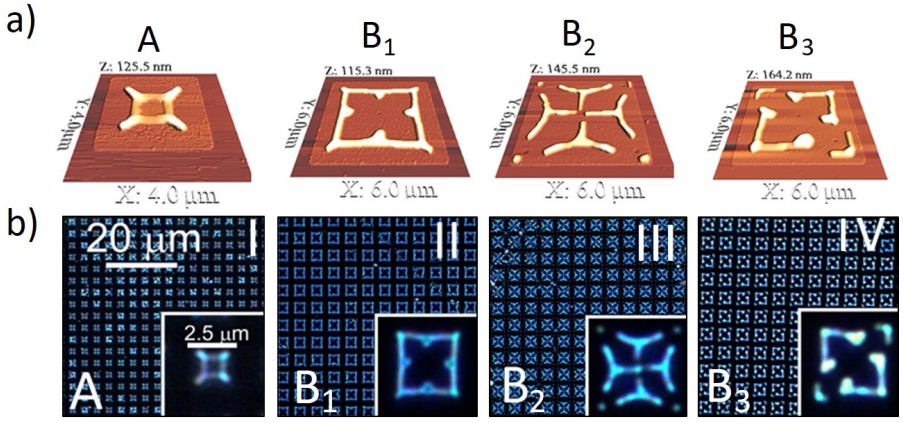


Figure 4.8: Structural and optical characterization of dewetted Si on $SiO_2$. a) 3D view of atomic force microscopy (AFM) images of patches annealed for 3 hours. b) Optical dark-field microscopy images. Each panel displays the full patterned area. The bottom right inset in each panel displays an enlarged view of a single dewetted patch. Panels from left to right display patches with an increasing level of complexity of the etched pattern within the main square [19].

For the sake of thoroughness we show here the possibility to engineer via solid state dewetting, more advanced device geometries with respect to simple isolated islands. Using electron-beam lithography (EBL) and reactive-ion etching (RIE) followed by solid state dewetting of an ultrathin silicon films on insulator (UT-SOI; 12 nm thick), allows to perfectly control the formation of a variety of monocrystalline nanostructures with high fidelity over hundreds of repetitions and extremely large scales. The dewetting evolution can be engineered to deterministically form a plethora of complex nanoarchitectures of connected islands and wires, with fluctuations of the main structural parameters as low as a few percentages [19].

Evolving from a simple square SOI patch (as previously shown for the SiGe-case) that leads to the formation of individual islands, it is possible to create larger patches (that would naturally split in many islands) and add simple features within, in order to modify the dewetting dynamics. The versatility and stability of this method are demonstrated by milling arrays of patterns featuring an increasing level of complexity, by etching holes or trenches in a square patch. After dewetting, complex patterns, including one to five holes favor the formation of a few islands and wire-like connected structures Figure 4.8).

A second case, more relevant to applications in photonics, are nano-wires obtained with the same method, exploiting lithography of a SOI and dewetting (Figure 4.9).

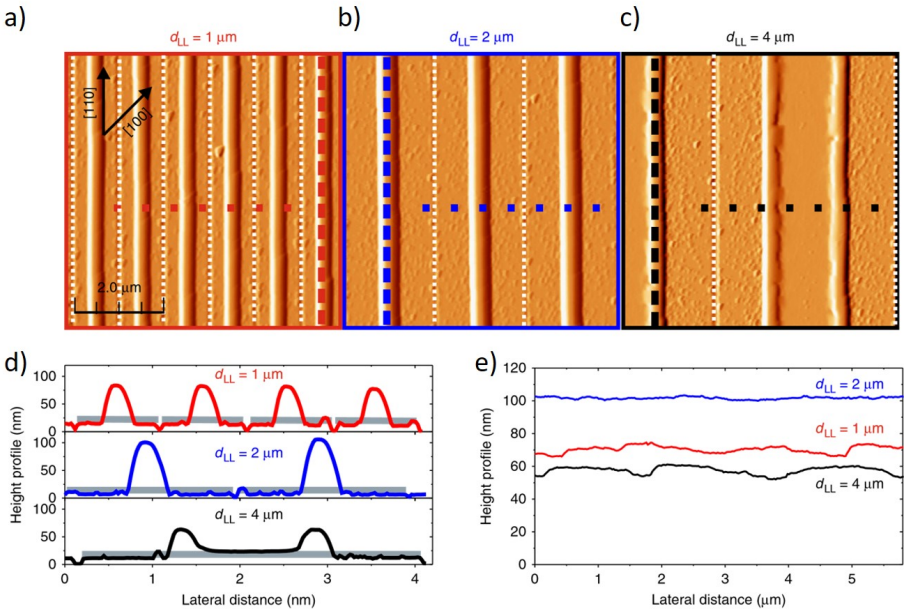


Figure 4.9: a)–c) Atomic force microscopy (AFM) images of parallel wires arrays dewetted at 720°C for 2 h for $d_{LL}$ = 1, 2 and 4 $\mu$m respectively, and a length of 75 $\mu$m. The width of the etched trenches was about 100 nm (highlighted by vertical, white dotted lines). Horizontal dashed lines highlight the height profile shown in d). Vertical dashed lines highlight the sagittal height profile shown in e). d) Transverse height profiles (from a)–c), respectively top, central and bottom panel). The shaded areas highlight the original UT-SOI profile before annealing. e) Sagittal profiles of the wires shown in a)–c) [160].

After the dewetting process, and for the small etched trenches ($d_{LL}$ = 1 and 2$\mu$m), collapsed in an individual wire, whereas for the bigger etched trenches ($d_{LL}$ = 4$\mu$m) were partially dewetted in two parallel counter-propagating rims, as revealed by AFM measurements (Figure 4.9 a–d)). These features are attributed to a faster dewetting dynamics (and in turn to an earlier onset of the morphological instabilities) associated to smaller radius (i.e. larger curvature at the surface [161]) even when considering a contact with a substrate [162].

For instance, through this nano-wire geometry, light can propagate over long distances by total internal reflection. As an example, we show an important preliminary result, where we extracted the photoluminescence spectrum of G-centers after the integration inside the wires fabricated via optical lithography and solid state dewetting (Figure 4.10).

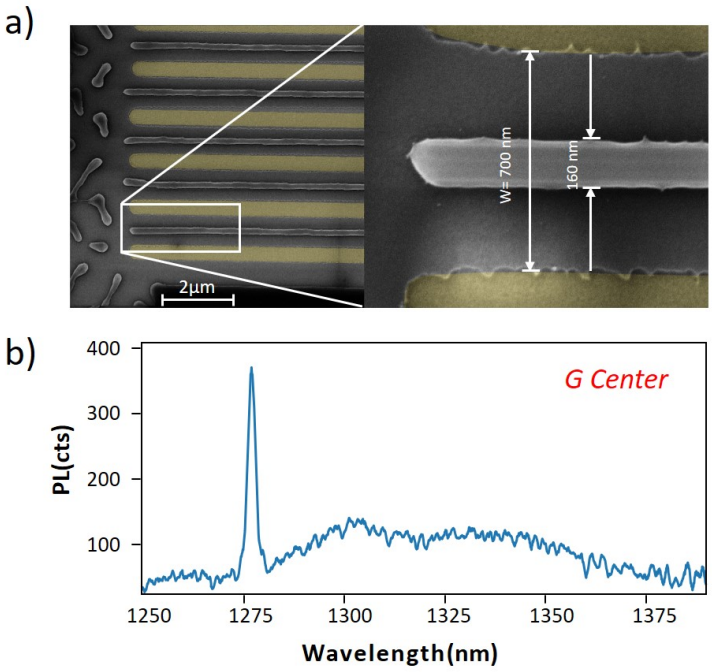


Figure 4.10: a) SEM image for an extremity of 5 parallel long nano-wires (length of 75 $\mu$m) [160]. b) PL spectrum for an ensemble of G centers detected inside a wire fabricated with optical lithography and solid state dewetting.

## 4.7 Conclusion

In this chapter we made a short introduction to the dewetting phenomenon, in which is provided with examples of application to color filter with resonant antennas and fabrication of wires and complex nanoarchitectures.

# Chapter 5

# Fabrication and Characterization of Si-based Mie Resonators

## 5.1 Abstract

In this chapter, we use low-resolution optical lithography joined with solid state dewetting (Defined in chapter 4.3) of crystalline, ultra-thin silicon on insulator (c-UT-SOI) to form monocrystalline, atomically-smooth, silicon-based Mie resonators in well controlled large periodic arrays (oppositely to the example shown in the previous chapter 4, about the spontaneous dewetting. The dewetted islands have a typical size of about 100 nm, that is about one order of magnitude smaller than the etching lateral resolution for our optical lithography tool. Exploiting a 2 $\mu$m thick $SiO_2$ layer (BOX) separating the islands and the underlying bulk, silicon wafer, we combine the resonant modes of the antennas with an etalon effect arising form the presence of the thick BOX. Our results demonstrate that templated dewetting enables to form defect-free, faceted islands that are much smaller than the nominal etching resolution and that an appropriate engineering of the substrate improves their scattering properties. This results was published on Journal of Optic Express in 2020. In the second part of this chapter we address more precisely the spatial and spectral mapping of multipolar modes of a Si island by hyper-spectral imaging. The simultaneous detection of several resonant modes allows us to clarify the role of the substrate highlighting spectral splitting of the magnetic quadrupolar mode and resulting in different spatial features of the field intensity. We explore theoretically and experimentally such spatial features. Details as small as 200 nm can be detected and agree with simulations based on the finite difference time domain method. The spectroscopic characterization has been performed at LENS laboratory/university of Florence only at visible frequency owing to limitations in the experimental apparatus in use. However, all these results can be exploited at near-infrared frequency by choosing larger particles. This observation is important in

view of integration of G-centers in Si-based Mie resonators as shown in the following chapters. This part was published on APL Photonics in 2022.

## 5.2 Introduction

Sub-micrometric, dielectric objects featuring high permittivity and reduced absorption losses enable for efficient light management, potentially enhancing and extending the performances of opto-electronic devices [163]. The resonant scattering supported by individual dielectric antennas is generally rather broad [144] (50-100 nm for the fundamental Mie resonances at visible and near-infrared frequency) and are strongly influenced by the coupling with the underlying substrate [138]. In addition, for individual resonators, the intensity contrast between maxima and minima is generally poor.

Common strategies for overcoming these limitations rely in coupling the nano-antennas together, forming complex oligomers and meta-surfaces, that can provide advanced functionalities and sharp resonances [163, 164]. However, these approaches require for advanced fabrication methods to precisely set size, shape and relative position of the monomers (e.g. forming narrow gaps in between them). Another powerful approach, that has been recently used to improve the use of dielectric Mie resonators as anti-reflection coatings, is the coupling of Fabry-Perot modes (formed within the effective medium containing Si-based nano-pillars) and Mie resonances (formed within the Si nano-pillars) in a single device [165].

Here we exploit the photonic modulation of the dielectric thick layers to extract more defined structural colors from dielectric Mie resonators. We fabricate monocrystalline Si-based islands via low-resolution optical lithography and plasma etching followed by solid state dewetting [166, 156, 167, 20, 19, 158, 160]. We show that the far-field scattering intensity of the Si-based islands sitting atop a 2 $\mu$m thick $SiO_2$ layer on bulk Si, can be efficiently coupled with etalon modes [138]. The Mie scattering efficiently out-couples the light interfering in the etalon according to the Si island size and re-directs the light at smaller angles with respect to the incident beam. From this combination spring structural colours covering the full visible spectrum and resonances with a high intensity contrast between maxima and minima. FDTD simulations account for this coupling showing that is a purely far-field effect with no modification of the local density of optical states (LDOS).

## 5.3 Experimental Methods

### 5.3.1 Fabrication of Si-based Mie resonators

The mono-crystalline, ultra-thin, silicon on insulator (c-UT-SOI) in use is a single-crystal (001) film, 125 $\sim$ nm thick atop 2 $\sim$ $\mu$m thick $SiO_2$ layer (buried oxide, BOX) on a bulk Si (001) wafer, Figure 5.3.1 a). It is thinned to about 20 $\sim$ nm by rapid thermal oxidation (RTO) at $\sim 950^{\circ}$C in $O_2$ atmosphere for 3 hours in order to transform the top part of the SOI in $SiO_2$. By dipping the oxidised samples in a HF-solution at 5% in de-ionised water (95%) the top $SiO_2$ layer is removed thus exposing the remaining

bottom SOI. Island fabrication is performed in two steps: 1) patterning by photolithography and 2) solid state dewetting via high temperature annealing by following well established methods [20, 158, 160, 159].

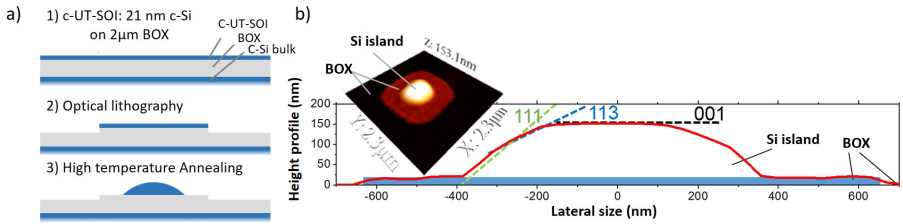


Figure 5.1: a) Scheme of the main fabrication steps. 1) Crystalline, ultra-thin silicon on insulator (c-UT-SOI): 21 nm of monocrystalline Si (c-Si) on 2 $\mu$m of silicon oxide (buried oxide, BOX). 2) Optical lithography and plasma etching. 3) High temperature annealing in ultra-high vacuum. b) Atomic force microscope profile of an individual island. The main crystal facets are highlighted. The inset shows a 3D representation of the island.

The photolithographic patterns are obtained by spin-coating a positive, photosensitive resist exposed to a near-UV laser (375 nm wavelength, fluency of about 2.7 mW) on a spot of about 2 $\mu$m (Dilase 250, from Kloe). The exposed portions of the resist are removed with a developer. Finally, a plasma etching step (70 seconds in CF4 plasma, obtained in plasma-enhanced chemical vapor deposition machine from Oxford Instruments) attacks the exposed parts of the SOI, leaving intact the protected parts. By changing the pitch between vertical and horizontal lines (e.g. from 3 to 4 $\mu$m) we define squares patches having variable size Figure 5.2 b).

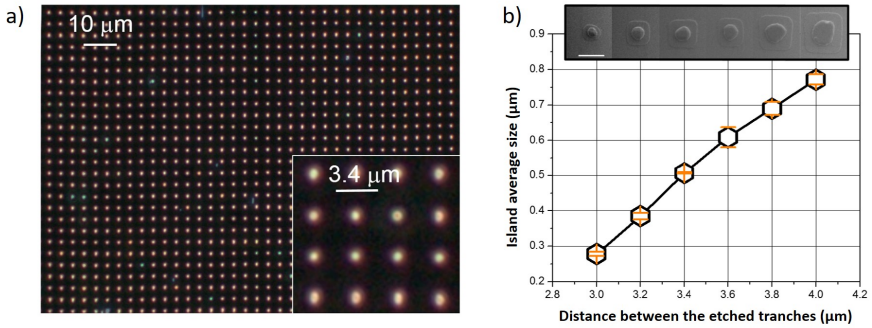


Figure 5.2: a) Optical dark-field image of a typical array of organized dewetted Si islands. The inset shows the homogeneity of the islands obtained with a periodicity of 3.4 $\mu$m. b) Average island size as a function between the etching pitch as obtained by scanning electron micrographs (SEM). The error bar represents the standard deviation. The line is a guide for the eyes. The top inset show a typical SEM for each etched pitch.

Before high-temperature annealing and dewetting the SOI are first chemically cleaned with acetone, ethanol, $O_2$ plasma and finally in a HF solution at 5% in de-ionised water under $N_2$ atmosphere in a glove box. The SOI samples are transferred to the ultra-high vacuum ($\sim 10^{-10}$ torr) of the MBE chamber (RIBER 32 MBE system). The annealing process is carried out in two stages, the first one is an *in-situ* cleaning where the temperature is risen at about 650°C for 30 min in order to remove any residual native oxide from the surface of the sample. The second annealing step induces the solid-state dewetting of the SOI when the temperature is increased at about 750°C for 30 minutes.

### 5.3.2 Structural Characterization

Dark field (DF) images and spectra were collected by using an optical microscope (ZEISS Axio Observer) mounting a 100× magnification objective lens (numerical aperture $NA = 0.9$) working both in bright and dark field configurations, coupled with a spectrometer and Si-based CCD linear array (Flame-T-VIS-NIR by Ocean Optics). In order to investigate individual islands, the scattered light was collected using an optical fiber (Ocean Optics multimode fiber, VIS-NIR, core diameter 200 mm) defining a lateral resolution of about 2 $\mu$m.

The Si islands were imaged via scanning electron microscopy (SEM) performed with a FEI Helios 600 Nano-Lab. Micrographs were acquired using a through-the-lens detector secondary electron detector (5 kV acceleration voltage), probe current of 0.17 nA and working distance of 4.2 mm. Atomic force microscopy (XE-100 AFM from Park systems) was performed in non-contact mode.

## 5.4 Results

At the end of the dewetting process we obtain monocrystalline and atomically smooth islands featuring the typical facets of the equilibrium shape of silicon Figure 5.3.1 b) [156, 167, 20, 19, 160, 168]. Large islands arrays Figure 5.2 a) can be fabricated with controlled size (base diameter from about 280 to 780 nm) and regular organization [167, 158, 168, 169] Figure 5.2 b). The homogeneous scattering color account for a good homogeneity, as also confirmed by the small fluctuation obtained by measuring the base size of several islands for each pitch (error bars in Figure 5.2 b). Islands height are in the 90 to 150 nm range, depending on the initial pitch size (see an example of large island in the AFM image in Figure 5.3.1 b). Smaller island size (e.g. featuring bright scattering at visible frequency) can be obtained by reducing the pitch of the lithographic step [167, 158, 168, 169] (not shown).

### 5.4.1 Dark-field Spectroscopy of Individual Mie Resonators

For optical spectroscopy at visible frequency (owing to the limits of our silicon-based detector) we chose a set of dewetted islands with increasing base diameter, from about 100 to 200 nm Figure 5.3 a) left column [167, 20, 168, 158]. Slight shape asymmetries observed in some island are ascribed to a non-complete dewetting that did not lead

to the final equilibrium shape of silicon crystals. In principle, these defects could be improved with a longer annealing time or a higher temperature.

Dark field images reveal a net colorization from blue to red, when increasing particle size (Figure 5.3 a), right column). The corresponding scattering spectra (normalised by the white lamp used for illumination) confirm this tendency, showing several sharp bands that increase in number at long wavelength for larger islands (Figure 5.3 b)) [20, 158].

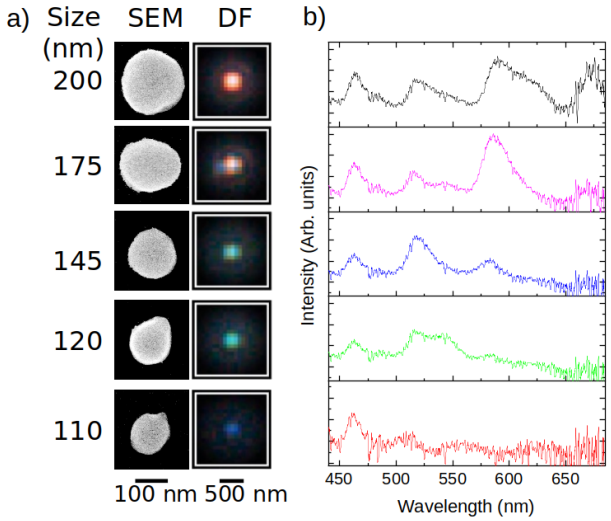


Figure 5.3: a) Left column: SEM images of crystalline Si dewetted islands. Their corresponding size is highlighted at their left. Right panel: dark-field optical microscope images of the islands shown in the left column. b) Dark-field scattering spectrum corresponding to the islands shown in a).

These resonances share a similar spectral position and spacing between them, although some differences (up to 25-30 nm) are observed (see also Figure 5.3) [138]. These differences can be accounted for by imperfections in the etching (locally thicker or thinner BOX), incomplete dewetting leaving some pristine c-UT-SOI nearby the islands, residual Si particles on the BOX nearby the islands, intermixing of Si and $SiO_2$ [81, 170, 171], and asymmetries in the dewetted islands [20].

### 5.4.2 Comparison With Etalon Reflection.

In order to confirm that the observed far field spectra are due to strong spectral variations of the driving field in the resonators related with constructive and destructive interference of the incident light at the air-$SiO_2$ and $SiO_2$-Si interfaces, we simulate the specular reflection from a bare 2 $\mu$m thick, flat $SiO_2$ layer atop bulk Si (that mimics the BOX underneath the dewetted islands, Figure 5.4 a) These simulations were compared with the dark field scattering spectrum of a large silicon island, Figure 5.4

b). The specular reflection at normal incidence (0 degrees) features 5 broad peaks in the investigated spectral range having a contrast of about 3 (Figure 5.4 a) top panel). For 70 degrees incidence (that is similar to the incidence angle of the light in dark-field configuration) the overall picture is similar but the peaks are only four, with a pronounced flattening at their top and with a lower contrast of roughly 2 Figure 5.4 a) bottom panel). These latter features are understood by observing the *s* and *p* polarized components of the reflection: they present maxima and minima in opposition of phase thus providing a more complex behavior with respect to the normal incidence case, where the two components are identical. Note that at this large incident angle, the *s* polarization is dominant with an intensity that is about double with respect to that one of the *p* counterpart.

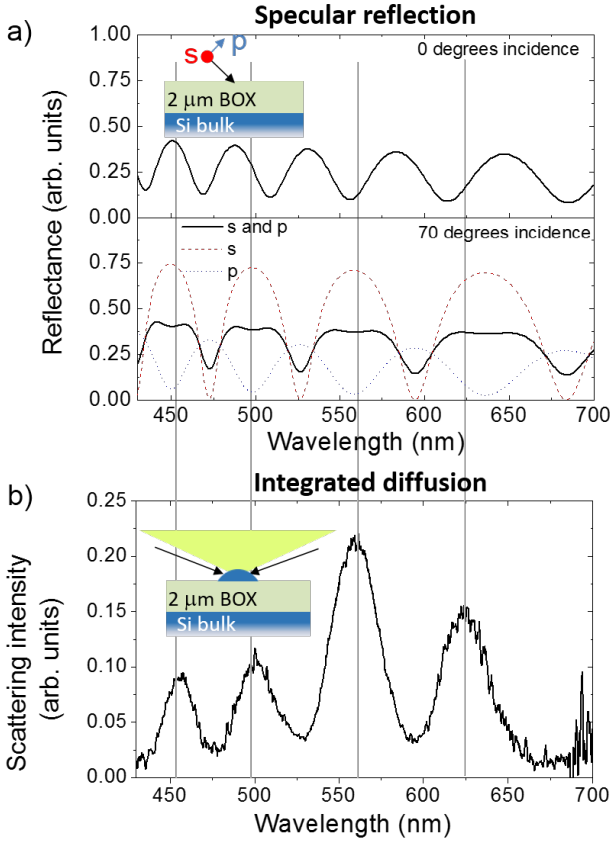


Figure 5.4: a) Simulated intensity of the specular reflection for s and p polarization from a 2 $\mu$m thick $SiO_2$ layer (BOX) atop Si bulk. Top panel: normal incidence. Bottom panel: 70 degrees incidence. The inset highlights the geometry considered in the model. b) Dark-field scattering spectrum of a dewetted island. The inset highlights excitation and collection conditions (respectively $\sim$70 degrees incidence and within a 64 degrees aperture cone).

The scattering spectrum of the individual Si island shows 4 peaks with a rather large intensity contrast (between 3 and 6, depending on the peak taken into account, Figure 5.4 b)). The spectral position and spacing between the scattering peaks show marked similarities with the reflection spectrum of the flat $SiO_2$ layer when comparing the case of *s* polarization at an incidence of 70 degrees (as highlighted by the vertical gray lines in Figure 5.4). Moreover, the broadening of the resonances observed in the scattering spectrum and in the *s* polarised reflection are rather similar: they show an increasing trend from about 25 nm for the shorter wavelength resonance up to 35 nm for the longer wavelength one. This broadening of the resonant scattering is 3 to 4 times smaller then what was reported for similar Si islands formed via solid state dewetting atop a 145 m thick BOX [20], where the etaloning effect is negligible [138].

Combining the sharper resonances springing from the etalon effect produced by the thick BOX atop the Si bulk and the broader Mie scattering (see also Figure 5.3) we obtain colours that are qualitatively similar to those obtained with in state-of-the-art in SiGe-based [158] and Si-based [172] Mie resonators (respectively obtained via templated dewetting and e-beam lithography and reactive ion etching). Provided the hybrid top-down/bottom-up approach in use, our resonators are not scattered and mixed in size as for purely bottom-up methods [173, 174] and can be organized in large and regular arrays featuring a small size dispersion. We also observe that the quality of the structural color is improved with respect to island obtained with similar approaches [20] and when embedded in transparent polymers [174].

The scattering data, linked to the reflection simulation of the silica etalon, lead to the conclusion that the *s* polarization is playing a major role in the observed structural color. In addition to the more intense *s* polarization excitation associated to the etalon effect (Figure 5.4 a) bottom panel), we expect less scattering around normal incidence for *p* polarization due to the electric dipole angular pattern [138].

Indeed, a marked similarity emerges when observing the spectrum of the *s* polarised specular reflection at 70 degrees of incidence (Figure 5.4 a) bottom panel) and the dark-field resonant scattering spectrum of the Si island (Figure 5.4 b)). This suggests that the Mie resonator back scatters some of the incident light reflected at the air-$SiO_2$ and $SiO_2$-Si interfaces. Note that, in the geometry of the dark-field experiment, the direct reflection of the incident beam (at about 70 degrees) is not detected. In fact, the areas nearby the islands are dark, as the numerical aperture of the detection is only 64 degrees. Thus, the resonant scattering redirects the reflected light at different angles with respect to the incident ones while preserving some of the features of the interference in the etalon.

## 5.5 Finite Element Simulations

To clarify the influence of the 2 $\mu$m thick BOX layer on the island scattering spectra, numerical calculations were performed with a commercial three-dimensional 3D finite-difference time domain (FDTD) code (CrystalWave, Photon Design). We consider a hemispherical Si island with 200 nm base diameter and a refractive index n = 4, neglecting absorption. The Si island is excited with a broadband point-like dipole (emitting at $\lambda$ = 600 nm, with a full width at half maximum FWHM = 300 nm) posi-

tioned in the middle of the island, with polarization parallel to the BOX surface. The flux of the Poynting vector across a box sensor, a cube of side 300 nm, positioned around the exciting dipole gives us the LDOS of the island at the dipole position [175].

In order to corroborate the picture that the scattering spectrum of the islands is strongly influenced by interference effects and is not due to a modification of the LDOS of the Si island, we compare the FDTD simulation of an hemispherical Si island placed atop of 2 $\mu$m thick layer of $SiO_2$ (n = 1.5) plus a 1 $\mu$m thick substrate of Si (n = 4) with the same island atop only 2 $\mu$m of $SiO_2$ (Figure 5.5). Parallel to the BOX surface, at a distance of 1 $\mu$m is positioned a planar sensor, that allows to simulate the collected far field spectra under different acquisition angles, reported in Figure 5.5 c). The simulations conditions are different with respect to the experimental ones and their aim is to explain the underlying phenomenology.

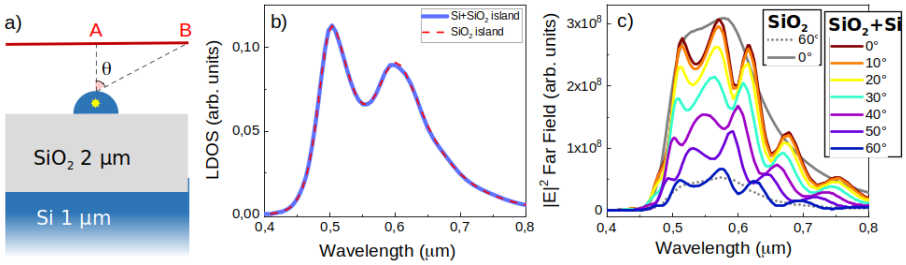


Figure 5.5: a) Sketch of the simulated structure: a hemispherical Si island on a substrate formed by a 2 $\mu$m $SiO_2$ layer atop 1 $\mu$m Si layer. The yellow star, in the middle of the island, represents the broadband point-like dipole (emitting with a central wavelength of 600 nm, with a full width at half maximum FWHM = 300 nm) that acts as excitation source. The red line indicates the far field sensor, positioned at a height such that the points A and B correspond to an acquisition angle $\theta$ of 0 degrees and 60 degrees, respectively. b) Local Density of States (LDOS) of the island sitting atop 2 $\mu$m $SiO_2$ layer only (red dashed line) and on 2 $\mu$m $SiO_2$ plus 1 $\mu$m Si (blue line). c) Colored lines: far field simulated spectra acquired at different values of theta for the island atop 2 $\mu$m $SiO_2$ plus 1 $\mu$m Si substrate (from $\theta$ = 0 to 60 degrees). The far field intensity from the island on 2 $\mu$m $SiO_2$ layer only, are represented for comparison in the two limit cases $\theta$ = 0 and 60 degrees) in grey (respectively continuous and dashed lines).

The LDOS spectra (Figure 5.5 b)) are calculated at the position of the exciting dipole by following reference [175] and are dominated by two resonances at about 500 nm and 600 nm, that can be identified as the electric (ED) and magnetic dipolar (MD) modes, respectively [138, 20, 158, 176]. The two curves, within the line thickness, are identical, giving an indication that the LDOS of the Si-island is not significantly modified by the presence of the Si substrate. On the contrary, the far field spectra are dramatically influenced by the presence of the Si substrate. Far-field spectra collected at different points of the far field sensor correspond to spectra detected at different ac-

quisition angles (Figure 5.5 c)). The simulation without the Si substrate shows smooth spectra (solid and dashed gray lines) where is possible to identify the ED and MD modes characterized by different relative weights. The scattering intensity at 0 degrees is about six times more intense with respect to that one at 60 degrees. The far field spectra obtained by taking into account the Si substrate show a clear intensity modulation superimposed on the smooth spectra obtained without Si substrate. The spectral position of the observed fringes shifts toward the blue by increasing the detection angle. A similar effect is observed by considering the specular reflection of a slab of 2 $\mu$m of $SiO_2$ on Si (not shown).

This study clearly confirms that the modulations observed in the far-field scattering intensity are not related to a modification of the LDOS of the Si islands. The important implication of this observation is that we do not expect any modulation or interference effect in the spectrum of a light emitter embedded in the islands as these modulations arise only in the far-field. They are rather related to the scattering by the Mie resonator of the incident light beam propagating and interfering in the $SiO_2$ layer sandwiched between the island and the bulk Si substrate. The emission spectrum of the G-centers embedded in the islands in fact, should not be affected by the presence of the BOX.

**Mie Modes Evolution With Buried Oxide Thickness**

A more precise understanding of the phenomenology presented before is provided by more systematic simulations of the light scattering by Si islands when changing the BOX thickness at a fixed illumination angle ($\theta$).

We study the modification on the scattering spectra of a single Si-based scatterer as a function of the thickness t of the $SiO_2$ substrate and of the illumination angle $\theta = 0$ by means of FDTD simulations with a commercial software Lumerical [177]. We consider a hemispherical Si island of diameter d=330 nm Figure 5.6 a), illuminated by a Total Field Scattered Field (TFSF) source, which launches a broad-band ($\lambda$=400-1200 nm) plane wave from the top, under normal incidence and filters out all the light that has not been scattered. The simulated source is polarized along the x axis.

Power transmission monitors are positioned around the TFSF source in order to obtain the total scattering cross section, and two field monitors intersect the particle (along the xz and yz plane) to monitor the local field intensity.

An additional monitor is placed on top of the island in the xy plane at a distance of 10 nm from the apex in order to simulate the near-field spatial profile of the electric field intensity. Perfectly Matching Layers (PMLs) are used to prevent any unphysical scattering from the simulation boundaries and to mimic semi-infinite substrates. Optical constants for Si and $SiO_2$ are taken from Palik [178].

Figure 5.6 b) reports the total scattering cross sections (Defined in Chapter 3.2.1) of the Si hemisphere, illuminated under normal incidence, for different values of the substrate thickness t. In particular, it is possible to follow the evolution of the modes from the yellow spectrum at the bottom, which is relative to the case of the island in air a sketch is reported in the inset of Figure 5.6 a), to the configuration with the maximal $SiO_2$ thickness of 2 $\mu$m (blue spectrum), which is the actual value of t in the experimentally investigated sample.

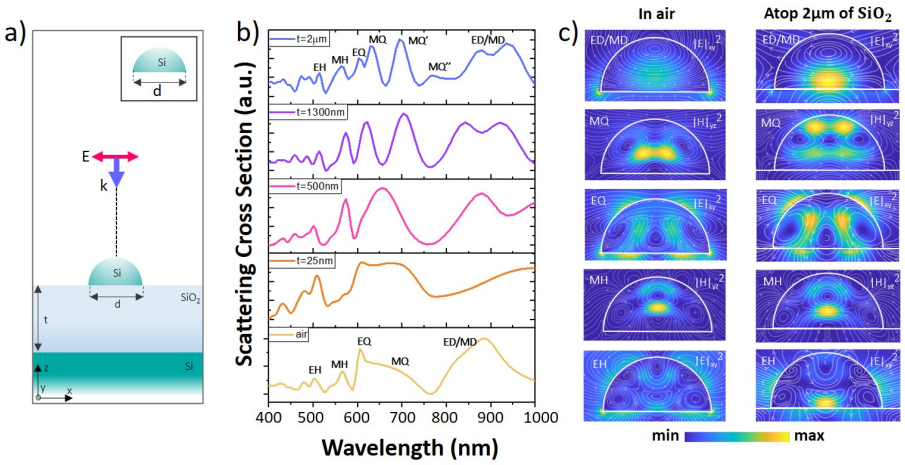


Figure 5.6: a) Sketch of the model used in the FDTD simulations; a Si hemisphere of diameter d is positioned atop a $SiO_2$ layer of thickness t, and a bulk Si substrate. The scatterer is illuminated by an x polarized total-field scattered-field (TFSF) source. The inset shows the bare case of the island in air, corresponding to the yellow spectrum of b) FDTD scattering cross sections (from bottom to top) for increasing values of t, t = 25 nm, t = 500 nm and 1300 nm respectively in orange, magenta and purple. c) Vertical crosscuts of the electromagnetic field intensity and current loops (represented by white arrows) of the multipolar resonances of the hemisphere in air. The maps, acquired at the wavelengths of the yellow spectrum, are reported from top to bottom in order of increasing energy: ED/MD ($\lambda$=800 nm), MQ ($\lambda$=660 nm), EQ ($\lambda$=605 nm), MH ($\lambda$=570 nm) and EH ($\lambda$=504 nm). d) Vertical crosscuts of the electromagnetic field intensity and current loops (represented by white arrows) of the multipolar resonances of the hemisphere on a $SiO_2$ layer of thickness t=2 $\mu$m. The maps, acquired at the wavelengths of the blue spectrum, are reported from top to bottom in order of increasing energy: ED/MD ($\lambda$=770 nm), MQ ($\lambda$=628 nm), EQ ($\lambda$=603 nm), MH ($\lambda$=563 nm) and EH ($\lambda$=514 nm).

The scattering cross sections for three selected values of t (i.e. t= 25 nm, 500 nm and 1300 nm), are reported in Figure 5.6 b), in orange, magenta and purple, respectively. The identification of these modes (electric hexapole EH, magnetic hexapole MH, electric quadrupole EQ, magnetic quadrupole (MQ) and electric and magnetic dipole ED/MD) which are reported in Table 5.1, is based on their field profile inside the particle, and identifying the corresponding current loops Figure 5.6 c).

First, electric and magnetic field inside the hemisphere suspended in air allow to identify the multipolar resonances, from the fundamental to higher-energy ones. In the near-field, the electric (magnetic) field profiles in the xz (yz) plane for electric

Table 5.1: Table in which we report all the Mie resonances found for the case of the island with d = 330 nm in air and on a thick substrate (t = 2000 nm). For each mode, we report the number of poles inside the electromagnetic field distributions in the vertical crosscuts

| | Number of poles | Island in air | Island on thick $SiO_2$ (t=2$\mu$m) |
|---|---|---|---|
| ED/MD | 1 | $\lambda = 920nm$ | $\lambda = 906nm$ |
| MQ | 4 | $\lambda = 660nm$ | MQ" ($\lambda = 766nm$)<br>MQ' ($\lambda = 695nm$)<br>MQ ($\lambda = 628nm$) |
| EQ | 4 | $\lambda = 605nm$ | $\lambda = 603nm$ |
| MH | 6 | $\lambda = 570nm$ | $\lambda = 563nm$ |
| EH | 6 | $\lambda = 504nm$ | $\lambda = 514nm$ |

(magnetic) resonances show bright lobes inside corresponding to the poles generated by current loops (white arrows in Figure 5.6 c). The number of poles is reported for each mode in the first column of Table 5.1.

The Effects of symmetry breaking with respect to the ideal case of a sphere in air (in which ED and MD are easily distinguishable) must be considered [179, 180]. We therefore refer to the broad band centered around 900 nm as ED/MD. We also identify the main higher-order resonances as MQ, EQ, MH and EH, of which we report the vertical crosscuts of E or H respectively at $\lambda$= 660 nm, 605 nm, 570 nm and 504 nm.

The same reasoning was adapted to assign the resonances of the particle sitting atop a $SiO_2$ substrate while t increases. It was recently shown [138, 181] (see also the previous Section in this chapter) that by increasing t, constructive and destructive interference of the incident light reflected from the $SiO_2$/Si-bulk interface arises, resulting into strong variations in the driving field of the resonator. The Mie scattering efficiently out-couples the light interfering in the etalon, and re-directs light at smaller angles with respect to the incident beam. From this combination structural colors spring, covering the full visible spectrum with resonances with a high intensity contrast between maxima and minima. However, a detailed identification of the actual physical origin of these sharp peaks has never been attempted so far.

While increasing t, we can follow the evolution of the vertical profiles of the electric (magnetic) field intensity along the xz (yz) plane of the main electric (magnetic) resonances in the scatterer Figure 5.6 d) for the main resonances of the blue spectrum on top of Figure 5.6 b), corresponding to the nominal $SiO_2$ thickness t=2 $\mu$m. Specifically, the maps of ED/MD, MQ, EQ, MH and EH correspond to $\lambda$=770 nm, 628 nm, 603 nm, 563 nm and 514 nm, respectively.

The original broad band corresponding to MQ in the yellow spectrum (scatterer in air) splits into three sharp peaks, all identifiable as magnetic quadrupole resonances from the analyzed current loops, to which we refer as MQ, MQ' and MQ". The list of all the modes arising for t=2 $\mu$m can be found in the third column of Table 5.1. The coupling between the scatterer and the interference arising from the $SiO_2$ layer, combined with the analysis of crosscuts of the electromagnetic field for every peak, therefore al-

lows to identify the modes and obtain information about the multipole characteristics of the island spectrum without any need of multipolar decomposition [182].

## 5.6 Conclusion

The use of solid state dewetting for the fabrication of ordered and disordered dielectric Mie resonators made of Si(Ge) has been largely addressed in the past years [20, 19, 158, 176, 183, 184]. However, obtaining ordered arrays of simple islands or complex nano-architectures required so far, e-beam lithography and reactive etching [164, 172] or direct etching via focused ion beam [167, 158, 159, 169]. Although very precise, these methods are rather costly and eventually difficult to extend to very large surfaces. Here we replaced these approaches extending the idea of templated dewetting to conventional optical lithography. This is a much less expensive technique and can, in principle, be extended to larger areas. In our case the lateral etching resolution was rather poor, only 2 $\mu$m. Although this does not allow for a large islands density (the minimal distance between island is about 2 $\mu$m), it is worth noting that large homogeneous arrays of nano-objects can be obtained. This is possible thanks to the dewetting approach, that leads to the collapse of all the c-UT-SOI present in the original patch in a single island, thus effectively gaining a factor of the order of 10 in lateral resolution [160]. These islands can be organized in large arrays with a fine size tuning and a small spread in size (size distribution is within 10% or smaller). This size distribution is improved with respect to previous reports of Si and SiGe templated-dewetting where the etching was performed with a focused ion beam [167, 158, 159, 169] and are similar to those reported for e-beam lithography and reactive ion etching [19, 160]. Aside, we also note that the use of this self-assembly method enables the formation of monocrystalline objects with atomically smooth, faceted interfaces [156, 167, 20, 160, 168, 183]. A feature that cannot be obtained with other conventional top-down methods that always induce a more or less pronounced roughness and it may be an advantage when electronic properties are concerned [160]. Finally, by means of FDTD simulations, we achieved a full comprehension of the sensitivity of Mie modes with respect to the thickness of the underlying buried oxide.

# Chapter 6

# Light Emitting Si-based Mie Resonators: Towards a Huygens Source of Quantum Emitters

## 6.1 Abstract

In this chapter we show that, via ion beam implant, light emitting G-centers can be directly embedded within Si-based Mie resonators previously obtained in chapter 5 by solid state dewetting (Defined in Chapter 4.3). Size- and position-dependent, directional light emission at 120 K is demonstrated experimentally and confirmed by Finite Difference Time Domain simulations. We estimate that, with an optimal coupling of the G-centers emission with the resonant antennas, a collection efficiency of about 90% can be reached using a conventional objective lens. The integration of these telecom-frequency emitters in resonant antennas is relevant for their efficient exploitation in quantum optics applications and more generally to Si-based photonic metasurfaces. The Photoluminescence measurememt is performed at the institute of Nanotechnology in Lyon (INL), under the supervision of Nicolas Chauvin. This result was published on Advanced Optical Materials in August 2022.

## 6.2 Introduction

Thanks to the transparency window and high permittivity of silicon, efficient optical devices have been implemented at near infrared frequencies for guided optics and integrated photonic circuits [185, 186]. Devices with relatively low Q-factors, such as dielectric Mie resonators, have been also used at shorter wavelengths for optical metasurfaces, structural color, anti-reflection coatings, quantum optics and much more [187, 188, 189].

The integration of light emitters in silicon however, has been limited by the indirect nature of its band-gap. Si-based, light-emitting metasurfaces [190] have been demon-

strated using more or less complex fabrication methods, such as spin coating colloidal quantum dots [191], or by atomic layer deposition [192] organic molecules [193], or coupling an emitting 2D material with sub-micrometric antennas [194, 195, 196]. These approaches do not embed the emitters in the core of the resonators, where the the electromagnetic field is stronger and electric- and magnetic-dipolar Mie modes can be tailored, providing more versatility for light management [133, 197, 198, 199], as for instance shown for rare earth emitters coupled with plasmonic antennas [200] and light-emitting Si-nanocrystals in $SiO_2$ pillars [201]. Moreover, the presence of interfaces (e.g. produced by top-down lithographic methods) may be detrimental for the excitonic recombination owing to high concentrations of extrinsic defects. Epitaxial growth of Ge quantum dots is a viable alternative to embed light emitters within silicon-based photonic devices (e.g. at defined positions within the antennas [202] or in a photonic crystal [203]). However, these kind of emitters suffer from a relatively low quantum efficiency.

Complex impurities in silicon are well-known light emitters that can be easily created via standard ion implant methods or via high-energy electron beams [10, 57, 41, 55] or by using our new approaches which's presented in Appendices (B and C) (via focus ion beam FIB, or laser irradiation). Very recently, they have been intensively investigated, especially in view of their exploitation as sources of single photons [204]. At low temperature ($\sim$10 K), their photoluminescence is composed of a sharp zero-phonon line (ZPL) and a low-energy phonon-side band covering a broad wavelength range [49, 43, 67, 68, 52, 44, 70, 56, 42]. Some of these impurities feature large quantum efficiency (e.g. of the order of unity [67]), relatively fast recombination lifetime (less than 10 ns [55]), large Debye-Waller factor (larger than 30% [68]) and a spin degree of freedom, offering a spin-photon interface [43, 42, 44]. In spite of their relevance in quantum optics, the integration of these emitters in photonic devices has been so far, mostly limited to photonic crystals and photonic metasurfaces demanding for complex fabrication steps (e.g. e-beam lithography and reactive ion etching) [8, 120, 205]. First examples of integrated photonic circuits have been very recently [69] accounting for the potential of point defects in Si.

Here we combine the features of dielectric, Si-based Mie resonators with light emitting impurities at telecom frequency, in order to obtain a directional light source and a large extraction efficiency. In analogy with the Kerker effect [133, 197, 198, 199] antennas (e.g. magnetic and electric dipolar modes) results in constructive and destructive interference that enhances or suppresses the scattering in specific directions, resulting in a strong light steering (analogous to with a Huygens-like light source). In order to achieve this result, we first integrate carbon-related impurities (G-centers) in self-assembled, atomically-smooth, Si-based sub-micrometric islands, acting as Mie resonators. We obtain these antennas by self-assembly via solid-state-dewetting: combining a top-down, low-resolution lithography step with a natural surface instability we produce atomically-smooth, monocrystalline and defect-free resonant antennas whose morphology is defined by the equilibrium shape of the Si crystal. We optimize 1) particle size providing resonant modes at the emitters' wavelength, 2) position (depth) of the emitters within the antennas to place them at the maximum of the electromagnetic field of the underlying Mie modes, and 3) proton fluence in order to maximise the number of

light emitting G-centers. Spectroscopic investigation of the ensemble is systematically adopted to characterize the combined antenna-emitter system that appears highly sensitive to all of the structural parameters at play. By setting the optimal island size, emitter position and proton fluence, we demonstrate that the far-field emission pattern of the near-infrared photoluminescence from the G-centers can be reconstructed up to 120 K, accounting for the high quality of our samples. Furthermore, the optimal coupling of the G-centers with the antennas provides a directional emission in the far-field allowing for a collection efficiency as large as 90% using conventional optics. These results are compared with Finite Difference Time Domain (FDTD) simulations accounting for the experimentally observed directional emission.

## 6.3 Experimental Section

***Measurement procedures***: Macro-photoluminescence measurements were performed at 12 K cooling the sample with a closed-cycle liquid-helium cryostat. The optical pumping was performed with a continuous wave (cw) laser diode at 532 nm focused onto the sample with a lens offering a focus spot of $\approx 75\ \mu$m. The PL emission was collected by a Cassegrain objective which collects light between 0.15 to 0.4 numerical aperture (NA) and focused on an optical fiber connected to a spectrometer coupled with a liquid nitrogen-cooled InGaAs detector enabling spectral detection from 900 to 1600 nm. For the angle-resolved photoluminescence spectroscopy the samples were cooled down to approximately 120 K with a liquid-nitrogen cryostat. The optical pumping was performed with a CW laser diode at 532 nm focused with a microscope objective ($\times$50, NA = 0.65). The PL signal was collected through the same objective and filtered by a band-pass filter within 1250-1300 nm. The output signal was projected onto the entrance of a spectrometer coupled to an InGaAs CMOS camera (NIRVANA Princeton).

***Simulation*** : The FDTD simulations were performed with the commercial software Ansys Lumerical Simulation. The refractive index of Silicon and Silica where taken from the materials database of the software. The simulation area was delimited by perfectly matched layer (PML) boundaries. The scattering cross-sections have been obtained using a cross section box placed outside a TFSF source. The representations of the electric dipole mode have been obtained by placing several monitors in the resonator. Two other monitors have been placed above and beneath the resonator to obtain the emitted power in the two directions as well as the far-field data.

## 6.4 Results

### 6.4.1 Sample Fabrication

We first provide a description of the sample fabrication to create Si-based, sub micrometric islands working as Mie resonators Figure 6.1 and their activation with G-centers via ion implant Figure 6.2.

Fabrication of Si resonant antennas via dewetting [157, 19, 160, 174] and the characterization of their optical properties under white light illumination have been exten-

sively addressed in the last years, and we thus refer the reader to the existing literature [181, 206]. The nano-fabrication was performed following these steps (Figure 6.1):

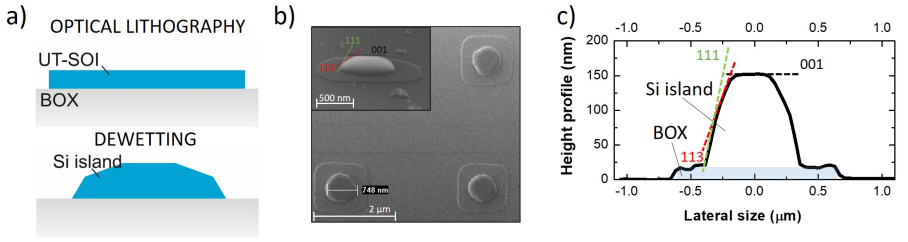


Figure 6.1: Sample fabrication. a) Optical lithography (top panel) is used to define $\sim$ $\mu$m sized, square patches of ultra-thin silicon on insulator (UT-SOI) atop a thick $SiO_2$ buried oxide (BOX) of 2 $\mu$m. High temperature annealing (bottom panel) in ultra-high vacuum (about $10^{-10}$ torr) is used to induce the solid-state dewetting of the UT-SOI patches in 3D islands (for more details on the dewetting method see references [157, 19, 160]. b) Scanning electron microscope (SEM) image dewetted islands from an array of Si-islands obtained dewetting $\sim$1.5 $\mu$m wide patches. The top right inset shows a SEM tilted view at 70 degrees of a dewetted island. The main crystallographic axes of the equilibrium shape of Si are highlighted. For an extensive SEM characterization of similar samples obtained with the same method see reference [181]. c) Height profile of a Si island form the array shown in b) obtained from an atomic force microscope image. The BOX is highlighted with a shaded area. The facets typical of the equilibrium shape of Si are highlighted with dashed lines and labelled.

1) Starting from a 125 nm thick silicon on insulator wafer (UT-SOI) atop 2 $\mu$m buried oxide (BOX), we progressively thinned the UT-SOI via thermal oxidation in a rapid thermal processor leaving at the end of the process a 20 nm Si layer atop the BOX. The thermal oxide formed on the UT-SOI was removed via chemical etching in HF solution.

2) By patterning the UT-SOI via low-resolution ($\sim$2 $\mu$m) photolithography and plasma etching, we formed $\mu$m sized, UT-SOI patches (Figure 6.1 a) top panel). We produced square patches with sides ranging from 700 nm to 1400 nm.

3) Solid-state dewetting of the UT-SOI patches was induced by high-temperature annealing in the ultra-high vacuum (static vacuum $\sim 10^{-10}$ torr) of a molecular beam epitaxy reactor (Figure 6.1 a), bottom panel). Scanning electron microscopy (SEM) images confirm the formation of the Si islands on the BOX (Figure 6.1, b) and c)). The investigated samples host arrays of resonators spaced a few microns from each other [181, 206]. Different spacing corresponds to different average island size. Thus, on each sample we investigate arrays of nominally identical resonators extending over about 50 $\mu$m $\times$ 50 $\mu$m, having bases and heights ranging between $\sim$280 nm to $\sim$770 nm and $\sim$80 nm to $\sim$200 nm respectively. Fluctuation in resonator size is less than 10%. For an extensive characterization of SEM images of a similar sample obtained in

the same dewetting conditions we refer the reader to reference [181]. These islands are monocrystalline and atomically smooth, featuring the typical facets of the equilibrium shape of silicon (113, 111 and 001), as highlighted on the atomic force microscope (AFM) height profile shown in Figure 6.1 b) and c). Further information on the dewetting method and Si islands features can be found in references [157, 19, 160] . From the SEM images and AFM profile, a square patch surrounding the Si islands is also visible. This is the result of a slight over-etch of the UT-SOI during the plasma etching step producing a $SiO_2$ pedestal. This feature (about 20 nm height) does not significantly modify the optical properties of the islands [181, 206].

4) After island formation carbon ions are implanted using various beam energies. By changing the energy of the implant we set different depths beneath the surface of the resonators at which G-centres will form (third and fourth panel of Figure 6.2 a)). For a fixed C dose of $10^{14}$ Ions/cm$^2$, we set the implant energy to 12, 18, 30 and 36 keV to go deeper inside the resonators. Figure 6.2 b), shows the corresponding implantation profiles (obtained with Montecarlo simulation using SRIM Software) at the center of a resonator (depths beneath the surface of the island at which G-centres will form, corresponding to the point of its maximal height). Given the uneven shape of the resonators, the corresponding implantation profile will be affected accordingly: the ions will stop at a different depth depending on the distance from the resonator center. This uneven implant profile will be considered in FDTD simulations to better model the light extraction phenomenon. We also took care to not implant the C ions in the bulk silicon below the BOX: irrespective of the C ions energy, the corresponding implant distribution outside a Si resonator (Figure 6.2 b)), is well confined within the $2\mu$m thick BOX (in which no G-centres will be formed). Following a standard fabrication process for G-centers used in bulk and SOI [17, 55], our sample underwent a rapid thermal annealing step at 1000°C under $N_2$ atmosphere for 20 s to repair the lattice damage that occurred during the carbon implant and incorporate C on substitutional lattice sites (not shown).

5) As a last step, in order to induce the interstitial Si that forms the G-center, the dewetted resonators underwent a proton irradiation step carried out at a beam energy of 90 keV with doses ranging from $6\times10^{13}$ Ions/cm$^2$ up to $3\times10^{15}$ Ions/cm$^2$ to activate the G-center emission (Figure 6.2 c)). The expected implant profile shows that, with and without the presence of a Si-island (Figure 6.2 d)), the protons stop always in the BOX. Thus, the G-centers are created only in the resonators (and not in the bulk Si, underneath the BOX) and the protons do not create unwanted defects around them as further confirmed by spectroscopy measurements as shown hereafter.

Upon dewetting and functionalization with G-centers, we do not observe any significant modification of the Si-based islands, which remain perfectly stable. Photoluminescence experiments can be conducted on the same sample many months apart. This is a further confirmation of the stability of these emitters that are robust against blinking, bleaching and thermal cycles [67, 68].

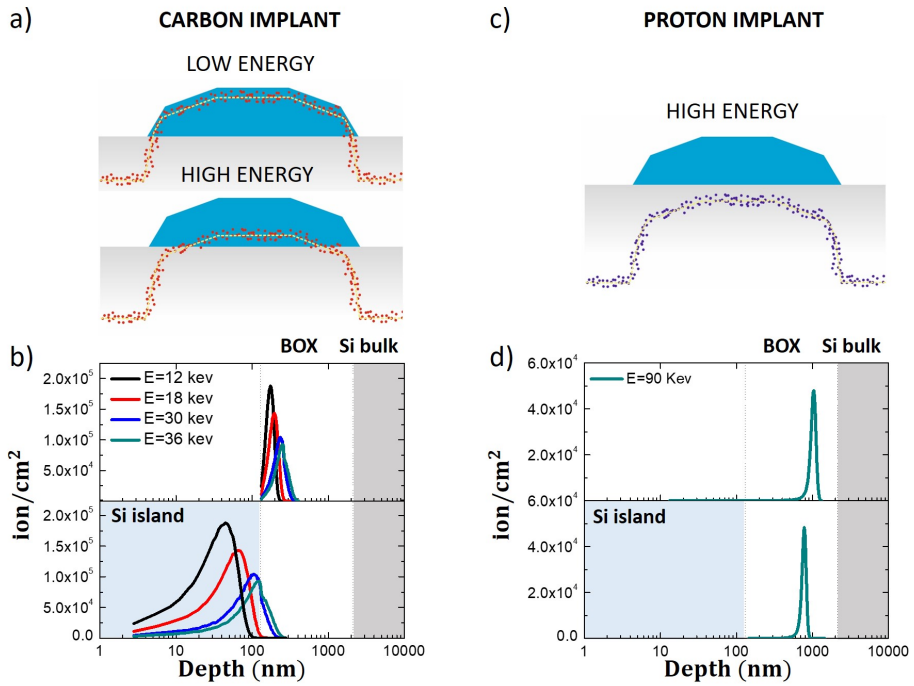


Figure 6.2: a) Scheme of the carbon implant in a Si island for low energy beam (top panel) and high energy beam (bottom panel). The ion implant was followed by a recrystallization step via rapid thermal annealing (not shown). b) SRIM simulation (Defined in Chapter A.10) of carbon implant for different beam energy in a 130 nm height Si-island (bottom panel) and in the buried oxide next to an island (BOX, top panel). c) Scheme of proton implant. d) SRIM simulation of proton implant at 90 keV through a 130 nm height Si island (bottom panel) and in the BOX, next to a Si island (top panel).

### 6.4.2 Photoluminescence Characterisation

In this section we address the experimental findings of the optimal fabrication parameters. Figure 6.3 displays macro-photoluminescence spectra collected from an area outside the resonant antennas arrays and from the brightest emitting antennas array. This analysis points out that we observe the typical spectrum of G-centers only from the areas of the sample covered by antennas, as expected from the SRIM simulations (Figure 6.2 b)-d)) accounting for a selective G-center activation. In the spectrum we distinguish the contribution of G-centers with the ZPL at 1278 nm and its phonon sideband, featuring the typical peak of the transverse acoustic contribution at the X points of the Brillouin zone (TA(X)) and the so-called E-line attributed to a local vibrational mode of the carbon atoms, as labelled in the spectrum of Figure 6.3 [55].

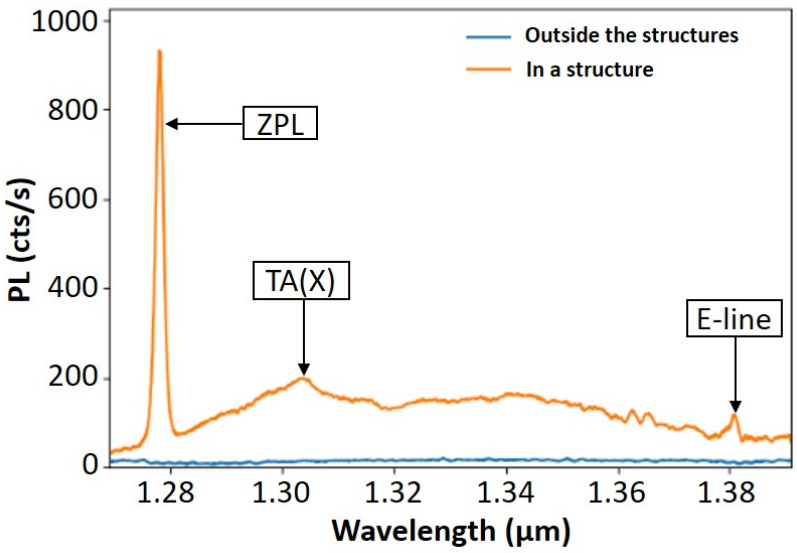


Figure 6.3: G-center spectrum. Comparison of the PL spectra collected at 12 K with an excitation by a laser diode emitting at 532 nm outside the islands array (blue curve) and for the brightest emitting islands array (orange curve).

We then study the influence of the proton dose on the photoluminescence intensity in order to find the best compromise between number of activated G-centers and creation of non-radiative defects. For all the investigated island sizes we observe an increase in the intensity of the PL with the proton dose up to an optimal value of $3\times10^{14}$ Ions/cm$^2$ beyond which the intensity decreases (Figure 6.4 a)). This result is comparable to that previously obtained by Berhanuddin et al. [80] with G-centers in bulk Si.

The previous analysis of macro-photoluminescence on islands arrays also provides information on the best resonator size and implantation energy (that is, C depth). To this end, we investigated arrays of islands irradiated with the same C dose but having different base size and using different carbon beam energy. We observe that the most intense signal was detected from the array of resonators with an average base of 507 nm and with carbon implanted with an energy of 30 keV, i.e. an average depth of implantation at 115 nm (Figure 6.1 b)). These results are shown in Figure 6.4 b), where we compare the spectra of islands with same base size, proton implant and carbon dose but implanted at 8 and 30 keV carbon beam energy determining an emission from a depth of about 42 and 115 nm, respectively.

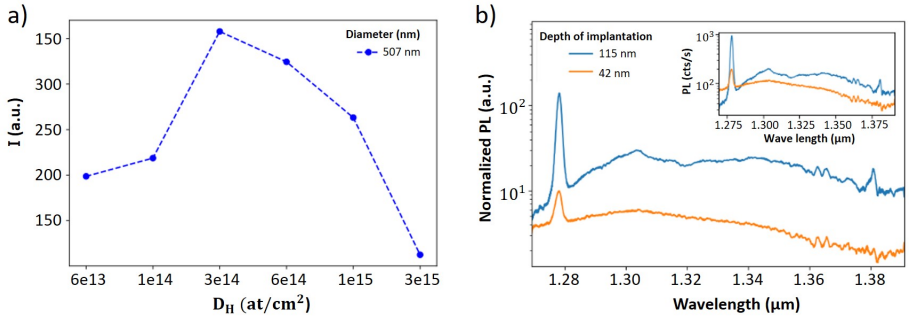


Figure 6.4: Macro photoluminescence. All the spectra were measured at 12 K with an excitation by a laser diode at 532 nm. a) Intensity of the ZPL as a function of the proton dose for resonators having a mean base diameter of 507 nm and implanted with carbon at 30 keV. c) Comparison of PL spectra for two resonators arrays having a mean base diameter of 507 nm and irradiated with the same proton dose of $3\times10^{14}$ Ions/cm$^2$, for C energy of 12 keV (orange line) and 30keV (blue line), corresponding to mean implantation depths of 42 nm and 115 nm, respectively. The intensity of the spectra are corrected considering the implant profile in the resonator (black lines) that accounts for a different number of embedded emitters. The inset shows the raw spectra before the normalization.

### 6.4.3 Numerical Optimization of The Fabrication Parameters

We now address the expected optical properties of the Mie resonators by considering a simplified 3D model of the resonator shape and placing individual dipole emitters within it.

In order to identify the optimal size of the Si islands to obtain Mie resonances near the wavelength of the ZPL of G-centers we carried out finite-difference time-domain (FDTD) simulations, studying the scattering cross-section under plane wave illumination from the top, as a function of the base diameter of the resonators (Figure 6.5 a)). We identified a broad resonance corresponding to the electric dipole mode (Figures 6.5 c) and d)) covering the wavelength of interest for G-center emission for diameters between 500 nm and 680 nm.

The low quality factor of lower order modes in Mie resonators (e.g. about 10 for electric and magnetic dipolar modes) is not suitable for the enhancement of the spontaneous emission rate of G-centers [202, 189] by promoting the so-called Purcell effect. However, using the reciprocity principle [207], we concluded that this mode is the one which can couple with the free space. Therefore, the emitted power to free space of an electric dipole embedded into the resonator is maximised when the dipole is placed at a maximum of the local electric field amplitude (i.e. in a so-called field "hot spot"). We confirmed this phenomenon by computing the emitted power in free space ($P_{front}$) for electric dipoles emitting at the wavelength of the ZPL of G-center and placed on the axis of symmetry of the resonator at different depths. Figures 6.5 c)

and d) highlight the concordance between $P_{front}$ and the resonance mode as expected by the reciprocity principle.

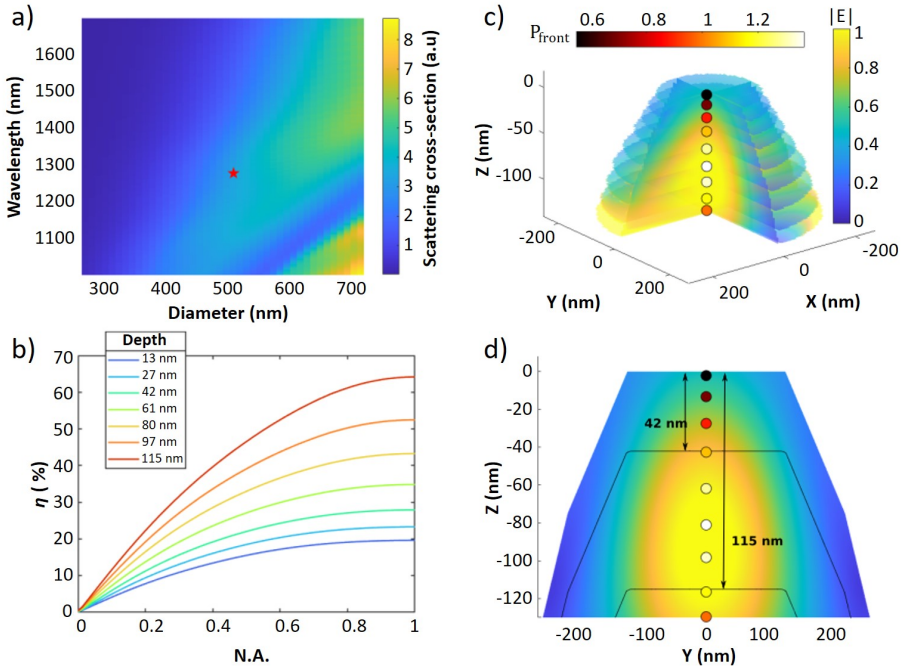


Figure 6.5: FDTD simulation. a) Total scattering cross-section (Defined in Chapter 3.2.1) of a resonator for different base diameters under plane wave illumination from the top, taking into account the presence of the BOX and the substrate. b) Computed extraction efficiency as a function of the numerical aperture (NA) of the collection optics for a dipole placed on the axis of symmetry of a resonator at different depths. c,d) 3D and 2D view of the internal electric field resulting from the excitation of the electric dipole mode at 1278 nm for a resonator having a base diameter of 507 nm. The colored spots represent the total power emitted in free space by electric dipoles emitting at 1278 nm and placed at the location of the spots. The black line (d) shows a 2D cut of the theoretical surface where G-centers are located in the resonator.

This method only gives us information on the power emitted into free space. However, what really matters to maximize the collection of the photoluminescence of a quantum emitter with conventional optics (e.g. a low NA objective lens), is to favor an upward directional scattering compared to the emission towards the underlying substrate. Therefore we also computed the extraction efficiency $\eta = \frac{P_{front}}{P_{tot}}$ depending on the depth of the dipole in the resonator. Figure 6.5 b) shows that the extraction efficiency increases with the depth of the dipole into the resonator which means that it is preferable to work with G-centers implanted deeper in the structure. Thus, in optimal

conditions of resonator size and position of the emitter, the collection efficiency largely exceed what could be expected from bulk Si or flat SOI, where only a few % of light is out-coupled into free-space and redistributed over the half solid-angle.

Our work compares favourably with the literature, thanks in part to the aforementioned advantages of placing the photon emitters within the bulk of the resonant antenna structures. We report the collection of 89% of photons emitted into the upper half space with an optical collection system of numerical aperture (NA) = 0.65, and 55% of the total number of photons emitted from the defect centres ($\eta$). We can compare this result with vertically standing semiconductor photonic nanowires which are well adapted to reach high collection efficiencies and to broadband operations. A collection efficiency of 43% was experimentally observed for a single quantum dot embedded in nanowire standing on a semiconductor substrate [208] and an efficiency of 72% was reported for a nanowire standing on a metallic substrate to reflect downward-emitted photons [209]. Our approach, relaxes the need for complex epitaxial fabrication and etching steps and allows, in principle, comparable performances. Similar systems are the so-called "photonic trumpet" structures (inverted cone shapes, presented in ref. [210]) which provide adiabatic expansion of a guided mode fed by photons from InAs quantum dot situated at their base, yielding vertical emission info free space. Such structures channel 95% of photons from the point emitter into the wanted guided mode, and then 59% of these photons to free space, yielding an overall extraction efficiency of 56%. Our system therefore delivers comparable performances with a far simpler and more robust photonic structure.

More similar structures to those presented in this paper, namely silicon nanodisks embedded with SiGe quantum dots [202], demonstrate Purcell enhancement factors of around 1.5 but do not distinguish between the enhanced emission rate of photons into the disks themselves (due to a reinforced optical density of states) and collection optimisation in free space due to directional control of emitted photons.

Advanced epitaxial growth and nano-fabrication methods can be used to embed light emitters in Fabry-Perot micro-pillars and photonic crystal nano-cavities offering a large enhancement of the radiative spontaneous emission rate and a shaping of the emission in the far-field [211]. In these cases collection efficiencies (expressed as the collection efficiency at the first lens, that is the same figure of merit that we use) ranging between 20 to 80% can be obtained. These values are comparable to our findings that are obtained with a much simpler device and fabrication methods.

When the emitters are not embedded within the resonant antennas the collection enhancement is usually more limited. In the case of perovskite nanocrystals coupled to $TiO_2$-based Mie resonators, the PL enhancement reached a value of 5 with respect to bare emitters [212]. This enhancement is not far from what was previously reported by dispersing colloidal quantum dots atop Si-based Mie resonators [191]. This latter analysis clearly points out the importance of embedding the emitters within the resonant cavities when targeting a large brightness of the sources (e.g. as for quantum optics applications).

The optimal size of the resonator obtained by experimental measurements is consistent with the results of the simulations since it is in the range in which we find the resonance (see the red star on Figure 6.5 a)) corresponding to the electric dipole mode (Figure 6.5 c) and d)). We notice that we do not obtain the diameter for which the sim-

ulation predicts the strongest resonance at 1278 nm. This difference can be explained by the approximations made in the simulations for which we considered an ideal shape of resonator, that is two stacked truncated cones, and we set an average height for the resonators. Moreover, the simulations do not take into account fluctuations of shape and height of the dewetted particles within a same array [213, 181].

The optimal carbon implantation energy obtained experimentally (Figure 6.4 b)), which corresponds to a deep implantation, is in agreement with the simulated results: a deeper implantation results in a larger extraction of light (Figure 6.5 b)). However, if we assume that the G-centers are mainly created on a surface conformal to that of the resonator and at a depth corresponding to the average depth of implanted carbon (black lines in Figure 6.5 d)), the probability of creating G-centers in a hot spot of the mode, and at the same time of coupling it with this mode, is increased for higher implantation depths. This explains why, at a fixed resonator size and proton dose, we obtain a more intense PL signal for the sample in which the carbon ions have been implanted at an average depth of 115 nm than that for which it is at 42 nm (inset of Figure 6.4 b)). Moreover, we see in Figure 6.5 d) that the theoretical surface in which the G-centers are mainly created is larger for a shallower implantation. This means that it is possible to create more emitters for shallower implantation. This implies that we obtain a brighter signal with a lower number of emitters, which shows the interest of placing the G-centers in the hot spot of the modes. Figure 6.4 b) shows the PL signal normalized by the theoretical effective surface over which G-centers are created for carbon implantation depths of 42 nm and 115 nm (black lines in Figure 6.5 d). This accounts for the different number of emitting defects considering that the density of G-centers is constant for the two samples given that they were implanted with the same carbon dose. This demonstrates the importance of controlling the placement of the emitters since we observe a difference in PL per unit of effective emission surface, in other words, per number of emitters, of more than one order of magnitude.

### 6.4.4 Angle-resolved Photoluminescence Spectroscopy

We now address the far-field emission pattern of the G-centers when embedded in the resonant antennas. As the experimental setup used for angle-resolved photoluminescence does not allow us to reach temperatures below 120 K, we have focused our study on the brightest array of resonators previously identified so as to have sufficient signal. Figure 6.6 a) shows the spectrum of angle-resolved photoluminescence obtained at 120 K on which we observe the red-shift and the broadening of the ZPL of the G-centers caused by the relatively high temperature [55]. However, we can see that we get enough signal to distinguish the emission from the G-centers, which allowed us to study their far-field emission profile, shown in Figure 6.6 c), using Fourier spectroscopy. In order to only collect the emission from the G-centers, we measured the far-field of the resonators in which the G-centers are embedded and we subtracted from it the measurement carried out on an area of SOI with no emitters.

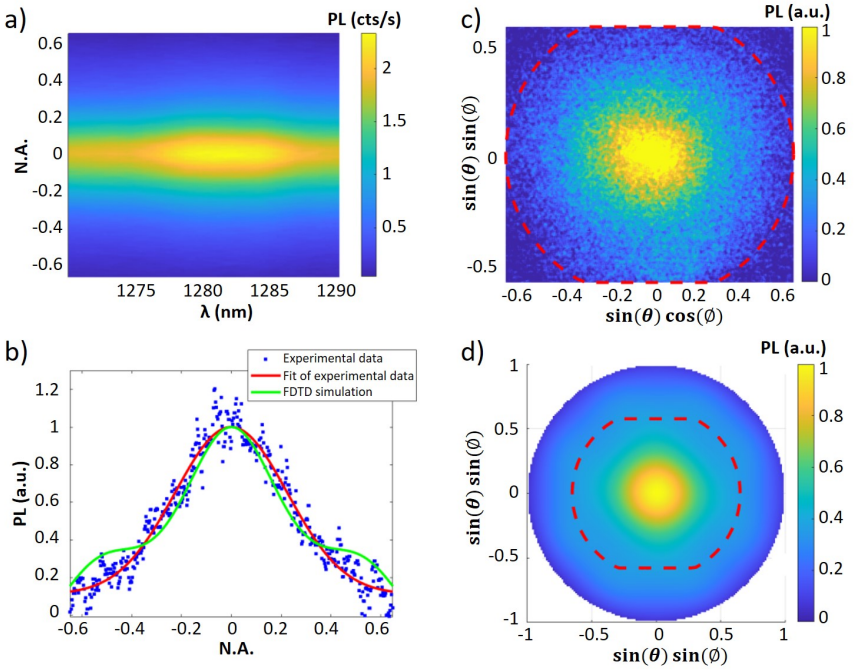


Figure 6.6: Angle-resolved spectroscopy. All the measurements have been carried out on the brightest structure at 120 K with an excitation by a laser at 532 nm. a)Angle-resolved photoluminescence pseudo-colour maps in linear scale. b) 2D cut along the $\sin(\phi) = 0$ direction of the far-field emission profile. The blue dots are the experimental data which are fitted by a Gaussian profile (red line) and the green line corresponds to the result obtain by FDTD simulation. c) Experimental and d) simulated normalized far-field emission profiles.

This measurement gives access to the angular distribution of the photons emitted by the G-centers by counting the number of photons emitted for each wave vector of the reciprocal space. The latter is characterized by its components $k_x = (2\pi/\lambda)\sin(\theta)\sin(\phi)$ and $k_y = (2\pi/\lambda)\sin(\theta)\cos(\phi)$ where $\theta$ is the polar emission angle and $\phi$ is the azimuth angle. The distribution obtained experimentally can be fitted by a Gaussian profile as shown by the 2D cut for $\sin(\phi) = 0$ in Figure 6.6 b) where the blue points represent the experimental data and the red line the Gaussian fit. Using this fit, we can estimate the transmission efficiency of the emission in the free space to an optical collection system of numerical aperture NA defined as $T(NA) = \frac{\int_0^{NA} G(x)dx}{\int_0^1 G(x)dx}$, where G(x) is the function given by the Gaussian fit. Thus, we estimate that for the microscope objective NA = 0.65 used for this experiment we collected 89% of the photons emitted into free space, and we can expect up to 93% of collection efficiency with NA = 0.8. These results show that the coupling of the G-centers with the resonant antennas leads to a strong directionality of the emission in the upwards direction, and so maximizes the collection

efficiency during transmission to optics with standard numerical apertures.

Further insight into the underlying phenomenology is obtained by representing the electric field intensity distribution obtained by FDTD simulation for the emission of a dipole positioned on the axis of symmetry of a Mie resonator at 115 nm from the top surface (optimal conditions of resonator size and dipole position). To confirm the directionality of the emission we also reported the Poynting vector (as arrows) showing that the dipole emits more power into free space than into the BOX and that a large part of the power emitted into free space can be collected with conventional optics.

The experimental results are compared with the predictions obtained by FDTD with a dipole placed on the axis of symmetry of the resonator at a depth of 115 nm (Figure 6.6 b) and d)). For numerical apertures lower than 0.35, the far-field profile predicted by this simulation is close to the Gaussian profile which fits the experimental data. On the other hand, for NA > 0.35 a small plateau appears in the simulated far-field profile that we cannot distinguish experimentally. This discrepancy between the simulation and the experimental results can have several origins, the first being the fluctuation of size and shape of the resonators in an array as explained previously. Another explanation is that we consider only one emitter in our simulation whereas there can be several in a single Si resonator at slightly different depths. Therefore our simulations do not take into account the collective effects of the various emitters as well as their distribution in the resonator. Consequently it is not possible to obtain an absolute quantitative prediction from the simulations. However, the similarities between the experimental and computed results allow us to qualitatively estimate the influence of the parameters such as the size of the resonator and the location of the emitters on the emission which results from the coupling between the two. In particular, the deeper the emitters are in the resonators, the larger the extraction efficiency (Figure 6.5 b)). This, added to the high directionality of the emission, allows us to improve the ratio of collected photons with respect to the total emission of a G-center (e.g. compared to what is obtained in flat SOI, without a photonic structure).

### 6.4.5 Electric Field Intensity Distribution

Figure 6.7 represents the electric field intensity distribution obtained by FDTD simulation for the emission of a dipole positioned on the axis of symmetry of a Mie resonator at 115 nm from the top surface. The base diameter of the resonator is 507nm and the surface of this latter is delimited by the blue lines. The grey line marks the delimitation between free space and the BOX. Finally, the arrows represent the Poynting vector and show that the system emits more power into free space than into the BOX. Moreover, the Poynting vectors illustrate the fact that a large part of the power emitted into free space can be collected with optics with standard numerical apertures (T=93% for NA=0.8). Figure 6.7 is introduced as a Graphical Abstract in order to illustrate the main idea of our work.

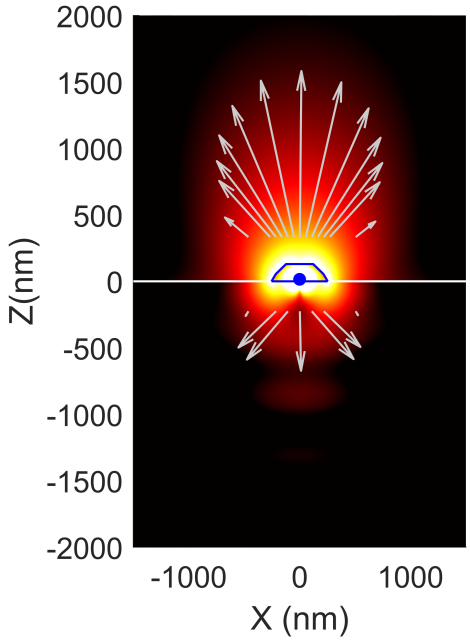


Figure 6.7: FDTD simulation of the electric field intensity distribution emitted by a dipole positioned on the axis of symmetry of the resonator at 115nm from the surface. The base diameter of the resonator is 507nm.

## 6.5 Conclusion

In conclusion, we showed for the first time Si-based sub-micrometric Mie resonators embedding quantum emitters featuring a bright and directional photoluminescence at near-infrared frequencies. Exploiting the dewetting instability of thin films, a hybrid top-down/bottom-up nano-fabrication method, we can form small resonators with low-resolution, optical lithographic methods. These antennas, unlike Si-based Mie resonators obtained via conventional top-down nano-fabrication approaches, are monocrystalline and defect free, with atomically smooth facets, thus limiting the defects at the air-Si interfaces. Engineering the implant profile of C ions and proton fluency, we can obtain light-emitting antennas featuring a high extraction efficiency, channeling up to 89% of the light towards a conventional objective lens, as verified by FDTD simulations. These results are important in view of the creation of individual emitters in Si-based nano-antennas, relaxing the need for complex photonic devices (e.g. photonic crystals, Fabry-Perot microcavities) and for applications in quantum optics, such as quantum cryptography and quantum computation.

# General Conclusions and Perspectives

The aim of this thesis was to explore a novel approach based on complex point defects in silicon-based devices for the fabrication of bright light sources. More specifically, we intended to study G-centers in silicon for the implementation of quantum light sources embedding them in dielectric antennas.

We overcome the limitations of most common fabrication methods for realizing Mie resonators demonstrating that, with a conventional top-down nano-fabrication approach, joined with a dewetting instability, we can form large arrays of small Si-based islands atop a thick $SiO_2$ (BOX): our method is based on patterning by optical lithography (low lateral resolution, about 2 $\mu$m) followed by solid state dewetting of a thin SOI substrate. Our antennas, unlike other Si-based resonators obtained with other methods (such as e-beam lithography and reactive ion etching), feature atomically smooth facets (no roughness on the surface). This limits the defects at the air-Si interface that could perturb the photoluminescence emission of the quantum emitters embedded within by trapping electrons or providing fast recombination channels for the photo-generated electrons.

These particles, featuring a large refractive index and reduced absorption losses at near-infrared frequency, sustain electric and magnetic multi-polar modes, providing a distinct approach for light management in several contexts of practical interest such as directional scattering, sensing and structural color. The merit of this PhD work was to add a new function to these Si-based antennas, that is light emission. This property is usually forbidden by the indirect nature of the Si band-gap.

Therefore, the challenge of this work was to fabricate well-localized and isolated Si-based monocrystalline islands, carefully studying their optical features to understand how their resonances form in frequency and in space (e.g. how the associated near field intensity is distributed within an island while addressing the effect of the underlying BOX and bulk Si). With these information we were able to activate the antennas with light emitting G-centers by implantation of carbon, hydrogen and recrystallization by high temperature annealing. The distance between the islands and the presence of a thick BOX underneath, allowed to produce localised light emitters with a mask-less approach.

Based on the detailed knowledge of island shape and resonances formed within, we were able to position the emitting defects by ion implant at the right position, where

the Mie modes feature their maximum. This allowed to maximise the light extraction and shaping the far-field emission pattern providing a directional, Huygens-like source. Thus, this thesis provided, a bright and directional photoluminescence emission at near-infrared frequencies, a large extraction efficiency channeling up to 89% of the light towards a conventional objective lens, as verified by FDTD simulations.

Within the time frame of this PhD it was not possible to study the photon statistic of the G-centers embedded within the dewetted islands showing the integration of individual emitters. We expect that, in the limit of low implanted carbon dose, the extraction of single photons from individual G-centers should allow for a much larger extraction with respect conventional SOI, that has been used so far. The coupling of the photoluminescence with the Mie resonances resulting in a directional emission and large extraction, should also relax the need of complex, sensitive and very expensive experimental setups (e.g. leveraging the need of integrating the main objective lens of the photoluminescence experimental setup within the cryostat, that has been mandatory so far for the observation of single quantum emitters in Si). The hope is that now, conventional confocal setups equipped with conventional NIR avalanche photodiodes might be enough to study quantum optics with impurities in Si.

Beyond the results shown in the manuscript, many results have not been finalised and we chose to add them at Appendices to this manuscript. Although not yet concluded, in these Appendices there are relevant data on experimental procedures developed to create G- and W- and C-centers by focused ion beam implant and by high-power laser pulses (respectively Appendix B and C). These results were obtained in collaboration with Dr. David Grojo (CNRS, Aix-Marseille Univ., LP3) and Prof. Nicolas Chauvin (INL of Lyon)).

The importance of using a focused ion beam implant relies in the possibility to localise the emitters with high precision (down to a few nm) and, in principle, active the emitters within a photonic or electronic device. During this PhD the implant of Si in a virgin SOI (no carbon implanted) did not provide a regular array of localised emitters in the FIB spots, likely for some issue during the ion implant. Nonetheless, these first results showed that, beyond individual W-centers obtained in the heavily implanted areas, localised emission of a plethora of other unknown emitters was observed (Appendix B). These latter are similar to some of those reported in Durand et al. [68] (e.g. SD-2 and SD-3 and SD-4) suggesting that, unlike the previous assessment attributing them to carbon related centers, their nature is related to self-interstitial or Si clusters. In collaboration with the INL Institute of Lyon, similar experiments have been conducted with a Ga- and a Ge-ion source. First results provided positive outcomes confirming the onset of localised emission (not reported, not shown).

A second approach for creating G- and W- and C-centers relies on the use of high-power, fs laser pulses (Appendix C). This is the first example of this kind in Si. These experiments were conducted on SOI and bulk Si for C-implanted and virgin materials. The experimental conditions (e.g. sample surface cleaning, laser power and number of pulses, post processing annealing). This ongoing activity have been addressed with encouraging results even more work is still needed to conclude the study. Next steps will address the focusing of the laser in diffraction-limited spots to localize the emitters and forming them in photonic and electronic structures.

Other results not shown include the activation of G-centers within more complex

structures, such as Si-based nanowires obtained via solid state dewetting. These structures can serve as Mie resonators, wave guide or electronic devices, such as field-effect transistor. A bright emission from G-centers embedded in the wires has been confirmed by photoluminescence experiments in collaboration with the INL Institute of Lyon. Ongoing activities on this topic in collaboration with the Italian CNR, are targeting the deposition of electric contact on the wires to fabricate a field effect transistor with embedded G-centers. The aim of this device will be to inject carriers in a controlled way in the emitters and study the effect of external electric field on the electronic states of the impurities (e.g. switching from the A to B form of the G-center). First devices will be ready for photoluminescence experiments in Autumn 2022.

# Appendix A

# Experimental Methods

## A.1 Abstract

In this chapter we provide a description of the main tools and experimental methods used in this PhD work. More specifically, this chapter is split into two parts; the first describes the fabrication techniques whereas the second the characterization techniques.

## A.2 Optical Lithography

This technique is highly developed and widely used for fabricating microelectronic circuits, for example using deep-UV machines allowing for an ultimate resolution of the order of 10 nm [214]. Generally speaking, optical lithography refers to a lithographic process that uses visible or ultraviolet light (10-400 nm wavelength) to transfer a pattern on a photoresist. The principal components of the photoresist are: polymer base resin, sensitizer and casting solvent. The polymer changes structure when exposed to UV radiation. The resists are usually classified into two categories, positive or negative. The positive and the negative resists are those that become more or less soluble in the developer when exposed to a radiation source, forming positive or negative images of the mask patterns on the wafer.

#### Generic Lithographic Process

First, the photoresist is placed in a substrate by spin coating where it is used for the fabrication of thin films to deposit uniform coating of organic materials on flat surfaces [215]. It is performed in four steps: deposition, spin-up, spin-off, and evaporation (Figure A.1 a)).

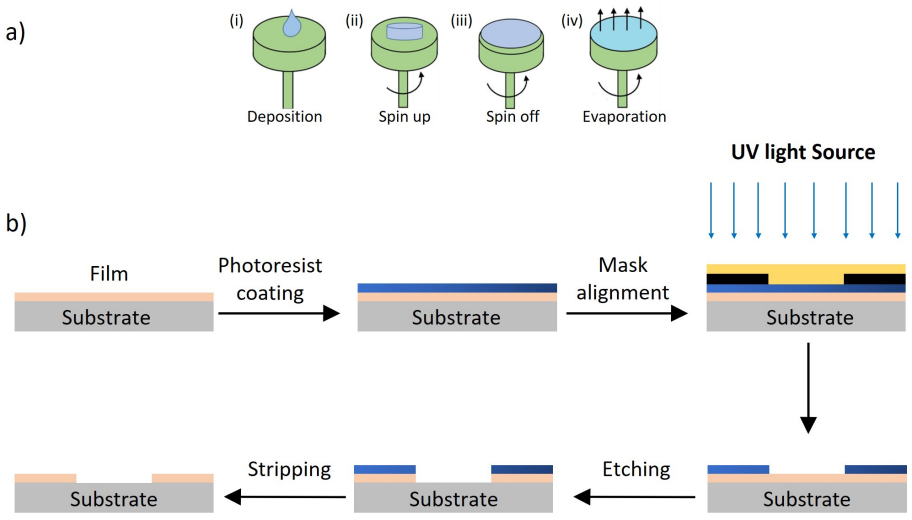


Figure A.1: a) schematic representation of thin film deposition and b) photolithographic process [216].

First, the photoresist is dropped on the wafer, e.g. from a pipette. Then, the wafer is rotated on a spinning wheel at high speed, starting and finishing by spin-up and spin-off while the thickness of the photoresist is controlled via the rotation speed. Finally, due to the rapid rotation, a uniform evaporation of the solvent occurs. The spin coating step is usually ended with a thermal treatment by depositing the sample onto a hot-plate (around $115^{o}$C) in order to evaporate the solvent of the resist.

Second, a patterned mask is aligned atop the substrate, as illustrated in Figure A.1 b), and exposed to electromagnetic radiation which modifies the molecular structure followed by a change in the solubility of the material [217]. After exposure, etching is carried out by substrate immersion in a developer solution. The developer solutions are typically aqueous and dissolve the areas of the photoresist exposed to light, thus producing a pattern that is a replica of the mask pattern. This step is commonly called lift-off. The resist patterns produced by lithography are not permanent elements of final devices, but only temporary copies of the desired features. The resist is used as a mask in a selective removal step, called etching.

The etching process can be chemical. In this case, a chemical reaction with the material of the substrate is exploited for its etching [142]. Other methods are ion bombardment (reactive ion etching technique, RIE [143, 144]) or plasma etching: the sample is bombarded with ions or a plasma (this is for instance, also used in the fabrication of superhydrophobic surface on metals, polymer, and elastomer [218]). In our fabrication process we used the tetra-fluoromethane (CF4) mixed with oxygen as a plasma to etch silicon (Si) and silicon dioxide ($SiO_2$). Finally, the remaining resist is stripped away using acetone and only the desired permanent structures remain on the sample.

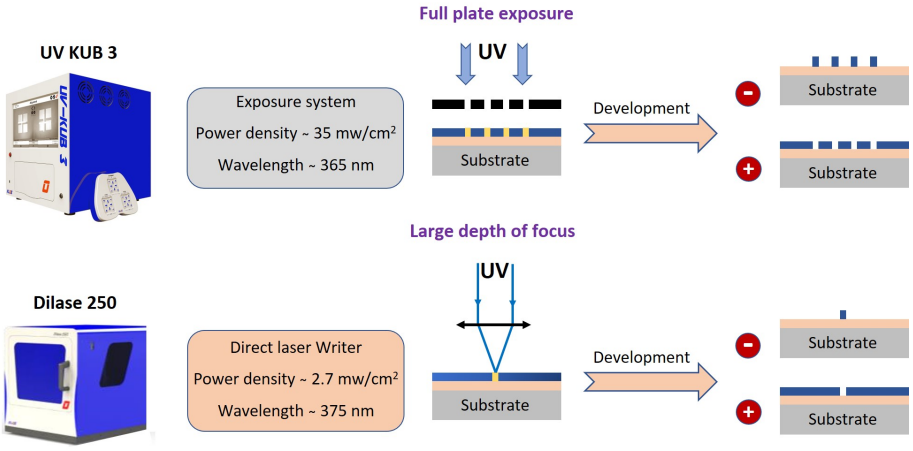


Figure A.2: schematic representation of the UV-KUB 3 and Dilase 250 lithography instruments.

In this thesis we used two instruments for the optical lithography, the first called UV-KUBE 3 and the second called Dilase 250 Figure A.2. The UV-KUB is a very compact exposure and masking system equipped with a LED-based optical head collimated and homogenous with a possibility to work on a continuous or pulsed mode. The power density is around 35 mW/cm$^2$ and the wavelength of the LED 365 nm. The system is controlled by a touch screen, the UV-KUB ensures safety through an entirely closed exposure chamber with both hard or soft contact modes available. The divergence angle of the light beam is less then 2° and offers the possibility to work in masking mode on thick layers without altering the rendering of edges of the patterns. This high-quality collimation allows to reach resolution of 2 $\mu$m without a vacuum contact mode.

The Dilase 250 is a laser-beam based lithography system with a power density around 2.7 mW/cm$^2$ at a wavelength of 375 nm. The specific optical treatment chain developed by Kloe gets a very large depth of focus controlled by a Kloe Design software. The high depth of focus resulting from the specific optical treatment line allows to write into thick films as easily than into thin films with the same edge vertically and very low roughness. The lateral resolution of the Dilase instrument is similar to the UV-KUBE, about 2 $\mu$m.

## A.3 Plasma Enhanced Chemical Vapor Deposition

The Plasma Enhanced Chemical Vapor Deposition (PECVD) is a growth technique where a material is deposited atop a wafer by introducing reactant gases between two parallel electrodes. These gases will be transformed into plasma by the capacitive coupling between these two electrodes. A large density of charged particles and Coulomb

interactions induce a chemical reaction and result in the final product being deposited on the substrate.

Our machine, called Plasma Pro NGP80 from OXFORD, is suitable to a small-scale production, and can process wafer pieces up to 200 mm in diameter (Figure A.5). The open load design allows fast wafer loading and unloading, ideal for research and prototyping. The electrostatic shield design configuration avoids energetic ion bombardment, providing low substrate damage.

The gases available for plasma creation are the ammonia ($NH_3$), silane ($SiH_4$), nitrous oxide ($N_2O$), tetrafluoromethane ($CF_4$) and nitrogen ($N_2$). This technique, is mainly used for the deposition of dielectric and passivation films such as silicon nitride $Si_3N_4$ or silicon dioxide $SiO_2$ at $300^oC$, where the optimized showerhead design delivers an excellent deposition uniformity. (Figure A.3).

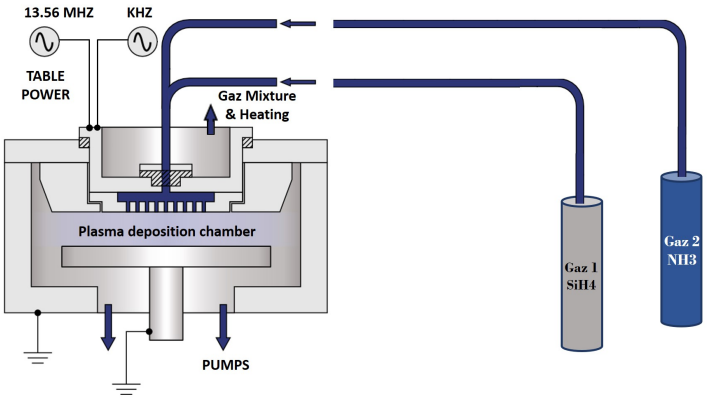


Figure A.3: PECVD scheme of the growth process, the gases are mixed and heated before being injected into the growth chamber.

The silicon nitride ($Si_3N_4$) deposited by the PECVD is largely hydrogenated, and rarely stochiometric. Concerning the structural level of $Si_3N_4$, this material is amorphous (differently from the materials grown via molecular beam epitaxy, MBE, where they are crystalline). The stochiometric chemical reaction for the $Si_3N_4$ deposited layer is given as follow:

$$3SiH_4(g) + 4NH_3(g) \longrightarrow Si_3N_4(s) + 12H_2(g) \tag{A.1}$$

Moreover, we have the possibility to locally introduce strain on Si by depositing thin films on top of it. Stress control is provided by selectable or mixed high/low frequency plasma power, enabling deposited films to be tuned for tensile, compressive or low stress.

Here I will give an example of depositing $Si_3N_4$ on top of some squared suspended membranes. These membranes are fabricated within a multilayered sample formed as follows: a mono-crystalline, silicon on insulator (c-SOI), 125 nm thick Si layer atop 2 $\mu$m thick $SiO_2$ layer (buried oxide, BOX) on a bulk Si (001) wafer. The fabrication is

performed in three steps: 1) patterning by photolithography via Dilase 250 with plasma etching, 2) dipping the SOI samples inside a buffered oxide etch (BOE) for 2 hours and 3) depositing $Si_3N_4$ on top of a membranes by PECVD.

Figure A.4 are shown three fabrication cases concerning membranes of different sizes. The ones in Figure A.4 a) and Figure A.4 b) have a lateral size of about 10 $\mu$m, while the ones in Figure A.4 c) have a size of about 20 $\mu$m.

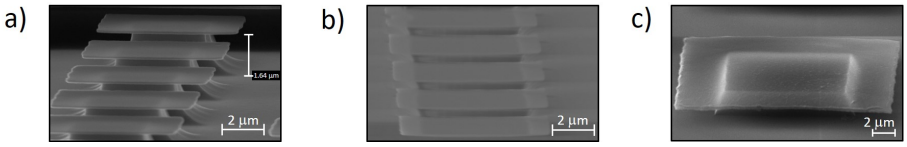


Figure A.4: SEM images for a fabricated membranes atop of a thick SOI. a) represent the case where no SiN is deposited and leading to have no strain, b) and c) represent the cases where the SiN is deposited at Low and High frequency plasma (100 W, 300W) thus leading to have tensile and compressive strain respectively.

In case a) there is no $Si_3N_4$ deposition, thus no stress on the membrane.

In case b) 25 nm of $Si_3N_4$ are deposited on the membranes at 300°C for 30 s employing 100 W of low frequency plasma power and leading to the introduction of tensile stress. Indeed, the suspended parts of the membranes bends upwards.

In case c) 100 nm of $Si_3N_4$ are deposited on the membranes at 300°C for 1 min employing 300 W of high frequency plasma power and leading to the introduction of compressive strain. Indeed, the suspended parts of the membranes bends downwards.

### Plasma Etching

Beside the materials deposition with the PECVD reactor, patterns fabricated on a photoresist atop a Si substrate by optical lithography (such as the membranes) can be etched using a combination of $CF_4$ and oxygen gases. The recipe is performed at a temperature of 50°C, for a 200 W of plasma power. While the pressure of the chamber is fixed at 100 mT.

Figure A.5: Plasma Pro NGP80 instrument

## A.4 Molecular Beam Epitaxy (MBE)

The Molecular beam epitaxy (MBE) is an growth process that takes place under ultra-high vacuum (UHV) conditions [219]. The MBE used in our lab, has three main chambers with different vacuum levels, from the load chamber (vacuum $\sim 10^{-6}$ torr), the introduction chamber (vacuum $\sim 10^{-9}$ torr) and the growth chamber that is under UHV ($\sim 10^{-10}$ torr, in order to completely remove any contamination during growth).

The available materials sources in our MBE are Si, Ge, and dopants such as B and Sb. Reflection high energy electron diffraction (RHEED), is a non-destructive technique used in-situ, in the growth chamber, to monitor the growth of the material layer by layer. A typical RHEED system consists in an electron gun producing a high energy beam typically between 15 and 30 keV which bombards the surface of the sample with an angle of 2 degrees incidence. At this energy the electrons are reflected on the surface and penetrate only in the last monolayer created. Hence, the information comes mainly from the last atomic plan. The electron diffraction is governed by the Bragg law, thus the reflected electron diffraction pattern is displayed on a phosphor screen used to establish the surface geometry and morphology. Several information can be extracted from the RHEED system obtained in the reciprocal space: the roughness, the mode of growth (2D or 3D), growth rate, crystal orientations, relaxation/strain [220].

Figure A.6 shows that we can also study as a function of the deposition time, the intensity of the reflected beam, until the deposition of one monolayer which correspond to one period. The period of observed oscillations indicates the growth rate where the term $\theta$ represents the number of monolayers thus, deposited at each stage of growth. In conclusion, this technique uses very small atomic fluxes that provide extremely precise control of deposited thickness and composition. In this PhD work, the MBE machine has been mostly used for solid state dewetting (Defined in Chapter 4.3) of thin SOI layers under high temperature annealing as explained later.

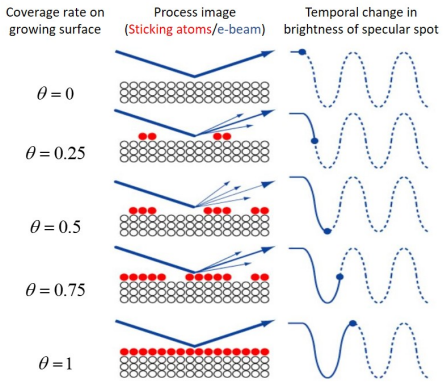


Figure A.6: Elastic scattering model of RHEED intensity oscillation in 2-dim epitaxial growth.

## A.5 Rapid Thermal Processing (RTP)

The rapid thermal processing (RTP, Jipelec JetFirst oven, Figure A.7) is a technique that allows for an extremely fast annealing using infrared halogen lamps, with heating ramps that can go up to 50°C per second with the possibility to work in air, secondary vacuum ($10^{-6}$ mbar), $N_2$, or forming gas ($N_2/H_2$). Also, this technique is well known as rapid thermal oxidation (RTO) when injecting $O_2$ in the chamber or rapid thermal annealing (RTA) in vacuum or $N_2$.

Thermal oxidation is a way to produce a thin layer of oxide on the surface of a wafer. The technique forces an oxidizing agent to diffuse into the wafer at high temperature and react with it. The process heats silicon wafers to high temperatures (over 1200°C) on a timescale of several minutes or less. The chemical reaction of an oxidized Si sample is given as follow:

$$Si + O_2 \longrightarrow SiO_2 \tag{A.2}$$

Diffusion can be described as a series of random steps that the particle takes as it moves from where it started. The diffusion coefficient D in ($m^2/s$) can be solved with Fick's laws of diffusion, which are broken up into two laws: Fick's first Law of Diffusion [221]:

$$J = D\frac{dc}{dx} \tag{A.3}$$

where, J is the solute flux and defined by the number of particles that are moving through a cross-sectional area per unit time and given in (mol $m^{-2}$ $s^{-1}$), $dc$ is the difference in solute concentration in ($mol/m^3$) and $dx$ is the characteristic length scale of the system in (m).

By changing the properties of the system, the diffusion coefficient changes. For example, at higher temperature, the diffusion coefficient is larger because the molecules have a larger thermal energy and thus mobility. The diffusion coefficient is also related to the viscosity of the solution. The larger the diffusion coefficient, the lower the viscosity as the rate of diffusion depends on the temperature of the system.

The thermal annealing process heats wafers at a specified temperature under nitrogen ($N_2$). During cooling, however, wafer temperatures must be brought down slowly to prevent dislocations and wafer breakage due to thermal shock. Problems with RTP include temperature measurement and thermal uniformity of the wafer. Excessive temperature gradients across the wafer cause thermoplastic stress that may lead to wafer warpage and/or slip.

In this PhD work, the RTP has been extensively used to create $SiO_2$ layers atop Si or SOI (e.g. for thinning the SOI or cleaning the surface) or to anneal the implanted Si and SOI wafers after ion implant to recrystallize the material.


Figure A.7: Jipelec JetFirst Rapid Thermal Processor

## A.6 Ellipsometry

Ellipsometry [222] is a very sensitive spectroscopic method, allowing to determine the optical parameters of a thin film such as the refractive index, extinction coefficient and thickness (up to several tens of microns) by measuring the change in polarization of a light beam upon reflection or transmission and compare it to a model. Our ellipsometer is a J. A. Woollam CO., lnc (ESM-300) Figure A.8 a).

The incident, white light wave is polarized linearly and changes its polarization upon reflection on the sample surface Figure A.8 b).

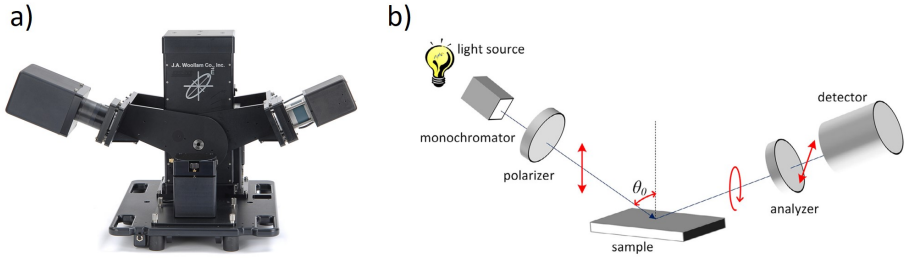


Figure A.8: a) J.A.Woollam CO.,lnc (ESM-300) Ellipsometry instrument. b) Sketch of an ellipsometry measurement technique. The sample is illuminated with a polarized light where the detector measures the modulated light intensity after passing through the rotating analyzer [223].

The measurement is based on the detection of two main parameters $\psi$ and $\Delta$ de-

scribing the polarization state of reflected light. The quantities $\psi$ and $\Delta$ are related to a complex reflection coefficient $R_p$ and $R_s$ through the following equation [223].

$$\rho = \frac{R_p}{R_s} = \tan\psi \exp i\Delta \tag{A.4}$$

Fresnel coefficients for reflection are defined as follows:

$$R_p = \frac{E_{rp}}{E_{ip}} = \frac{N_1 \cos\theta_0 - N_0 \cos\theta_1}{N_1 \cos\theta_0 + N_0 \cos\theta_1} \tag{A.5}$$

$$R_s = \frac{E_{rs}}{E_{is}} = \frac{N_0 \cos\theta_0 - N_1 \cos\theta_1}{N_0 \cos\theta_0 + N_1 \cos\theta_1} \tag{A.6}$$

where $\theta_0$,$\theta_1$ and $N_0$,$N_1$ are the angles and the complex refractive index of incident and reflected beams of light. $E_{ip}$, $E_{is}$, denote the component of the electric fields of incident light in $p$ and $s$ directions, while $E_{rp}$, $E_{rs}$ the relevant reflected light components Figure A.9. The complex refractive index is given as follow N = n - ik, with n represent the real part, k the extinction coefficient and i the imaginary unit.

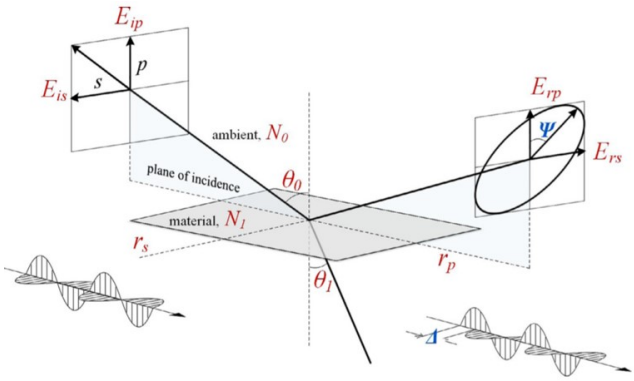


Figure A.9: principle and geometry of ellipsometric measurement [223].

In order to extract the thickness of a layer from the measured parameters $\psi$ and $\Delta$, equation A.4, we should keep in mind that the ellipsometry is a model-dependent method, meaning that a numerical analysis of the experimental data, based on mathematical models, is required to obtain the physical properties of the studied sample.

Some parameters of this model are adjusted such that the experimental data match the data calculated from the model as closely as possible. Additionally, this technique has the advantage of being non-destructive, very accurate and also no special calibration and preparation is needed.

Figure A.10 represent an example of an Ellipsometry measurement of the refractive index of $SiO_2$ layer grown by PECVD at 300°C on Si substrate as function of the wavelength.

In this PhD work, the ellipsometer has been widely used to calibrate the oxidation or etching rate of Si upon RTP or plasma etching as well as SiN deposition by PE-CVD.

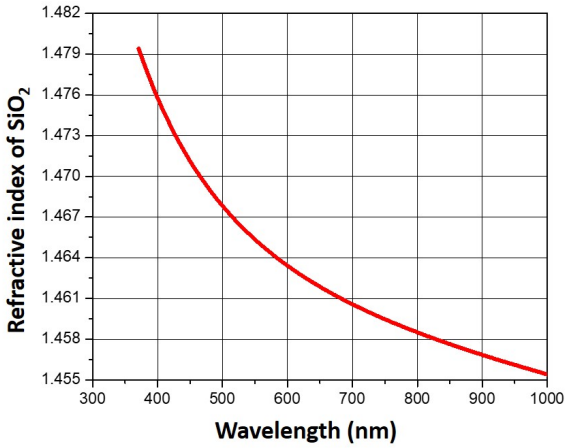


Figure A.10: Ellipsometry measurement of the refractive index of $SiO_2$ as function of the wavelength (nm).

## A.7 Atomic Force Microscopy (AFM)

Atomic Force Microscopy (AFM) is a technique for measuring the topography of the sample surface with atomic resolution. Our instrument is an XE-100 SPM. The whole system is managed and controlled with the help of a computer using the XE Data Acquisition Program (PSIA). A sketch of the AFM setup is shown in Figure A.11.

1) The support of the tip consists of a cantilever, where the tip is placed just at the end of it.

2) The laser beam is focused on the back side of a cantilever and then reflected to a mirror, to finally interact with a position sensitive photodetector (PSPD). After the displacements of the AFM tip on the surface, the alignment of the laser beam on the tip makes possible to follow the resulting evolution of the Van Der Waals interactions between the tip and the surface of the sample. Depending on the deviation of the laser beam on the tip, detected by the photodetector, the topography of the surface is thus followed. AFM relies on the forces between the tip and sample, by measuring the deflection of the cantilever the forces can be extracted as follows:

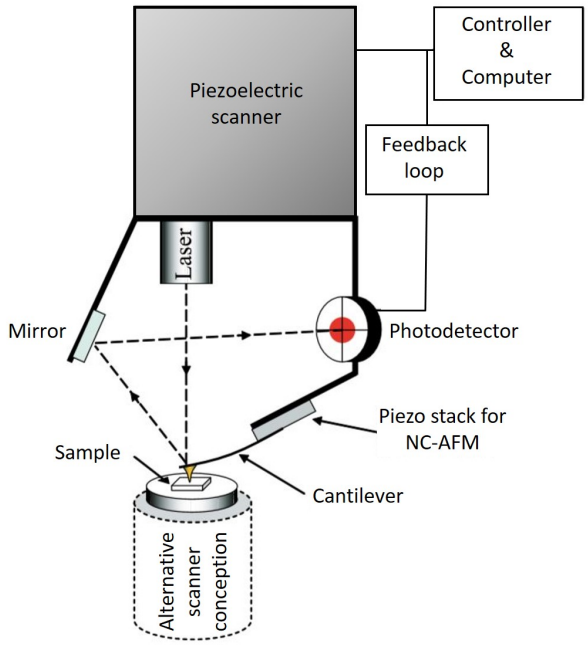


Figure A.11: Illustration of the working principle of the AFM.

$$F = -KZ \tag{A.7}$$

where F is the force, K the stiffness of the lever and Z the cantilever displacement. Three different modes can be used: contact mode, non-contact mode, and tapping mode (Figure A.12).

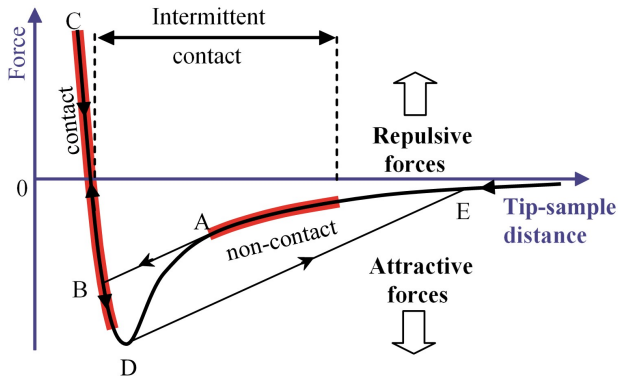


Figure A.12: Potential experienced by an AFM tip approaching the surface.

In the contact mode, the lever presses on the sample and allows the direct measurement of the repulsive force between the electrons of the sample and the tip. In the tapping mode, the cantilever is set in oscillation with a constant and high amplitude, allowing the tip to hit on the surface of the sample at each vibration. The attractive forces exerted by the sample on the tip make the variation of amplitude of the cantilever, then making it possible to trace the topography of the surface. In the non-contact mode, the cantilever stays close to the sample with a constant and small oscillation amplitude, thus conserving a higher distance between the tip and the sample (few hundred of nanometers).

The tip used should be very sharp, ideally of atomic size, in order to achieve a resolution in the same order of magnitude. In this thesis, a non-contact mode is used with a sharp tip of around 20 nm radius of curvature Figure A.13.

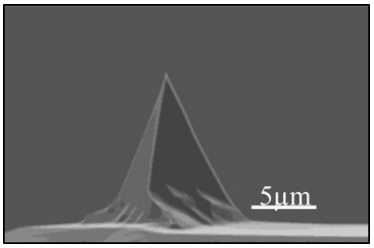


Figure A.13: Back-scattered SEM images of the AFM tips [224].

## A.8 Scanning Electron Microscopy (SEM)

Scanning electron microscopy, is a technique based on the interactions between a material and an electron beam. It allows to obtain high-resolution images, of the order of ten nanometers, thanks to the short electron wavelength.

The main components of a scanning electron microscope are: the electron source, a column maintained under a secondary vacuum, a set of electromagnetic lenses aligned in a way to obtain a fine electron beam focused on the sample, a turntable allowing to install the samples, an electron detector coupled to a signal amplifier and finally an image display system. The sketch of the SEM column is presented in Figure A.14

The electrons are emitted by an electron gun (e.g. a very sharp metallic cathode). Applying a voltage between the cathode and the anode makes possible to obtain a very intense electric field. The samples must be conductive in order to evacuate the charges accumulating on the surface, while for the non-conductive samples may be observed after being metallized.

Different interactions can be generated when the incident electron beam hits the sample surface: emission of secondary electrons SE, back scattered electrons (BSE) and the X ray (Figure A.15).

The emission of secondary electrons is generated by inelastic collision between the primary electrons of the beam and those of the atoms of the sample. These electrons

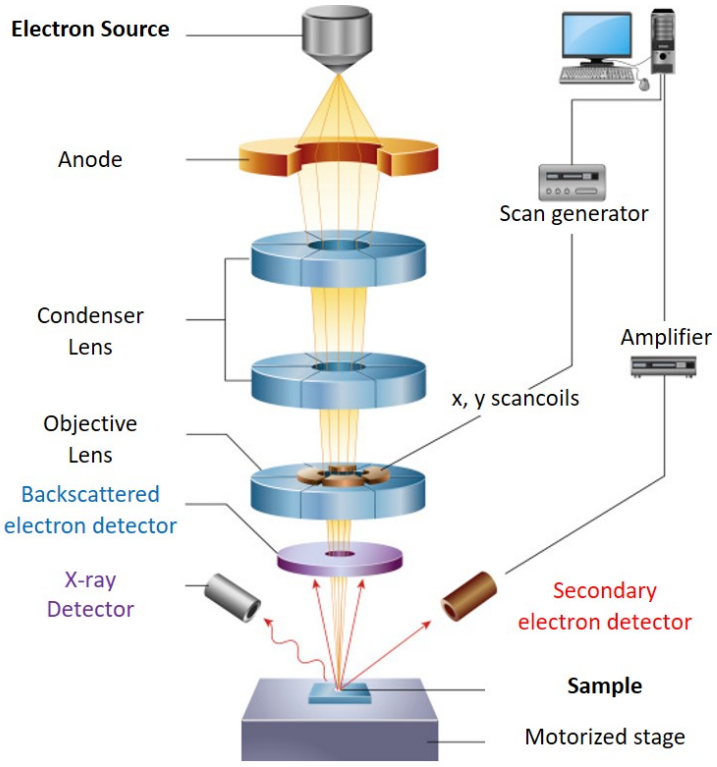


Figure A.14: sketch for a classical column of a scanning electron microscopy (SEM).

have a low energy and therefore are emitted near the surface, which corresponds to a volume of a few $nm^3$.

The emission of the backscattered electrons, corresponds to the primary electrons that are re-emitted after an elastic shock with the nuclei of the atoms or inelastic shocks with the electron's orbital. These electrons, have an energy close to the primary electrons and an associated volume of 0.5 to 1 $\mu m^3$.

Finally, the X-ray emissions are a consequence of the stripping of electrons from the different electronic shells of atoms. The ejected electron is immediately replaced by an electron from the adjacent shell with the emission of a photon. The associated volume is of the order of $\mu m^3$.

Experimentally, the images taken in this thesis, are performed with a FEI Helios 600 Nano-Lab. The majority of the micrographs are carried out with the secondary electrons through a lens detector of 5 kV acceleration voltage, a probe current of 0.17 nA and a working distance of 4.2 mm.

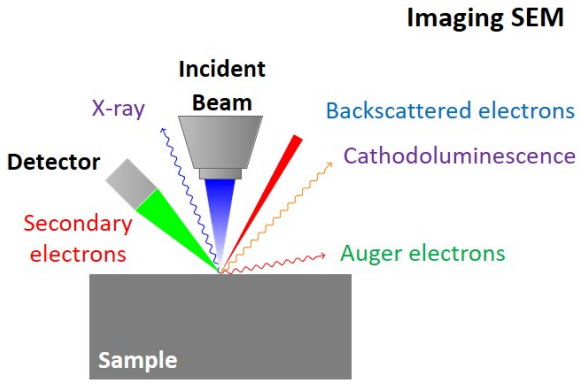


Figure A.15: products of the interactions between the electron beam and the target material, imaging SEM.

## A.9 Transmission Electron Microscopy (TEM)

The transmission electron microscopy, is a technique very similar to the scanning electron microscopy. For both microscopes, an electron gun produces a coherent electron beam accelerated by a cathode. The field effect emission is used for this purpose, then a set of lenses focus the electron beam on the sample. In the TEM the sample is very thin at the order of a hundred nanometer, so electrons can pass through the specimen, depending on sample density and electron acceleration voltage [225].

As the sample used in TEM is thin, the transmitted beam is observed directly on a fluorescent screen Figure A.16 b), while with the SEM the signal passes through a detector, since the thickness of the sample avoids any transmission and only particles emitted close to the surface are caught. This is in fact the main difference between the TEM and the SEM.

Transmission electron microscopy, requires a sample preparation in order to obtain a thin lamella with overall thickness less than 200 nm. This can be achieved by mechanical polishing followed by a precision ion polishing system. Generally, the mechanical polishing does not allow the sample thickness to be less than a $\mu$m; that's why this step is followed by bombarding the sample with ions (e.g. $Ar^+$ in order to reach about 100 nm).

The high-resolution mode in TEM allows us to observe in diffraction contrast, the atomic columns of the sample, the dislocations and the stacking faults defects that can be occur in a crystalline material. In addition, the images in high resolution make possible to determine the relative positions of atoms in a layer, with the aim of determining the stress using the phase analysis technique [220]. The diffraction essentially comes from elastically scattered electrons. The electrons scattered inelastically and whose interactions with matter have produced secondary electrons, Auger, backscattered, and X photons provide spectral information on chemical or electronic properties [226] Figure A.16 a).

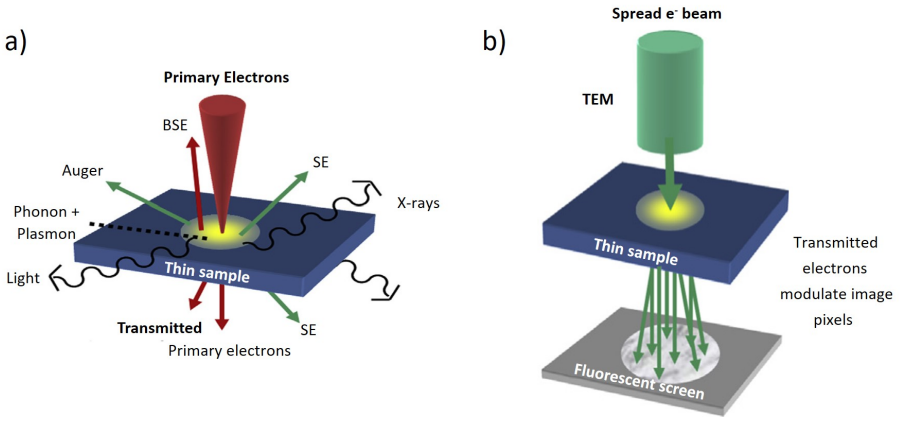


Figure A.16: a) interaction of incoming primary electrons with a sample, b) parallel image acquisition in TEM.

## A.10 Stopping/Transport and Range of Ions in Matter: SRIM Software

The SRIM or TRIM (The Stopping/Transport and Range of Ions in Matter) Monte Carlo simulation code is used to compute a number of parameters relevant to ion beam processing of materials. It computes a common radiation damage exposure unit, known as atomic displacements per atom (dpa), a standard measure of primary radiation damage production. The use of SRIM for this purpose has been evaluated and comparisons have been made with an internationally-recognized standard definition of dpa, as well as more detailed atomistic simulations of atomic displacement cascades. SRIM accepts complex targets made of compound materials with up to eight different layers, providing as a result, the final 3D distribution of the ions, all kinetic phenomena associated with the ion's energy loss (e.g. target damage, sputtering, ionization, and phonon production).

I used the SRIM software to estimate the ions implantation depth depending on the ions and the energy used. Figure A.17 represents the ion distribution profile as function of the depth (nm) for carbon and proton. The example show that through SRIM software we are able to change either the energy (e.g. 12 and 30 keV) or the ions (e.g. carbon or proton). From the energies used for carbon, it shown that at 12 keV the emitters are located at around 42 nm below the Si surface while at higher energy (E=30 keV) the emitters are much deeper at around 97 nm. For the proton we usually worked on high energy (90 keV) in order to make sure that the ions will stop only the $SiO_2$ (while by stopping in the Si substrate lead to activate unwanted defect).

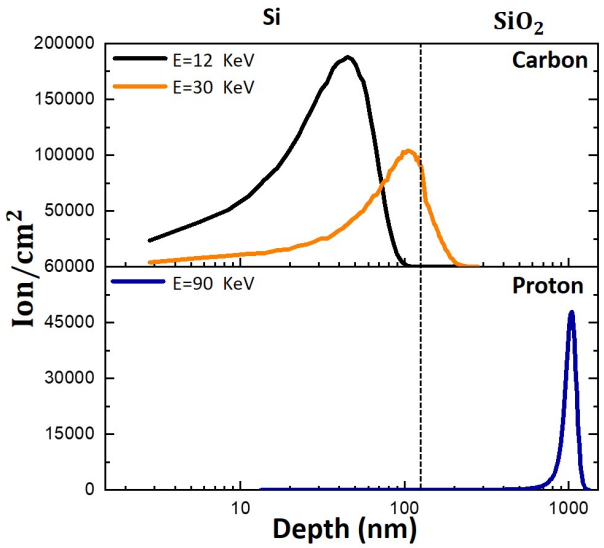


Figure A.17: SRIM simulations of carbon and protons ion range as a function of depth (nm) for implant in a 125 nm thick SOI at 12, 30 keV for carbon and 90 keV for proton. The profiles are obtained integrating over 300 000 ions.

## A.11 Ion Beam Implanters

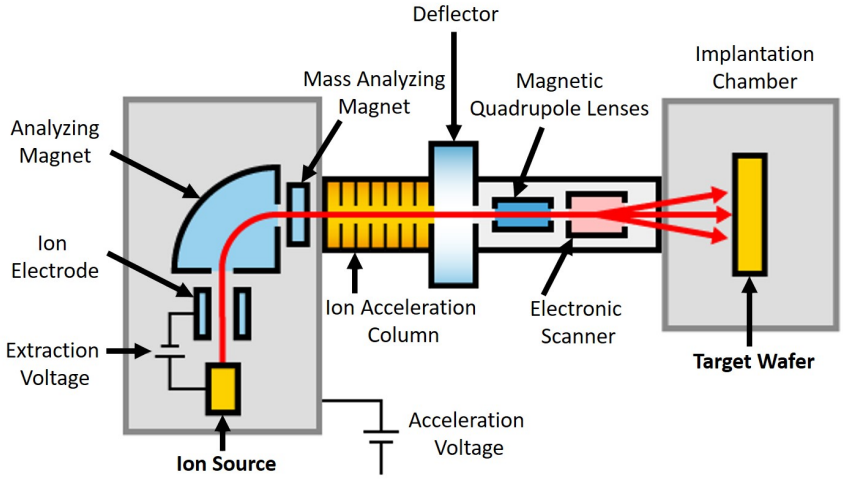


Figure A.18: schematic representation of the ion beam implanter setup.

In a conventional ion implanter, as shown in Figure A.18, an ion beam is emitted from a source by using an extraction Voltage (kV) and passed through an analyzing magnet where the ions pass through. Thus, ions having identical energies but different masses experience a different magnetic force as they pass through the magnetic field altering their pathways. As a result, only the desired ions of a particular atomic mass unit are allowed to pass through a pre-positioned orifice in the analyzing magnet. After passing through the mass analyzing magnet the ion beam is accelerated to a desired energy by an accelerator (high voltage power supplies up to 200 kV). Negative ions are changed into positive ions by a charge exchange process involving collisions with a chemically inert gas such as argon. The positive ions then pass through an electronic scanner (vertical and horizontal) to finally reach a target wafer where they impact the wafer and are implanted. During ion implantation the target wafer is uniformly irradiated by a beam of ions or molecules, of a specific species and prescribed energy.

Ion beam implanters are used to implant or dope silicon wafers with impurities to produce n or p type doped regions. In this thesis we used the ion beam implanters to implant the samples with carbon and proton at a certain energy and dose, with the goal to fabricate and activate the G centers. The implantation is carried out by using the facilities of Ion Beam Service at Aix-en-Provence in France and at the department of "Nuclear Solid-State Physics" university of Leipzig in Germany through Sebastian Pezzagna and Jan Meijer.

## A.12 Focused Ion Beam (FIB)

The focused ion beam was mainly developed during the late 1970s and the early 1980s, and the first commercial instruments were introduced in the late 20th century [227]. It is a technique based on the ions-materials interactions. These interactions partly destroys the surface during the sample analysis. This explains why the FIB is also used for nanofabrication and etching.

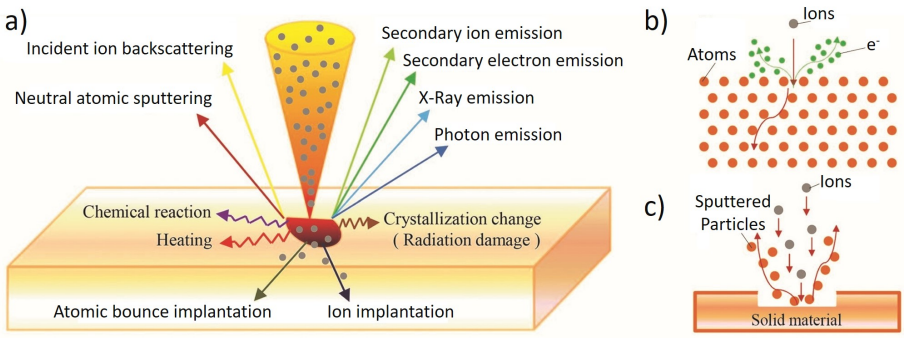


Figure A.19: a) The basic interaction mechanism between the ion beam and solid material. b) microscopic interaction mechanism between ions and atoms. c) Result of etching [228].

The main components of the FIB Figure A.20 are very similar to that of the SEM. The beam is generated by applying a strong electric field to a sharp tip (e.g. of Ga, AuGe, AuSi) maintained at the eutectic temperature, to obtain positively charged ions. A condenser lens leads to condense the ion beam whereas a control of the ion current is obtained by passing the beam through a diaphragm. The Wien filter allows the separation of the ionic species according to their atomic mass, by applying an electromagnetic field [229]. The use of the mass diaphragms located under the Wien filter makes possible to select the mass of the ions that will be used for the experiments.

The main effects of the ions bombardment on a material are shown in Figure A.19. Beside the backscattered ions, the photon emitted, the secondary electron and ion emitted, there are several effects, like ion implantation, production of vacancies and dislocations, amorphization, swelling, rippled nanostructure, deformation damage caused by elevated temperature, and gas contamination [228].

For monoatomic, solid sources, like Ga, it is not necessary to filter the ions emitted by the source. The presence of the Wien filter and the mass diaphragms is not mandatory [230]. When using an alloy ion sources, such as AuSi, it becomes mandatory to filter the ions emitted by the source, in order to use only one chemical species. By looking to the $Si^{+}$ and $Si^{++}$ ions, each have three isotopes ($^{27}Si$, $^{28}Si$, $^{29}Si$) which are separated by the Wien filter. Since these isotopes have masses very close, we must use a diaphragm of about 10 $\mu$m of diameter, in order to filter only one of the isotopes. The proper mass trajectory remains straight and passes through the mass selection aperture while the other masses are stopped. Finally, the focusing of the incident beam on the sample is carried out using an objective lens where a turntable allows to install the samples.

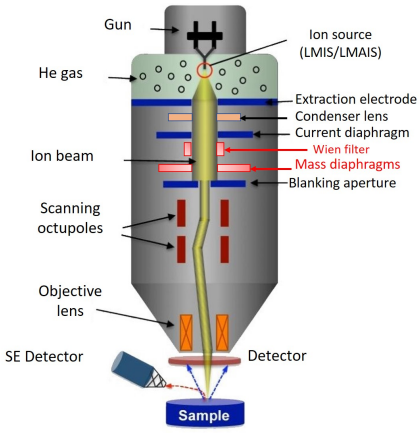


Figure A.20: schematic of the focus ion beam column [231].

Two FIB where used in this PhD work. The first is a Nano-space form Orsay Physics, working in ultra high vacuum with an ultimate resolution of around 15 nm, while the second one is a commercial FIB Tescan Lyra system, working in a secondary vacuum with an ultimate resolution of around 80 nm. Both instruments are dual-beams

and are coupled with a scanning electron microscope (Figure A.21). The acceleration energy can be varied between 5 and 30 keV. This dual-beams equipment can use a simple liquid metal ion source (LMIS), but also a liquid metal alloy ion source (LMAIS) like AuGe or AuSi.


Figure A.21: a dual beam Tescan LYRA1 XMH FIB SEM instrument.

## A.13 Photoluminescence Spectroscopy

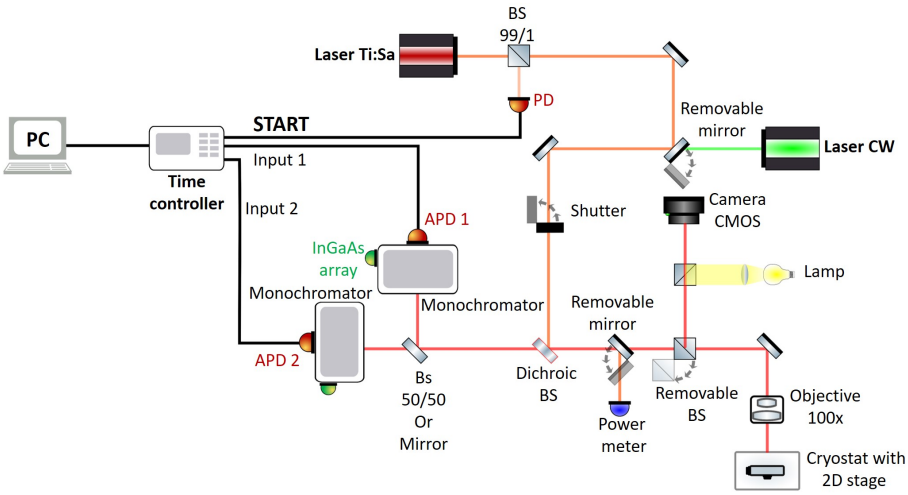


Figure A.22: scheme of the experimental setup used for Micro-PL measurements.

The micro photoluminescence (PL) spectroscopy described in this paragraph (Figure A.22) is that in use within the European Laboratory for Non-Linear Spectroscopy

(LENS) University of Florence. All the experiments have been performed at low temperature (10 K, liquid helium). The samples are placed in a low-vibration Janis ST-500 continuous He-flow cryostat, which, in turn, is mounted on a x-y translation stage to scan the samples surface.

The samples temperature is controlled by acting on the He flux and finely with an electric heater on the sample holder. The liquid helium flows due to a pressure difference thus avoiding the need of a pump, drastically reducing the mechanical vibrations. The samples are kept in vacuum atmosphere (down to $10^{-6}/10^{-7}$ mbar), created by means of a sequence of a turbomolecular and rotative pumps.

The PL signal is collected by a home-made confocal microscope setup equipped with an infinity corrected objective (100x Mitutoyo, 378-864-5, NA = 0.7). The luminescence is then spectrally dispersed by an Acton SP2300i spectrograph in Czerny-Turner configuration, mounting a 600 gr/mm grating blazed at 1000 nm, and detected using a Nitrogen-cooled InGaAs array (OMA V-512). The spatial resolution of the system is about 700 nm and the spectral resolution is about 400 $\mu$eV.

For the time-integrated measurements the excitation source is a CW diode-pumped solid state laser at 532 nm (CNI MLL-III-532), while for the time resolved measurements the excitation is provided by a mode-locked Ti:Sapphire tunable laser (Spectra Physics Tsunami, 700-900 nm spectral range, 200 fs pulse duration, 12.2 ns pulse period), pumped by a frequency doubled CW Nd-YAG laser, for the time resolved measurements. In this case, the spectrally dispersed luminescence is selected using the exit slit of the spectrograph and sent to a single photon counting InGaAs/InP APD (ID Quantique ID230). The APD signal is then processed with the ID900 Time controller interfaced with the PC. The time resolution of the system is around 100 ps.

## A.14 Conclusion

In this chapter we provided a description of the main tools and experimental methods used in this thesis. Set of techniques are used in the fabrication of the dielectric Mie resonator like Si particle which act as nano antennas for manipulating light. Some other techniques are used in the characterization like (AFM, SEM, PL...).

In chapter 5 we provided in details the fabrication technique of a silicon-based Mie resonators for an ultra-thin silicon on insulator (c-UT-SOI) by using the combination of optical lithography and solid state dewetting.

# Appendix B

# Creation of Light Emitters Via Focused Ion Beam Implant

## B.1 Experimental Methods

This Appendix is dedicated to ion implant via Focused Ion Beam (FIB). A AuSi liquid-metal alloy ion-source. The goal was to create single W centers in a commercial SOI wafer whose upper silicon layer was thinned up to 4 nm followed by a 60 nm thick $^{28}$Si layer grown by chemical vapor deposition. The buried oxide (BOX) was 145 nm thick on Si bulk. The sample was provided by the CEA laboratory in Grenoble, provided within the OCTOPUS ANR Project by Dr. Jean-Michel Gerard).

The isotopes of Si ions emitted from the source ($^{27}$Si, $^{28}$Si, and $^{29}$Si) have been separated by a Wien filter, where a diaphragm of about 10 $\mu$m of diameter is used to filter only the $^{28}$Si isotope. For optimizing the creation of single W-centers via FIB in ultra-high vacuum by implanting $^{28}Si^{+}$ ions we used a beam energy of 30 keV (only with this energy we succeed to separate the three isotopic species).

Matrices of $10\times10$ implantation spots have been created (the distance between spots is 3 $\mu$m). Two main implant parameters were changed, first the implantation dose $D$ (e.g.: $D$, $D\times3$, $D\times10$, $D\times30$, $D\times100$, $D\times300$, $D\times1000$, $D\times3000$) and second by increasing the de-focus of the main objective lens of the FIB leading to an increase in the FIB spot diameter (150, 180, 280, 500, 600 nm), while the dose will decrease with the equation B.1. The proposed implantation map is displayed on Figure B.1.

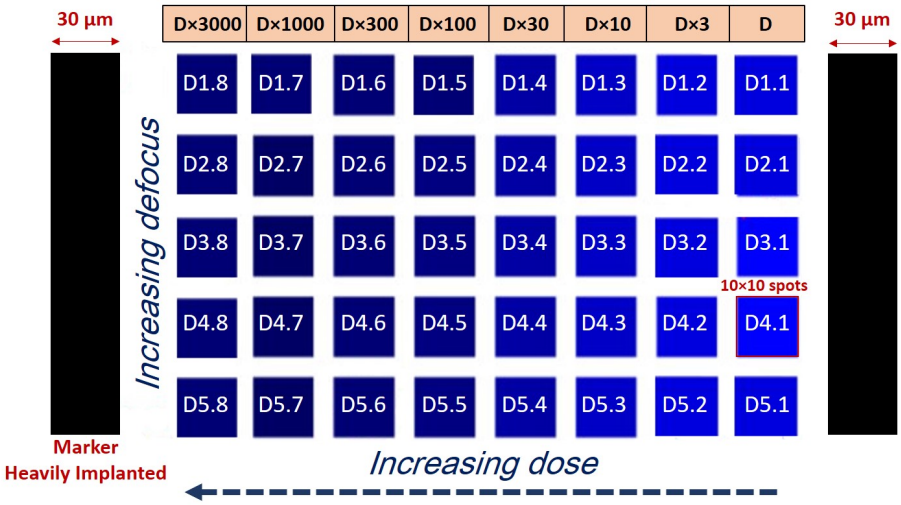


Figure B.1: proposed implantation map

The implantation ion dose is related to three main parameters: the ion beam current, the area of the spot size and the implant time. The formula is given as follows:

$$D = \frac{(\frac{Ion\ beam\ current\ (A)}{q(C)})}{Area\ of\ the\ spot(cm^2)} \times Implant\ time(s) \tag{B.1}$$

Where $q$ is the elementary charge and equal to $\sim 1.60 \times 10^{-19}$ C. The ion beam current and the spot size are measured during experiment in 2 pA and 150 nm, respectively.

The same quantity can be expressed as number of ions reaching the sample divided by the impacted surface:

$$D = \frac{Nb}{Area\ of\ the\ spot(cm^2)} \tag{B.2}$$

The implant time was chosen at 53 ns (that corresponds to the shortest allowed time for the FIB in use) and the area of the spot is calculated as follows:

$$Area\ of\ the\ spot = \pi r^2 = \frac{\pi}{4}(d)^2 = \frac{\pi}{4}(7.510^{-6})^2 = 5.62 \times 10^{-11} cm^2 \tag{B.3}$$

where $r$ is the radius of the spot and $d$ the spot diameter.

In average, the number of ions $Nb$ that reach the sample in a defined time window is calculated as follows:

$$Nb = \frac{Beam\ Current(C/s) \times Implant\ Time(s)}{q(C)} \tag{B.4}$$

In the case of shortest duration of 53 ns, $Nb$ is:

$$Nb/Implant\ Time(s) = \frac{2.10^{-12} \times 53 \times 10^{-9}}{1.602 \times 10^{-19}} = 0.66\ ions \tag{B.5}$$

Thus, the dose $D$ is given by:

$$D = \frac{0.66\ ions}{4.18 \times 10^{-11} cm^2} = 1.6 \times 10^{10} ions/cm^2 \tag{B.6}$$

The number of ions $Nb$ for different time duration is given as follows: $Nb$ = 0.66, 1.98, 6.6, 19.8, 66, 198, 660, 1980. It corresponds to doses of: $D = 1.6 \times 10^{10}$, $4.7 \times 10^{10}$, $1.6 \times 10^{11}$,$4.7 \times 10^{11}$,$1.6 \times 10^{12}$, $4.7 \times 10^{12}$, $1.6 \times 10^{13}$, $4.7 \times 10^{13}$.

Remarks: We selected a range of doses starting from lower values with respect to Froch et al, [232], where arrays of Si ions implanted into diamond were created via FIB starting from doses of $5 \times 10^{12}$ to $2.5 \times 10^{15}$ cm$^{-2}$.

### B.1.1 Poisson Distribution

The Poisson distribution can be used to estimate how many times an event is likely to occur over a defined time interval. In the case of ion implant with a FIB we assume that the number of ions present in a single pulse undergoes random fluctuations around an average value defined by the current of the beam. A Poissonian distribution can answer questions such as *"what is the probability to have only n ions that will interact with the solid material?"*. The formula is given as follows [233]:

$$P(n) = \frac{< n >^n \exp - < n >}{n!} \tag{B.7}$$

where $n$ is the number of ions, $< n >$ is the average number of ions (set by the beam current) and $P(n)$ is the probability to have $n$ ions as a function of $< n >$. Now, in order to determine what is the probability to have $n$ ions in a FIB impact on the sample for a defined period of time, we can use the former formula as follows (e.g. for $n$ = 1, 2, ..., n)

$$P(1) = \frac{< n >^1 \exp - < n >}{1!} \tag{B.8}$$

$$P(2) = \frac{< n >^2 \exp - < n >}{2!} \tag{B.9}$$

$$..... \tag{B.10}$$

$$P(n) = \frac{< n >^n \exp - < n >}{n!} \tag{B.11}$$

These curves for $P(n)$ for a given $n$ can be represented as a function of $< n >$ (Figure B.2).

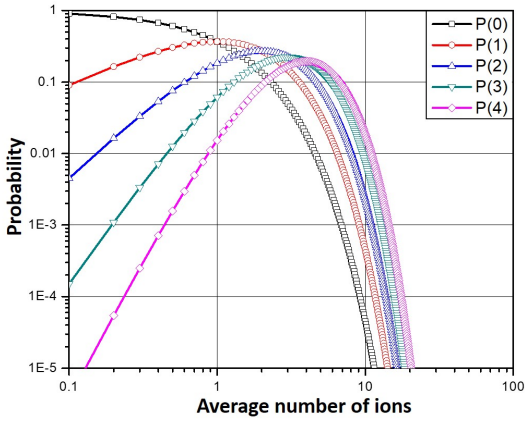


Figure B.2: Poisson distribution probability as function of the average number of ions

From these distributions for the different $n$ it is possible to extract the corresponding probabilities to impact the sample for $n$ = 0, 1, 2, 3, 4,..., $n$ ions in a given experimental condition, such as the average number of ions in the beam (Nb) that in turns depends on beam current and implant time Figure B.3.

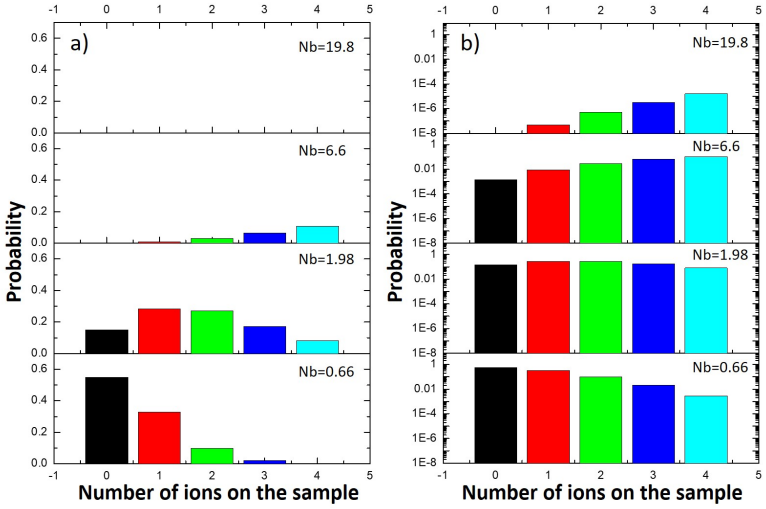


Figure B.3: Probabilities for impacting the sample with $n$ ions ($n$ = 0, 1, 2, 3, 4) for the different experimental conditions used in the experiment, that is Nb = 0.66, 1.98, 6.6, 19.8 ions, or, t = 53 ns,159 ns, 530 ns, 1590 ns. a) and b) represent the probability at Linear and Logarithmic scale respectively.

For a number of ions Nb = 0.66, the probability to have 0 ions is about 55% and for 1 ion is about 30%. For $n > 1$ the probability is sensibly lower. By increasing the

number of ions to 1.98, 6.6 and 19.8, this lead to have a similar probability for (0, 1, 2, 3 and 4 ions) that impact the sample. This leads us to conclude, that the best case to work with and study the effect of individual Si ions impacting the sample, is the first case, where $Nb = 0.66$.

We note that, in Figure B.3 the probabilities of $n = 0$ to 4 ions for larger Nb (e.g. Nb = 66, 198, 660, 1980), are not visible. This is because the associated probabilities are negligible and cannot be seen in the graph scale.

### B.1.2 Ion Distribution Profile

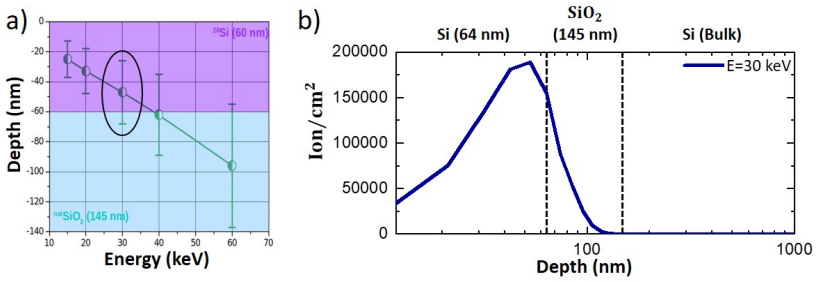


Figure B.4: a) representing the variation of the depth as function of the Si ions energy. b) SRIM simulations (Defined in Chapter A.10) of silicon ion range as a function of depth (nm) for implant in a 64 nm $^{28}$Si SOI at 30 keV. The profile are obtained integrating over 300 000 ions.

The corresponding Figure B.4 a) shows that by changing the implant energy of Si ions we are able to go deeper inside Si and $SiO_2$. Figure B.4 b) represents the ion distribution profile for a 300000 ions implanted in $^{28}$SOI layer. The simulation show that the 30 keV implant in $^{28}$Si stops in the bottom $^{28}$silicon layer of the SOI while producing interstitial Si.

### B.1.3 Photoluminescence Spectroscopy

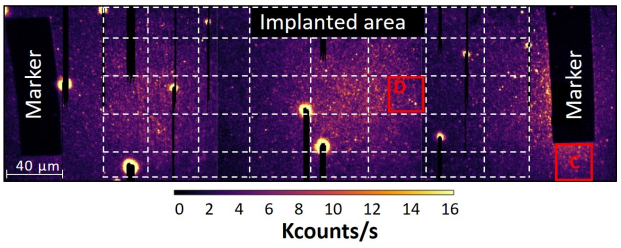


Figure B.5: Photoluminescence (PL) map of the SOI sample implanted with $^{28}$Si at different Matrix doses

Figure B.5 represents the photoluminescence (PL) map of the SOI sample implanted with $^{28}$Si at different matrix doses. The big white dashed rectangles are guides for the eyes splitting the stripes with different ions doses. The red squares (C and D) represent the areas where the photoluminescence of an isolated spots are measured. The big bright circles are dust and the dark lines are due to a switching of the superconducting detector to normal metal phase due to high contrast.

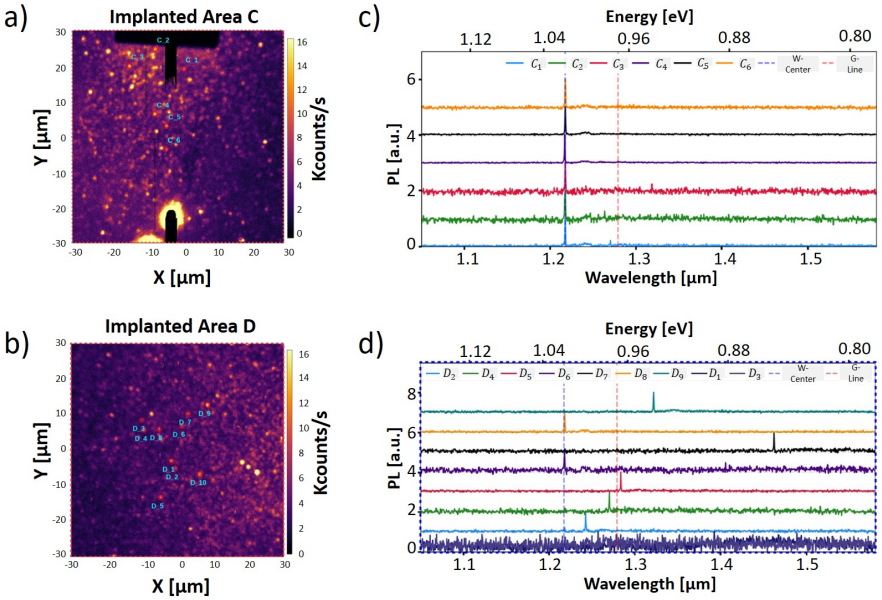


Figure B.6: a) and b) PL map of the two red dashed squared (C and D) highlight in Figure B.5. c) and d) PL spectrum detected in an isolated W-centers at the position indicated by the blue circles in a) and b).

Data presented here are recorded at a temperature 30 K under a green (CW 532-nm) laser excitation at an optical power of 10 $\mu$W.

Unfortunately, we do not see any implantation pattern corresponding to the design previously described. Fluorescent defects are randomly distributed in space. At the Marker (the two rectangular areas at the side of the patterns) there is no photoluminescence owing to the Si amorphization from the very large dose supplied.

Figure B.6 a) and b) represent the PL map of the two red dashed squared (C and D) highlight in Figure B.5. The implanted area C is close to the Marker while D represent an implantation area randomly chosen. Figure B.6 c) and d) represent the PL spectrum detected in an isolated W-centers at the position indicated by the blue circles in a) and b) respectively.

In Figure B.6 d) few of the isolated spot detected ($D_6$ and $D_7$) have a Zero Phonon Line (ZPL) corresponding to the W center energy, while approaching to the region close to the marker (high implant dose) square C, all the isolated spots detected Figure

B.6 c) have a ZPL at a different energy. This is interpreted as a signature of fact that in these areas the implantation dose wasn't enough to create W-center.

It is interesting to note that in the areas with large ion doses, as in C, the ZPL are compatible with some of the emitters reported in reference [68] and that are not yet attributed to a specific impurity complex. In this case, only Si ions were implanted, suggesting the possibility that these emitters could be associated to clusters of self-interstitial with, likely, more than 3 Si in the cluster (as for the W center that is instead detected in the areas implanted with lower doses).

**Post implant annealing**

With the target to improve the PL intensity of the isolated W centers, low temperature annealing at 250°C for 30 min is used after implant. As a result, we observed only defects with broad PL spectrum and no ZPL Figure B.7.

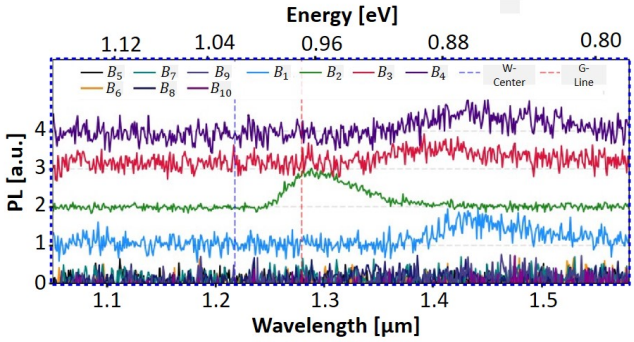


Figure B.7: PL spectrum detected in an isolated W-centers at a random position after sample annealing

This suggest some issue in the annealing process that was performed as we expected an enhancement as previously shown for similar samples.

## B.2 Conclusion

The patterns of the ion implantation was not visible. We have however observed plenty of isolated spots randomly distributed spatially on the implanted areas. Before annealing, we have detected plenty of defects with a ZPL, with a great proportion being W-centers. While at low-temperature annealing, we haven't observed any W-centers but only defects with a broad PL spectrum.

# Appendix C

# Creation of Light Emitters Via Laser Irradiation

## C.1 Abstract

Here we address the creation of ensembles of G- and W-centers via laser irradiation. This is an alternative method to FIB or full wafer ion implant that could be more convenient in view of creating the emitters *ad-hoc*, in a deterministic manner by using conventional fs laser *operando*. Working on a impurity-free sample, it is possible to directly observe the PL emission pulse after pulse, so to create only one emitter. This has been shown in diamonds [32, 33] and could be repeated with Si sample.

## C.2 Experimental Methods

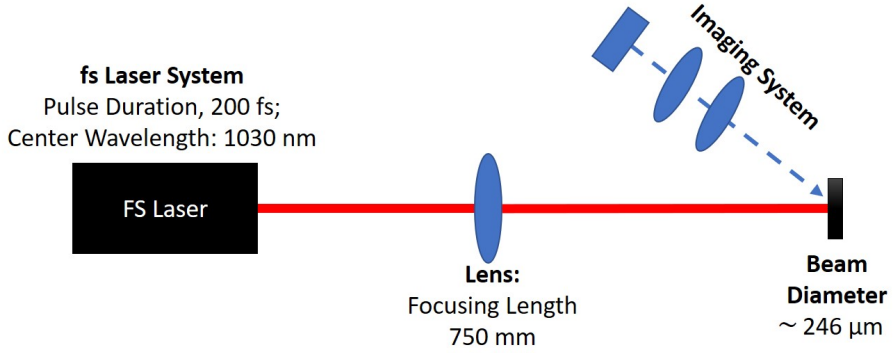


Figure C.1: schematic representation of the setup used to activate the W and G center.

Surface contamination of the SOI (220 nm Si layer atop 2.5 $\mu$m silicon dioxide $SiO_2$) is first removed with acetone. The implanted samples were either carbon free or implanted, in order to create W and G-centers. The infrared laser pulses are delivered by an optical parametric amplifier pumped with pulses of 500 $\mu$J at 1030 nm (Pharos, Light Conversion). The duration of the laser pulses is around 200 fs. An aspheric lens (f = 750 mm) focuses the beam onto the sample, which is mounted on XYZ motorized stages (Figure C.1. Motion in the XY plane allows positioning of the sample on a specific patterns and choosing the number of pulses. Micrometer precision Z-axis motion and in-situ surface microscopy imaging (10 $\times$, tilted at 45°) ensures the positioning at the best focus. The craters are characterized by means of confocal microscopy (Leica DCM3D, 460 nm illumination, 150$\times$ objective lens), allowing us to measure the ablated area with sub-micrometer lateral precision.

We produced a matrix of laser spots changing laser energy (95, 143, 175, 218 $\mu$J) and number of pulses (from 1 to 5), in order to find the good compromise to reach, either a maximum of photoluminescence (PL) extraction or to detect a single photon source (with the micro PL measurement).

**Laser Flux**

The Laser flux, it's defined as the energy per area while representing the energy density at a specific position and it's expressed, for a Gaussian beam as [234] (Figure C.2):

$$F = F_{Peak}.\exp\left(\frac{-2R^2}{w^2}\right) \tag{C.1}$$

$$F_{Peak} = \frac{2E}{\pi w^2} \tag{C.2}$$

Where $F$ represents the flux of the laser ($\mu$J/$\mu$m$^2$), $F_{Peak}$ represents the peak flux, $R$ the distance from the center; $w$ is the waist of the beam and $E$ the pulse energy ($\mu$J). If the $w$ is known, the flux distribution can be known using equation C.1 and C.2.

The diameter of the beam at a wavelength ($\lambda$ = 1030 nm), a focal laser diameter (D = 4 mm is the size of the focus spot) and the focus length (f = 750 mm which's the distance between the focus and the lens position) can be estimated as follow:

$$D = 2 \times w = \left(\frac{4 \times \lambda}{\pi}\right) \times \left(\frac{f}{D}\right) = \left(\frac{4 \times 1030.10^{-9}}{\pi}\right) \times \left(\frac{750}{4}\right) = 2{,}46 \times 10^{-5}\ m = 246\ \mu m \tag{C.3}$$

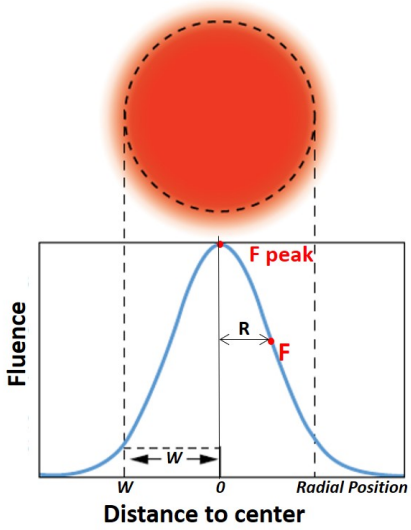


Figure C.2: Laser flux

## C.3 Photoluminescence Spectroscopy Results

### Influence of The Carbon Dose

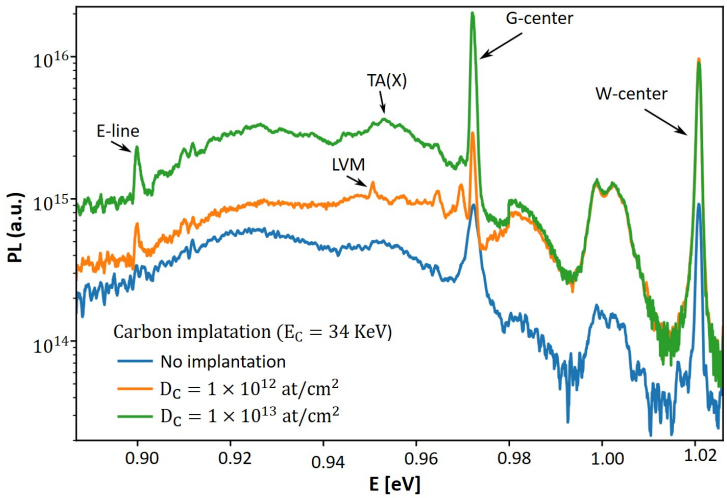


Figure C.3: PL spectra obtained with SOI samples irradiated by 3 laser pulses with an energy of 218 µJ at $\lambda = 1030nm$ with an excitation by laser at 405 nm at 12K. The label of the plots correspond to the C implantation parameters.

Figure C.3 represents the PL spectra of three samples which differ by the carbon dose used during the implantation. For each spectrum the Si signal is of the same order of magnitude which allows comparison between spectra. The first sample not implanted, while the second and the third samples were implanted at an energy of 34 keV with a doses of $10^{12}$ at/cm$^2$ and $10^{13}$ at/cm$^2$ respectively. Different observation can be made from this figure. Firstly, concerning the G-centers (ZPL at 0.9 eV, E- Line at 0.90 eV), we can see that the intensity of the ZPL increases on raising the dose of carbon (from $10^{12}$ to $10^{13}$ at/cm$^2$).

For the sample that was not implanted with carbon, the signals of the two centers (W and G) appears but with an amplitude lower by an order of magnitude with respect to the implanted ones. This PL signal in carbon-free samples is attributed to residual carbon in the upper layers of the SOI and to the manufacturing process that embeds C in the Si crystal during laser exposure. In order to confirm this observation, we produced new samples that were cleaned by rapid thermal oxidation in order to better remove or passivate the C impurities on the sample surface Figure C.4. Indeed, the protective $SiO_2$ formed on the surface was very effective in avoiding sample contamination from unwanted C. In carbon-free samples passivated by oxidation and expsed to laser, no G-center formation was observed.

For the W-centers (ZPL at 1.08 eV, LVM at 0.951 eV) that are formed by Si interstitial we observe a similar intensity for the C implanted samples and a 1 order of magnitude lower intensity for the carbon free sample. This shows that the creation of W-centers is more effective in presence of carbon doping.

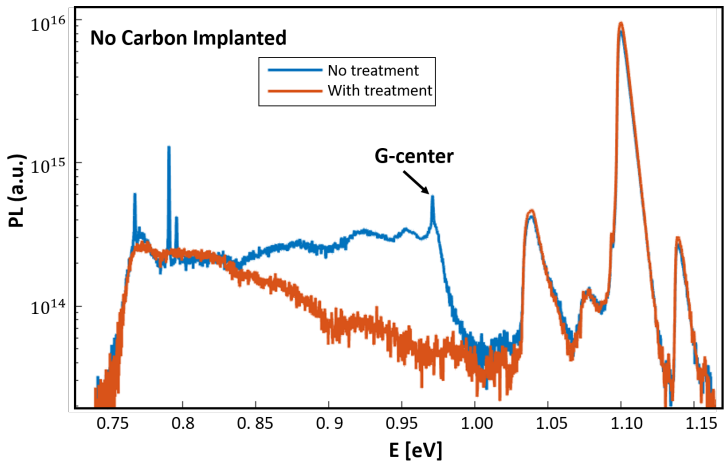


Figure C.4: Comparison between macro-PL spectra obtained for two samples (with and without RTO treatment). The two samples have no carbon implantation, but they are irradiated by 3 laser pulses with an energy of 218 $\mu$J at $\lambda = 1030nm$.

**Effect of Low-Temperature Annealing**

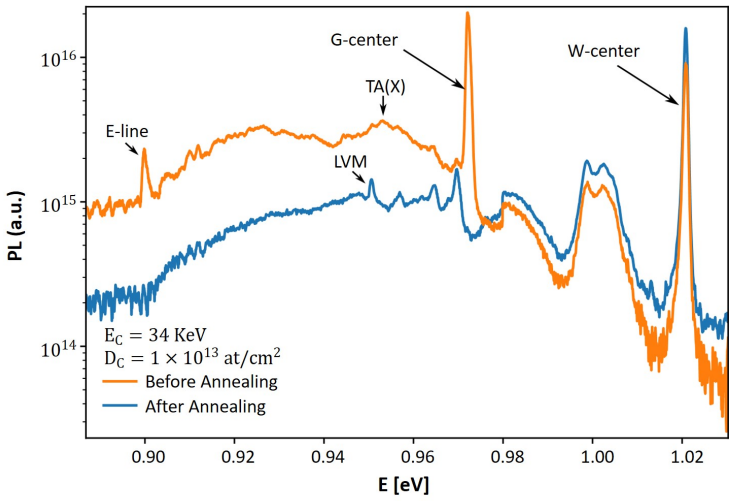


Figure C.5: Comparison between macro-PL spectra obtained for two samples irradiated by 3 laser pulses with an energy of 218 $\mu$J at $\lambda = 1030nm$ with an excitation by laser at 405 nm at 12 K. The two samples have the same carbon implantation parameters but one of them undergone a second annealing.

For G-centers created by the classical protocol using protons, it has been demonstrated experimentally that a way to enhance the PL emission, up to a factor of 8, is to perform a flash annealing under $N_2$ atmosphere during 5 min at 125 °C [235]. For the same reason, two SOI samples irradiated in the same conditions (carbon dose $10^{13}$ at/cm$^2$, at 34 keV, irradiated by 3 laser pulses with an energy of 218 $\mu$J) are studied here: the first is annealed and the second one is not. Figure C.5 represent the spectra obtained by macro-PL measurement for these two samples.

The final, low-temperature annealing has a dramatic effect on the G-centers, totally opposite to was previously observed for the samples created by proton irradiation, since in the present case of laser irradiation it annihilates them. Indeed, it appears all the typical lines associated to the PL of G-centers disappears.

On the contrary, the PL of the W-centers is enhanced by a factor of 1.75 and we find the typical shape of their phonon sideband, including the LVM line.

## C.4 Conclusion

In conclusion, we demonstrated that this lases-based approach allows to create both W- and G-centers in a specific area impacted by the radiation. Moreover it is possible to isolate W-centers with a second annealing. For the further study of these samples, several approaches are considered.

First of all, we are irradiating the Mie resonators (island and wires) obtained in optical lithography and solid state dewetting previously described. with the same philosophy by variating the energy and the number of pulses. The goal is to enhance the PL intensity of the defects first to have Purcell effect and second to create a lasing for example if possible in future with this very precise method. By noting that we can go down to 5 nm spot size, which will pave the way to other more precise study e.g we can activate island by island, etc.

Second a micro-PL study will be carried on both samples in order to see the lower limit of the area in which the emitters can be created with the laser pulses and try to determine the specific location of each centers. this lead maybe at a certain point to have a single photon emission.

# Appendix D

# Fine Structures of the G-center Zero-Phonon Line

## D.1 Abstract

In order to study and control the fine structure of the G-centers we adopted a conventional method that was previously used in the literature: applying an external strain to modify the electronic states. So far, this task was implemented on macroscopic, bulk samples mounted in appropriate cells allowing for uniaxial stress in a well defined crystallographic direction (e.g. by changing the orientation of the sample). Here, instead of using macroscopic setups for strain we produced thin suspended membranes of Si with embedded carbon ions. We applied a static strain by deposition of SiN via plasma enhanced chemical vapor deposition (PECVD). Depending on the deposition condition the strain can be, in principle compressive or tensile.

We performed micro photoluminescence observations on strained freestanding membranes and compared with the measurements of residual stress by micro-Raman spectroscopy.

## D.2 Fabrication Method

These membranes are fabricated within a multilayered sample formed as follows: a mono-crystalline, silicon on insulator (c-SOI) 125 nm thick Si layer atop 2 $\mu$m thick $SiO_2$ layer (buried oxide, BOX) on a bulk Si (001) wafer. We adopted a method to apply a stress on the membrane, as represent in Figure D.1:
-Case a): first patterning the SOI sample by photolithography (via Dilase 250 or UV KUBE 3 with plasma etching joined considering that the etching must reach the $SiO_2$), second dipping the SOI samples inside a buffered oxide etch (BOE) for 2 hours and third depositing $Si_3N_4$ on top of a membranes by the PECVD.

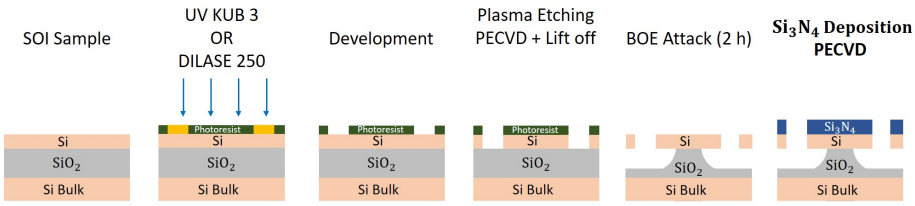


Figure D.1: Fabrication scheme of the membrane.

## D.3 Results

### D.3.1 Micro-Raman Spectroscopy

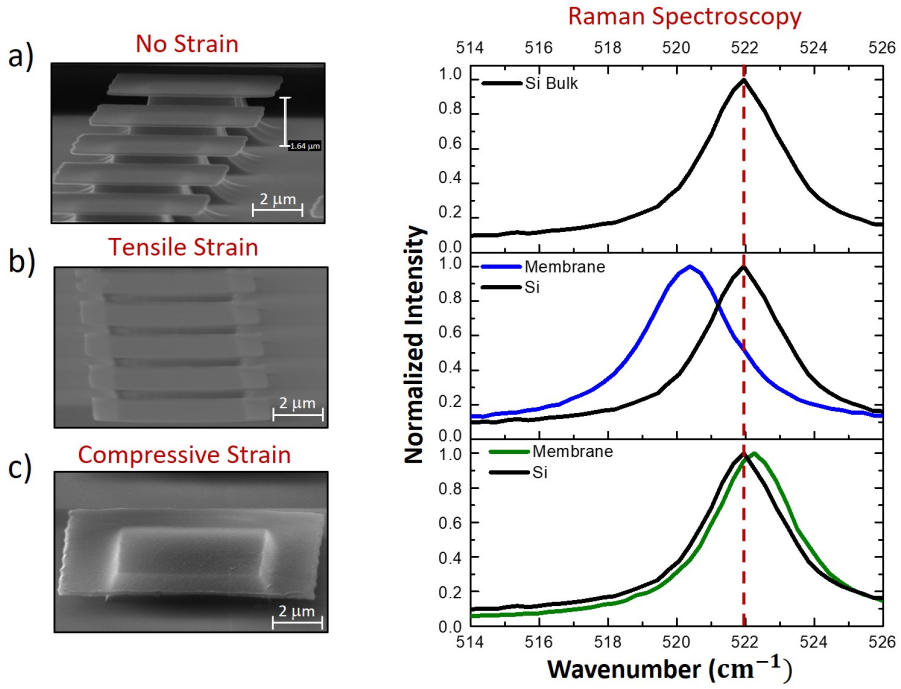


Figure D.2: Micro-Raman Spectroscopy on the membrane with and without the presence of $Si_3N_4$ deposition.

The micro-Raman spectroscopy, was performed on these membranes, where different local strain cases are shown bellow in Figure D.2:

Case a) there is no $Si_3N_4$ deposition, thus resulting no stress.

Case b) 25 nm of $Si_3N_4$ are deposited on the membranes at 300°C for 30s employing 100 W of low-frequency plasma power and leading to the introduction of tensile stress. Indeed, the suspended parts of the membranes bends upwards.

Case c) 100 nm of $Si_3N_4$ are deposited on the membranes at 300°C for 1 min employing 300 W of high-frequency plasma power and leading to the introduction of compressive strain. Indeed, the suspended parts of the membranes bends downwards.

### D.3.2 Film Stress Calculation

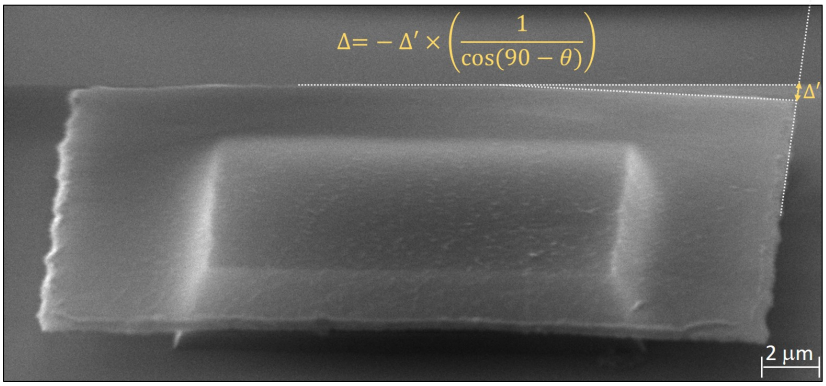


Figure D.3: SEM image taken with an angle of ($\theta$ = 70°) for a 20 $\mu$m membrane.

The stress applied on a substrate when covered with a lattice-mismatched layer can be calculated as follows:

$$\sigma = \frac{\Delta}{r^2} \times \frac{(t_{substrate})^2}{t_{film}} \times \frac{E}{3(1-\upsilon)} \tag{D.1}$$

Where $\sigma$ is the film stress, $\Delta$ is the change in wafer bow, r is the radius of the scan, $t_{substrate}$, $t_{film}$ are the substrate and the film thickness, E is the Young modulus, $\upsilon$ is the Poisson ratio.

Young's modulus (E) is the modulus of elasticity under tension or compression. In other words, it describes how stiff a material is or how readily it bends or stretches. Young's modulus relates stress (force per unit area) to strain (proportional deformation) along an axis or line. Poisson's ratio is the ratio of transverse strain to corresponding axial strain on a material stressed along one axis.

Delta is calculated as follow (negative due to the compressive strain):

$$\Delta = -\Delta' \times (\frac{1}{\cos(90-\theta)}) = -0.7 \times \frac{1}{\cos(20)} = -0.74\mu m \tag{D.2}$$

Where $\Delta'$ is extracted from Figure D.3, $\theta$ is the angle in which the SEM image is taken ($\theta$ = 70°), $t_{substrate}$ = 125 nm, $t_{film}$ = 100 nm and r = 5$\mu m$ (suspended part).

For Silicon,

$$\sigma = \frac{\Delta}{r^2} \times \frac{t_{substrate}^2}{t_{film}} \times 6.16 \times 10^{11} dynes/cm^2 \tag{D.3}$$

$$\sigma = \frac{-740}{(5000)^2} \times \frac{125^2}{100} \times 6.16 \times 10^{11} = -27.75 \times 10^8 dynes/cm^2 \tag{D.4}$$

$$\sigma = -0.277\ GPa = -277\ MPa \tag{D.5}$$

The film stress value extracted from the suspended membrane (-0.277 GPa) is more or less comparable to the value extracted from OXFORD Figure D.4 where they found a value of around -0.493 GPa for SiN deposited on Si.

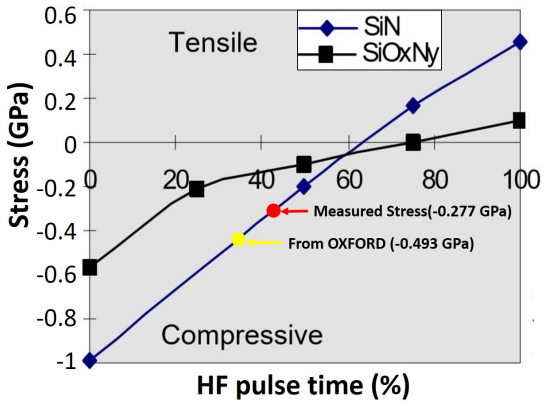


Figure D.4: mixing of High and Low frequency power allows controlling film stress and film density.

**For a Tensile Strain**

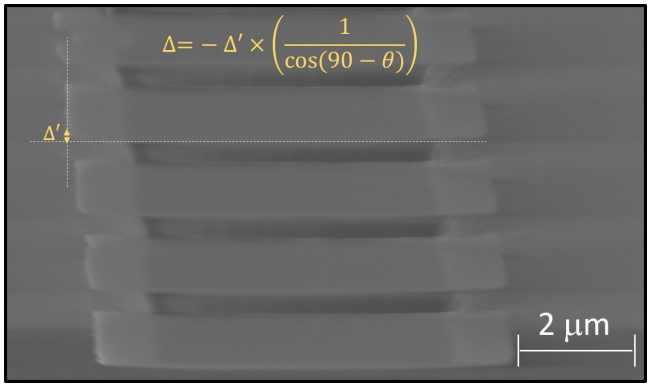


Figure D.5: SEM image taken with an angle of ($\theta = 7^\circ$) for a 10 $\mu$m membrane.

The film stress is extracted from equation D.1 while Delta is calculated as follow (positive due to the Tensile strain):

$$\Delta = \Delta' \times (\frac{1}{\cos(90-\theta)}) = 0.28 \times \frac{1}{\cos(83)} = 4\mu m \tag{D.6}$$

Where $\Delta'$ is extracted from Figure D.5 with a value of ($\Delta'$= 0.28 $\mu$m), $\theta$ is the angle in which the SEM image is taken ($\theta$ = 7°), $t_{substrate}$ = 125 nm, $t_{film}$ = 25 nm and r = 0.8$\mu m$ (suspended part).

For Silicon,

$$\sigma = \frac{\Delta}{r^2} \times \frac{t_{substrate}^2}{t_{film}} \times 6.16 \times 10^{11} dynes/cm^2 \tag{D.7}$$

$$\sigma = \frac{40000}{(800)^2} \times \frac{125^2}{25} \times 6.16 \times 10^{11} = 24000 \times 10^8 dynes/cm^2 \tag{D.8}$$

$$\sigma = 24\ GPa = 24\ 000\ MPa \tag{D.9}$$

### D.3.3 Micro-Photoluminescence Spectroscopy

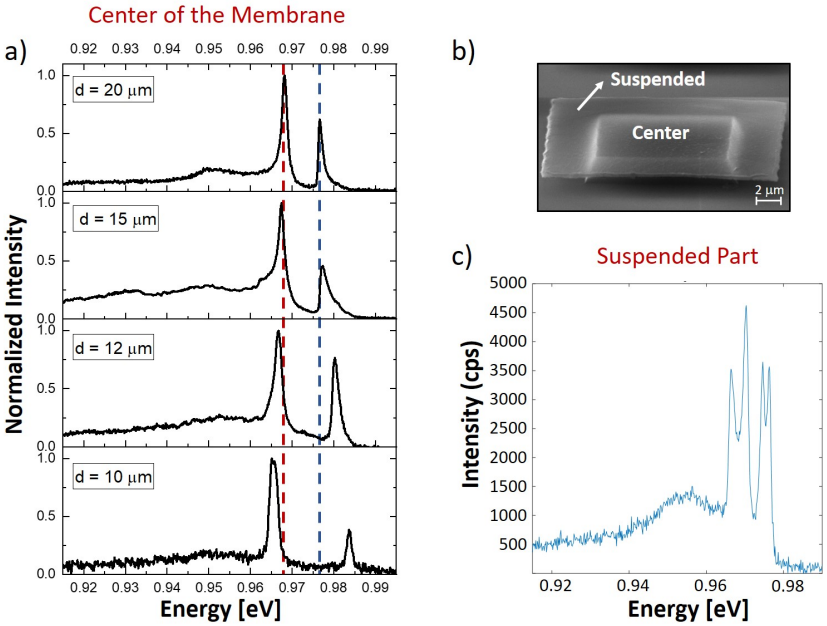


Figure D.6: a) and c) represent the PL spectrum recorded at the center and at the suspended part of the membrane. b) represent an SEM image for a 20 $\mu$m membrane, the image shows the center and the suspended part of the membrane in which the PL is carried out.

The samples are characterized by spatially-resolved photoluminescence (PL) spectroscopy with a home-made confocal microscope setup built in a closed-cycle He cryostat, as described in Appendix A. The data presented here are recorded at 10 K under CW laser at 532 nm excitation at a power of 2 mW. The pulsed laser used in time resolved experiment is at 850 nm.

We study membranes of different lateral size. Figure D.6 a) represents the PL spectrum recorded at the center of the membranes for different size (10, 12, 15 and 20 $\mu$m). While Figure c) show the PL spectrum on the suspended part of the membrane at its corner.

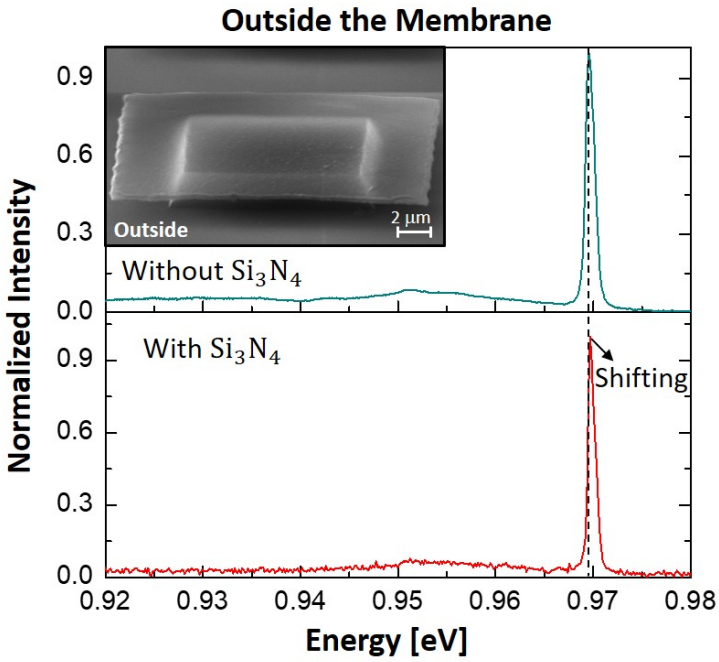


Figure D.7: represent the PL spectrum recorded in an area outside the membrane.

By measuring the PL outside a SOI membrane (125/2 $\mu$m) with deposited $Si_3N_4$ (70 nm) deposited atop we see only a very small shift of the ZPL peak with respect to a spectrum measured on a flat SOI samples without the deposition of the $Si_3N_4$ layer Figure D.7. This might be ascribed to the much larger value of $r^2$ that largely reduces the value of $\sigma$ and to the fact that the SOI is still bound to the underlying buried oxide (see Equation C1).

On the membranes, generally speaking, we observe a splitting of the ZPL G-center emission in two main peaks. This is consistent with uniaxial strain aligned along the in-plane 100 direction[236] (see later) and can be thus attributed to the strain applied by the $Si_3N_4$. The splitting is inversely proportional to the membrane extension, more the size of the membrane increases, the distance between the high and the low energy

will decrease as represent in Figure D.6 a).

In some cases in the suspended part of the membrane, we also observe a splitting in 4 peaks Figure D.6 c). This suggests that the strain in these parts is not uniaxial but includes some components in the 111 or 110 directions. In these cases in fact, 4 peaks appear [236] (see later).

### D.3.4 Time-resolved PL

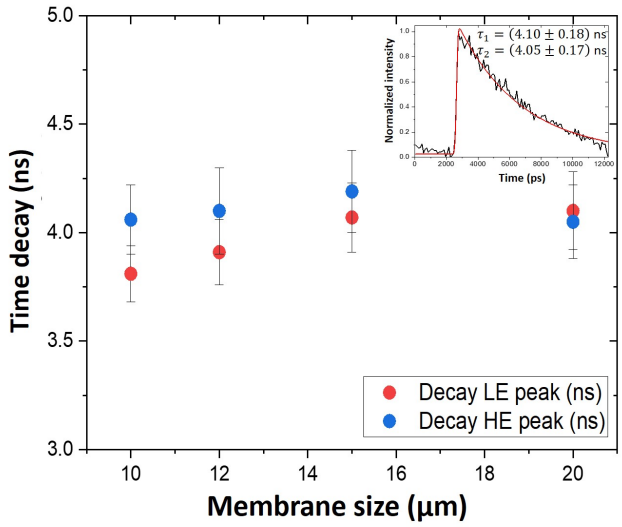


Figure D.8: Time-resolved PL decay recorded with a 200-fs pulse duration pulsed laser at 850 nm at the center of the membrane. Top right, represent the normalized intensity of the time-resolved PL as function of the time, the red line represents data fitting with a bi-exponential function

Figure D.8 represents the time-resolved PL decay recorded for low and high energy (LE, HE) PL components (as in Figure D.6) as function of the membrane size. The top right inset represents the normalized intensity of the time-resolved PL as function of time for low and high energy peaks ($\tau_1$,$\tau_2$ refer to the LE and HE peak respectively). The red line represents data fitting with a bi-exponential decay function. The lifetime of the two split components is, within the error bar, similar for the two components and is about 4 ns, with a small increasing trend with increasing membrane size.

## D.4 Comparison With The Literature

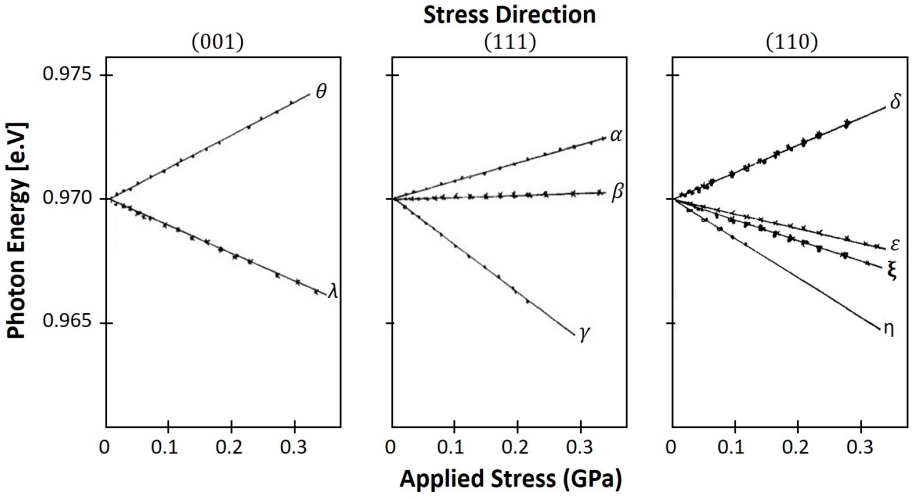


Figure D.9: Energies of the 0.97 eV line stress-split components under compression along (001), (111) and (110). Sample data are shown by crosses for $\pi$ polarization (electric vector parallel to the stress) and by circles for $\sigma$ polarisation (electric vector perpendicular to the stress). For (110) stress there are two inequivalent directions: open circles give $\sigma$ along $(11\bar{2})$ and full circles sigma along (111), The full curves have been calculated using the parameters derived from monoclinic I theory, [236]

Foy et al. [236] studied the effect of uniaxial stress on the 0.97 eV line in irradiated silicon samples. The samples were cut from ingots of Mullard silicon such that the long axis always corresponded with the required direction of stress ((001), (110) or (111)). Compressive stresses of up to 0.32 GPa were applied on the sample by an oil ram pressing on steel pistons.

The effects of uniaxial compressive stresses along the (001), (111) and (110) axes are shown in Figure D.9. In both absorption and luminescence the number of stress-split components seen in each polarisation was consistent with the centre being a $\pi$ oscillator (i.e. a (110) electric dipole) at a monoclinic I centre (Kaplyanskii 1964).

Foy et al. found a splitting of the ZPL spectrum into only two components [236] for stress along the 001 direction. When the stress is in 111 or 110 the number of split lines can be three or four. This suggests that in the corner of the membranes the stress cannot be considered uniaxial.

# Appendix E

# Digital Etching

## E.1 Experimental methods

With the digital etching experiment we progressively thinned by oxidation the top part of the implanted silicon on insulator (10 nm in each oxidation cycle at 750°C):

a) Compare the PL intensity with the implant profile.

b) Understand the role of defects at the interfaces and passivation via $SiO_2$.

c) Progressively reduce the number of defects to see the single emitter.

The temperature (750°C) is chosen based on the results of Werner et al [237], where the carbon diffusion profiles observed at temperatures above 800°C show highly non-regular behavior. The diffusion results are interpreted in terms of the kick-out mechanism.

The investigated wafer consists on a commercial SOI wafer, the resulting stack is made of a 125 nm Si layer separated from the substrate by 2 $\mu$m thick layer made of thermal silicon oxide.

Following the standard process for fabricating G-centers, when first the investigated sample received the carbon ions implantation's at (E=12 keV, Dose=$7.4\times10^{14}$ at/cm$^2$), and then the proton irradiation at (E=90 keV, Dose=$1\times10^{14}$ at/cm$^2$).

The digital etching process of each cycle Figure E.1 is carried out by thinning 10 nm SOI by rapid thermal oxidation (RTO) at 750° C in $O_2$ atmosphere for 1 hours and half in order to transform the top part of the SOI in $SiO_2$. By dipping the oxidized samples in a HF-solution at 5% in de-ionized water (95%) the top $SiO_2$ layer is removed thus exposing the remaining bottom SOI.

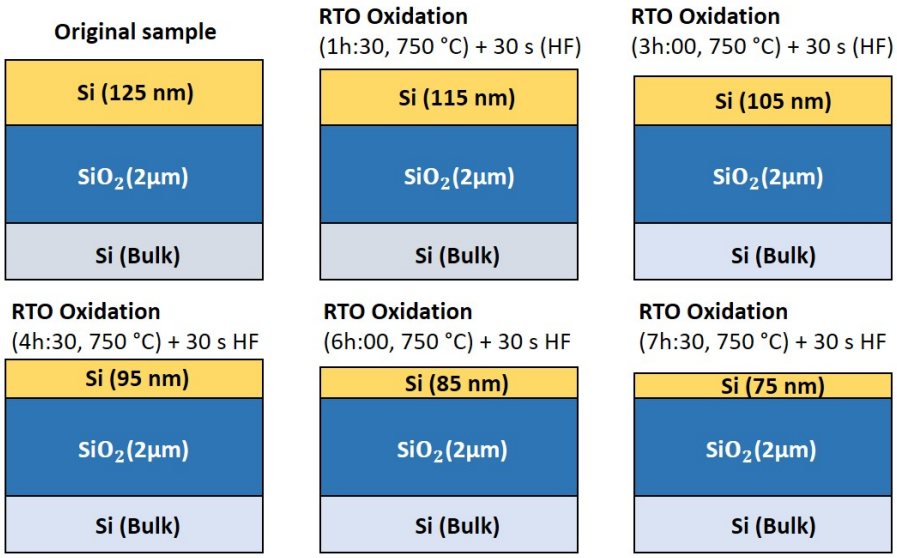


Figure E.1: method of fabrication

## E.2 Photoluminescence Spectroscopy

The samples are characterized by spatially-resolved photoluminescence (PL) spectroscopy in home-made confocal microscope setup (Mitutoyo 100x NIR Objective) built in a closed-cycle He cryostat, as described in chapter 2. The data presented here are recorded at 10K under CW532-nm excitation at a power of 2mW.

Figure E.2 represent the photoluminescence spectrum of each oxidized cycle. starting from the original sample, the first oxidized cycle (with and without the presence of the $SiO_2$), then the second, third, forth, and the fifth cycle.

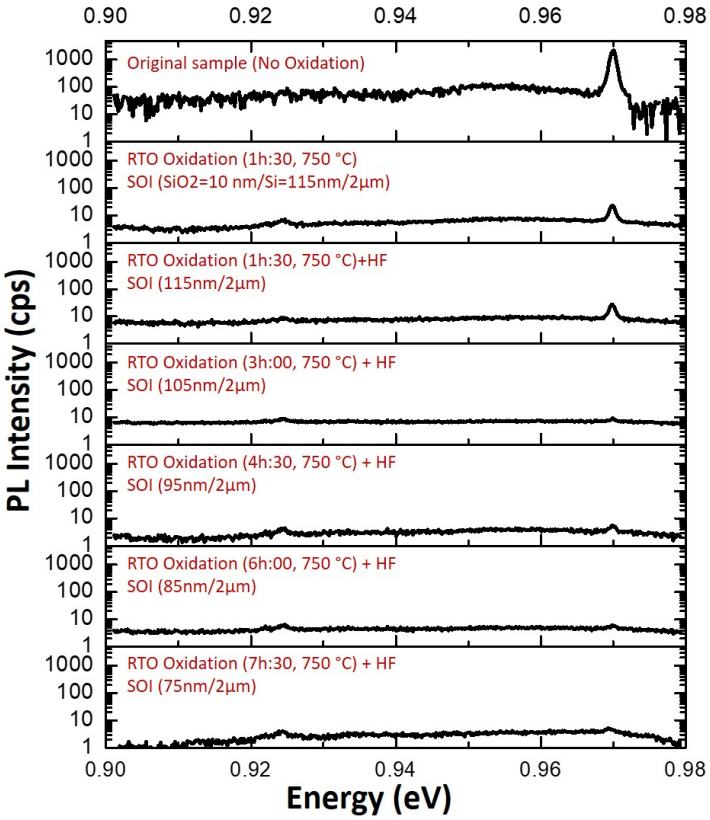


Figure E.2: Photoluminescence (PL) spectrum of each oxidized cycle

## E.3 Discussion

A signal was seen only from the original sample (not oxidized) while there is no signal from the oxidized samples. It seems that we killed the G center after the oxidation. The main reason is that we increase the surface roughness after each oxidation cycles Figure E.3, and this lead to create a non radiative centers where carrier can recombine rapidly.

Figure E.3 represent the roughness profile for the second and for the fifth oxidation cycle (case A and B).
For case A: the oxidation was performed at 750°C for 3h:00, and the average roughness is shown to be around 0.3681 nm which is extracted from the WSXM software.
For case B the oxidation was preformed at 750°C for 7h:30 min with an the roughness of about 3.1377 nm. This is proof that, after doing the oxidation we increase the roughness of the surface. While Figure E.4 show a trends, between the oxidized and not oxidized samples in which has been presented as a support information.

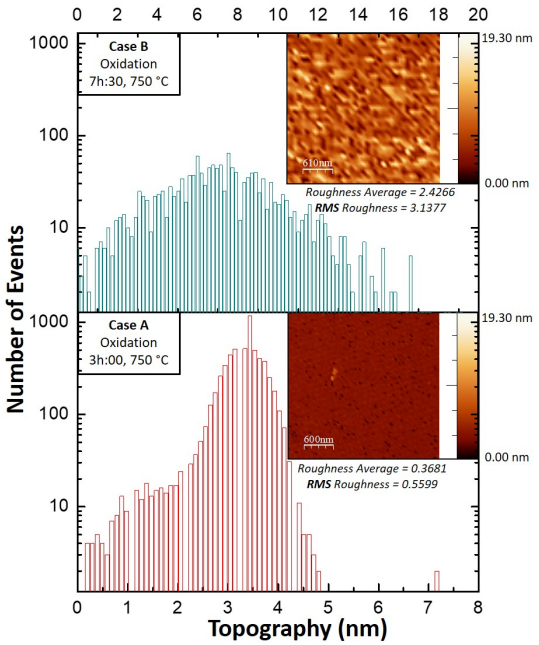


Figure E.3: atomic force microscope roughness profile for the second and for the fifth oxidation cycle (Case A and B).The inset on the top right shows a $3 \times 3$ $\mu$m$^2$ images of the surface for each case.

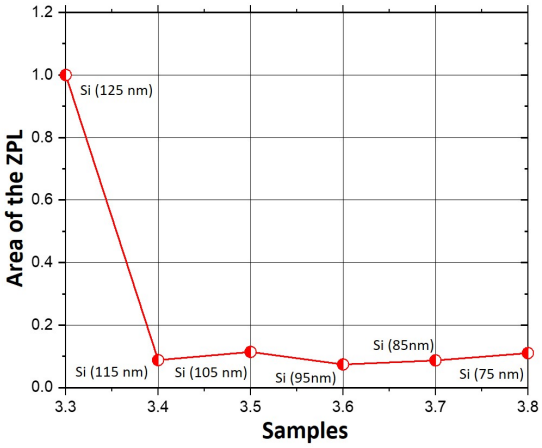


Figure E.4: Area of the Zero phonon line of each oxidized cycle

# Bibliography


[1] H. Rong, R. Jones, A. Liu, O. Cohen, D. Hak, A. Fang, and M. Paniccia, "A continuous-wave raman silicon laser," *Nature*, vol. 433, pp. 725–728, feb 2005.

[2] G. T. Reed, G. Mashanovich, F. Y. Gardes, and D. J. Thomson, "Silicon optical modulators," *Nature Photonics*, vol. 4, pp. 518–526, jul 2010.

[3] Y. Akahane, T. Asano, B.-S. Song, and S. Noda, "High-q photonic nanocavity in a two-dimensional photonic crystal," *Nature*, vol. 425, pp. 944–947, oct 2003.

[4] M. Notomi, A. Shinya, S. Mitsugi, G. Kira, E. Kuramochi, and T. Tanabe, "Optical bistable switching action of si high-q photonic-crystal nanocavities," *Optics Express*, vol. 13, no. 7, p. 2678, 2005.

[5] S. Matsuo, A. Shinya, C.-H. Chen, K. Nozaki, T. Sato, Y. Kawaguchi, H. Taniyama, and M. Notomi, "20-gbit/s directly modulated photonic crystal nanocavity laser with ultra-low power consumption," *Optics Express*, vol. 19, p. 2242, jan 2011.

[6] M. Fujita, S. Takahashi, Y. Tanaka, T. Asano, and S. Noda, "Simultaneous inhibition and redistribution of spontaneous light emission in photonic crystals," *Science*, vol. 308, pp. 1296–1298, may 2005.

[7] S. Ossicini, L. Pavesi, and F. Priolo, *Light emitting silicon for microphotonics*, vol. 194. Springer Science & Business Media, 2003.

[8] S. G. Cloutier, P. A. Kossyrev, and J. Xu, "Optical gain and stimulated emission in periodic nanopatterned crystalline silicon," *Nature materials*, vol. 4, no. 12, pp. 887–891, 2005.

[9] H. Wang, A. Chroneos, C. A. Londos, E. N. Sgourou, and U. Schwingenschlögl, "Carbon related defects in irradiated silicon revisited," *Scientific Reports*, vol. 4, may 2014.

[10] G. Davies, "The optical properties of luminescence centres in silicon," *Physics Reports*, vol. 176, pp. 83–188, may 1989.

[11] K. Thonke, H. Klemisch, J. Weber, and R. Sauer, "New model of the irradiation-induced 0.97-ev (g) line in silicon: A cs-si complex," *Physical Review B*, vol. 24, pp. 5874–5886, nov 1981.

[12] R. J. Spry and W. D. Compton, "Recombination luminescence in irradiated silicon," *Phys. Rev.*, vol. 175, pp. 1010–1020, Nov 1968.

[13] A. Kurkjian, *Confocal microscopy for T centres in silicon*. PhD thesis, Science: Department of Physics, 2020.

[14] Y. Baron, A. Durand, T. Herzig, M. Khoury, S. Pezzagna, J. Meijer, I. Robert-Philip, M. Abbarchi, J.-M. Hartmann, S. Reboh, J.-M. Gérard, V. Jacques, G. Cassabois, and A. Dréau, "Single g centers in silicon fabricated by co-implantation with carbon and proton," *arXiv*, 2022.

[15] M. S. Skolnick, A. G. Cullis, and H. Webber, "Defect photoluminescence from pulsed-laser-annealed ion-implanted si," *Applied Physics Letters*, vol. 38, pp. 464–466, mar 1981.

[16] F. Priolo, T. Gregorkiewicz, M. Galli, and T. F. Krauss, "Silicon nanostructures for photonics and photovoltaics," *Nature Nanotechnology*, vol. 9, pp. 19–32, jan 2014.

[17] D. D. Berhanuddin, M. A. Lourenço, R. M. Gwilliam, and K. P. Homewood, "Co-implantation of carbon and protons: An integrated silicon device technology compatible method to generate the lasing g-center," *Advanced Functional Materials*, vol. 22, pp. 2709–2712, apr 2012.

[18] A. Kavokin, J. J. Baumberg, G. Malpuech, and F. P. Laussy, "Microcavities," *Oxford University Press*, dec 2007.

[19] M. Naffouti, R. Backofen, M. Salvalaglio, T. Bottein, M. Lodari, A. Voigt, T. David, A. Benkouider, I. Fraj, L. Favre, *et al.*, "Complex dewetting scenarios of ultrathin silicon films for large-scale nanoarchitectures," *Science advances*, vol. 3, no. 11, p. eaao1472, 2017.

[20] M. Abbarchi, M. Naffouti, B. Vial, A. Benkouider, L. Lermusiaux, L. Favre, A. Ronda, S. Bidault, I. Berbezier, and N. Bonod, "Wafer scale formation of monocrystalline silicon-based mie resonators via silicon-on-insulator dewetting," *ACS nano*, vol. 8, no. 11, pp. 11181–11190, 2014.

[21] M. Langione, C. Tillemann-Dick, A. Kumar, V. Taneja, and https://www.bcg.com/publications/2019/quantum-computers-create-value when, "Where will quantum computers create value-and when?," *BCG*, vol. 1, no. 1, p. 1, 2019.

[22] M. Biondi, A. Heid, N. Henke, N. Mohr, L. Pautasso, I. Ostojic, L. Wester, and R. Zemmel, "https://www.mckinsey.com/business-functions/mckinsey-digital/our-insights/quantum-computing-use-cases-are-getting-real-what-you-need-to-know," *McKinsey Digital*, vol. 1, no. 1, p. 1, 1.

[23] A. Acín, I. Bloch, H. Buhrman, T. Calarco, C. Eichler, J. Eisert, D. Esteve, N. Gisin, S. J. Glaser, F. Jelezko, *et al.*, "The quantum technologies roadmap: a european community view," *New Journal of Physics*, vol. 20, no. 8, p. 080201, 2018.

[24] X. Xue, M. Russ, N. Samkharadze, B. Undseth, A. Sammak, G. Scappucci, and L. M. K. Vandersypen, "Quantum logic with spin qubits crossing the surface code threshold," *Nature*, vol. 601, pp. 343–347, jan 2022.

[25] A. Noiri, K. Takeda, T. Nakajima, T. Kobayashi, A. Sammak, G. Scappucci, and S. Tarucha, "Fast universal quantum gate above the fault-tolerance threshold in silicon," *Nature*, vol. 601, pp. 338–342, jan 2022.

[26] M. T. Mądzik, S. Asaad, A. Youssry, B. Joecker, K. M. Rudinger, E. Nielsen, K. C. Young, T. J. Proctor, A. D. Baczewski, A. Laucht, V. Schmitt, F. E. Hudson, K. M. Itoh, A. M. Jakob, B. C. Johnson, D. N. Jamieson, A. S. Dzurak, C. Ferrie, R. Blume-Kohout, and A. Morello, "Precision tomography of a three-qubit donor quantum processor in silicon," *Nature*, vol. 601, pp. 348–353, jan 2022.

[27] X. Xue, B. Patra, J. P. van Dijk, N. Samkharadze, S. Subramanian, A. Corna, B. Paquelet Wuetz, C. Jeon, F. Sheikh, E. Juarez-Hernandez, *et al.*, "Cmos-based cryogenic control of silicon quantum circuits," *Nature*, vol. 593, no. 7858, pp. 205–210, 2021.

[28] A. M. J. Zwerver, T. Krähenmann, T. F. Watson, L. Lampert, H. C. George, R. Pillarisetty, S. A. Bojarski, P. Amin, S. V. Amitonov, J. M. Boter, R. Caudillo, D. Correas-Serrano, J. P. Dehollain, G. Droulers, E. M. Henry, R. Kotlyar, M. Lodari, F. Lüthi, D. J. Michalak, B. K. Mueller, S. Neyens, J. Roberts, N. Samkharadze, G. Zheng, O. K. Zietz, G. Scappucci, M. Veldhorst, L. M. K. Vandersypen, and J. S. Clarke, "Qubits made by advanced semiconductor manufacturing," *Nature Electronics*, vol. 5, pp. 184–190, mar 2022.

[29] R. Stockill, C. Le Gall, C. Matthiesen, L. Huthmacher, E. Clarke, M. Hugues, and M. Atatüre, "Quantum dot spin coherence governed by a strained nuclear environment," *Nature communications*, vol. 7, no. 1, pp. 1–7, 2016.

[30] M. Gurioli, Z. Wang, A. Rastelli, T. Kuroda, and S. Sanguinetti, "Droplet epitaxy of semiconductor nanostructures for quantum photonic devices," *Nature materials*, vol. 18, no. 8, pp. 799–810, 2019.

[31] P. M. Koenraad and M. E. Flatté, "Single dopants in semiconductors," *Nature materials*, vol. 10, no. 2, pp. 91–100, 2011.

[32] Y.-C. Chen, P. S. Salter, M. Niethammer, M. Widmann, F. Kaiser, R. Nagy, N. Morioka, C. Babin, J. Erlekampf, P. Berwian, *et al.*, "Laser writing of scalable single color centers in silicon carbide," *Nano letters*, vol. 19, no. 4, pp. 2377–2383, 2019.

[33] Y.-C. Chen, B. Griffiths, L. Weng, S. S. Nicley, S. N. Ishmael, Y. Lekhai, S. Johnson, C. J. Stephen, B. L. Green, G. W. Morley, *et al.*, "Laser writing of individual nitrogen-vacancy defects in diamond with near-unity yield," *Optica*, vol. 6, no. 5, pp. 662–667, 2019.

[34] I. Aharonovich and E. Neu, "Diamond nanophotonics," *Advanced Optical Materials*, vol. 2, no. 10, pp. 911–928, 2014.

[35] J. Riedrich-Möller, L. Kipfstuhl, C. Hepp, E. Neu, C. Pauly, F. Mücklich, A. Baur, M. Wandt, S. Wolff, M. Fischer, *et al.*, "One-and two-dimensional photonic crystal microcavities in single crystal diamond," *Nature nanotechnology*, vol. 7, no. 1, p. 69, 2012.

[36] L. Li, T. Schröder, E. H. Chen, M. Walsh, I. Bayn, J. Goldstein, O. Gaathon, M. E. Trusheim, M. Lu, J. Mower, *et al.*, "Coherent spin control of a nanocavity-enhanced qubit in diamond," *Nature communications*, vol. 6, no. 1, pp. 1–7, 2015.

[37] G. Zhang, Y. Cheng, J.-P. Chou, and A. Gali, "Material platforms for defect qubits and single-photon emitters," *Applied Physics Reviews*, vol. 7, no. 3, p. 031308, 2020.

[38] M. Atatüre, D. Englund, N. Vamivakas, S.-Y. Lee, and J. Wrachtrup, "Material platforms for spin-based photonic quantum technologies," *Nature Reviews Materials*, vol. 3, no. 5, pp. 38–51, 2018.

[39] H. Seo, A. L. Falk, P. V. Klimov, K. C. Miao, G. Galli, and D. D. Awschalom, "Quantum decoherence dynamics of divacancy spins in silicon carbide," *Nature communications*, vol. 7, no. 1, pp. 1–9, 2016.

[40] A. Lohrmann, B. Johnson, J. McCallum, and S. Castelletto, "A review on single photon sources in silicon carbide," *Reports on Progress in Physics*, vol. 80, no. 3, p. 034502, 2017.

[41] C. Chartrand, L. Bergeron, K. Morse, H. Riemann, N. Abrosimov, P. Becker, H.-J. Pohl, S. Simmons, and M. Thewalt, "Highly enriched $^{28}$si reveals remarkable optical linewidths and fine structure for well-known damage centers," *Physical Review B*, vol. 98, no. 19, p. 195201, 2018.

[42] L. Bergeron, C. Chartrand, A. Kurkjian, K. Morse, H. Riemann, N. Abrosimov, P. Becker, H.-J. Pohl, M. Thewalt, and S. Simmons, "Characterization of the t center in $^{28}$si," *arXiv preprint arXiv:2006.08794*, 2020.

[43] L. Bergeron, C. Chartrand, A. Kurkjian, K. Morse, H. Riemann, N. Abrosimov, P. Becker, H.-J. Pohl, M. Thewalt, and S. Simmons, "Silicon-integrated telecommunications photon-spin interface," *Physical Review X Quantum*, vol. 1, no. 2, p. 020301, 2020.

[44] A. Kurkjian, D. Higginbottom, C. Chartrand, E. MacQuarrie, J. Klein, N. Lee-Hone, J. Stacho, C. Bowness, L. Bergeron, A. DeAbreu, *et al.*, "Optical observation of single spins in silicon," *arXiv preprint arXiv:2103.07580*, 2021.

[45] M. Garside and https://www.statista.com/topics/1959/silicon, "Silicon - statistics and facts," *Statista*, vol. 1, no. 1, p. 1, 2021.

[46] D. Thomas and J. Hopfield, "Isoelectronic traps due to nitrogen in gallium phosphide," *Physical Review*, vol. 150, no. 2, p. 680, 1966.

[47] M. R. Castell, D. A. Muller, and P. M. Voyles, "Dopant mapping for the nanotechnology age," *Nature Materials*, vol. 2, no. 3, pp. 129–131, 2003.

[48] N. Dotti, F. Sarti, S. Bietti, A. Azarov, A. Kuznetsov, F. Biccari, A. Vinattieri, S. Sanguinetti, M. Abbarchi, and M. Gurioli, "Germanium-based quantum emitters towards a time-reordering entanglement scheme with degenerate exciton and biexciton states," *Physical Review B*, vol. 91, no. 20, p. 205316, 2015.

[49] M. Hollenbach, Y. Berencén, U. Kentsch, M. Helm, and G. V. Astakhov, "Engineering telecom single-photon emitters in silicon for scalable quantum photonics," *Optics Express*, vol. 28, no. 18, pp. 26111–26121, 2020.

[50] M. Bruel and B. A. Auberton-Hervé, "Smart-cut: a new silicon on insulator material technology based on hydrogen implantation and wafer bonding," *Japanese journal of applied physics*, vol. 36, no. 3S, p. 1636, 1997.

[51] O. Kononchuk and B.-Y. Nguyen, *Silicon-on-insulator (SOI) technology: Manufacture and applications*. Elsevier, 2014.

[52] E. MacQuarrie, C. Chartrand, D. Higginbottom, K. Morse, V. Karasyuk, S. Roorda, and S. Simmons, "Generating t centres in photonic silicon-on-insulator material by ion implantation," *New Journal of Physics*, vol. 23, no. 10, p. 103008, 2021.

[53] F. Priolo, T. Gregorkiewicz, M. Galli, and T. F. Krauss, "Silicon nanostructures for photonics and photovoltaics," *Nature nanotechnology*, vol. 9, no. 1, pp. 19–32, 2014.

[54] L. Weiss, A. Gritsch, B. Merkel, and A. Reiserer, "Erbium dopants in nanophotonic silicon waveguides," *Optica*, vol. 8, no. 1, pp. 40–41, 2021.

[55] C. Beaufils, W. Redjem, E. Rousseau, V. Jacques, A. Y. Kuznetsov, C. Raynaud, C. Voisin, A. Benali, T. Herzig, S. Pezzagna, J. Meijer, M. Abbarchi, and G. Cassabois, "Optical properties of an ensemble of g-centers in silicon," *Physical Review B*, vol. 97, no. 3, p. 035303, 2018.

[56] P. Udvarhelyi, B. Somogyi, G. Thiering, and A. Gali, "Identification of a telecom wavelength single photon emitter in silicon," *Physical review letters*, vol. 127, no. 19, p. 196402, 2021.

[57] G. Davies, S. Hayama, L. Murin, R. Krause-Rehberg, V. Bondarenko, A. Sengupta, C. Davia, and A. Karpenko, "Radiation damage in silicon exposed to high-energy protons," *Physical Review B*, vol. 73, no. 16, p. 165202, 2006.

[58] G. Davies, A. Oates, R. Newman, R. Woolley, E. Lightowlers, M. Binns, and J. Wilkes, "Carbon-related radiation damage centres in czochralski silicon," *Journal of Physics C: Solid State Physics*, vol. 19, no. 6, p. 841, 1986.

[59] E. B. Davies and L. Parns, "Trapped modes in acoustic waveguides," *Q. J. Mech. Appl. Math.*, vol. 51, pp. 477–492, 1988.

[60] A. Bean, R. Newman, and R. Smith, "Electron irradiation damage in silicon containing carbon and oxygen," *Journal of Physics and Chemistry of Solids*, vol. 31, no. 4, pp. 739–751, 1970.

[61] K. O'donnell, K. Lee, and G. Watkins, "Origin of the 0.97 ev luminescence in irradiated silicon," *Physica B+ C*, vol. 116, no. 1-3, pp. 258–263, 1983.

[62] G. Davies, E. Lightowlers, and Z. E. Ciechanowska, "The 1018 mev vibronic band in silicon," *Journal of Physics C: Solid State Physics*, vol. 20, no. 2, p. 191, 1987.

[63] A. Safonov, E. Lightowlers, G. Davies, P. Leary, R. Jones, and S. Öberg, "Interstitial-carbon hydrogen interaction in silicon," *Physical review letters*, vol. 77, no. 23, p. 4812, 1996.

[64] D. Dhaliah, Y. Xiong, A. Sipahigil, S. M. Griffin, and G. Hautier, "First principles study of the t-center in silicon," *arXiv preprint arXiv:2202.04149*, 2022.

[65] L. Canham, K. Barraclough, and D. Robbins, "1.3-$\mu$m light-emitting diode from silicon electron irradiated at its damage threshold," *Applied physics letters*, vol. 51, no. 19, pp. 1509–1511, 1987.

[66] K. Murata, Y. Yasutake, K.-i. Nittoh, S. Fukatsu, and K. Miki, "High-density g-centers, light-emitting point defects in silicon crystal," *Aip Advances*, vol. 1, no. 3, p. 032125, 2011.

[67] W. Redjem, A. Durand, T. Herzig, A. Benali, S. Pezzagna, J. Meijer, A. Y. Kuznetsov, H. Nguyen, S. Cueff, J.-M. Gérard, *et al.*, "Single artificial atoms in silicon emitting at telecom wavelengths," *Nature Electronics*, vol. 3, no. 12, pp. 738–743, 2020.

[68] A. Durand, Y. Baron, W. Redjem, T. Herzig, A. Benali, S. Pezzagna, J. Meijer, A. Y. Kuznetsov, J.-M. Gérard, I. Robert-Philip, M. Abbarchi, V. Jacques, G. Cassabois, and A. Dreau, "Broad diversity of near-infrared single-photon emitters in silicon," *Physical Review Letters*, vol. 126, no. 8, p. 083602, 2021.

[69] M. Prabhu, C. Errando-Herranz, L. De Santis, I. Christen, C. Chen, and D. R. Englund, "Individually addressable artificial atoms in silicon photonics," *arXiv preprint arXiv:2202.02342*, 2022.

[70] Y. Baron, A. Durand, P. Udvarhelyi, T. Herzig, M. Khoury, S. Pezzagna, J. Meijer, I. Robert-Philip, M. Abbarchi, J.-M. Hartmann, *et al.*, "Detection of single w-centers in silicon," *arXiv preprint arXiv:2108.04283*, 2021.

[71] A. Ramdas and S. Rodriguez, "Spectroscopy of the solid-state analogues of the hydrogen atom: donors and acceptors in semiconductors," *Reports on Progress in Physics*, vol. 44, no. 12, p. 1297, 1981.

[72] G. Smit, S. Rogge, J. Caro, and T. Klapwijk, "Stark effect in shallow impurities in si," *Physical Review B*, vol. 70, no. 3, p. 035206, 2004.

[73] M. Abbarchi, F. Troiani, C. Mastrandrea, G. Goldoni, T. Kuroda, T. Mano, K. Sakoda, N. Koguchi, S. Sanguinetti, A. Vinattieri, *et al.*, "Spectral diffusion and line broadening in single self-assembled ga as/ al ga as quantum dot photoluminescence," *Applied physics letters*, vol. 93, no. 16, p. 162101, 2008.

[74] M. Abbarchi, T. Kuroda, T. Mano, M. Gurioli, and K. Sakoda, "Bunched photon statistics of the spectrally diffusive photoluminescence of single self-assembled gaas quantum dots," *Physical Review B*, vol. 86, no. 11, p. 115330, 2012.

[75] N. Ha, T. Mano, Y.-L. Chou, Y.-N. Wu, S.-J. Cheng, J. Bocquel, P. M. Koenraad, A. Ohtake, Y. Sakuma, K. Sakoda, *et al.*, "Size-dependent line broadening in the emission spectra of single gaas quantum dots: Impact of surface charge on spectral diffusion," *Physical Review B*, vol. 92, no. 7, p. 075306, 2015.

[76] F. Fávaro de Oliveira, D. Antonov, Y. Wang, P. Neumann, S. A. Momenzadeh, T. Häußermann, A. Pasquarelli, A. Denisenko, and J. Wrachtrup, "Tailoring spin defects in diamond by lattice charging," *Nature communications*, vol. 8, no. 1, pp. 1–8, 2017.

[77] M. Kasperczyk, J. A. Zuber, A. Barfuss, J. Kölbl, V. Yurgens, S. Flågan, T. Jakubczyk, B. Shields, R. J. Warburton, and P. Maletinsky, "Statistically modeling optical linewidths of nitrogen vacancy centers in microstructures," *Physical Review B*, vol. 102, no. 7, p. 075312, 2020.

[78] T. Ishikawa, K.-M. C. Fu, C. Santori, V. M. Acosta, R. G. Beausoleil, H. Watanabe, S. Shikata, and K. M. Itoh, "Optical and spin coherence properties of nitrogen-vacancy centers placed in a 100 nm thick isotopically purified diamond layer," *Nano Letters*, vol. 12, no. 4, pp. 2083–2087, 2012.

[79] A. L. Crook, C. P. Anderson, K. C. Miao, A. Bourassa, H. Lee, S. L. Bayliss, D. O. Bracher, X. Zhang, H. Abe, T. Ohshima, E. L. Hu, and D. D. Awschalom, "Purcell enhancement of a single silicon carbide color center with coherent spin control," *Nano Letters*, vol. 20, no. 5, pp. 3427–3434, 2020.

[80] D. D. Berhanuddin, M. A. Lourenço, R. M. Gwilliam, and K. P. Homewood, "Co-implantation of carbon and protons: An integrated silicon device technology compatible method to generate the lasing g-center," *Advanced Functional Materials*, vol. 22, no. 13, pp. 2709–2712, 2012.

[81] F. Leroy, Y. Saito, S. Curiotto, F. Cheynis, O. Pierre-Louis, and P. Müller, "Shape transition in nano-pits after solid-phase etching of $sio_2$ by si islands," *Applied Physics Letters*, vol. 106, no. 19, p. 191601, 2015.

[82] C. V. Thompson, "Solid-state dewetting of thin films," *Annual Review of Materials Research*, vol. 42, pp. 399–434, 2012.

[83] F. Leroy, F. Cheynis, Y. Almadori, S. Curiotto, M. Trautmann, J. Barbé, P. Müller, *et al.*, "How to control solid state dewetting: A short review," *Surface Science Reports*, vol. 71, no. 2, pp. 391–409, 2016.

[84] R. Proux, M. Maragkou, E. Baudin, C. Voisin, P. Roussignol, and C. Diederichs, "Measuring the photon coalescence time window in the continuous-wave regime for resonantly driven semiconductor quantum dots," *Physical Review Letters*, vol. 114, no. 6, p. 067401, 2015.

[85] H. S. Nguyen, G. Sallen, M. Abbarchi, R. Ferreira, C. Voisin, P. Roussignol, G. Cassabois, and C. Diederichs, "Photoneutralization and slow capture of carriers in quantum dots probed by resonant excitation spectroscopy," *Physical review B*, vol. 87, no. 11, p. 115305, 2013.

[86] D. Karaiskaj, M. Thewalt, T. Ruf, M. Cardona, H.-J. Pohl, G. Deviatych, P. Sennikov, and H. Riemann, "Photoluminescence of isotopically purified silicon: how sharp are bound exciton transitions?," *Physical Review Letters*, vol. 86, no. 26, p. 6010, 2001.

[87] M. Cardona and M. L. Thewalt, "Isotope effects on the optical spectra of semiconductors," *Reviews of modern physics*, vol. 77, no. 4, p. 1173, 2005.

[88] M. Steger, A. Yang, M. Thewalt, M. Cardona, H. Riemann, N. Abrosimov, M. Churbanov, A. Gusev, A. Bulanov, I. Kovalev, *et al.*, "High-resolution absorption spectroscopy of the deep impurities s and se in $^{28}$si revealing the $^{77}$se hyperfine splitting," *Physical Review B*, vol. 80, no. 11, p. 115204, 2009.

[89] M. Steger, K. Saeedi, M. Thewalt, J. Morton, H. Riemann, N. Abrosimov, P. Becker, and H.-J. Pohl, "Quantum information storage for over 180 s using donor spins in a $^{28}$si "semiconductor vacuum"," *Science*, vol. 336, no. 6086, pp. 1280–1283, 2012.

[90] K. Saeedi, S. Simmons, J. Z. Salvail, P. Dluhy, H. Riemann, N. V. Abrosimov, P. Becker, H.-J. Pohl, J. J. Morton, and M. L. Thewalt, "Room-temperature quantum bit storage exceeding 39 minutes using ionized donors in silicon-28," *Science*, vol. 342, no. 6160, pp. 830–833, 2013.

[91] K. J. Morse, R. J. Abraham, A. DeAbreu, C. Bowness, T. S. Richards, H. Riemann, N. V. Abrosimov, P. Becker, H.-J. Pohl, M. L. Thewalt, *et al.*, "A photonic platform for donor spin qubits in silicon," *Science advances*, vol. 3, no. 7, p. e1700930, 2017.

[92] T. Sekiguchi, M. Steger, K. Saeedi, M. L. W. Thewalt, H. Riemann, N. V. Abrosimov, and N. Nötzel, "Hyperfine structure and nuclear hyperpolarization observed in the bound exciton luminescence of bi donors in natural si," *Phys. Rev. Lett.*, vol. 104, p. 137402, Apr 2010.

[93] R. E. George, W. Witzel, H. Riemann, N. V. Abrosimov, N. Nötzel, M. L. W. Thewalt, and J. J. L. Morton, "Electron spin coherence and electron nuclear

double resonance of bi donors in natural si," *Phys. Rev. Lett.*, vol. 105, p. 067601, Aug 2010.

[94] D. Basov, R. Averitt, and D. Hsieh, "Towards properties on demand in quantum materials," *Nature materials*, vol. 16, no. 11, pp. 1077–1088, 2017.

[95] B. Keimer and J. Moore, "The physics of quantum materials," *Nature Physics*, vol. 13, no. 11, pp. 1045–1055, 2017.

[96] C. C. Lo, A. Persaud, S. Dhuey, D. Olynick, F. Borondics, M. C. Martin, H. A. Bechtel, J. Bokor, and T. Schenkel, "Device fabrication and transport measurements of finfets built with $^{28}$si soi wafers toward donor qubits in silicon," *Semiconductor science and technology*, vol. 24, no. 10, p. 105022, 2009.

[97] K. M. Itoh and H. Watanabe, "Isotope engineering of silicon and diamond for quantum computing and sensing applications," *MRS communications*, vol. 4, no. 4, pp. 143–157, 2014.

[98] P. Becker, D. Schiel, H. Pohl, A. Kaliteevski, O. Godisov, M. Churbanov, G. Devyatykh, A. Gusev, A. Bulanov, S. Adamchik, *et al.*, "Large-scale production of highly enriched $^{28}$si for the precise determination of the avogadro constant," *Measurement Science and Technology*, vol. 17, no. 7, p. 1854, 2006.

[99] R. Maurand, X. Jehl, D. Kotekar-Patil, A. Corna, H. Bohuslavskyi, R. Laviéville, L. Hutin, S. Barraud, M. Vinet, M. Sanquer, *et al.*, "A cmos silicon spin qubit," *Nature communications*, vol. 7, no. 1, pp. 1–6, 2016.

[100] V. Mazzocchi, P. Sennikov, A. Bulanov, M. Churbanov, B. Bertrand, L. Hutin, J. Barnes, M. Drozdov, J. Hartmann, and M. Sanquer, "99.992% $^{28}$si cvd-grown epilayer on 300 mm substrates for large scale integration of silicon spin qubits," *Journal of Crystal Growth*, vol. 509, pp. 1–7, 2019.

[101] G. Grossmann, K. Bergman, and M. Kleverman, "Spectroscopic studies of double donors in silicon," *Physica B+ C*, vol. 146, no. 1-2, pp. 30–46, 1987.

[102] C. P. Foy, M. C. do Carmo, G. Davies, and E. C. Lightowlers, "Uniaxial stress measurements on the 0.97 eV line in irradiated silicon," *Journal of Physics C: Solid State Physics*, vol. 14, pp. L7–L12, jan 1981.

[103] I. Buyanova, A. Henry, B. Monemar, J. Lindström, and G. Oehrlein, "Photoluminescence of defects induced in silicon by sf6/o2 reactive-ion etching," *Journal of applied physics*, vol. 78, no. 5, pp. 3348–3352, 1995.

[104] S. Lindner, A. Bommer, A. Muzha, A. Krueger, L. Gines, S. Mandal, O. Williams, E. Londero, A. Gali, and C. Becher, "Strongly inhomogeneous distribution of spectral properties of silicon-vacancy color centers in nanodiamonds," *New Journal of Physics*, vol. 20, no. 11, p. 115002, 2018.

[105] S. Li, J.-P. Chou, A. Hu, M. B. Plenio, P. Udvarhelyi, G. Thiering, M. Abdi, and A. Gali, "Giant shift upon strain on the fluorescence spectrum of vnnb color centers in h-bn," *npj Quantum Information*, vol. 6, no. 1, pp. 1–7, 2020.

[106] J. Q. Grim, A. S. Bracker, M. Zalalutdinov, S. G. Carter, A. C. Kozen, M. Kim, C. S. Kim, J. T. Mlack, M. Yakes, B. Lee, *et al.*, "Scalable in operando strain tuning in nanophotonic waveguides enabling three-quantum-dot superradiance," *Nature materials*, vol. 18, no. 9, pp. 963–969, 2019.

[107] J. Meijer, S. Pezzagna, T. Vogel, B. Burchard, H. Bukow, I. Rangelow, Y. Sarov, H. Wiggers, I. Plümel, F. Jelezko, *et al.*, "Towards the implanting of ions and positioning of nanoparticles with nm spatial resolution," *Applied Physics A*, vol. 91, no. 4, pp. 567–571, 2008.

[108] N. Raatz, C. Scheuner, S. Pezzagna, and J. Meijer, "Investigation of ion channeling and scattering for single-ion implantation with high spatial resolution," *physica status solidi (a)*, vol. 216, no. 21, p. 1900528, 2019.

[109] T. Jung, J. Görlitz, B. Kambs, C. Pauly, N. Raatz, R. Nelz, E. Neu, A. M. Edmonds, M. Markham, F. Mücklich, *et al.*, "Spin measurements of nv centers coupled to a photonic crystal cavity," *APL Photonics*, vol. 4, no. 12, p. 120803, 2019.

[110] S. Tamura, G. Koike, A. Komatsubara, T. Teraji, S. Onoda, L. P. McGuinness, L. Rogers, B. Naydenov, E. Wu, L. Yan, *et al.*, "Array of bright silicon-vacancy centers in diamond fabricated by low-energy focused ion beam implantation," *Applied Physics Express*, vol. 7, no. 11, p. 115201, 2014.

[111] T. Lühmann, N. Raatz, R. John, M. Lesik, J. Rödiger, M. Portail, D. Wildanger, F. Kleißler, K. Nordlund, A. Zaitsev, *et al.*, "Screening and engineering of colour centres in diamond," *Journal of Physics D: Applied Physics*, vol. 51, no. 48, p. 483002, 2018.

[112] J. Riedrich-Möller, S. Pezzagna, J. Meijer, C. Pauly, F. Mücklich, M. Markham, A. M. Edmonds, and C. Becher, "Nanoimplantation and purcell enhancement of single nitrogen-vacancy centers in photonic crystal cavities in diamond," *Applied Physics Letters*, vol. 106, no. 22, p. 221103, 2015.

[113] T. Schröder, M. E. Trusheim, M. Walsh, L. Li, J. Zheng, M. Schukraft, A. Sipahigil, R. E. Evans, D. D. Sukachev, C. T. Nguyen, *et al.*, "Scalable focused ion beam creation of nearly lifetime-limited single quantum emitters in diamond nanostructures," *Nature communications*, vol. 8, no. 1, pp. 1–7, 2017.

[114] T. Schenkel, A. Persaud, S. Park, J. Nilsson, J. Bokor, J. Liddle, R. Keller, D. Schneider, D. Cheng, and D. Humphries, "Solid state quantum computer development in silicon with single ion implantation," *Journal of Applied Physics*, vol. 94, no. 11, pp. 7017–7024, 2003.

[115] A. M. Jakob, S. G. Robson, V. Schmitt, V. Mourik, M. Posselt, D. Spemann, B. C. Johnson, H. R. Firgau, E. Mayes, J. C. McCallum, *et al.*, "Deterministic shallow dopant implantation in silicon with detection confidence upper-bound to 99.85% by ion–solid interactions," *Advanced Materials*, vol. 34, no. 3, p. 2103235, 2022.

[116] K. Groot-Berning, T. Kornher, G. Jacob, F. Stopp, S. T. Dawkins, R. Kolesov, J. Wrachtrup, K. Singer, and F. Schmidt-Kaler, "Deterministic single-ion implantation of rare-earth ions for nanometer-resolution color-center generation," *Physical Review Letters*, vol. 123, no. 10, p. 106802, 2019.

[117] A. W. Elshaari, W. Pernice, K. Srinivasan, O. Benson, and V. Zwiller, "Hybrid integrated quantum photonic circuits," *Nature photonics*, vol. 14, no. 5, pp. 285–298, 2020.

[118] J. Fait, S. Putz, G. Wachter, J. Schalko, U. Schmid, M. Arndt, and M. Trupke, "High finesse microcavities in the optical telecom o-band," *Applied Physics Letters*, vol. 119, no. 22, p. 221112, 2021.

[119] "B. lefaucher, j. b. jager and j. m. gerard, private communication," 2021.

[120] L. Zhu, S. Yuan, C. Zeng, and J. Xia, "Manipulating photoluminescence of carbon g-center in silicon metasurface with optical bound states in the continuum," *Advanced Optical Materials*, vol. 8, no. 8, p. 1901830, 2020.

[121] C. Schuck, X. Guo, L. Fan, X. Ma, M. Poot, and H. X. Tang, "Quantum interference in heterogeneous superconducting-photonic circuits on a silicon chip," *Nature communications*, vol. 7, no. 1, pp. 1–7, 2016.

[122] J. Sprengers, A. Gaggero, D. Sahin, S. Jahanmirinejad, G. Frucci, F. Mattioli, R. Leoni, J. Beetz, M. Lermer, M. Kamp, *et al.*, "Waveguide superconducting single-photon detectors for integrated quantum photonic circuits," *Applied Physics Letters*, vol. 99, no. 18, p. 181110, 2011.

[123] W. Redjem, A. Durand, T. Herzig, A. Benali, S. Pezzagna, J. Meijer, A. Y. Kuznetsov, H. S. Nguyen, S. Cueff, J.-M. Gérard, I. Robert-Philip, B. Gil, D. Caliste, P. Pochet, M. Abbarchi, V. Jacques, A. Dréau, and G. Cassabois, "Single artificial atoms in silicon emitting at telecom wavelengths," *Nature Electronics*, vol. 3, pp. 738–743, nov 2020.

[124] A. Beveratos, S. Kühn, R. Brouri, T. Gacoin, J.-P. Poizat, and P. Grangier, "Room temperature stable single-photon source," *The European Physical Journal D - Atomic, Molecular and Optical Physics*, vol. 18, pp. 191–196, feb 2002.

[125] G. Davies, E. C. Lightowlers, and Z. E. Ciechanowska, "The 1018 mev (w or i1) vibronic band in silicon," *Journal of Physics C: Solid State Physics*, vol. 20, pp. 191–205, jan 1987.

[126] S. Hayama, G. Davies, and K. M. Itoh, "Photoluminescence studies of implantation damage centers in si30," *Journal of Applied Physics*, vol. 96, pp. 1754–1756, aug 2004.

[127] C. Lethiec, J. Laverdant, H. Vallon, C. Javaux, B. Dubertret, J.-M. Frigerio, C. Schwob, L. Coolen, and A. Maître, "Three-dimensional orientation measurement of a single fluorescent nanoemitter by polarization analysis," *arXiv*, 2013.

[128] R. Acharya, "Interaction of waves with medium," *Elsevier*, pp. 57–86, 2017.

[129] G. Mie, "Beiträge zur optik trüber medien, speziell kolloidaler metallösungen," *Annalen der Physik*, vol. 330, no. 3, pp. 377–445, 1908.

[130] C. F. Bohren and D. R. Huffman, "Absorption and scattering of light by small particles," *Wiley*, apr 1998.

[131] A. García-Etxarri, R. Gómez-Medina, L. S. Froufe-Pérez, C. López, L. Chantada, F. Scheffold, J. Aizpurua, M. Nieto-Vesperinas, and J. J. Sáenz, "Strong magnetic response of submicron silicon particles in the infrared," *Opt. Express*, vol. 19, pp. 4815–4826, Mar 2011.

[132] A. I. Kuznetsov, A. E. Miroshnichenko, Y. H. Fu, J. Zhang, and B. Luk'yanchuk, "Magnetic light," *Scientific Reports*, vol. 2, jul 2012.

[133] M. Kerker, D.-S. Wang, and C. L. Giles, "Electromagnetic scattering by magnetic spheres," *J. Opt. Soc. Am.*, vol. 73, pp. 765–767, Jun 1983.

[134] N. Bonod and Y. Kivshar, "All-dielectric mie-resonant metaphotonics," *Comptes Rendus. Physique*, vol. 21, pp. 425–442, dec 2020.

[135] P. Albella, R. A. D. L. Osa, F. Moreno, and S. A. Maier, "Electric and magnetic field enhancement with ultralow heat radiation dielectric nanoantennas: Considerations for surface-enhanced spectroscopies," *ACS Photonics*, vol. 1, 2014.

[136] Y. H. Fu, A. I. Kuznetsov, A. E. Miroshnichenko, Y. F. Yu, and B. Luk'yanchuk, "Directional visible light scattering by silicon nanoparticles," *Nature Communications*, vol. 4, feb 2013.

[137] S. Person, M. Jain, Z. Lapin, J. J. Sáenz, G. Wicks, and L. Novotny, "Demonstration of zero optical backscattering from single nanoparticles," *Nano Letters*, vol. 13, pp. 1806–1809, mar 2013.

[138] J. van de Groep and A. Polman, "Designing dielectric resonators on substrates: Combining magnetic and electric resonances," *Optics Express*, vol. 21, p. 26285, oct 2013.

[139] P. Spinelli, M. Verschuuren, and A. Polman, "Broadband omnidirectional antireflection coating based on subwavelength surface mie resonators," *Nature Communications*, vol. 3, jan 2012.

[140] P. Spinelli, B. Macco, M. A. Verschuuren, W. M. M. Kessels, and A. Polman, "Al2o3/tio2 nano-pattern antireflection coating with ultralow surface recombination," *Applied Physics Letters*, vol. 102, p. 233902, jun 2013.

[141] M. Garín, R. Fenollosa, R. Alcubilla, L. Shi, L. F. Marsal, and F. Meseguer, "All-silicon spherical-mie-resonator photodiode with spectral response in the infrared region," *Nature Communications*, vol. 5, mar 2014.

[142] J. Proust, F. Bedu, S. Chenot, I. Soumahoro, I. Ozerov, B. Gallas, R. Abdeddaim, and N. Bonod, "Chemical alkaline etching of silicon mie particles," *Advanced Optical Materials*, vol. 3, pp. 1280–1286, may 2015.

[143] K. E. Chong, B. Hopkins, I. Staude, A. E. Miroshnichenko, J. Dominguez, M. Decker, D. N. Neshev, I. Brener, and Y. S. Kivshar, "Observation of fano resonances in all-dielectric nanoparticle oligomers," *Small*, vol. 10, pp. 1985–1990, feb 2014.

[144] T. Coenen, J. van de Groep, and A. Polman, "Resonant modes of single silicon nanocavities excited by electron irradiation," *ACS Nano*, vol. 7, pp. 1689–1698, jan 2013.

[145] A. B. Evlyukhin, S. M. Novikov, U. Zywietz, R. L. Eriksen, C. Reinhardt, S. I. Bozhevolnyi, and B. N. Chichkov, "Demonstration of magnetic dipole resonances of dielectric nanospheres in the visible region," *Nano Letters*, vol. 12, pp. 3749–3755, jun 2012.

[146] D. J. Srolovitz and M. G. Goldiner, "The thermodynamics and kinetics of film agglomeration," *JOM*, vol. 47, pp. 31–36, mar 1995.

[147] J. W. Drelich, L. Boinovich, E. Chibowski, C. D. Volpe, L. Hołysz, A. Marmur, and S. Siboni, "Contact angles: history of over 200 years of open questions," *Surface Innovations*, vol. 8, pp. 3–27, feb 2020.

[148] A. Sharma and E. Ruckenstein, "Dewetting of solids by the formation of holes in macroscopic liquid films," *Journal of Colloid and Interface Science*, vol. 133, pp. 358–368, dec 1989.

[149] R. V. Zucker, *Capillary-driven shape evolution in solid-state micro-and nanoscale systems*. PhD thesis, Massachusetts Institute of Technology, 2015.

[150] L. Vitos, A. Ruban, H. L. Skriver, and J. Kollár, "The surface energy of metals," *Surface science*, vol. 411, no. 1-2, pp. 186–202, 1998.

[151] W. W. Mullins, "Theory of thermal grooving," *Journal of Applied Physics*, vol. 28, pp. 333–339, mar 1957.

[152] W. Zhang and I. Gladwell, "Evolution of two-dimensional crystal morphologies by surface diffusion with anisotropic surface free energies," *Computational Materials Science*, vol. 27, pp. 461–470, jun 2003.

[153] W. Carter, A. Roosen, J. Cahn, and J. Taylor, "Shape evolution by surface diffusion and surface attachment limited kinetics on completely faceted surfaces," *Acta Metallurgica et Materialia*, vol. 43, pp. 4309–4323, dec 1995.

[154] D. T. Danielson, D. K. Sparacin, J. Michel, and L. C. Kimerling, "Surface-energy-driven dewetting theory of silicon-on-insulator agglomeration," *Journal of Applied Physics*, vol. 100, p. 083507, oct 2006.

[155] E. Jiran and C. V. Thompson, "Capillary instabilities in thin films," *Journal of Electronic Materials*, vol. 19, pp. 1153–1160, nov 1990.

[156] M. Aouassa, L. Favre, A. Ronda, H. Maaref, and I. Berbezier, "The kinetics of dewetting ultra-thin si layers from silicon dioxide," *New Journal of Physics*, vol. 14, p. 063038, jun 2012.

[157] M. Abbarchi, M. Naffouti, B. Vial, A. Benkouider, L. Lermusiaux, L. Favre, A. Ronda, S. Bidault, I. Berbezier, and N. Bonod, "Wafer scale formation of monocrystalline silicon-based mie resonators via silicon-on-insulator dewetting," *ACS Nano*, vol. 8, pp. 11181–11190, nov 2014.

[158] T. Wood, M. Naffouti, J. Berthelot, T. David, J.-B. Claude, L. Métayer, A. Delobbe, L. Favre, A. Ronda, I. Berbezier, N. Bonod, and M. Abbarchi, "All-dielectric color filters using SiGe-based mie resonator arrays," *ACS Photonics*, vol. 4, pp. 873–883, mar 2017.

[159] M. Naffouti, T. David, A. Benkouider, L. Favre, A. Ronda, I. Berbezier, S. Bidault, N. Bonod, and M. Abbarchi, "Fabrication of poly-crystalline si-based mie resonators via amorphous si on sio2 dewetting," *Nanoscale*, vol. 8, no. 14, pp. 7768–7768, 2016.

[160] M. Bollani, M. Salvalaglio, A. Benali, M. Bouabdellaoui, M. Naffouti, M. Lodari, S. D. Corato, A. Fedorov, A. Voigt, I. Fraj, L. Favre, J. B. Claude, D. Grosso, G. Nicotra, A. Mio, A. Ronda, I. Berbezier, and M. Abbarchi, "Templated dewetting of single-crystal sub-millimeter-long nanowires and on-chip silicon circuits," *Nature Communications*, vol. 10, dec 2019.

[161] D. J. Srolovitz and S. A. Safran, "Capillary instabilities in thin films. i. energetics," *Journal of Applied Physics*, vol. 60, pp. 247–254, jul 1986.

[162] M. K. Santala and A. M. Glaeser, "Rayleigh instabilities in crystalline solids: Evolution of finite-aspect-ratio pore channels in sapphire," *Acta Materialia*, vol. 56, pp. 1967–1980, may 2008.

[163] T. Liu, R. Xu, P. Yu, Z. Wang, and J. Takahara, "Multipole and multimode engineering in mie resonance-based metastructures," *Nanophotonics*, vol. 9, pp. 1115–1137, mar 2020.

[164] Y. Yang, I. I. Kravchenko, D. P. Briggs, and J. Valentine, "All-dielectric metasurface analogue of electromagnetically induced transparency," *Nature Communications*, vol. 5, dec 2014.

[165] A. Cordaro, J. van de Groep, S. Raza, E. F. Pecora, F. Priolo, and M. L. Brongersma, "Antireflection high-index metasurfaces combining mie and fabry-pérot resonances," *ACS Photonics*, vol. 6, pp. 453–459, jan 2019.

[166] C. V. Thompson, "Solid-state dewetting of thin films," *Annual Review of Materials Research*, vol. 42, pp. 399–434, aug 2012.

[167] M. Aouassa, I. Berbezier, L. Favre, A. Ronda, M. Bollani, R. Sordan, A. Delobbe, and P. Sudraud, "Design of free patterns of nanocrystals with ad hoc features via templated dewetting," *Applied Physics Letters*, vol. 101, p. 013117, jul 2012.

[168] I. Berbezier, M. Aouassa, A. Ronda, L. Favre, M. Bollani, R. Sordan, A. Delobbe, and P. Sudraud, "Ordered arrays of si and ge nanocrystals via dewetting of pre-patterned thin films," *Journal of Applied Physics*, vol. 113, p. 064908, feb 2013.

[169] M. Naffouti, T. David, A. Benkouider, L. Favre, A. Delobbe, A. Ronda, I. Berbezier, and M. Abbarchi, "Templated solid-state dewetting of thin silicon films," *Small*, vol. 12, pp. 6115–6123, sep 2016.

[170] F. Leroy, T. Passanante, F. Cheynis, S. Curiotto, E. Bussmann, and P. Müller, "Catalytically enhanced thermal decomposition of chemically grown silicon oxide layers on si (001)," *Applied Physics Letters*, vol. 108, p. 111601, 2016.

[171] M. Trautmann, F. Cheynis, F. Leroy, S. Curiotto, and P. Müller, "Interplay between deoxidation and dewetting for ultrathin soi films," *Applied Physics Letters*, vol. 110, p. 161601, 2017.

[172] V. Flauraud, M. Reyes, R. Paniagua-Dominguez, A. I. Kuznetsov, and J. Brugger, "Silicon nanostructures for bright field full color prints," *Acs Photonics*, vol. 4, pp. 1913–1919, 2017.

[173] W. Chaabani, J. Proust, A. Movsesyan, J. Beal, A.-L. Baudrion, P.-M. Adam, A. Chehaidar, and J. Plain, "Large-scale and low-cost fabrication of silicon mie resonators," *ACS nano*, vol. 13, pp. 4199–4208, 2019.

[174] A. Benali, J.-B. Claude, N. Granchi, S. Checcucci, M. Bouabdellaoui, M. Zazoui, M. Bollani, M. Salvalaglio, J. Wenger, and L. Favre, "Flexible photonic devices based on dielectric antennas," *Journal of Physics: Photonics*, vol. 2, p. 015002, 2020.

[175] D. Pellegrino, D. Balestri, N. Granchi, M. Ciardi, F. Intonti, F. Pagliano, A. Y. Silov, F. W. Otten, T. Wu, K. Vynck, P. Lalanne, A. Fiore, and M. Gurioli, "Nonlorentzian local density of states in coupled photonic crystal cavities probed by near- and far-field emission," *Physical Review Letters*, vol. 124, p. 123902, mar 2020.

[176] M. Bouabdellaoui, S. Checcucci, T. Wood, M. Naffouti, R. P. Sena, K. Liu, C. M. Ruiz, D. Duche, J. L. Rouzo, and L. Escoubas, "Self-assembled antireflection coatings for light trapping based on sige random metasurfaces," *Phys. Rev. Materials*, vol. 2, p. 035203, 2018.

[177] J. Pond and M. Kawano, "Virtual prototyping and optimization of novel solar cell designs," *SPIE*, jun 2010.

[178] E. D. Palik, *Handbook of optical constants of solids*, vol. 3. Academic press, 1998.

[179] N. A. Butakov and J. A. Schuller, "Designing multipolar resonances in dielectric metamaterials," *Scientific Reports*, vol. 6, dec 2016.

[180] J. Berzinš, S. Indrišiūnas, K. van Erve, A. Nagarajan, S. Fasold, M. Steinert, G. Gerini, P. Gečys, T. Pertsch, S. M. B. Bäumer, and F. Setzpfandt, "Direct and high-throughput fabrication of mie-resonant metasurfaces via single-pulse laser interference," *ACS Nano*, vol. 14, pp. 6138–6149, apr 2020.

[181] D. Toliopoulos, M. Khoury, M. Bouabdellaoui, N. Granchi, J.-B. Claude, A. Benali, I. Berbezier, D. Hannani, A. Ronda, J. Wenger, M. Bollani, M. Gurioli, S. Sanguinetti, F. Intonti, and M. Abbarchi, "Fabrication of spectrally sharp si-based dielectric resonators: combining etaloning with mie resonances," *Optics Express*, vol. 28, p. 37734, dec 2020.

[182] T. G. Habteyes, I. Staude, K. E. Chong, J. Dominguez, M. Decker, A. Miroshnichenko, Y. Kivshar, and I. Brener, "Near-field mapping of optical modes on all-dielectric silicon nanodisks," *ACS Photonics*, vol. 1, pp. 794–798, aug 2014.

[183] M. Naffouti, M. Salvalaglio, T. David, J.-B. Claude, M. Bollani, A. Voigt, A. Benkouider, L. Favre, A. Ronda, and I. Berbezier, "Deterministic three-dimensional self-assembly of si through a rimless and topology-preserving dewetting regime," *Physical Review Materials*, vol. 3, p. 103402, 2019.

[184] M. Salvalaglio, M. Bouabdellaoui, M. Bollani, A. Benali, L. Favre, J.-B. Claude, J. Wenger, P. de Anna, F. Intonti, and A. Voigt, "Hyperuniform monocrystalline structures by spinodal solid-state dewetting," *Physical Review Letters*, vol. 125, p. 126101, 2020.

[185] P. Dong, Y.-K. Chen, G.-H. Duan, and D. T. Neilson, "Silicon photonic devices and integrated circuits," *Nanophotonics*, vol. 3, pp. 215–228, aug 2014.

[186] S. Bernabé, Q. Wilmart, K. Hasharoni, K. Hassan, Y. Thonnart, P. Tissier, Y. Désières, S. Olivier, T. Tekin, and B. Szelag, "Silicon photonics for terabit/s communication in data centers and exascale computers," *Solid-State Electronics*, vol. 179, p. 107928, may 2021.

[187] A. I. Kuznetsov, A. E. Miroshnichenko, M. L. Brongersma, Y. S. Kivshar, and B. Luk'yanchuk, "Optically resonant dielectric nanostructures," *Science*, vol. 354, nov 2016.

[188] B. Sain, C. Meier, and T. Zentgraf, "Nonlinear optics in all-dielectric nanoantennas and metasurfaces: a review," *Advanced Photonics*, vol. 1, p. 1, apr 2019.

[189] J. Liu, , M. Shi, Z. Chen, S. Wang, Z. Wang, and S. Zhu, "Quantum photonics based on metasurfaces," *Opto-Electronic Advances*, vol. 4, no. 9, pp. 200092–200092, 2021.

[190] S. Bidault, M. Mivelle, and N. Bonod, "Dielectric nanoantennas to manipulate solid-state light emission," *Journal of Applied Physics*, vol. 126, p. 094104, sep 2019.

[191] I. Staude, V. V. Khardikov, N. T. Fofang, S. Liu, M. Decker, D. N. Neshev, T. S. Luk, I. Brener, and Y. S. Kivshar, "Shaping photoluminescence spectra with magnetoelectric resonances in all-dielectric nanoparticles," *ACS Photonics*, vol. 2, pp. 172–177, jan 2015.

[192] B. Zhou, , M. Liu, Y. Wen, Y. Li, and R. Chen, "Atomic layer deposition for quantum dots based devices," *Opto-Electronic Advances*, vol. 3, no. 9, pp. 19004301–19004314, 2020.

[193] F. Todisco, R. Malureanu, C. Wolff, P. A. D. Gonçalves, A. S. Roberts, N. A. Mortensen, and C. Tserkezis, "Magnetic and electric mie-exciton polaritons in silicon nanodisks," *Nanophotonics*, vol. 9, pp. 803–814, mar 2020.

[194] S. Lepeshov, M. Wang, A. Krasnok, O. Kotov, T. Zhang, H. Liu, T. Jiang, B. Korgel, M. Terrones, Y. Zheng, and A. Alú, "Tunable resonance coupling in single si nanoparticle–monolayer ws2 structures," *ACS Applied Materials and Interfaces*, vol. 10, pp. 16690–16697, apr 2018.

[195] A. F. Cihan, A. G. Curto, S. Raza, P. G. Kik, and M. L. Brongersma, "Silicon mie resonators for highly directional light emission from monolayer MoS2," *Nature Photonics*, vol. 12, pp. 284–290, apr 2018.

[196] T. Bucher, A. Vaskin, R. Mupparapu, F. J. F. Löchner, A. George, K. E. Chong, S. Fasold, C. Neumann, D.-Y. Choi, F. Eilenberger, F. Setzpfandt, Y. S. Kivshar, T. Pertsch, A. Turchanin, and I. Staude, "Tailoring photoluminescence from mos2 monolayers by mie-resonant metasurfaces," *ACS Photonics*, vol. 6, pp. 1002–1009, mar 2019.

[197] M. Decker, I. Staude, M. Falkner, J. Dominguez, D. N. Neshev, I. Brener, T. Pertsch, and Y. S. Kivshar, "High-efficiency dielectric huygens' surfaces," *Advanced Optical Materials*, vol. 3, pp. 813–820, feb 2015.

[198] V. E. Babicheva and A. B. Evlyukhin, "Resonant lattice kerker effect in metasurfaces with electric and magnetic optical responses," *Laser and Photonics Reviews*, vol. 11, p. 1700132, oct 2017.

[199] H. K. Shamkhi, K. V. Baryshnikova, A. Sayanskiy, P. Kapitanova, P. D. Terekhov, P. Belov, A. Karabchevsky, A. B. Evlyukhin, Y. Kivshar, and A. S. Shalin, "Transverse scattering and generalized kerker effects in all-dielectric mie-resonant metaoptics," *Physical Review Letters*, vol. 122, p. 193905, may 2019.

[200] B. Choi, M. Iwanaga, Y. Sugimoto, K. Sakoda, and H. T. Miyazaki, "Selective plasmonic enhancement of electric- and magnetic-dipole radiations of er ions," *Nano Letters*, vol. 16, pp. 5191–5196, jul 2016.

[201] A. Capretti, A. Lesage, and T. Gregorkiewicz, "Integrating quantum dots and dielectric mie resonators: A hierarchical metamaterial inheriting the best of both," *ACS Photonics*, vol. 4, pp. 2187–2196, aug 2017.

[202] V. Rutckaia, F. Heyroth, A. Novikov, M. Shaleev, M. Petrov, and J. Schilling, "Quantum dot emission driven by mie resonances in silicon nanostructures," *Nano Letters*, vol. 17, pp. 6886–6892, oct 2017.

[203] S. Yuan, X. Qiu, C. Cui, L. Zhu, Y. Wang, Y. Li, J. Song, Q. Huang, and J. Xia, "Strong photoluminescence enhancement in all-dielectric fano metasurface with high quality factor," *ACS Nano*, vol. 11, pp. 10704–10711, oct 2017.

[204] M. Khoury and M. Abbarchi, "A bright future for silicon in quantum technologies," *Journal of Applied Physics*, vol. 131, p. 200901, may 2022.

[205] F. Tian, H. Sumikura, E. Kuramochi, M. Takiguchi, M. Ono, A. Shinya, and M. Notomi, "All-optical dynamic modulation of spontaneous emission rate in hybrid optomechanical emitter-cavity systems," *Optica*, vol. 9, p. 309, mar 2022.

[206] N. Granchi, M. Montanari, A. Ristori, M. Khoury, M. Bouabdellaoui, C. Barri, L. Fagiani, M. Gurioli, M. Bollani, M. Abbarchi, and F. Intonti, "Near-field hyper-spectral imaging of resonant mie modes in a dielectric island," *APL Photonics*, vol. 6, p. 126102, dec 2021.

[207] A. Vaskin, R. Kolkowski, A. F. Koenderink, and I. Staude, "Light-emitting metasurfaces," *Nanophotonics*, vol. 8, pp. 1151–1198, jul 2019.

[208] M. E. Reimer, G. Bulgarini, A. Fognini, R. W. Heeres, B. J. Witek, M. A. M. Versteegh, A. Rubino, T. Braun, M. Kamp, S. Höfling, D. Dalacu, J. Lapointe, P. J. Poole, and V. Zwiller, "Overcoming power broadening of the quantum dot emission in a pure wurtzite nanowire," *Physical Review B*, vol. 93, p. 195316, may 2016.

[209] J. Claudon, J. Bleuse, N. S. Malik, M. Bazin, P. Jaffrennou, N. Gregersen, C. Sauvan, P. Lalanne, and J.-M. Gérard, "A highly efficient single-photon source based on a quantum dot in a photonic nanowire," *Nature Photonics*, vol. 4, pp. 174–177, jan 2010.

[210] P. Stepanov, A. Delga, N. Gregersen, E. Peinke, M. Munsch, J. Teissier, J. Mørk, M. Richard, J. Bleuse, J.-M. Gérard, and J. Claudon, "Highly directive and gaussian far-field emission from "giant" photonic trumpets," *Applied Physics Letters*, vol. 107, p. 141106, oct 2015.

[211] P. Senellart, G. Solomon, and A. White, "High-performance semiconductor quantum-dot single-photon sources," *Nature Nanotechnology*, vol. 12, pp. 1026–1039, nov 2017.

[212] I. Suarez, T. Wood, J. P. M. Pastor, D. Balestri, S. Checcucci, T. David, L. Favre, J. B. Claude, D. Grosso, A. F. Gualdron-Reyes, M. Abbarchi, and M. Gurioli, "Enhanced nanoscopy of individual cspbbr3 perovskite nanocrystals using dielectric sub-micrometric antennas," *APL Materials*, vol. 21109, 2020.

[213] M. Abbarchi, M. Naffouti, M. Lodari, M. Salvalaglio, R. Backofen, T. Bottein, A. Voigt, T. David, J.-B. Claude, M. Bouabdellaoui, A. Benkouider, I. Fraj, L. Favre, A. Ronda, I. Berbezier, D. Grosso, and M. Bollani, "Solid-state dewetting of single-crystal silicon on insulator: effect of annealing temperature and patch size," *Microelectronic Engineering*, vol. 190, pp. 1–6, apr 2018.

[214] I. Tiginyanu, V. Ursaki, and V. Popa, "Nanoimprint lithography (NIL) and related techniques for electronics applications," *Elsevier*, pp. 280–329, 2011.

[215] C. J. Lawrence, "The mechanics of spin coating of polymer films," *Physics of Fluids*, vol. 31, no. 10, p. 2786, 1988.

[216] B. S. Yilbas, A. Al-Sharafi, and H. Ali, "Surfaces for self-cleaning," *Elsevier*, pp. 45–98, 2019.

[217] C. Acikgoz, M. A. Hempenius, J. Huskens, and G. J. Vancso, "Polymers in conventional and alternative lithography for the fabrication of nanostructures," *European Polymer Journal*, vol. 47, pp. 2033–2052, nov 2011.

[218] J. P. Fernández-Blázquez, D. Fell, E. Bonaccurso, and A. del Campo, "Superhydrophilic and superhydrophobic nanostructured surfaces via plasma treatment," *Journal of Colloid and Interface Science*, vol. 357, pp. 234–238, may 2011.

[219] S. Franchi, "Molecular beam epitaxy," *Elsevier*, pp. 1–46, 2013.

[220] Jean-BenoîtClaude, *Etude des mécanismes de nanogravure par FIB-LMAIS*. PhD thesis, Aix-Marseille Université, 2017.

[221] L. Zhou, K. Nyberg, and A. C. Rowat, "Understanding diffusion theory and fick's law through food and cooking," *Advances in Physiology Education*, vol. 39, pp. 192–197, sep 2015.

[222] K. Vedam, "Spectroscopic ellipsometry: a historical overview," *Thin Solid Films*, vol. 313-314, pp. 1–9, feb 1998.

[223] K. Dorywalski, I. Maciejewski, and T. Krzyżyński, "Spectroscopic ellipsometry technique as a materials characterization tool for mechatronic systems—the case of composition and doping concentration monitoring in SBN crystals," *Mechatronics*, vol. 37, pp. 33–41, aug 2016.

[224] Y. Oni, K. Hao, S. Dozie-Nwachukwu, J. D. Obayemi, O. S. Odusanya, N. Anuku, and W. O. Soboyejo, "Gold nanoparticles for cancer detection and treatment: The role of adhesion," *Journal of Applied Physics*, vol. 115, no. 8, p. 084305, 2014.

[225] B. T. Tomoda, P. H. Yassue-Cordeiro, J. V. Ernesto, P. S. Lopes, L. O. Péres, C. F. da Silva, and M. A. de Moraes, "Characterization of biopolymer membranes and films: Physicochemical, mechanical, barrier, and biological properties," *Elsevier*, pp. 67–95, 2020.

[226] M.-F. Fiawoo, *Etude par microscopie électronique en transmission dela germination et de la croissance des nanotubes decarbone synthétisés à moyenne température*. PhD thesis, Université Paris Sud - Paris XI, 2009.

[227] S. Reyntjens and R. Puers, "A review of focused ion beam applications in microsystem technology," *Journal of Micromechanics and Microengineering*, vol. 11, pp. 287–300, jul 2001.

[228] P. Li, S. Chen, H. Dai, Z. Yang, Z. Chen, Y. Wang, Y. Chen, W. Peng, W. Shan, and H. Duan, "Recent advances in focused ion beam nanofabrication for nanostructures and devices: fundamentals and applications," *Nanoscale*, vol. 13, no. 3, pp. 1529–1565, 2021.

[229] W. H. J. Andersen, "Optimum adjustment and correction of the wien filter," *British Journal of Applied Physics*, vol. 18, pp. 1573–1579, nov 1967.

[230] W. Wien, "Untersuchungen über die electrische entladung in verdünnten gasen," *Annalen der Physik*, vol. 301, no. 6, pp. 440–452, 1898.

[231] D. C. Bell, M. C. Lemme, L. A. Stern, J. R. Williams, and C. M. Marcus, "Precision cutting and patterning of graphene with helium ions," *Nanotechnology*, vol. 20, p. 455301, oct 2009.

[232] J. E. Fröch, A. Bahm, M. Kianinia, Z. Mu, V. Bhatia, S. Kim, J. M. Cairney, W. Gao, C. Bradac, I. Aharonovich, and M. Toth, "Versatile direct-writing of dopants in a solid state host through recoil implantation," *Nature Communications*, vol. 11, oct 2020.

[233] M. S. Lafleur, P. F. Hinrichsen, P. C. Landry, and R. B. Moore, "The poisson distribution," *The Physics Teacher*, vol. 10, pp. 314–321, sep 1972.

[234] M. Garcia-Lechuga, O. Utéza, N. Sanner, and D. Grojo, "Evidencing the nonlinearity independence of resolution in femtosecond laser ablation," *Optics Letters*, vol. 45, p. 952, feb 2020.

[235] D. Berhanuddin, *Generation and characterisation of the carbon g-centre in silicon*. PhD thesis, University of Surrey, 2015.

[236] C. P. Foy, M. C. do Carmo, G. Davies, and E. C. Lightowlers, "Uniaxial stress measurements on the 0.97 eV line in irradiated silicon," *Journal of Physics C: Solid State Physics*, vol. 14, pp. L7–L12, jan 1981.

[237] P. Werner, U. Gösele, H.-J. Gossmann, and D. C. Jacobson, "Carbon diffusion in silicon," *Applied Physics Letters*, vol. 73, pp. 2465–2467, oct 1998.